Seismic site response characterisation supported by geostatistical analysis, geomodelling and numerical simulations:

Application to seismically active regions of Haiti

A thesis submitted for the degree of

Doctor of Sciences

presented by

Valmy DORIVAL

University of Liege
Department of Geology
Georisk & Environment Unit

January 2026

Seismic site response characterisation supported by geostatistical analysis, geomodelling and numerical simulations:

Application to seismically active regions of Haiti

A thesis submitted for the degree of
Doctor of Sciences

presented by

Valmy DORIVAL

Members of the Doctoral Jury:

Professor Nathalie Fagel
Liège Université, Belgium — *President*

Dr. Hans-Balder Havenith
Liège Université, Belgium — *Supervisor*

Professor Kelly Guerrier
Université d'Etat d'Haïti, Haiti — *Co-Supervisor*

Dr. Sonia Devi
Liège Université, Belgium — *Secretary*

Professor Frédéric Nguyen
Liège Université, Belgium

Dr. Sophia Ulysse
Université d'Etat d'Haïti, Haiti

Dr. Afifa Imtiaz
Eidgenössische Technische Hochschule Zürich, Switzerland

Acknowledgements

This doctoral thesis represents the outcome of several years of academic works and investigations. Its completion would not have been possible without the guidance, support and encouragement of many individuals and institutions, to whom I would like to express my deepest gratitude.

My sincere thanks go first to my supervisor, Dr. Hans-Balder Havenith, for his constant guidance, insight and support throughout this research. His expertise and constructive feedback were essential in shaping this work and addressing the various methodological and interpretative challenges encountered. I am also grateful to my co-supervisor, Dr. Kelly Guerrier, for his invaluable advice and for facilitating the fieldwork, providing practical support and ensuring that the data acquisition campaigns were conducted efficiently and safely.

I would like to thank the other members of the doctoral committee, Dr. Sophia Ulysse and Dr. Frederic Nguyen, for their constructive comments and suggestions.

I wish to extend my sincere gratitude to the members of the Georisk & Environment group at the Department of Geology – University of Liege for the stimulating and collaborative academic environment. In particular, I would like to thank Dr. Yawar Hussain and Dr. Lena Cauchie, formers postdoc researchers at the Department of Geology – University of Liege, for their valuable assistance with seismological data acquisition and processing, and Dr. Farkhod Hakimov (RWTH Aachen) for his support and discussions related to data analysis, modelling activities and interpretation of results.

I am especially grateful to Prof. Dominique Boisson, the coordinator of the research unit *URGéo – Faculté des Sciences – Université d'Etat d'Haïti*, for his support and confidence in my work throughout this thesis, and to all my colleagues at *URGéo* who significantly contributed to the progress of this research. I express my gratitude to Mr. Garry Jourdan, who also made a doctoral thesis in the framework of the same research project, Mr. Exumé J. M. Fontaine and Mr. Ronald Jerome for their practical support and cooperation during the data acquisition campaigns. I would also like to thank the group of students at *Faculté des Sciences – Université d'Etat d'Haïti*, Mr. Danielo Guerrier, Mrs. Jemima Baptichon and Mr. Jeff Divisien, who worked with me throughout the data collection campaigns in the framework of their graduation project.

I gratefully acknowledge the *Académie de Recherche et d'Enseignement Superieur – ARES* for the scholarship that made this doctoral work possible. I also thank the *Bureau des Mines et de l'Energie – Haïti* for providing access to data and resources essential to the completion of this study.

Finally, I would like to express my sincere gratitude to my family and my friends for their constant support and encouragement throughout this journey. I also wish to thank all those who, in one way or another, contributed to the completion of this thesis.

Remerciements

Cette thèse de doctorat est le résultat de plusieurs années de travaux universitaires et de recherches. Je n'aurais pas pu la mener à bien sans les conseils, le soutien et les encouragements de nombreuses personnes et institutions, auxquels je tiens à exprimer ma profonde gratitude.

Je tiens tout d'abord à remercier sincèrement mon directeur de thèse, Dr. Hans-Balder Havenith, pour ses conseils, ses idées et son soutien constants tout au long de cette recherche. Son expertise et ses commentaires constructifs ont été essentiels pour façonner ce travail et relever les différents défis méthodologiques et interprétatifs rencontrés. Je suis également reconnaissant à mon co-directeur de thèse, Dr. Kelly Guerrier, pour ses précieux conseils et pour avoir facilité le travail sur le terrain, en apportant un soutien pratique et en veillant à ce que les campagnes de collecte de données se déroulent de manière efficace et sûre.

Je tiens à remercier les autres membres du comité de la thèse, Dr. Sophia Ulysse et Dr. Frederic Nguyen, pour leurs commentaires et suggestions constructifs.

Je tiens à exprimer ma sincère gratitude aux membres du groupe Géorisques & Environnement du Département de Géologie de l'Université de Liège pour l'environnement académique stimulant et collaboratif. Je tiens tout particulièrement à remercier Dr. Yawar Hussain et Dr. Lena Cauchie, anciens chercheurs postdoctoraux au Département de Géologie de l'Université de Liège, pour leur précieuse aide dans l'acquisition et le traitement des données sismologiques, ainsi que Dr. Farkhod Hakimov (RWTH Aachen) pour son soutien et ses discussions concernant l'analyse des données, les étapes de modélisation et l'interprétation des résultats.

Je suis particulièrement reconnaissant au professeur Dominique Boisson, coordonnateur de l'unité de recherche URGéo de la Faculté des Sciences de Université d'État d'Haïti, pour son soutien et sa confiance dans mon travail tout au long de cette thèse, ainsi qu'à tous mes collègues de l'URGéo qui ont contribué de manière significative à l'avancement des travaux de recherche. Je tiens à exprimer ma gratitude à M. Garry Jourdan, qui a également rédigé une thèse de doctorat dans le cadre du présent projet de recherche, à M. Exumé J. M. Fontaine et à M. Ronald Jerome pour leur soutien pratique et leur coopération lors des campagnes d'acquisition de données. Je tiens également à remercier le groupe d'étudiants de la Faculté des Sciences de l'Université d'État d'Haïti, M. Danielo Guerrier, Mme Jemima Baptichon et M. Jeff Divisien, qui ont travaillé avec moi tout au long des campagnes de collecte de données dans le cadre de leur projet de fin d'études.

Je remercie chaleureusement l'Académie de Recherche et d'Enseignement Supérieur (ARES) pour le financement du projet qui a rendu possible ce travail de doctorat. Je remercie également le Bureau des Mines et de l'Énergie (BME, Haïti) pour avoir facilité l'accès à des données et ressources indispensables à la réalisation de cette étude.

Enfin, je tiens à exprimer ma sincère gratitude à ma famille et à mes amis pour leur soutien et leurs encouragements constants tout au long de ce parcours. Je tiens également à remercier toutes les personnes qui, d'une manière ou d'une autre, ont contribué à la réalisation de cette thèse.

Abstract

Earthquakes constitute one of the most destructive natural hazards, particularly in regions where complex geological settings coincide with high structural vulnerability. Haiti, located along the boundary between the Caribbean and North American plates, has experienced historical damaging earthquakes, and most recently the 12 January 2010 and the 14 August 2021 events. These earthquakes demonstrated that site effects play an important role in amplifying ground motion and controlling damage patterns, especially in urban areas constructed on soft sediments. The modelling of these effects is therefore essential for improving seismic hazard assessment and risk mitigation strategies in regions potentially exposed to major earthquake impacts.

The present study investigates local seismic amplification through an integrated framework combining geophysical-seismological surveys, geostatistical analysis, 3D geomodelling and numerical modelling in two seismically active regions of Haiti: Anse-à-Veau, near the Enriquillo-Plantain Garden Fault zone, and Cap-Haitien, near the Septentrional Fault zone. These sites were selected due to their geological context and historical seismicity.

In Anse-à-Veau, the study relies on geophysical methods, including ambient noise analysis using horizontal-to-vertical spectral ratios, earthquake recordings processed as standard spectral ratio, multichannel analysis of surface waves, seismic refraction tomography, and electrical resistivity tomography. In Cap-Haitien, the limited geophysical data are completed by borehole with standard penetration test from previous seismic microzonation studies. Geophysical parameters such as fundamental frequency, amplitude and shear wave velocity are analysed using geostatistical methods, including exploratory data analysis, variogram modelling, kriging and cokriging to generate spatially coherent site characterisation maps.

Three-dimensional geomodels are constructed for the two study areas coupled with geostatistical simulations and implicit modelling techniques to represent the geometry of the superficial deposits overlying the bedrock. These geomodels provide the structural basis for two-dimensional numerical simulations of seismic wave propagation. The modelled site response is compared with measured standard spectral ratios, allowing for the validation of the dynamic models and subsurface geometries.

The results demonstrate that sediment thickness and impedance contrast influence largely the local seismic amplification in the two study areas, locally enhanced by topographic effects. Soft alluvial deposits generate strong low frequency amplification, while colluvial and soft limestone units contribute to minor site effects. The agreement between observed and modelled site responses confirms the robustness of the proposed integrated methodology. This work contributes to seismic microzonation in Haiti and establishes a transferable framework for local seismic hazard assessment in regions characterized by geological complex settings and limited data availability.

Résumé

Les séismes constituent l'un des aléas naturels les plus destructeurs, notamment dans les régions où des conditions géologiques complexes coïncident avec une forte vulnérabilité structurelle. Haïti, située à la frontière des plaques caraïbe et nord-américaine, a connu des séismes historiques dévastateurs, et plus récemment ceux du 12 janvier 2010 et du 14 août 2021. Ces séismes ont démontré que les effets locaux jouent un rôle important dans l'amplification des mouvements du sol et la distribution des dommages, en particulier dans les zones urbaines construites sur des sédiments meubles. La modélisation de ces effets est donc essentielle pour améliorer l'évaluation de l'aléa sismique et les stratégies de réduction des risques dans les régions potentiellement exposées à des séismes majeurs.

La présente étude s'intéresse aux effets d'amplification sismique locale à travers un cadre intégré combinant investigations géophysiques et sismologiques, analyse géostatistique, géomodélisation 3D et modélisation numérique dans deux régions sismiquement actives d'Haïti : Anse-à-Veau, près de la zone de faille d'Enriquillo-Plantain Garden, et Cap-Haïtien, près de la zone de faille septentrionale. Ces sites ont été sélectionnés en raison de leur contexte géologique et de leur sismicité historique. À Anse-à-Veau, l'étude s'appuie sur des méthodes géophysiques classiques, notamment l'analyse du bruit ambiant par les rapports spectraux horizontal/vertical, les enregistrements sismiques traités selon le rapport spectral standard, l'analyse multicanaux des ondes de surface, la tomographie de réfraction sismique et la tomographie de résistivité électrique. Au Cap-Haïtien, les données géophysiques, limitées, sont complétées par des forages avec test de pénétration standard réalisés dans le cadre d'études de microzonage sismique antérieures. Les paramètres géophysiques, tels que la fréquence fondamentale, l'amplitude et la vitesse des ondes de cisaillement, sont analysés par des méthodes géostatistiques, incluant l'analyse exploratoire des données, la modélisation du variogramme, le krigeage et le cokrigeage, afin de générer des cartes de caractérisation de site spatialement cohérentes.

Des géomodèles 3D sont construits pour les deux zones d'étude, couplés à des simulations géostatistiques et des techniques de modélisation implicite, afin de représenter la géométrie des dépôts superficiels recouvrant le substratum rocheux. Ces géomodèles constituent la base structurale de la simulation numérique de la propagation des ondes sismiques. La réponse de site modélisée est comparée aux rapports spectraux standards mesurés, permettant ainsi la validation des modèles dynamiques employés et la géométrie du sous-sol.

Les résultats démontrent que l'épaisseur des sédiments et le contraste d'impédance influencent fortement l'amplification sismique locale dans les deux zones d'étude, localement renforcée par des effets topographiques. Les dépôts alluviaux meubles génèrent de forte amplification à basse fréquence, alors que les colluvions et les formations calcaires contribuent à des effets de site mineurs. La concordance entre les réponses de site observées et modélisées confirme la robustesse de la méthodologie intégrée proposée. Ce travail contribue au microzonage sismique en Haïti et établit un cadre transposable pour l'évaluation locale des aléas sismiques dans les régions caractérisées par des contextes géologiques complexes et une disponibilité limitée des données.

Table of Contents

1 Introduction

1.1 General context

Earthquakes are the most sudden destructive natural events we face (Aki and Richards 2002). In a matter of seconds, they can bring down buildings, sever infrastructure and cause extensive human and economic losses. In some cases, the primary earthquake event is only the beginning, as secondary hazards such as landslides, tsunamis or soil liquefaction can follow. Despite significant scientific progress in understanding tectonic processes and seismic wave propagation, earthquakes remain inherently unpredictable in terms of precise time and location. This unpredictability has shifted the focus of seismic risk management toward preparedness, prevention and mitigation, using probabilistic and deterministic methods.

Major seismic disasters in recent decades have demonstrated how vulnerable our cities can be when the ground starts to shake. One of the most striking examples is the 1985 Mexico earthquake (Mw 8.0). Even though the epicentre was hundreds of kilometres away from the capital, the city experienced long and intense shaking, leading to the collapse of many large buildings (Anderson et al. 1986). The disaster revealed how the natural environment can strongly influence the level of damage.

Another highly instructive event is the 1995 Kobe earthquake in Japan (Mw 6.9). Despite the Japan strong culture of earthquake awareness, the sudden rupture beneath the city caused widespread destruction, including the collapse of elevated highways and severe losses in densely populated neighbourhoods. The Kobe earthquake highlighted how vulnerable even well-prepared urban areas can be when a large earthquake occurs (Wald 1996).

A different type of tragedy occurred during the 2003 Bam earthquake in Iran (Mw 6.6). Here, the moderate magnitude masked the potential for disaster, but the combination of fragile adobe housing, high population density, and the timing of the earthquake led to more than 25 000 deaths (Bouchon et al. 2006). Bam demonstrated that the social and structural vulnerability of a community can be just as important as the strength of the earthquake itself. In 2008, the Wenchuan earthquake in China (Mw 7.9) caused widespread destruction across mountainous regions of Sichuan Province (Hartzell et al. 2013). Entire villages were buried under landslides, and major infrastructure systems (such a numerous flyovers, bridges, dams) failed.

The 2010 Haiti earthquake (Mw 7.0) remains one of the most tragic disasters of the 21st century. Located at the boundary of two tectonic plates (the Caribbean Plate and the North American Plate**,** Fig. 1.1), the territory of Haiti lies within a region of high seismic activity. The country has experience numerous major earthquakes throughout its history (Scherer 1912; Woodring et al. 1924; Bakun et al. 2012; Flores et al. 2012), and more recently, the 14 August 2021 earthquake in the Nippes department (Calais et al. 2022; Raimbault et al. 2023; Douilly et al. 2023) and the 12 January 2010 earthquake, much more devastating than the previous, as it caused widespread

destruction in the capital, Port-au-Prince, and surrounding areas (Calais et al. 2010; Rathje et al. 2011; Marshall et al. 2011; Paultre et al. 2013).

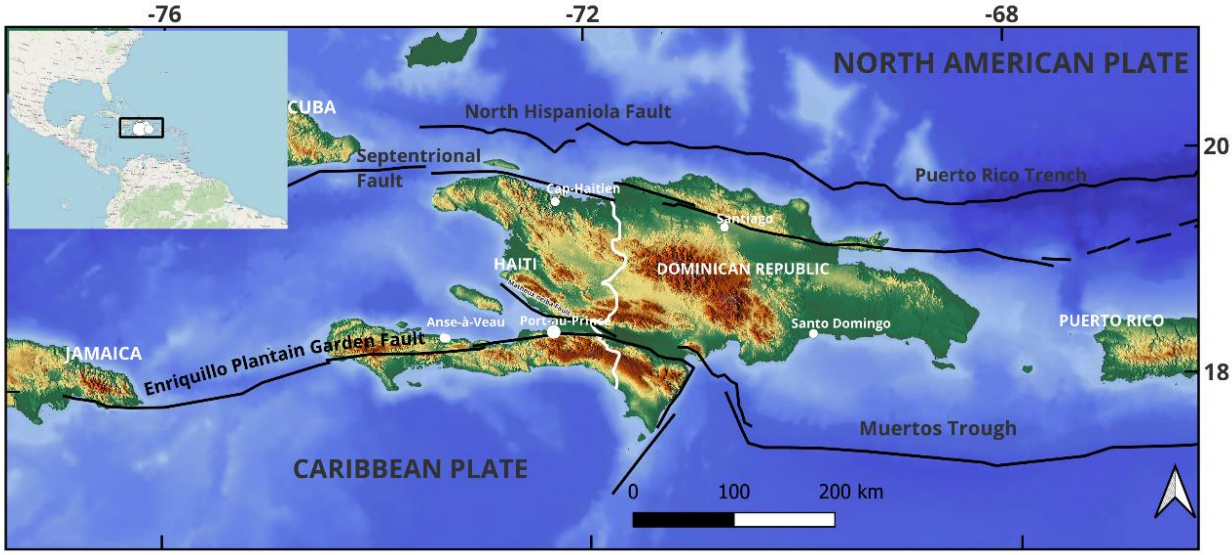

Fig. 1.1 Geographic and tectonic settings of Haiti (western part of Hispaniola Island) at the boundary of the Caribbean and the North American plates.

The recent earthquakes demonstrated the vulnerability of the country to seismic hazard and emphasized the importance of constructing houses and infrastructure that meet earthquake-resistant standards (Marshall et al. 2011; Paultre et al. 2013), understanding the seismic hazard and how communities are affected by earthquakes, how they prepare for seismic events, and how they contribute to the seismic hazard assessment (Calais et al. 2020). By understanding and assessing the seismic hazard, we can reduce the vulnerability and, therefore, the seismic risk in Haiti.

Studies on seismic hazard assessment have been completed in Haiti after the 12 January 2010 earthquake such as the production of the probabilistic seismic hazard maps by Frankel et al. (2011). The maps produced provide ground motion values that generally decrease with distance from the seismic sources according to the phenomenon of attenuation (Aki and Richards 2002). However, the areas with soft soils or complex topographies require special attention during seismic hazard assessments to ensure that local seismic amplification are properly considered (Borcherdt and Gibbs 1976; Geli et al. 1988). By integrating the site effects, the assessment can provide a more realistic understanding of the risk which is very important in urban areas with concentrated infrastructure (de Risi et al. 2019).

After the 12 January 2010 earthquake, several studies have been also carried out for the local seismic hazard assessment in the capital Port-au-Prince (Hough et al. 2011; Bertil et al. 2013; St-Fleur et al. 2016; Ulysse et al. 2018), in Cap-Haitien, the north of the country (Bertil et al. 2014), and Fonds-Parisien, 37 km to the west of Port-au-Prince (Ulysse et al. 2021). Although the extent of structural damage in the 2010 earthquake was largely due to poor construction, these studies

show that a lot of damage observed during the 2010 earthquake can be explained by the geological and morphological conditions of the local ground.

The present thesis is about site amplification, geomodelling and seismic shaking simulation based on geostatistical analysis of geophysical-seismological data in two seismically active areas of Haiti: Anse-à-Veau, in the Enriquillo Plantain Garden Fault zone, and Cap-Haitien, in the Septentrional Fault zone (Fig. 1.1). Anse-à-Veau has been affected by several historical earthquakes (Scherer 1912; Woodring et al. 1924; Flores et al. 2012) and the recent 2021 Nippes earthquake; Cap-Haitien has been hit by the devastating 7 May 1842 earthquake (Scherer 1912; Woodring et al. 1924; Flores et al. 2012). The thesis is a part of a PRD (*Projet en Recherche et Développement*): Earthquake Hazard and Vulnerability assessment – developing innovative solutions for sustainable Risk Reduction and Communication in Haiti.

This work includes the first investigation on site amplification assessment carried out in the region of Anse-à-Veau. The city of Cap-Haitien and surroundings have been investigated in the framework of the seismic mircrozonation of Cap-Haitien (Bertil et al. 2014), but the present study is supported by geostatistical analysis of the data, geomodelling and 2D dynamic modelling. Local seismic response based on geophysical methods, geomodelling and numerical simulations has been also characterized in the eastern zone of the Enriquillo Plantain Garden Fault by Ulysse et al. (2018; 2021), but, in the present work, the geophysical methods (supported by geostatistical analysis) are applied to areas located in coastal setting with more complex geological context. The geostatistical methods have become very popular over the past 20 years in general geosciences and has various applications, such as interpolation between scalar values, stress ellipticity (Mukul 1998), soil properties (Bourennane 1997) or geophysical prospecting (Bourges et al. 2012). Here, we try to take benefit of these capabilities to improve the local seismic hazard assessment in Haiti.

1.2 Seismically induced hazards – focus on site amplification

Studies on local seismic amplification have been critical for understanding the distribution of the damage observed during an earthquake and the seismic hazard in seismically active areas (Borcherdt and Gibbs 1976; Bard and Bouchon 1980; Bard et al. 1988; Ohmachi et al. 1988; Borcherdt and Glassmoyer 1992; Seed et al. 1991; Homan and Eastwood 2001; Zhou 2018; Luo et al. 2020; Hartzell et al. 1994; Spudich et al. 1996; Assimaki et al. 2005). The amplification can happen in soft soils or unconsolidated sediments (lithological site effects), or in complex topographies like hills or ridges (topographic effects; see location of related effects in Fig. 1.2). They are the earthquake direct effects. The earthquake can also trigger other effects like soil liquefaction and landslides, which are considered as earthquake-induced effects. Liquefaction is linked to the dynamic behaviour of a soil, making it go from a solid and stable consistency to a liquid and unstable state during dynamic stress such as seismic acceleration (Youd and Idriss 2001; Andrus and Stokoe 2000; Idriss and Boulanger 2006). Landslides are mass movements of soil or rock down a slope that can be triggered by a variety of factors including earthquakes (Havenith et

al. 2022; Gorum et al. 2011). The present work is, however, focused on the direct effects and viscoelastic types (amplification) of seismic deformation as described below.

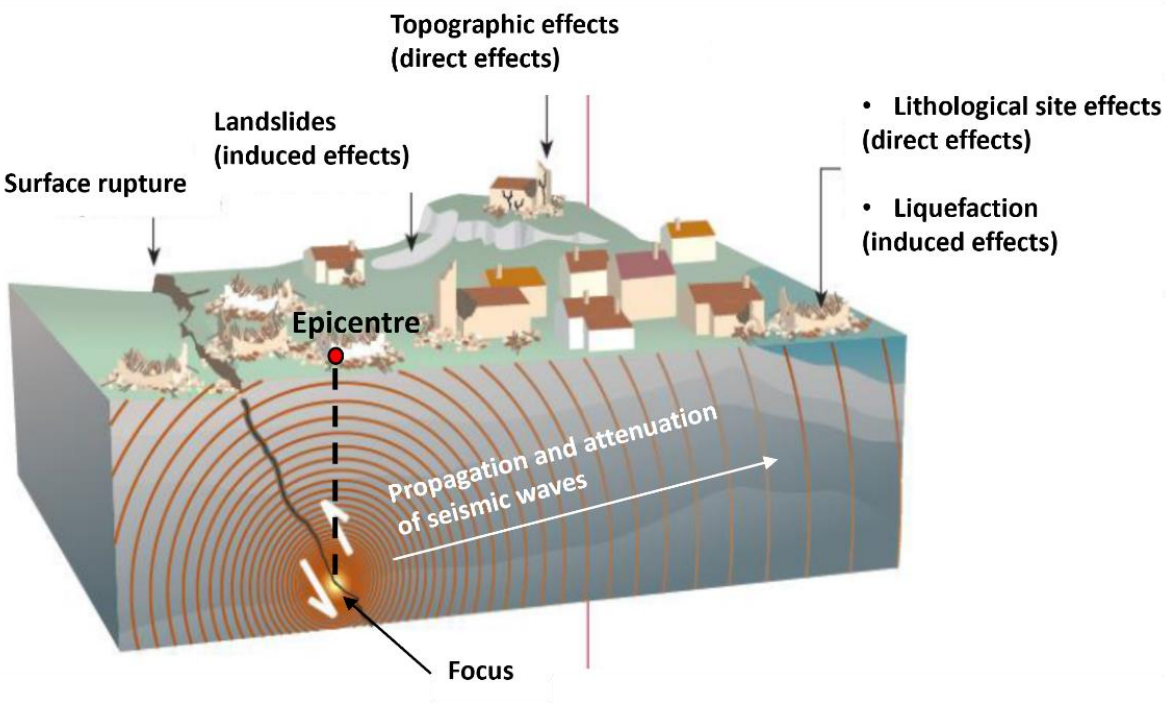

Fig. 1.2 Schematic representation of seismic hazards including the earthquake direct and induced effects (modified from Bertil et al. 2013).

1.2.1 Lithological site effects

Consequences of lithological site effects are observed during earthquakes, when areas built on soft soils, alluvial or unconsolidated sediments suffer greater damage than those built on hard rock. Soft soils slow down the seismic waves and amplify them, while harder and more compact soils allow them to propagate more quickly and attenuate their intensity on the ground (Borcherdt and Gibbs 1976; Bard and Bouchon 1980). Case studies of different earthquakes around the world provide concrete examples of how lithology influences the effects of an earthquake.

The 1985 Mexico earthquake is a classic case of site amplification due to lithology (Bard et al. 1988). The significant destruction in Mexico City, located 400 km from the epicentre, was caused by the amplification of ground motions due to the soft lacustrine clay deposits (Ohmachi et al. 1988). The 1989 Loma Prieta earthquake highlighted the lithological effects, particularly in the urban area of San Francisco where the shaking was amplified by the soft alluvial soils in the San Francisco Bay area (Borcherdt and Glassmoyer 1992; Seed et al 1991). The 1999 Kocaeli earthquake in Turkey (Homan and Eastwood 2001) also demonstrated the impact of the lithology on the intensity of shaking (Kudo et al. 2002). The areas with soft soils experienced seismic amplification due to their low resistance to the propagation of seismic waves.

During the 2010 Haiti earthquake, the capital Port-au-Prince and surroundings experienced seismic amplification, particularly in areas built on soft soils, which contribute to the intensity of the vibrations felt on the ground and the worsening of the damage (Rathje et al. 2011). Bertil et al. (2013) mapped these site effects in the framework of the seismic microzonation of Port-au-Prince completed after the earthquake. St-Fleur et al. (2016) investigated the site effects in the Port-au-Prince metropolitan area by analysing earthquakes with magnitude under 5 occurred between 2010 and 2013, as well as available geotechnical and geophysical data. Ulysse et al. (2018) used a geophysical-seismological approach that include ambient noise and earthquake recordings, seismic and electrical profiles, and existing geotechnical data to better understand the ground motion amplification on the Gros-Morne hill area, in the southeastern part of Port-au-Prince. Cox et al. (2011) also provided a seismic site classification microzonation for the city of Port-au-Prince based on 35 shear wave velocity profiles and a geologic map developed from a combination of field mapping and geomorphic interpretation of a digital elevation model.

1.2.2 Topographic effects

The effect of topography is linked to the change observed in the intensity and the duration of the shaking due to the variations in land morphology such as the presence of hills, valleys or ridges (Zhou 2018; Luo et al. 2020). Indeed, the top of a hill may experience significantly stronger shaking compared to the base of the hill due to the focusing of seismic energy. Topographic amplification is not commonly incorporated in seismic microzonation because its significant effect is assumed to be rare (Hough et al. 2010).

Several studies have been carried out on the influence of topographic effects on seismic waves propagation following some major earthquakes. Hartzell et al. (1994) investigated the role of local topography on the site response at Robinwood Ridge, California after the 1989 Loma Prieta earthquake. Spudich et al. (1996) studied directional topographic site response at Tarzana observed in aftershocks of the 1994 Northridge, California, earthquake. Assimaki et al. (2005) illustrated how soil stratigraphy and material heterogeneity can influence the topographic of surface ground motion based on parametric investigation and recorded field evidence from the 1999 Athens earthquake. Hough et al. (2010) show that topographic amplification contributed to localized damage observed in Petion-Ville, on the hills above Port-au-Prince, during the 2010 Haiti earthquake. The studies completed by Ulysse et al. (2018; 2018a) and St-Fleur et al. (2016) also indicate the contribution of topography to the site effects observed in the Port-au-Prince region during the 2010 earthquake (see examples of related modelling results in Fig. 1.3).

1.3 Modelling of seismic site amplification

The modelling process involves the creation of geomodels (geomodelling) that provide a detailed understanding of subsurface structures and numerical models (dynamic modelling) that are used as environment to simulate the propagation of seismic waves.

Geomodels are increasingly constructed in several studies including site amplification and landslides modelling (Ulysse et al. 2018a; Havenith et al. 2018; Hakimov et al. 2024). Panzera et al. (2022) reconstructed a 3D model of the subsurface from a large dataset of geological and geophysical data for site amplification modelling of an area in the upper Rhone valley, in the southwestern part of Switzerland. Seismic microzonation studies are also increasingly relying on geomodels for numerical modelling of seismic ground motion as showed by Hakimov et al. (2024) in the case of Dushanbe city, the capital of Tajikistan.

The site of Gros-Morne hill, in the southeastern part of Port-au-Prince (Haiti), was investigated by Ulysse et al. (2018a) using geological and numerical models to understand the ground motion amplification that might have influenced the 2010 event damage pattern in the area. The models were based on multiple geophysical–seismological data and attributed the strong seismic amplification effects to the influence of local topography and soil characteristics.

Local effects assessment based on dynamic numerical modelling are used in various studies (Klin et al. 2010; Gaudiosi et al. 2014; Chaljub et al. 2015; Smerzini et al. 2017). To simulate the combined effect of topographic and geological controls in slope response to seismic motions, Luo et al. (2020) used 2D and 3D dynamic numerical modelling. The models were created using high resolution digital elevation model from a UAV (Unmanned Aerial Vehicle), and geological properties from geophysical surveys. Their simulation results highlighted the importance of considering the combined topographic and lithological effects in the hazard assessment of seismically induced slope failures.

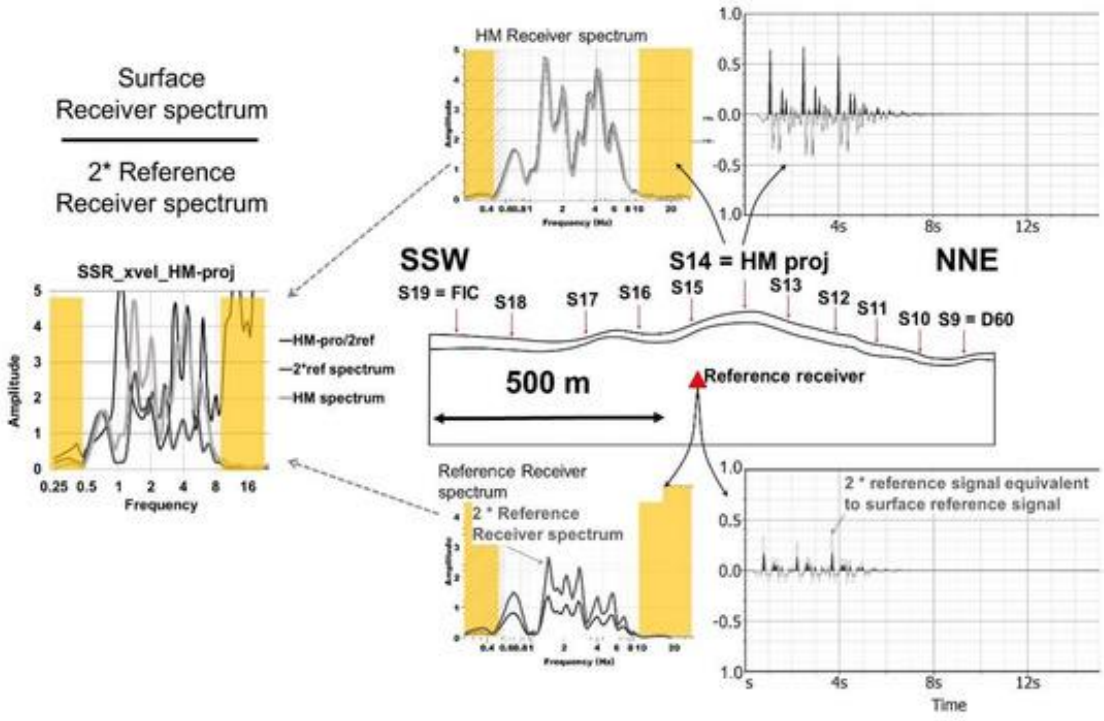

Fig. 1.3 Example of numerical modelling produced by Ulysse et al. (2018a) to simulate the local seismic response at the Gros-Morne hill (the southeastern part of Port-au-Prince, Haiti).

The simulation by dynamic numerical modelling is often performed on 2D geological cross-sections extracted from the 3D geomodels. In the case of Gros-Morne hill (the southeastern part of Port-au-Prince, Haiti), Ulysse et al. (2018a) used 2D geological cross-sections extracted from the 3D geomodel to calculate the local seismic response by 2D dynamic numerical modelling. Hakimov et al. (2024) applied the same procedure to Dushanbe city, the capital of Tajikistan. However, a procedure based on 1D simulation was used by St-Fleur et al. (2016) for the region of Port-au-Prince. They proposed a simplified lithostratigraphic map and used available geotechnical and geophysical data to produce representative soil columns in the vicinity of each available seismological stations to compute numerical transfer functions. Fig. 1.4 illustrates the comparison of the 1D numerical transfer functions (according to St-Fleur et al. 2016) computed at the studied sites with the corresponding standard spectral ratio (SSR) and horizontal-to-vertical earthquake spectral ratio (HVEQ) results.

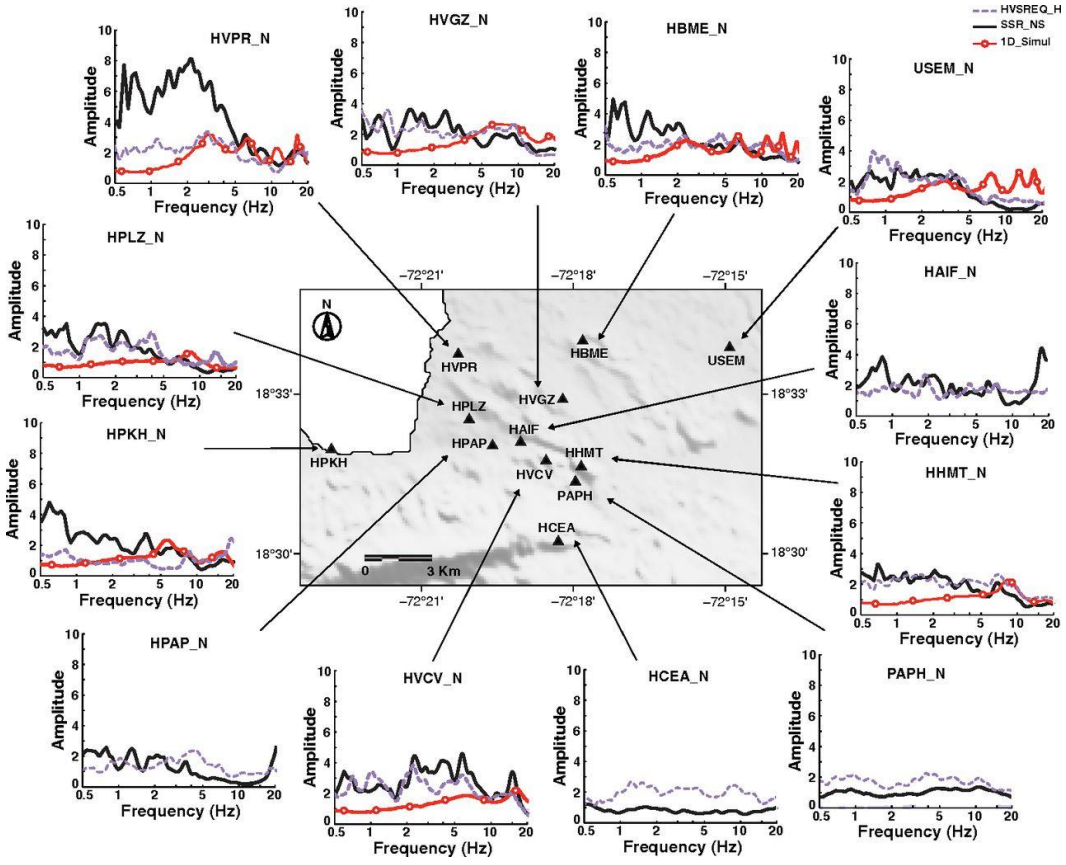

Fig. 1.4 Results of numerical modelling obtained by St-Fleur et al. (2016) for the Port-au-Prince region from 1D simulations. The red lines represent the 1D simulation of the seismic response of the soil. The other lines represent the results from experimental geophysical-seismological methods.

The integration of 3D and numerical modelling to site effects analysis (Hakimov et al. 2024) provides a robust framework for understanding and predicting ground motion variability across a study area. The geomodels used to perform the numerical modelling can be constructed within a

geostatistical framework which characterize the spatial distribution of geological formations, sediment thickness, and near-surface material properties (Dorival et al. 2025).

1.4 Geostatistical analysis of geophysical-seismological data

Geostatistics were initially developed to analyse geological data in the mining sector (Matheron 1970; Armstrong and Carignan 1997) but can be applied to any natural phenomenon that presents a spatial distribution according to a certain structure (Chauvet 1999). They are now widely used in geophysics, especially in seismic and geomechanical studies, to model spatially correlated data and improve our understanding of subsurface properties.

Several studies demonstrated the application of geostatistical methods in seismic data analysis, estimation and mapping of earthquake ground motion (Carr and Glass 2007; Kim et al. 2017; Lombardo and Tanyas 2022). Torcal et al. (1999) used a geostatistical conditional simulation to calculate the probability of occurrence of earthquakes belonging to a seismic series. Thompson et al. (2010) adopted a geostatistical approach based on region-specific data to estimate site response spectral amplifications with great spatial resolution and accuracy.

To investigate the probable scenario responsible for an earthflow in Kanima (Kyrgyzstan) occurred in April 2004, Danneels et al. (2008) created a 3D model using geostatistical analysis of geophysical-seismological data from an adjacent slope. Sgobba et al. (2024) performed a geostatistical modelling to identify dependencies between empirical amplification functions of sites in central Italy and the main geological and geophysical characteristics of the region.

1.5 Objectives and structure of the thesis

The general objective of the present thesis is to study the site effects that can amplify the ground shaking in two seismically active areas in Haiti (Anse-à-Veau and Cap-Haitien, Fig. 1.1). The reports on the damage caused by historical earthquakes (Scherer 1912; Flores et al. 2012) demonstrated that our two study areas have been submitted to site effects that aggravated the destruction of already poorly built houses. The recent 2021 Nippes earthquake showed evidence of site effects in Anse-à-Veau as well as the seismic microzonation in Cap-Haitien (Bertil et al., 2014).

The specific objectives are to:

- Characterise the superficial layers according to their compactness and their configuration, and construct site characterisation maps.
- Estimate the depth of the superficial deposits according to their contrast with the bedrock, and construct geomodels.
- Calculate the local seismic response according to dynamic numerical modelling applied to the constructed geomodels.

The implementation is summarized in Fig. 1.5. The data used for the first study area were collected during geophysical-seismological surveys carried out in Anse-à-Veau in the framework of the thesis. For the second study area, we use the data from the seismic microzonation of Cap-Haitien (Bertil et al. 2014) realized on behalf of the Haitian government by a cooperation of the BRGM (*Bureau de Recherches Géologiques et Minières*, France), the BME (*Bureau des Mines et de l'Energie*, Haiti), and the LNBTP (*Laboratoire National du Bâtiment et des Travaux Publics*, Haiti).

The site effect potential is first mapped according to experimental methods using the geophysical-seismological data, then supported by geomodelling and dynamic numerical modelling to simulate the ground shaking.

The surveys carried out at Anse-à-Veau include ambient noise and earthquake recordings processed in terms of horizontal to vertical spectral ratios (HVSR or H/V) and standard spectral ratios (SSR) respectively, seismic surveys along profiles processed as seismic refraction tomography (SRT) and multichannel analysis of surface wave (MASW), and electrical resistivity measurements along profiles processed as electrical resistivity tomography (ERT). All related results were then submitted to geostatistical analysis to produce site classification maps, geomodels and seismic simulation shaking using 2D dynamic modelling.

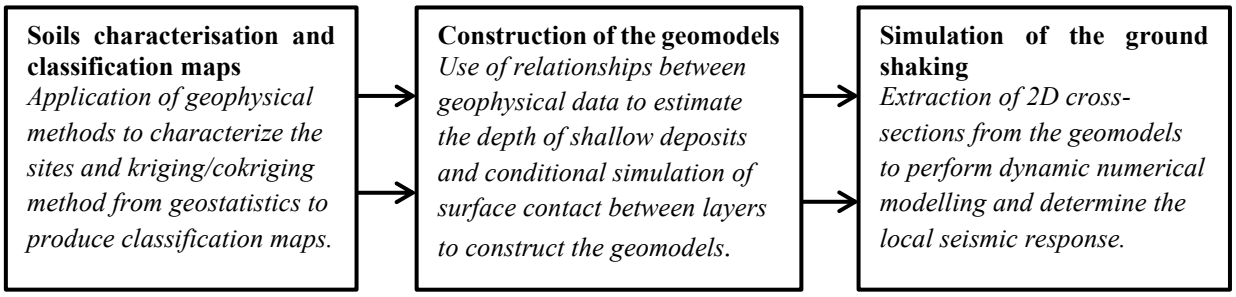

Fig. 1.5 Schematic representation of the workflow used in the present study.

The data compiled from the seismic microzonation of Cap-Haitien include ambient noise recordings, seismic measurements along profiles and geotechnical data from boreholes drilling. They were directly submitted to geostatistical analysis as they were already processed in the microzonation reports according to the same geophysical methods.

The geostatistical analysis was performed using R Statistical Software (R Core Team 2024). The geomodelling and the dynamic numerical modelling were respectively completed with the software Leapfrog Works (Sequent Limited ©) and the Universal Distinct Element Code software (UDEC, Itasca consulting group ©).

In chapter 2, we present the tectonic setting and the regional seismic hazard of Haiti and a detailed presentation of the study areas with seismotectonic and geological context.

The chapter 3 presents the geophysical-seismological methods with explanations of their applications to site effects assessment, the geostatistical methods as well as the geomodelling and dynamic numerical modelling methods.

In chapter 4, we present the data processing with the geophysical software, the soils characterisation according to geological interpretation and geophysical results.

The site classification maps using geostatistical analysis are presented in chapter 5 as well as ground motion maps for a reference earthquake using ground motion prediction equation (GMPE).

We present the geomodelling process and related results in chapter 6 with description of the input data obtained from geostatistical conditional simulation with the R Statistical Software and their integration to the software Leapfrog Works.

In chapter 7, we present the ground shaking simulation on 2D cross-sections extracted from prebuilt geomodels using dynamic numerical modelling with UDEC.

The general discussions and conclusions are respectively presented in chapter 8 and 9.

2 Study area

This chapter includes a general presentation of Haiti with its tectonic setting, geomorphological and seismological context in the first section. The other sections present the two study areas (Anse-à-Veau and Cap-Haitien) with detailed features on the seismotectonic and geological context of each region.

2.1 Tectonic setting and seismic hazard of Haiti

Haiti is located on the western part of the Hispaniola Island in the tectonic transition marked by the frontal subduction of the North American plate beneath the Caribbean plate (Fig. 2.1a), which is a wide complex zone partitioned between crustal faults within the island, and subduction zones off the northern and the southern coasts (Ali et al. 2008; Frankel et al. 2011). The island is crossed by two major strike-slip faults, the Septentrional and Enriquillo Plantain Garden faults in the northern and southern parts respectively, and by poorly known thrust faults such as the Matheux-Neiba fault in the middle part of the island (Mann et al. 1984; Calais et al. 2002). The northern coast of the island is located on an especially active subduction zone in the North Hispaniola Fault zone with a sequence of four large thrust earthquakes occurred from 1946 to 1953 (Frankel et al. 2011). The southeast marks the transition between the east end of the Enriquillo-Plantain Garden fault and the west end of the Muertos Trough which has some characteristics of a subduction zone off the southern coast (Mauffret and Leroy 1999; McCann 2006; Frankel et al. 2011).

The geographic and structural sets of the territory are made up of a series of anticlinal ranges separated by synclinal depressions from north to south. The anticlinal ranges are represented by two distinct units: the northern-central and southern mountains ranges separated by the synclinal depression called *La Plaine du Cul-de-Sac* (Butterlin, 1960). The general topography is linked, in large part, to the Pliocene Orogeny and, even more, to the posterior relative movements related to the faults dynamic (Butterlin 1960).

The southern mountains ranges are marked by the geographic and structural set of the southern peninsula with *Massif de la Hotte* in the west and *Massif de la Selle* in the east. The two highest peaks in the country are in the southern peninsula with *Pic Macaya* (~2400 m) in *Massif de la Hotte* and *Pic la Selle* (2680 m) in *Massif de la Selle* (Woodring et al. 1924; Butterlin 1960). The peninsula has an E-W general direction and includes a succession of faulted anticlines from *Massif de la Hotte* to *Massif de la Selle* (BME 2005). The first study area (Anse-à-Veau) is located on the northern coast of the southern peninsula.

The central and northern mountains form the anticlinal ranges roughly separated by synclinal depressions from the north of *La Plaine du Cul-de-Sac* to the north of Haiti (Woodring et al. 1924; Butterlin 1960; BME 2005). The northernmost mountain range, called *Massif du Nord*, is an anticlinal complex zone with NW-SE direction marked by the presence of inverse faults (BME 2005). *Massif du Nord* is separated from the sea by a coastal plain, *La Plaine du Nord*, that

represents the collapsed northeastern slope of the massif (Butterlin 1960; BME 2005). The second study area (Cap-Haitien) is located on the northern coast, in the geographic and structural set of *La Plaine du Nord*.

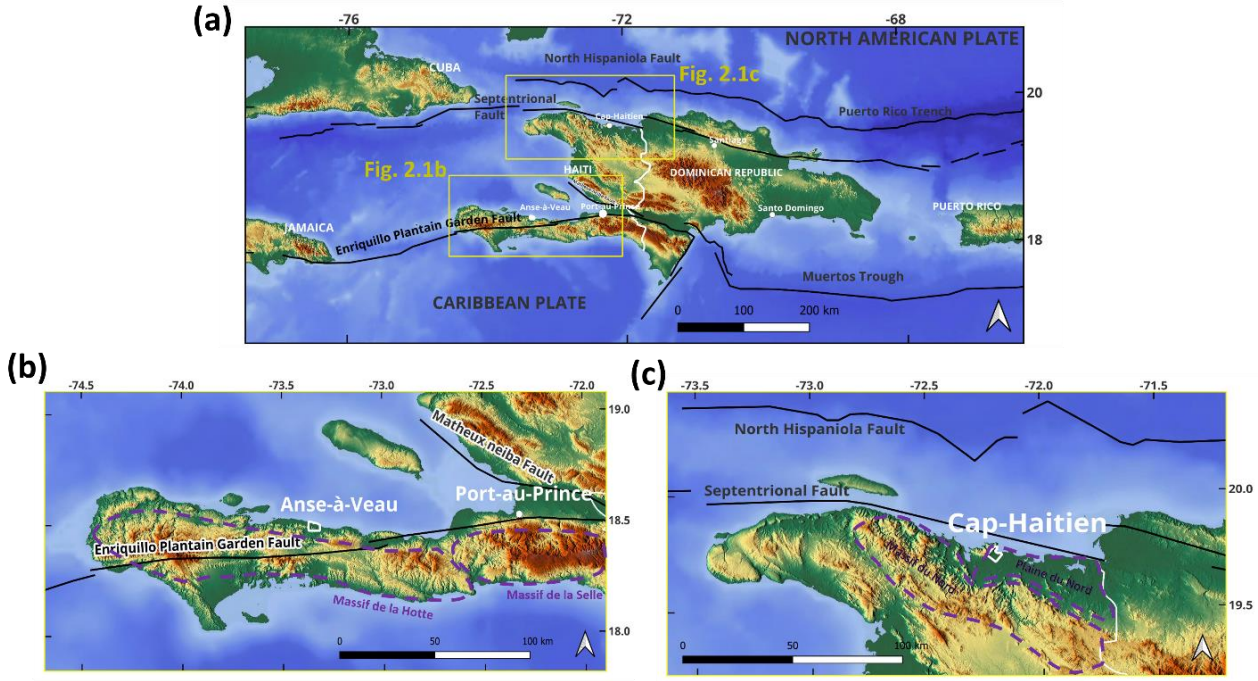

Fig. 2.1 (a) Seismotectonic context of Hispaniola Island (Haiti and Dominican Republic) with the main active faults in black lines (Calais et al. 2022; Bakun et al. 2012; Frankel et al. 2011). **(b)** The southern peninsula in the first study region with the southern mountains ranges: *Massif de la Hotte* in the west and *Massif de la Selle* in the east. **(c)** The northern coast in the second study region with the northernmost mountain range, *Massif du Nord*, and the coastal plain, *La Plaine du Nord*.

The relative motion between the Caribbean and North American plates is about 20 mm/yr and distributed between the subduction zones and the crustal faults (DeMets et al. 2000; Ali et al. 2008). In the seismic hazard assessment for Haiti by Frankel et al. (2011), the Septentrional Fault (SF) was inferred to accommodate 12 mm/yr, the Enriqillo Plantain Garden Fault (EPGF), 7 mm/yr, and the poorly known Matheux-Neiba Fault (MNF), 1 mm/yr. They followed the same basic methodology used to make the national seismic hazard maps in the United States (Frankel et al. 1996). First, they identified the seismic sources basing on the seismotectonic setting of Haiti (DeMets et al. 2000; Mann et al. 1984, 2002; Calais et al. 2002). The seismic sources include the major crustal faults and subduction zones (Calais et al. 2010; McCann 2006; Manaker et al. 2008; Prentice et al. 2003, 2010), as well as the spatially smoothed seismicity described in Frankel (1995) to incorporate the minor unmodeled faults that cannot be explicitly included in the hazard calculation and the random events outside the major crustal faults zone. Then, they applied a set of attenuation relations (Boore and Atkinson 2008; Campbell and Bozorgnia 2008; Chiou and Youngs 2008) to compute the ground motion values and produce the seismic hazard maps.

The seismic hazard maps in Fig. 2.2 present the peak ground accelerations (PGA) corresponding to 10% (Fig. 2.2a) and 2% (Fig. 2.2b) probabilities of exceedance (PE) in 50 years. They were produced after the 2010 earthquake by Frankel et al. (2011) assuming firm-rock site conditions. According to these maps, Haiti is subject to significant levels of seismic hazard across much of its territory. High hazard levels are particularly evident along the EPGF and SF systems, as well as along the North Hispaniola Fault and the Muertos Trough. In the case of 2% PE 50 years scenario, elevated hazard is also observed along the Matheux-Neiba Fault (MNF). Frankel et al. (2011) attributed this elevated (but less certain) hazard at low exceedance probability (along the MNF) to the long recurrence interval inferred from the fault relatively low slip rate estimated at ~1 mm/yr.

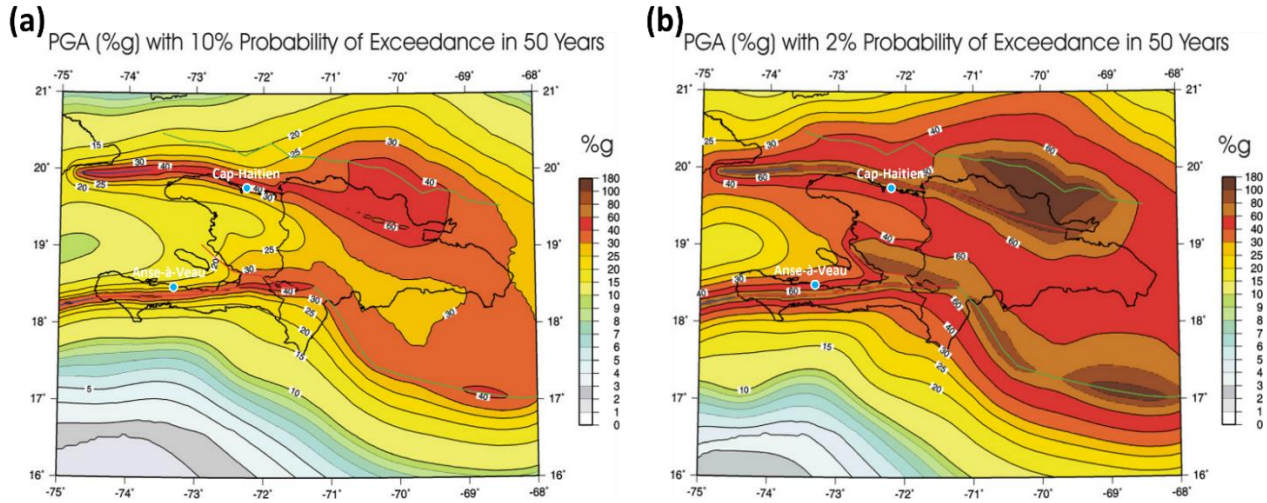

Fig. 2.2 Seismic hazard maps of Haiti produced after the 12 January 2010 earthquake by Frankel et al. (2011). **(a)** Hazard map of PGA (%g) with 10% probability of exceedance in 50 years, for a firm-rock site condition. **(b)** Hazard map of PGA (%g) with 2% probability of exceedance in 50 years, for a firm-rock site condition.

The eastern area of the EPGF across the southern peninsula had been investigated after the 2010 earthquake in the Port-au-Prince region (St-Fleur et al. 2016; Ulysse et al. 2018, 2018a), and 37 km to east of Port-au-Prince (Ulysse et al. 2021). At that time, it was established that western areas of the EPGF (near Anse-à-Veau, our study area 1) could have been hit in the future; this happened, indeed, on 14 August 2021. In Fig. 2.3, we present two examples of damage caused by the two major recent earthquakes occurred along the EPGF.

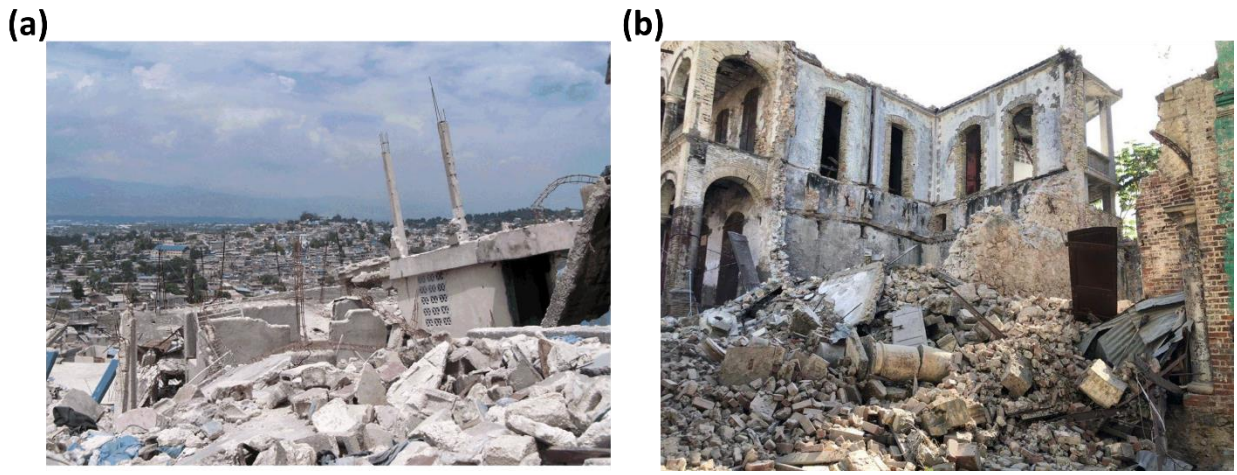

Fig. 2.3 (a) Example of damages caused by the 12 January 2010 earthquake in Port-au-Prince (illustrated by Rathje et al. (2011) in Damage patterns in Port-au-Prince during the 2010 Haiti earthquake). **(b)** Example of destruction caused by the 14 August 2021 earthquake in the southern peninsula (image by USAID's Bureau for Humanitarian Assistance).

2.2 Anse-à-Veau: study area 1

2.2.1 Seismotectonic context of the Anse-à-Veau region

Anse-à-Veau is a municipality in the Nippes department of Haiti marked by intense seismic activity. The region belongs to the geographic and structural set of the western part of the southern peninsula (Fig. 2.4) in the fault zone of the Enriquillo Plantain Garden Fault (EPGF). The peninsula is crossed by the fault, in a roughly east-west direction, at a few kilometres to the south of the study area. To the west, the EPGF continues to Plantain Garden in Jamaica. To the east, it extends to the Enriquillo Valley in the Dominican Republic where it might be connected to the Muertos Trough (Mauffret and Leroy 1999).

At the 73° W longitude, a possible segment boundary is observed in the EPGF trace (Frankel et al. 2011) where it makes a left transtensional step forming the Miragoane pull-apart basin (Momplaisir 1986; see central part of the map in Fig. 2.4). This segment boundary was considered as the westward limit to estimate the characteristic earthquake magnitude of the EPGF in the hazard calculation by Frankel et al. (2011). The fault was modelled as a vertical dipping fault because it was not clear whether its average behaviour can be represented by south dipping fault as suggested by some evidence from geologic mapping (Prentice et al. 2010).

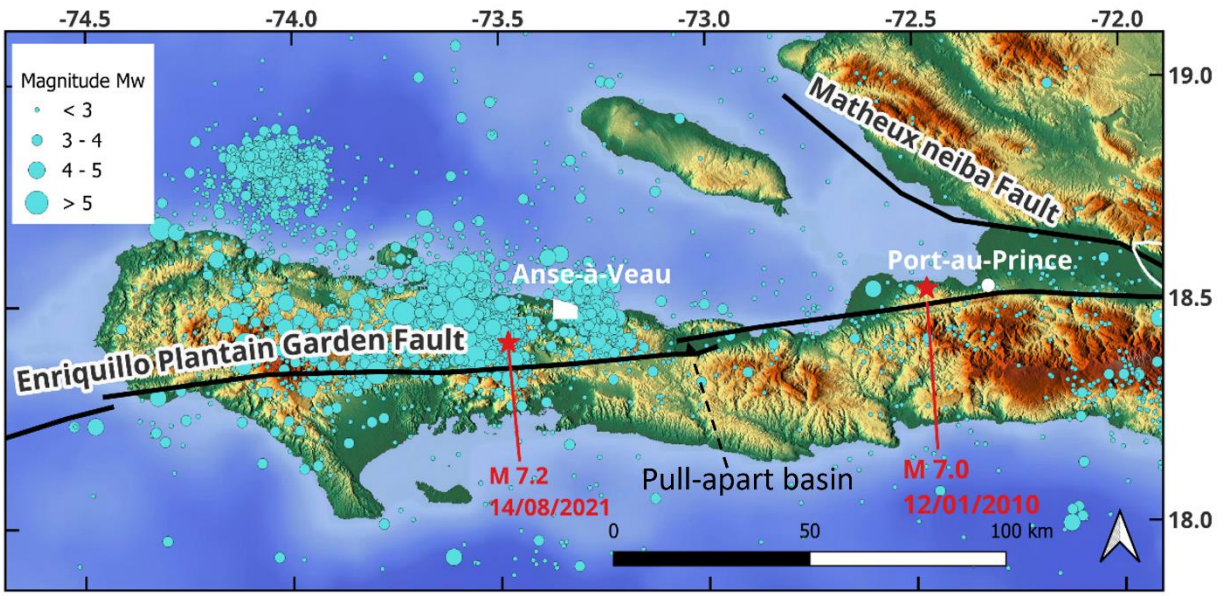

Fig. 2.4 Seismotectonic context of the southern peninsula with the Enriquillo Plantain Garden Fault (EPGF), the two recent major earthquakes in red stars (Calais et al. 2022; Bakun et al. 2012; Frankel et al. 2011) and the seismic activity (represented by the cyan dots with the size as magnitude) recorded in the region from 2019 to 2023 by the platform *Ayiti Séismes* (https://ayiti.unice.fr/ayiti-seismes/).

The EPGF has a slip rate of 7 ± 2 mm/yr with a left-lateral strike-slip motion according to the interseismic plate coupling and strain partitioning in the Northeastern Caribbean by Manaker et al. (2008). The fault system was modelled as a single vertical fault. The analysis of GPS and InSAR data by Calais et al. (2010) following the 2010 earthquake provides a 5 ± 1 mm/yr of transpression, combining left-lateral strike-slip and 2 ± 1 mm/yr of reverse slip for the EPGF system. In the coseismic slip distribution of the 2010 earthquake by Symithe et al. (2013), an increase of calculated Coulomb stress was found on the EPGF to the west of the 2010 rupture, to the east near Port-au-Prince, and also on the near-surface segment adjacent to the rupture.

The historical earthquakes of 1701, 1751 and 1770 are thought to have occurred along the EPGF system (Scherer 1912; Ali et al. 2008; Bakun et al. 2012). The 8 April 1860 earthquake with a magnitude of 6.2 to 6.5 (Scherer 1912; Woodring et al. 1924) might have occurred outside the main trace of the EPGF on a secondary structure, probably offshore (Bakun et al. 2012). The 12 January 2010 earthquake is now also considered to have occurred outside the main trace of the EPGF, on an unmapped north-dipping fault in the EPGF system, the Léogane Fault, according to fault modelling of coseismic deformation measured with GPS instruments and interferometric synthetic aperture radar (Calais et al. 2010). The studies completed after the main earthquake for aftershocks locations and fault geometry (Douilly et al. 2013; de Lépinay et al. 2011) show that the rupture was complex, which suggests that other structures might have been involved.

Locations of the epicentres of the historical seismic events near Anse-à-Veau could not be precisely determined and are based on current knowledge of the regional geology and active faults, as well as damage reports (Scherer 1912; Flores et al. 2012). The first reported seismic event is

the 8 April 1860 earthquake with a tsunami observed along the coast. From 1909 to 1922, several strong shakings were felt at Anse-à-Veau. In October 1952, a tremor of intensity IX and magnitude Ms = 5.9, located at a depth of 24 km, was felt in Anse-à-Veau. The shakings also occurred in January and February 1953 but were considered like probable aftershocks of the earthquake of October 1952 (Flores et al. 2012). The reports suggest that the distribution of the damage observed was related to the local conditions of the soil.

The area of Anse-à-Veau experienced a certain quiet period after the October 1952 earthquake and the aftershocks of 1953 (Flores et al. 2012). From the year 2015, the Technical Unit of Seismology (UTS, *Bureau des Mines et de l'Energie*, Haiti) has started recording weak to moderate tremors in that area, which did not produce any damage but created great panic among the people. In April 2021, a first moderate earthquake has been recorded near the area. The quake has also been felt by many people but did neither cause significant damage.

The 14 August 2021 earthquake is the most recent major event in the western part of the peninsula; it was felt throughout the whole country as well as in the Dominican Republic and Cuba. The mainshock had a magnitude of 7.2 with an optimal centroid source depth at 6 km and a source mechanism that combines strike-slip and reverse faulting (Calais et al. 2022). It presents the same aftershocks distribution and coseismic slip north of the EPGF like the 12 January 2010 earthquake, starting with a significant component of reverse faulting motion on an eastern segment, which propagated westward with later mostly strike-slip motion (Calais et al. 2022a).

The town of Anse-à-Veau was not strongly affected by the 2021 earthquake or the aftershocks like the bigger cities of Les Cayes and Jeremie in the Sud and Grand-Anse departments. Fig. 2.5 presents a map of the damage on the houses caused by the earthquake across the southern peninsula (map produced by the *Centre d'opérations d'urgence national – Système national de gestion des risques et desastres*, Haiti). With a magnitude M_W 7.2, the 2021 earthquake was stronger than the 2010 event (M_W 7.0), but had a lower impact (with about 2250 fatalities in 2021 and up to 300 000 in 2010) because it mostly affected rural area with low population density. However, in terms of earthquake-induced effects, the 2021 event caused widespread slope failures across the southern peninsula that was more intense than in 2010 (Havenith et al. 2022). An example of a landslide caused by the 2021 earthquake along the national road RN7, connecting Les Cayes and Jeremie, is presented in Fig 2.6.

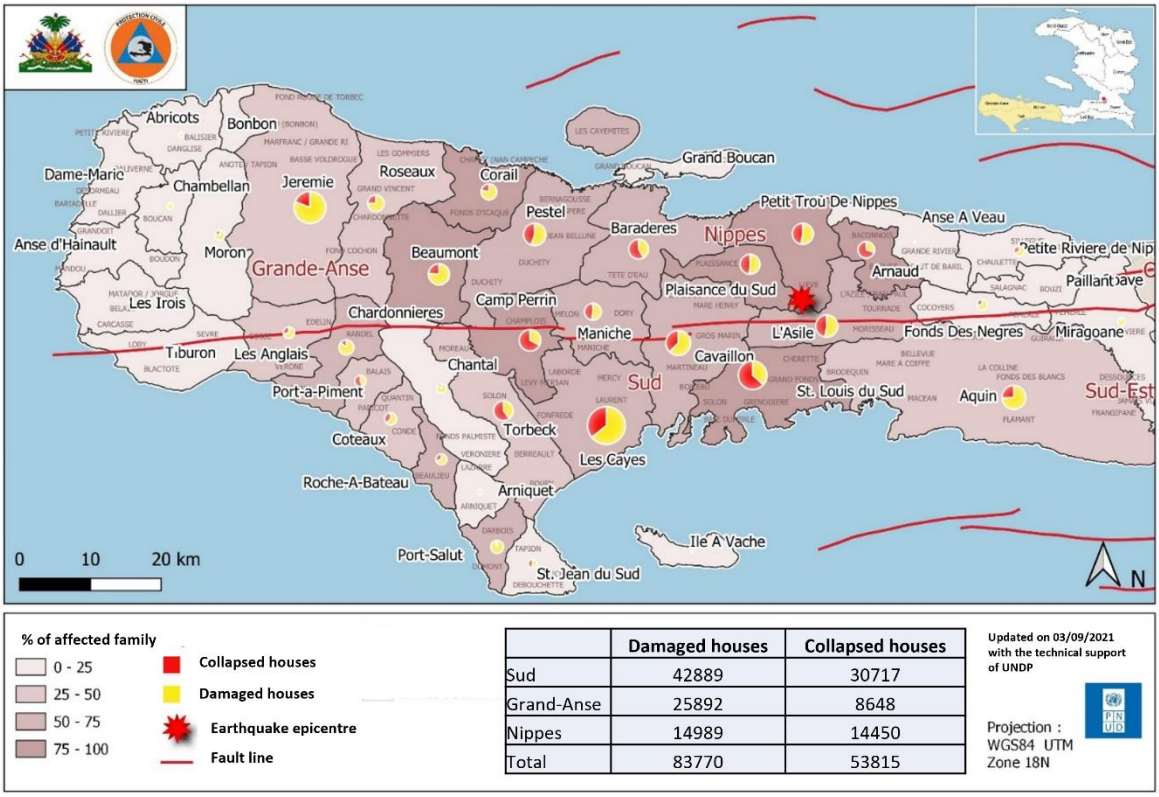

	Damaged houses	Collapsed houses
Sud	42889	30717
Grand-Anse	25892	8648
Nippes	14989	14450
Total	83770	53815

Fig. 2.5 Damages caused across the southern peninsula (Nippes, Sud and Grand-Anse) by the 14 August 2021 earthquake (map produced by *Centre d'opérations d'urgence national, Système national de gestion des risques et desastres*, Haiti).

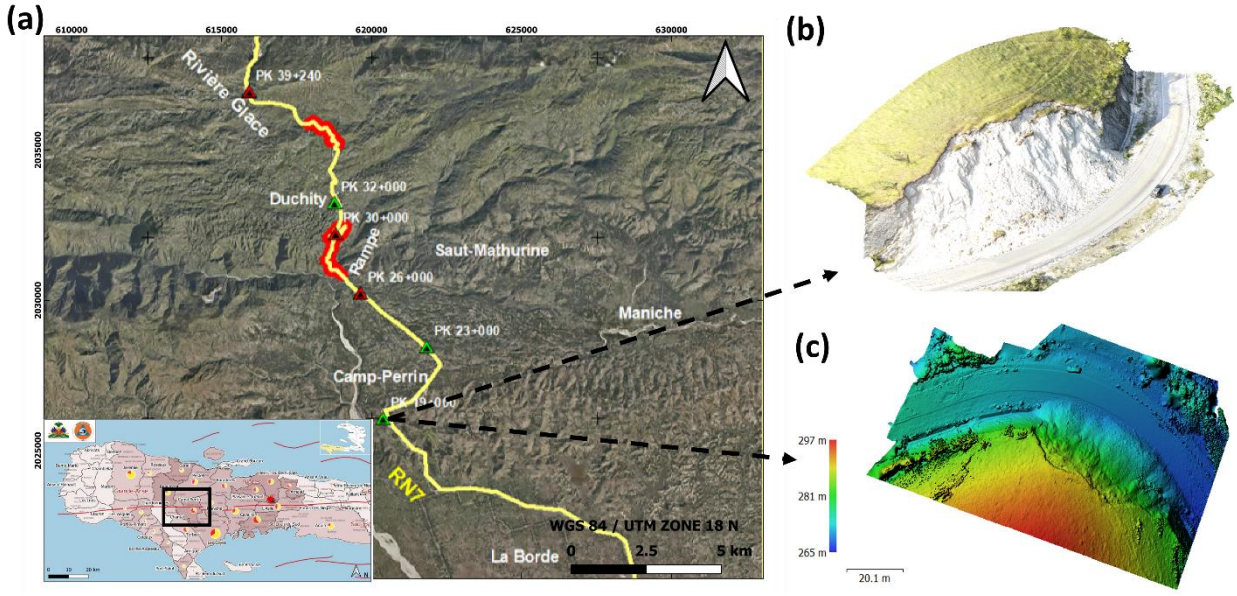

Fig. 2.6 Example of a landslide caused by the 2021 earthquake along the national road RN7. **(a)** Section of the RN7 connecting Les Cayes and Jeremie (see Fig. 2.5). **(b)** 3D image of the landslide constructed in Agisoft Metashape® from photos collected by a drone. **(c)** Digital elevation model of the same landslide constructed in Agisoft Metashape® (Victor and Dorival 2022).

2.2.2 Geology of the study area 1 (Anse-à-Veau)

The geology of the study area 1 (Fig. 2.7b) is made of sedimentary rocks as described by the regional geological map of Haiti (*Carte géologique d'Haïti au 1/250 000ème, Bureau des Mines et de l'Energie*, BME 2005). The oldest formations date back to the upper Cretaceous and are characterized by massive pelagic limestone (**Cs** on the map) from the Senonian and stratified or massive pelagic limestones (**Ep** on the map) from the upper Paleocene to lower and middle Eocene. The Paleocene and Eocene series generally form the sides of the anticlines which are mainly made of formations from the upper Cretaceous in several parts of *Massif de la Hotte* in the southern peninsula.

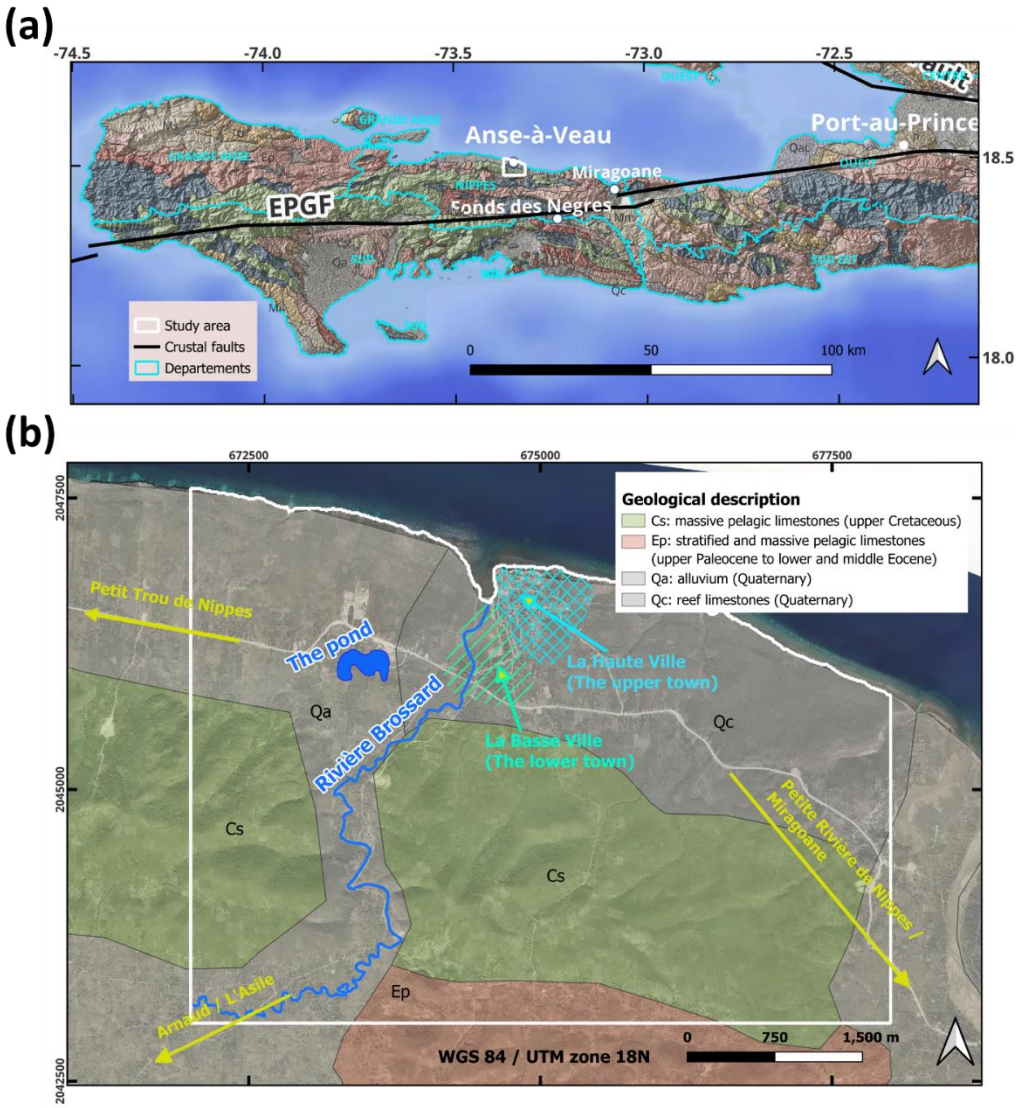

Fig. 2.7 (a) The geology of the southern peninsula from the current Haitian geological map (BME 2005) with the Enriquillo Plantain Garden Fault (EPGF). **(b)** The geology of Anse-à-Veau from the current Haitian geological map (BME 2005) with the location of *La Haute Ville*, *La Basse Ville*, *Rivière Brossard*, the pond and the three main exits with yellow arrows.

The recent formations are of Quaternary age. They are represented either by alluvial material (**Qa** on the map) along *Riviere Brossard* (the river that crosses the study area), around the pond, and at *La Basse Ville* (the lower town), in the western part of the town of Anse-à-Veau (Fig. 2.7b), or by reef limestones (**Qc** on the map) beneath *La Haute Ville* (the upper town) and in the easternmost portion of the study area (Fig. 2.7b) due to a rapid uplift of the island in the Quaternary.

The alluvium is made of clays and sands deposits around the river and the pond. In the westside, they can be related to an erosion of the northern slope of the mountain. The soil becomes lateritic and finer in some parts at the south of *La Haute Ville* and can be related to a thicker unconsolidated clay deposit. The contact between *La Haute Ville* and *La Basse Ville* is formed by some sand quarries and marly limestones with variable clay content in the S-N direction.

The damage observed at Anse-à-Veau during the recent earthquake are mainly concentrated at *La Basse Ville* built on the Quaternary alluvium along the river (*Rivière Brossard*), while *La Haute Ville* built on the reef limestone was slightly affected. These observations are very consistent with the ones in the reports of the historical earthquakes (Scherer 1912; Flores et al. 2012).

2.2.3 Seismic hazard of the Anse-à-Veau region

The seismic hazard maps presented above in Fig. 2.2 indicate a relatively simple distribution of peak ground acceleration values (PGA) over the country. However, those maps do not account for the dynamic response of the possible presence of near-surface soft sediment layers; they were computed for bedrock conditions. Furthermore, they reflect very short-period (or high frequency) motion, essentially around 0 second (or typically >10 Hz). In the seismic design of buildings, the spectral accelerations (SA) are preferred. They correspond to the maximum acceleration experienced by a simplified model of a building within a given range of natural periods subject to a seismic ground motion. The maps of two spectral accelerations (S_S and S_1) with a 2% probability of exceedance in 50 years are presented in Fig. 2.8 for the region of Anse-à-Veau and its surroundings (the southern peninsula).

S_S is the spectral acceleration at short period ($T = 0.2\,s$ and $f = 5\,Hz$). S_1 is the spectral acceleration at one-second period ($T = 1\,s$ and $f = 1\,Hz$). They are the input parameters for computing the standard elastic response spectra proposed by ASCE/IBC (American Society of Civil Engineers, International Building Code) and adopted in the CNBH (National Building Code of Haiti). S_S and S_1 were determined from probabilistic seismic hazard assessment (PSHA) after the 2010 earthquake by Frankel et al. (2011).

The spectral accelerations for the study area of Anse-à-Veau are in the range $1.29 - 1.47g$ for S_S and the range $0.38 - 0.48g$ for S_1. The S_S is more important for Anse-à-Veau as it represents the peak acceleration likely to affect the type of structures (houses with ~2 stories) commonly found in the area. These maps do not take potential site effects into account.

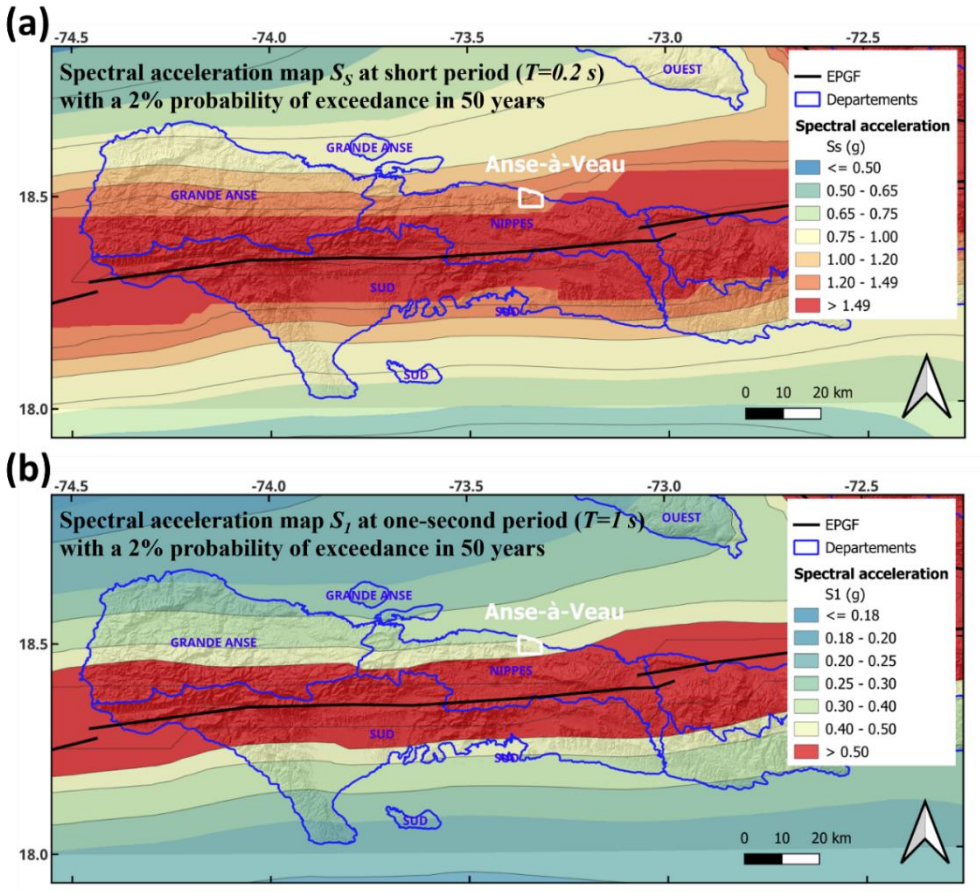

Fig. 2.8 Hazard maps across the southern peninsula for spectral accelerations determined from probabilistic seismic hazard assessment (PSHA) after the 2010 earthquake by Frankel et al. (2011). The colour scale is different in the two maps. **(a)** Spectral acceleration S_S at short period (T=0.2 s) with a 2% probability of exceedance in 50 years. **(b)** Spectral acceleration S_1 at one-second period (T=1 s) with a 2% probability of exceedance in 50 years.

The region of Anse-à-Veau represents an area of significant interest due to its location within a zone of elevated seismicity and its documented history of damaging earthquakes. Other regions in Haiti, such as the one of Cap-Haitien in the north, are also exposed to higher seismic hazards. Cap-Haitien is, actually, situated in close proximity to the Septentrional Fault (SF). Its historical record of destructive earthquakes, combined with the scientific expectation of a future seismic along the SF underscores the need for detailed seismic hazard in this area.

2.3 Cap-Haitien: study area 2

2.3.1 Seismotectonic context of the Cap-Haitien region

Cap-Haitien is the metropolis of the North department and second most important city of Haiti (after the capital Port-au-Prince). The region belongs to the geographic and structural set of *La Plaine du Nord* just south of the Septentrional Fault along the northern coast of the country (see location in Fig. 2.9). A small part of the study area is in the southeastern slope of *Morne du Cap*, an outlier of *Massif du Nord* with an altitude of 800 m (Woodring et al. 1924; Butterlin 1960).

The Septentrional Fault (SF) is known as the Oriente fault zone in the south of Cuba (Manaker et al. 2008). From there, it runs eastward off the northern coast of Haiti as the Septentrional Fault (SF), crosses the Cibao Valley (north of the Dominican Republic) and extends to gradually merge with the Puerto-Rico Trench through a series of faults splitting off the main trace (Prentice et el. 2003; Manaker et al. 2008). At the 71.7° W longitude, an offset of possible segment boundary is observed on the fault where it is well expressed on land in the northwest of the Dominican Republic. The portion of the SF off the northern coast of Haiti is capable of an earthquake with moment magnitude of 6.9 according to Manaker al. (2008). In the Dominican Republic, an earthquake along the SF could have magnitude of 7.5-7.7 (Manaker al. 2008).

The slip rate on the SF is about 9 ± 3 mm/yr according to paleoseismic investigations along the fault in north of the Dominican Republic (Prentice et al. 2003). The kinematic model from interseismic velocities by Calais et al. (2010) shows a slip rate of 12 ± 2 mm/yr on the fault zone. Based on kinematic block modelling, Symithe et al. (2015) predicts pure strike-slip motion of ~10 mm/yr along the SF.

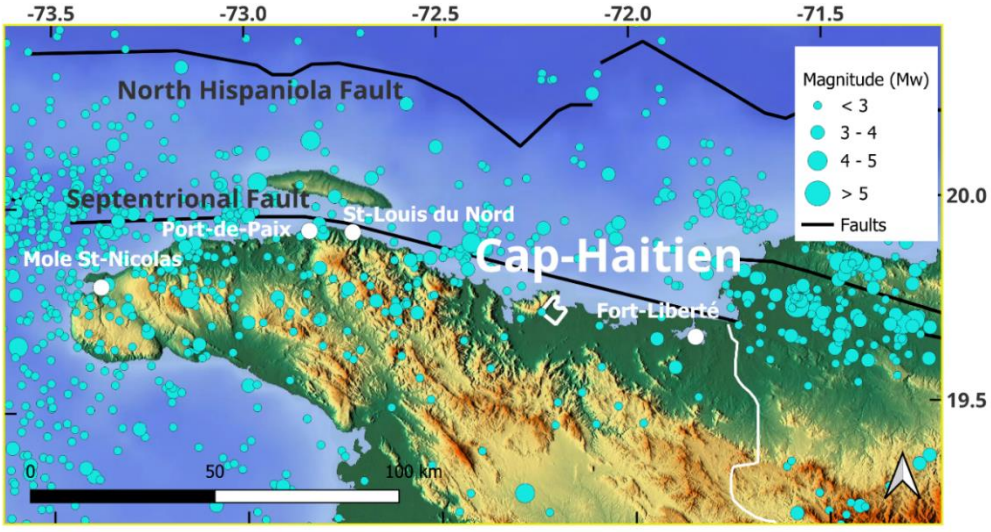

Fig. 2.9 Seismotectonic context of the northern coast with the Septentrional Fault (SF), the North Hispaniola Fault (NHF) and the seismic activity (represented by the cyan dots with the size as magnitude) recorded in the region from 2019 to 2024 by the platform *Ayiti Séismes* (https://ayiti.unice.fr/ayiti-seismes/).

The Septentrional Fault is assumed to be responsible for the large 1842 and 1887 earthquakes with estimated magnitude of 8.0 and 7.75, respectively, occurred in the north of Hispaniola (McCann 2006). The first one occurred on 7 May 1842 and destroyed the towns of Fort Liberté, Cap-Haitien, St-Louis du Nord, Port-de-Paix, Môle St-Nicolas along the northern coast of Haiti, and Santiago de Los Caballeros in northern Dominican Republic (Scherer 1912; Woodring et al. 1924; Flores et al. 2012). The event ruptured a 300 km-long portion of the western SF according to Mann et al. (1998). Based on empirical scaling laws, Ali et al. (2008) modelled a rupture of 20 km wide with an average slip of 5 m. The second one occurred on 23 September 1887 and was especially disastrous for the northwest peninsula as it nearly destroyed all the houses in Môle St-Nicolas (Scherer 1912; Woodring et al. 1924). Ali et al. (2008) estimated a rupture area of 175 × 20 km for this earthquake and an average slip of 5 m.

The 7 May 1842 earthquake caused the death of about half of the population of Cap-Haitien (Scherer 1912; Woodring et al. 1924). Port-de-Paix suffered more, as everything collapsed and was overwhelmed by the sea wave (Scherer 1912). The occurrence of this earthquake was probably due to almost vertical displacement of the sea bottom along the fault zone off the coast of the Northwest peninsula (Woodring et al. 1924). The 23 September 1887 earthquake was far less severe for Cap-Haitien than the previous one. Intensity of a tsunami observed in Môle St-Nicolas indicated that this earthquake was also due to vertical displacement of the sea bottom, but probably farther southwest than the displacement causing the 1842 earthquake (Woodring et al. 1924).

Apart from the 1842 and 1887 earthquakes, the region of Cap-Haitien had been affected by other seismic events (Flores et al. 2012). The 20 April 1962 earthquake with an estimated magnitude of 6.6 is the strongest recorded in the region during the instrumental period (Bertil et al. 2014). The event caused very little damage in Cap-Haitien and was rather associated with the North Hispaniola fault (Bertil et al. 2014), in the subduction zone, north of the Septentrional Fault.

2.3.2 Geology of the study area 2 (Cap-Haitien)

The geology presented here are based on the national geological map of Haiti (*Carte géologique d'Haïti au 1/250 000ème, Bureau des Mines et de l'Energie*, BME 2005) and the geological mapping carried out in the framework of the seismic microzonation of Cap-Haitien (Monthel et al. 2013). According to the Haitian geological map by the BME (Fig. 2.10a), the second study area can be characterized by two geological formations: a sedimentary formation made of alluvium from the Quaternary age, and a volcano-sedimentary formation made of andesites from the Cretaceous. The andesites are attached to *Morne du Cap* in the west of the study area. The other formations in *Morne du Cap* are made of sedimentary limestones platforms from the upper Senonian-Cretaceous, and from the upper Paleocene to lower and middle Eocene.

The geological mapping completed by Monthel et al. (2013) during the seismic microzonation of Cap-Haitien is much more detailed (Fig. 2.10b) than the Haitian geological map by the BME (Fig. 2.10a). The alluvial plain in the BME map (Fig. 2.10a) remains nearly unchanged but includes some enclaves of marshy areas, abandoned meanders and anthropogenic formations (Fig. 2.10b).

In the plain, the alluvial deposits are characterized by sands and silts, the marshy areas by silts, and the abandoned meanders by sands, gravels and pebbles. The transition zone between the alluvial plain and the southeastern slope of *Morne du Cap* is made of colluvium characterized by silts, gravels and blocks.

The southeastern slope of *Morne du Cap* is made of volcano-sedimentary facies and volcanites from the upper Cretaceous as well as karstified limestones, granitoids and limestone scree from the Eocene-Miocene or Quaternary (Fig. 2.10b). The volcanites are characterized by pyroclastic flows and breccias made of andesites. The slope includes (in its central part) a landslide area made of limestone blocks in clay-carbonate matrix from the Quaternary age.

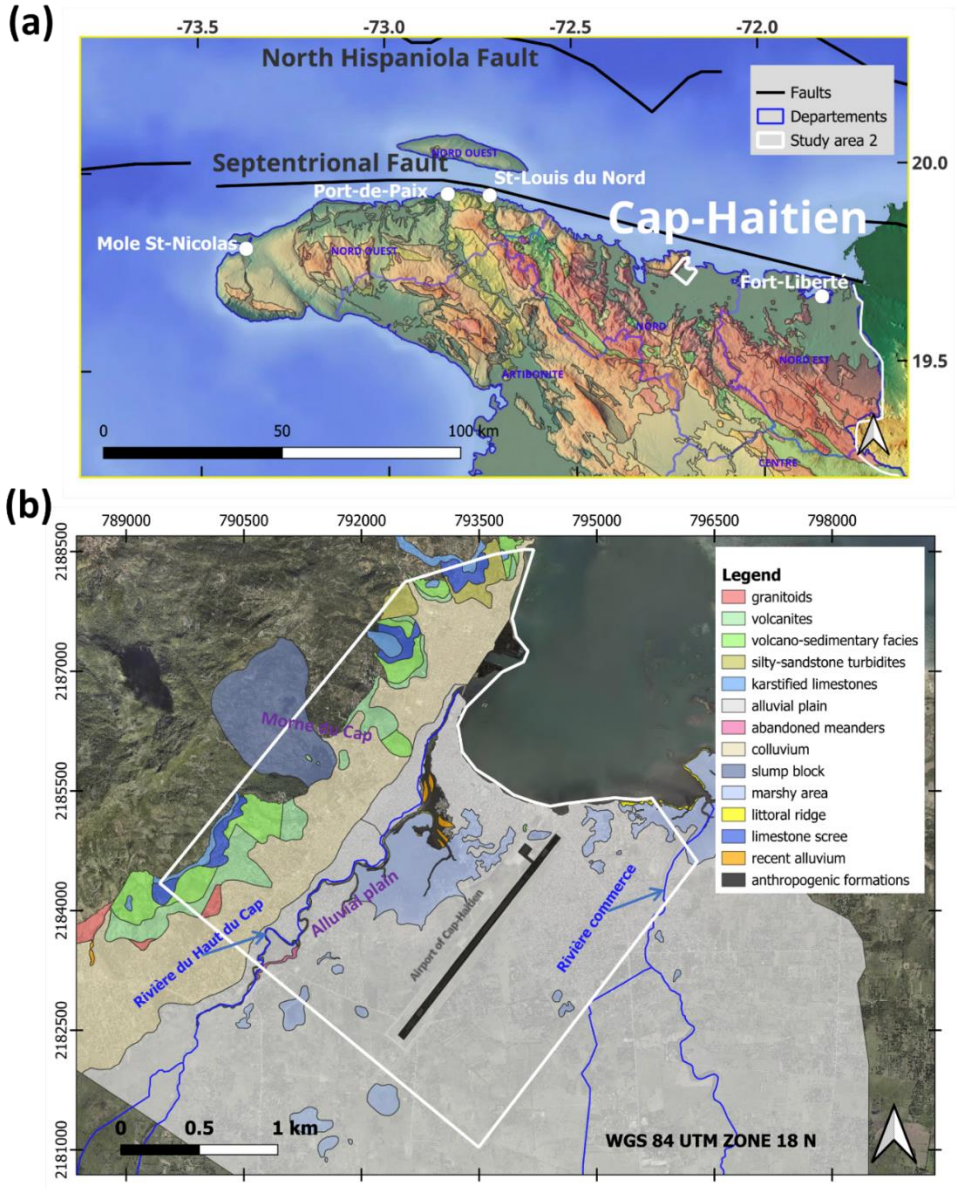

Fig. 2.10 (a) The geology of North Haiti from the current Haitian geological map (BME 2005) with the Septentrional Fault (SF). **(b)** The geology of Cap-Haitien from the geological mapping carried out by Monthel et al. (2013) for the seismic microzonation.

2.3.3 Seismic hazard of the Cap-Haitien region

The maps of S_S (the spectral acceleration at short period $T = 0.2\ s$) and S_1 (the spectral acceleration at one-second period $T = 1\ s$) with a 2% probability of exceedance in 50 years are presented in Fig. 2.11 for the north of Haiti (including the Cap-Haitien region). The values of S_S and S_1 are in the range $1.29 - 1.54g$ and $0.47 - 0.58g$, respectively, for the study area of Cap-Haitien. These accelerations were determined for a firm-rock site condition (then do not take potential site effects into account) from probabilistic seismic hazard assessment (PSHA) after the 2010 earthquake by Frankel et al. (2011). Like for Anse-à-Veau, the S_S is more important for Cap-Haitien as it represents the peak acceleration likely to affect the type of structures (houses with ~2 stories) commonly found in the region.

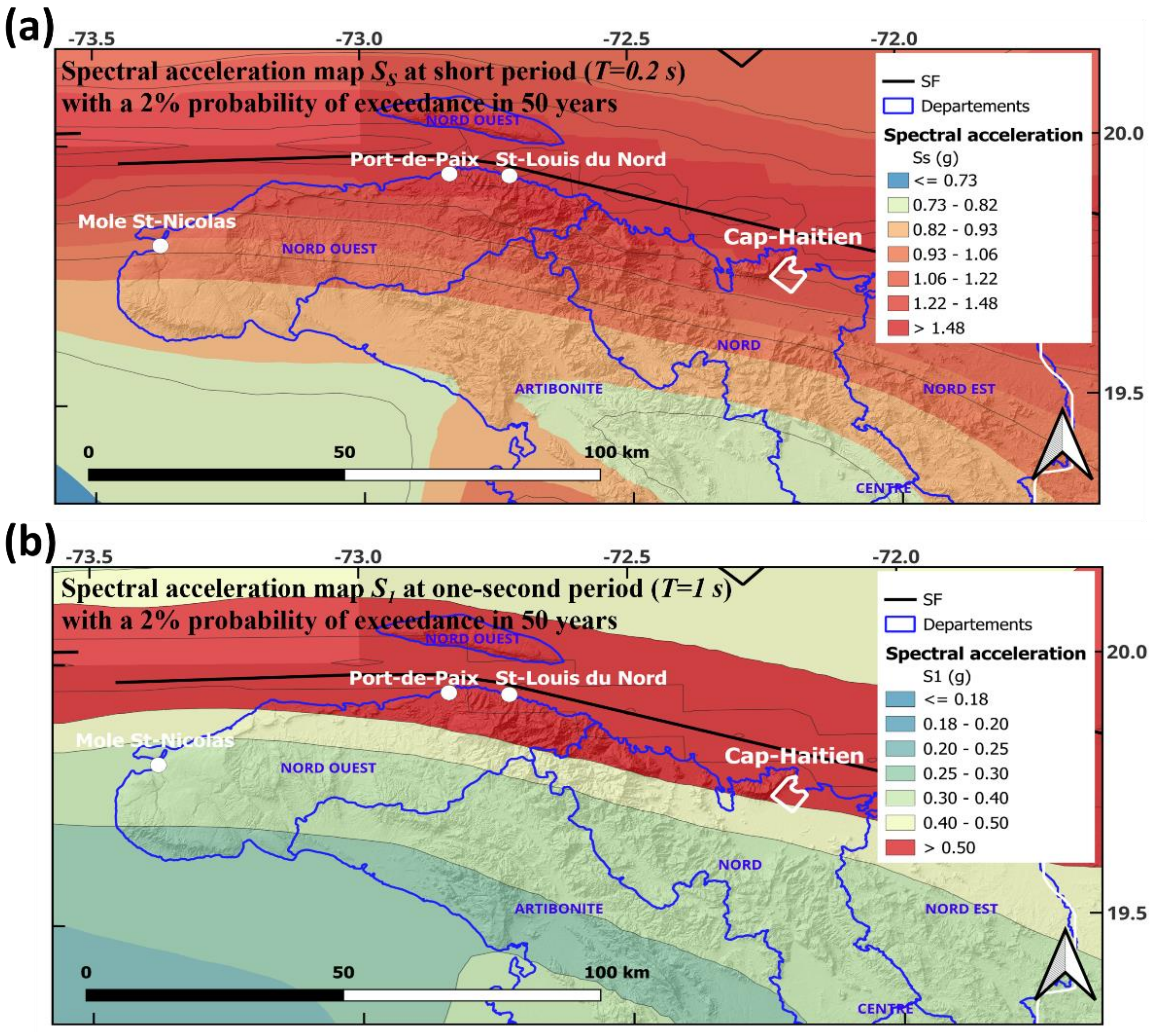

Fig. 2.11 Hazard maps across the north of Haiti (include the study area of Cap-Haitien) for spectral accelerations determined from probabilistic seismic hazard assessment (PSHA) after the 2010 earthquake by Frankel et al. (2011). The colour scale is different in the two maps. **(a)** Spectral acceleration S_S at short period (T=0.2 s) with a 2% probability of exceedance in 50 years. **(b)** Spectral acceleration S_1 at one-second period (T=1 s) with a 2% probability of exceedance in 50 years.

In the seismic microzonation (Bertil et al. 2014; Bertil et al. 2014a; Roullé et al. 2014), homogeneous zones of Cap-Haitien were defined in terms of geology, resonance frequency and mechanical properties. They determined a representative soil column for each zone to perform 1D seismic response simulations.

Fig. 2.12 presents a map of soil classes and their elastic response spectra for Cap-Haitien produced for the seismic microzonation, employing 1D non-linear simulations across 9 initial zones. The simulation outputs were first compared, and then the zones that exhibit similar seismic response characteristics were grouped to form 5 distinct soil classes (class 1 to 5) and the outcropping rock class 0. The response spectra (with 5% damping) were constructed for each class, following the recommendations of the International Building Code (IBC). The results show that the alluvial plain is defined by the presence of very soft soils, which result in response spectra featuring a wide constant-acceleration plateau and a relatively low spectral acceleration level.

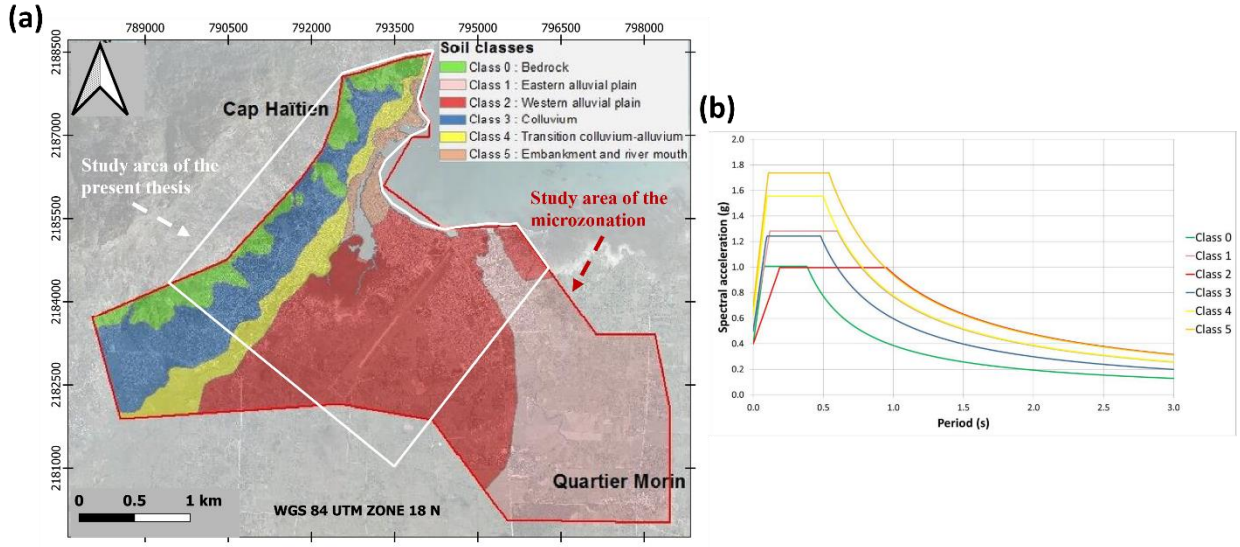

Fig. 2.12 **(a)** Map of soil classes zoning for Cap-Haitien produced by Bertil et al. (2014a). **(b)** Elastic response spectra for the 6 soil classes determined in the framework of the seismic microzonation of Cap-Haitien (Bertil et al. 2014; Bertil et al. 2014a; Roullé et al. 2014).

Like in Anse-à-Veau, the reports on the 1842 earthquake (Scherer 1912; Woodring et al. 1924) suggest that the alluvium formation in the plain amplified the shakings and aggravated the damage in the city of Cap-Haitien. The methodology followed in the present study is expected to explain the observed seismic shaking effects and their spatial variability.

3 Methods

The methods presented here are divided into two categories: the geophysical-seismological methods (section 3.1), and the modelling methods (section 3.2). The geophysical-seismological methods include ambient noise and earthquake recordings, seismic waves velocity and electrical resistivity profiles carried out in the region of Anse-à-Veau in the frame of the thesis. The modelling methods include the geostatistical, geomodelling and numerical modelling methods.

3.1 Geophysical-seismological methods

3.1.1 Ambient noise HVSR measurements

The ambient noise HVSR (horizontal-to-vertical or H/V spectral ratio) method is an experimental technique frequently adopted in seismic microzonation studies to identify possible site effects (Bard et al. 1999; SESAME 2004). The technique became popular after some Japanese publications (Nakamura and Saito 1983) and is sometimes referred to as the Nakamura method (Nakamura 1989, 2000, 2009), but is now more widely called HVSR method because it consists in dividing the spectrum of the horizontal components by the spectrum of the vertical component of ambient noise or earthquake motions (Nakamura 1989; Bard et al. 1999; Bonnefoy-Claudet et al. 2006). Currently, the earthquake hazard research community recognizes the potential of this method to give a correct estimate of the natural frequency of a site (SESAME 2004) although the theoretical background is not clear (Lachet and Bard 1994).

The current method is based on the analysis of microtremor or ambient noise as the name suggests. The ambient noise is a low amplitude mechanical vibration generated by natural or anthropogenic sources. From the recording of the ambient noise, the HVSR (or H/V spectral ratio) is calculated, which reflects the relative amplification of the horizontal components of the shaking with respect to the vertical one. The H/V ratio makes it possible to obtain a pseudo transfer function at the point of measurement. The peak presented by the H/V curve provides a good estimate of the S-waves resonance frequency (and therefore that of the ground). In contrast, the corresponding amplitude systematically underestimates the amplitude of the transfer function. It should therefore be considered as a relative value to be compared with other measurement sites.

Due to its low-cost and its rapid implementation based mostly on ambient noise, the method is widely employed in local seismic hazard mapping. The H/V spectral ratio can help identify the presence of shallow sedimentary layers that may significantly amplify the ground motion but may not fully capture deep geologic features or complex heterogeneity of the subsurface (Haghshenas et al. 2008). For comprehensive seismic hazard assessment, it should be combined with other geophysical and geotechnical data as well as site-specific analysis.

In the case of a soft 1D sedimentary layer (having a strong impedance contrast with the bedrock), we can relate the thickness of the layer h to its fundamental resonance frequency f_0 by the expression:

$$\boldsymbol{f_0 = \frac{V_S}{4h}} \tag{3.1}$$

Where:

- h: average thickness of the soft layer,
- V_S: average velocity of propagation of S-waves in the soft layer,
- f_0: fundamental resonance frequency of the soft layer.

The ambient noise measurements in the region of Anse-à-Veau (study area 1) were carried out by an 'all-in-one' seismic station including both a sensor and a digitizer: the Tromino (Fig. 3.1). According to the manufacturer (the Italian company Micromed ©), the bandwidth of the sensor works on the following frequency range: 0.1-1024 Hz. The recordings vary from 20 to 30 minutes with an acquisition rate of 128 samples per second. We followed the technical guidelines from the SESAME European research project (SESAME 2004) to reduce the influence of experimental conditions such as the presence of wind and unwanted vibrations (Chatelain et al. 2007).

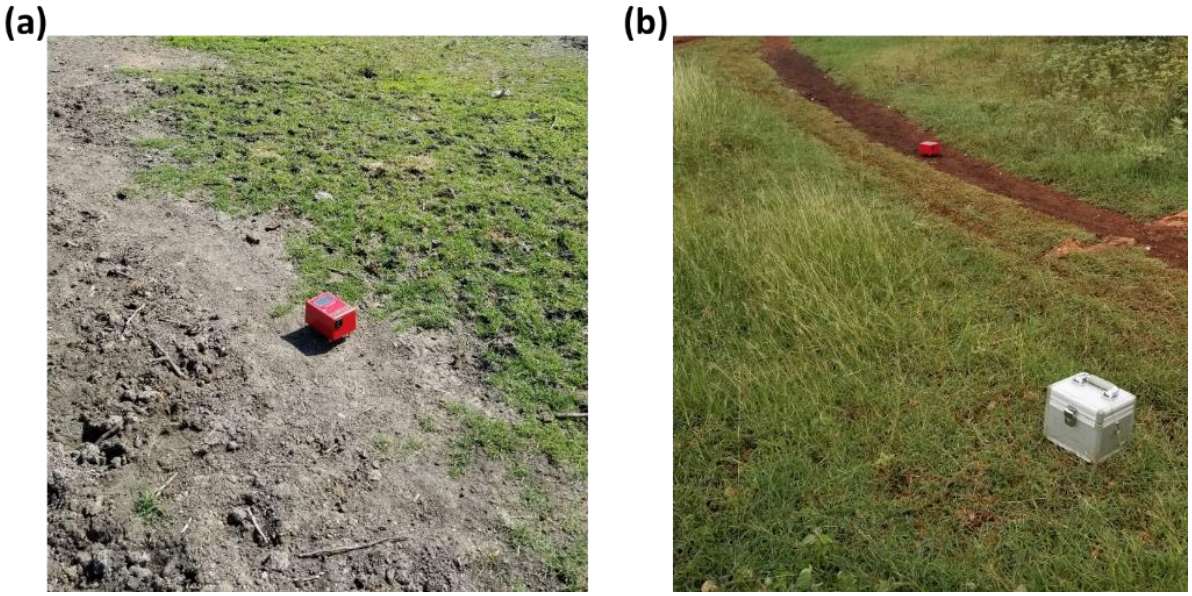

Fig. 3.1 The device Tromino (15×10 cm, about 10 cm high) used for the ambient noise HVSR measurements carried out in **(a)** the alluvial deposit near the pond of Anse-à-Veau and **(b)** the laterite to the south of *La Haute Ville* (the upper town of Anse-à-Veau).

The HVSR data were processed using the Geopsy software (Wathelet et al. 2020). The process is summarized in Fig. 3.2. The final results are an average curve (the H/V curve) as a function of the frequency, and an azimuth graphs characterizing the principal direction of the wave polarisation.

The time windows used have a length between 20 and 40 s and can overlap by 5%. The anti-triggering algorithm to avoid the transient noises is based on the comparison between the short term (STA) and long term (LTA) average amplitudes. The values for STA, LTA, minimum STA/LTA and maximum STA/LTA are 2, 30, 0.2 and 2.5 s, respectively. The smoothing function of Konno & Ohmachi are applied with a bandwidth coefficient *b* of 40 and a cosine taper of 5%. The analysis is made in the frequency range 0.25-25 Hz.

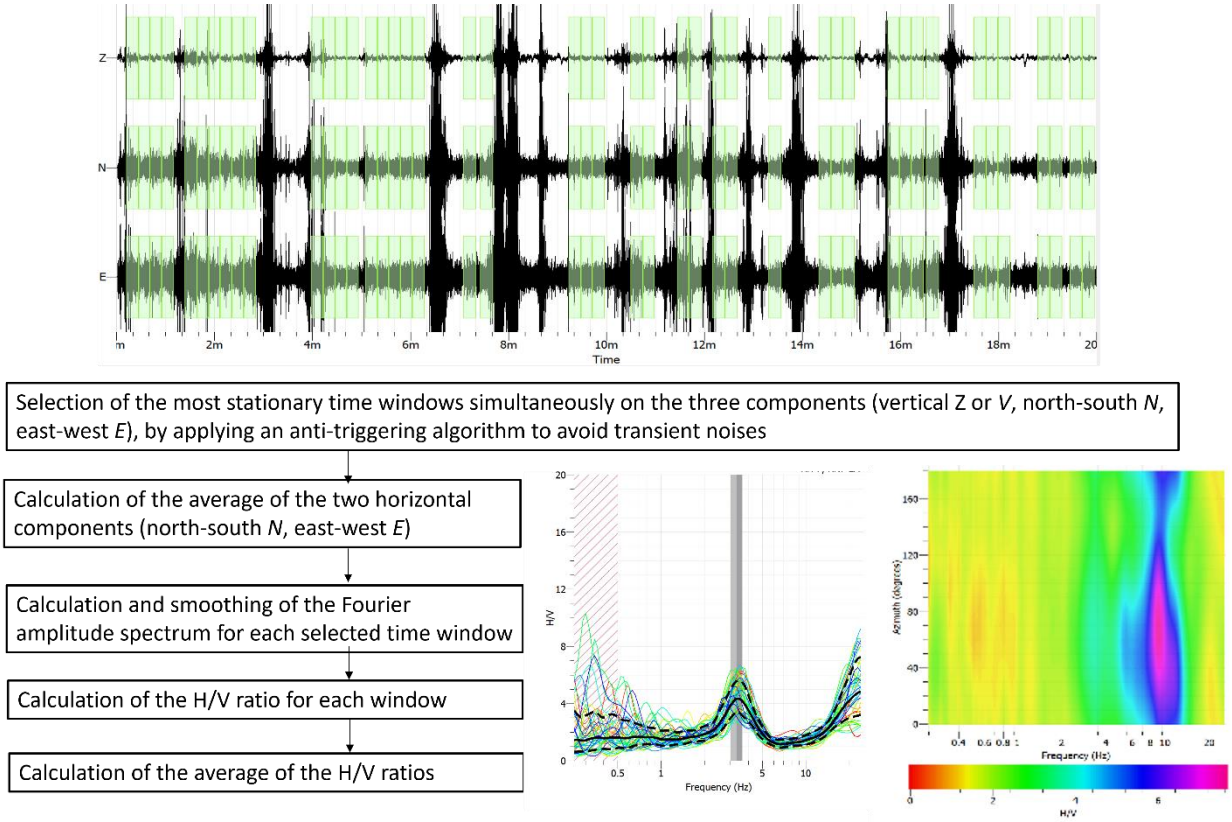

Fig. 3.2 Schematic representation of the HVSR processing workflow according to the software Geopsy.

3.1.2 Earthquake recordings

The earthquake recordings were mainly used in our case for the application of the Standard Spectral Ratio (SSR) method (Borcherdt 1970; Borcherdt and Gibbs 1976; Field and Jacob 1995). The SSR procedure (see schematic representation in Fig. 3.3) is a direct geophysical-seismological approach that allows the estimation of empirical amplification function by comparing earthquake recordings on a target site with the recording of the same earthquake on a close-by reference site. When combining with other methods, such as the H/V spectral ratio (HVSR), the SSR can improve

the accuracy of site response estimates. While the H/V method uses one seismic station on the assumption that the vertical component of the vibration is not influenced by the local structure, the application of the SSR technique requires at least one station installed on a reference site (reference station) free from any site amplification, and one or more other stations installed on the target site (target station) where some amplifications are expected.

The SSR method consists in determining the ratio of the Fourier spectrum of the ground motion recorded by the target station, to the spectrum of the ground motion recorded by the reference station (Borcherdt 1970; Borcherdt and Gibbs 1976). The approach allows to capture deep geologic features and complex heterogeneity of the subsurface such as the 2D/3D effects characterized by the generation of surface waves at the edges of a sedimentary basin (Cornou and Bard 2003). The reference station must be located on a hard rock (free of any lithological and topographic effect) with a distance to the target site small compared to the distance to the event epicentre in order to reduce the source and propagation effects (Field and Jacob 1995).

The SSR can be expressed as:

$$\boldsymbol{SSR(f)} = \frac{\boldsymbol{S_{target}(f)}}{\boldsymbol{S_{reference}(f)}} \tag{3.2}$$

Where:

- $S_{target}(f)$: spectral amplitude of the ground motion recorded by the target station,
- $S_{reference}(f)$: spectral amplitude of the ground motion recorded by the reference station.

The application of the SSR requires the recording of a statistically significant number of earthquakes to reduce the variability due to the 3-D geometry of the interfaces of sedimentary layers. This is not suitable for low seismicity region, but very useful in high seismicity region like Haiti. For instance, this method has been applied to estimate site amplification effect by other studies in some areas along the Enriquillo Plantain Garden Fault (EPGF) after the 2010 Haiti earthquake (St-Fleur et al. 2016; Ulysse et al. 2018, 2021).

For the present study, the seismic events were recorded by four digital broadband seismometers CMG-6TD (Fig. 3.4) designed and manufactured by Guralp Systems Limited ©. The installations were carried out during the geophysical-seismological surveys in the region of Anse-à-Veau (Nippes department) in January 2022. Two seismometers were installed in Anse-à-Veau (the study area 1) for site amplification study, the other ones in Miragoane and Fonds des Nègres (two other municipalities in the Nippes department) for seismological recordings in the EPGF zone. The seismometers were configured to record continuously at a sampling of 200 Hz using the software *Scream* provided by the manufacturer Guralp Systems Limited ©.

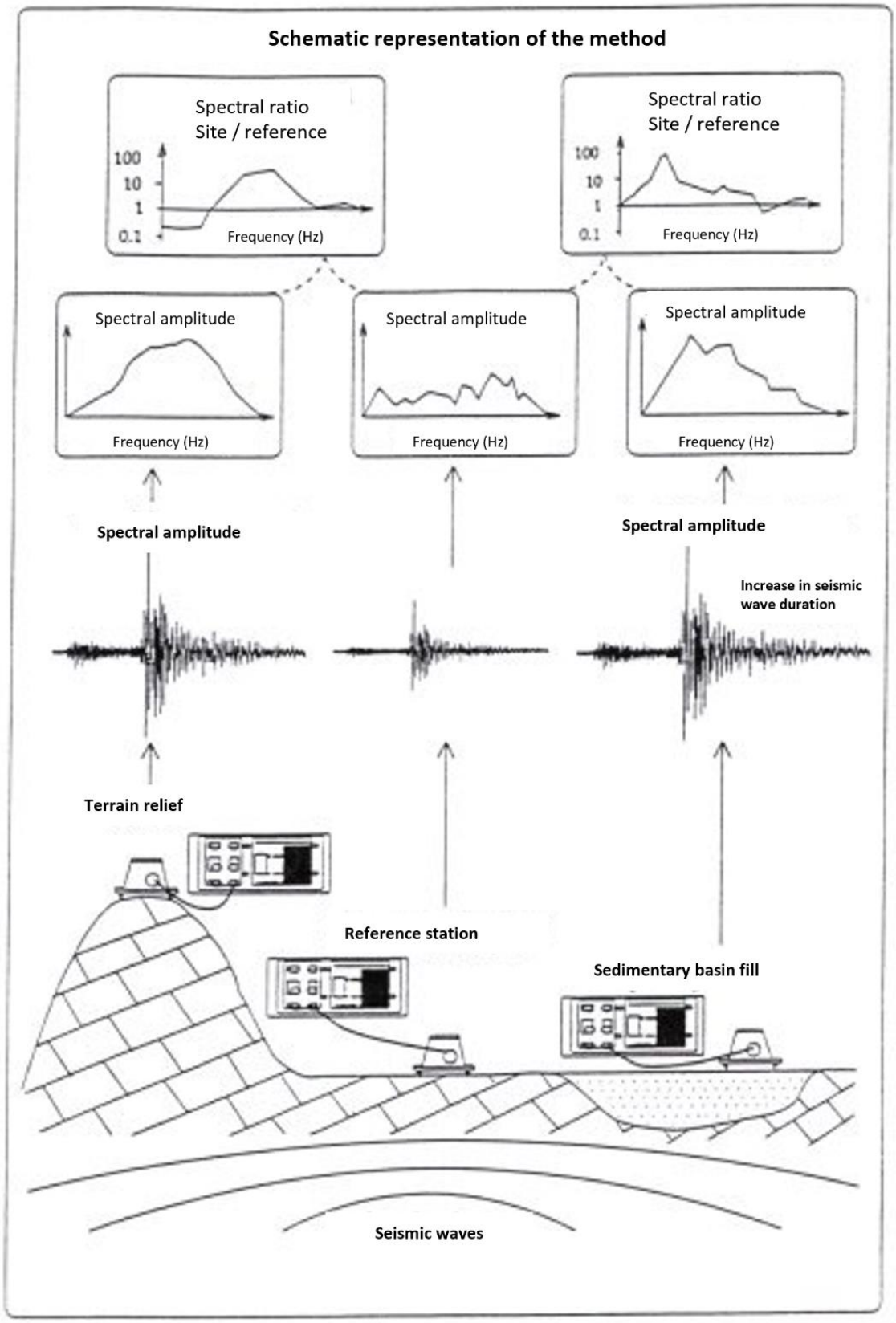

Fig. 3.3 Schematic representation of the standard spectral ratio (SSR) method (modified from Duval 1994).

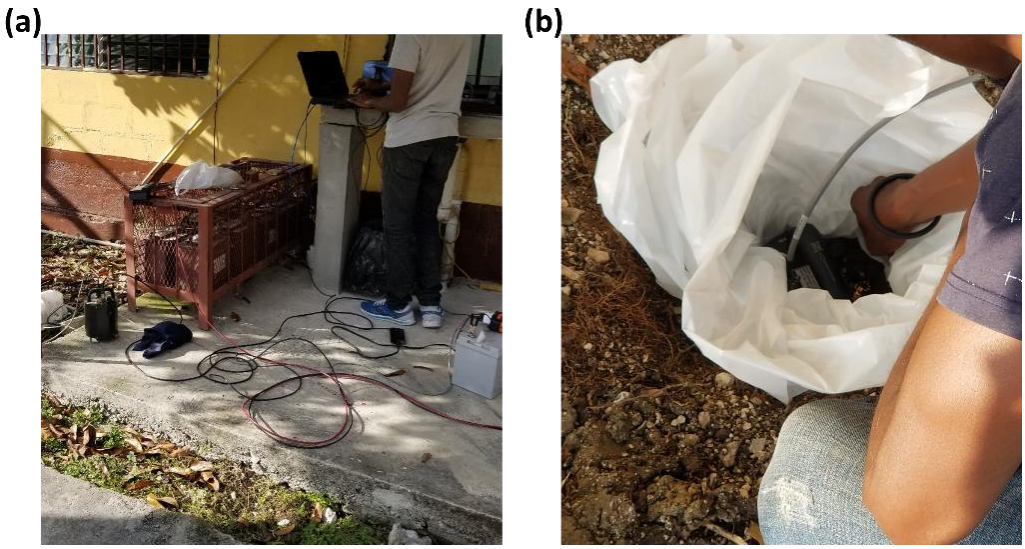

Fig. 3.4 The Guralp CMG-6TD used for the earthquake recordings in the region of Anse-à-Veau. **(a)** setting; **(b)** installation.

3.1.3 Seismic profiles

Seismic methods use the propagation of mechanical waves (body waves or surface waves) in the subsurface to determine the velocity distribution and thus locate the interfaces between different materials or layers. The velocity distribution is related to the properties of the materials or layers which allow to represent the subsurface and support local seismic amplification assessment.

The body waves include the longitudinal (compressional-dilatational) P-waves and the transverse (shear) S-waves (Bormann et al. 2012). The surface waves include the Rayleigh (LR or R) waves and the Love (LQ or G) waves formed by constructive interference of the body waves at the free surface (Bormann et al. 2012). The P and S-waves velocities through an isotropic homogeneous linearly elastic medium are expressed as:

$$V_P = \sqrt{\frac{K+\frac{4}{3}G}{\rho}} \tag{3.3}$$

$$\boldsymbol{V_S = \sqrt{\frac{G}{\rho}}} \tag{3.4}$$

Where:

- V_P and V_S: P-waves and S-waves velocities through the medium,
- K and G: bulk and shear moduli that respectively define the incompressibility and rigidity of the medium,
- ρ: the density of the medium.

The two seismic methods (see set up and used equipment in Figs. 3.5 and 3.6) applied in Anse-à-Veau to calculate the P-waves and S-waves velocities (V_P and V_S) are the seismic refraction tomography (SRT) and the multichannel analysis of surface waves (MASW). The SRT provides a cross-section representing the different P-wave velocities of the soil layers below the line of the profile. The MASW provides a profile of S-waves velocities as a function of the depth.

The SRT method (Lankston 1989; Zhang and Toksöz 1998) allows to model the P-waves velocity distribution of the subsoil in 2D or 3D from the times of first arrival of the waves observed on the seismic recordings. The procedure is based on the displacement velocities of the P-waves obtained by using the refraction properties of the wave at the interfaces between layers where seismic waves travel at different velocity. The P-wave arrives first at the sensors and is easily recognizable. The method involves creating an initial velocity model, for which the travel times are calculated along 'rays' and compared with the measured travel times; then, the model is iteratively modified in order to minimise the difference between the calculated and measured travel times. The objective is to find the minimum travel time between the source and the receiver for each source-receiver pair. Indeed, the maximum time might include slow or indirect paths while the minimum time is cleaner and more reliably associated with first-arrival energy. The final model gives a good estimation of the thickness and the basic form of the subsurface layers, as long as the P-waves velocity increase with depth.

The MASW (1D) method (Park et al. 1999; Xia et al. 1999) allows to obtain a profile of S-waves velocity (V_S) as a function of depth using surface wave methods based on the inversion of the dispersion of surface waves (mainly Rayleigh waves) assuming plane waves propagating in a horizontally stratified medium. The procedure involves the calculation of a dispersion curve from the seismic recordings and the inversion of this dispersion curve to find the 1D S-wave velocity (V_S) profile, considering that Rayleigh waves travel with a phase velocity of about $0.92V_S$ (Bormann et al. 2012). The basic idea lies in the fact that in a heterogeneous medium, the phase velocity of Rayleigh waves is a function of the frequency and the mechanical characteristics of the medium. Thus, if the dispersion curve is measured, it is in principle possible to find the characteristics of the medium crossed using the inversion operation. From the 1D S-waves velocity profile, it is possible to deduce a standardized geomechanical parameter, V_{S30}, which is involved in soil classification according to the International Building Code or the Eurocode 8 (IBC or EC8). The V_{S30} is an average of the S-waves velocity over the first 30 meters below the profile on the measurements site.

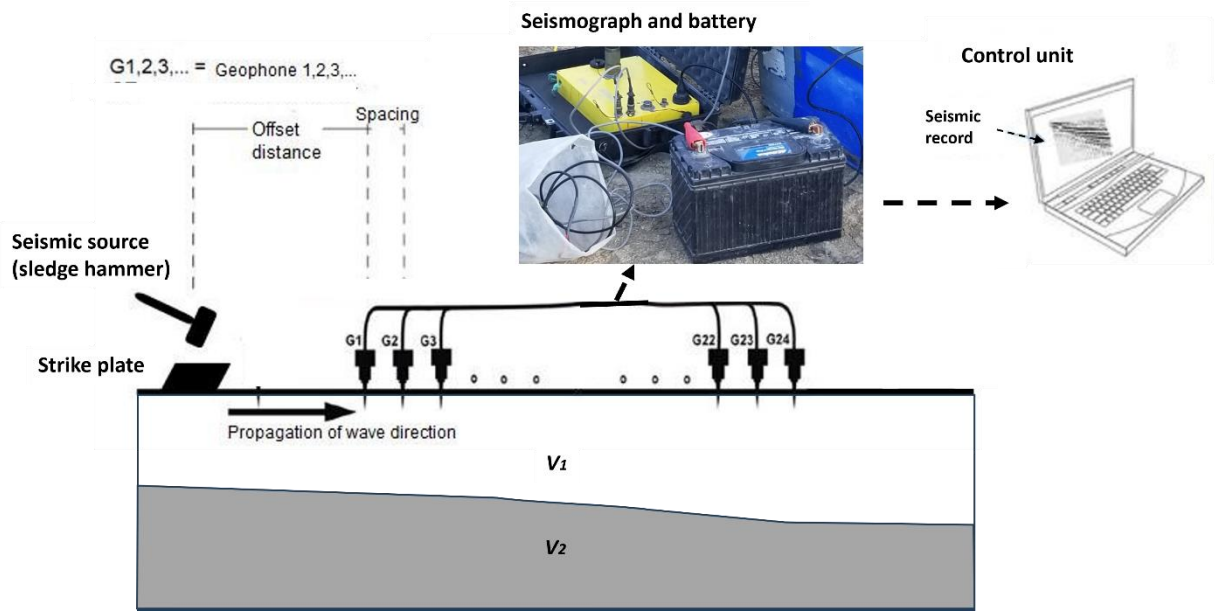

Fig. 3.5 Example of field measurement configuration (modified from Hadi et al. 2021) for seismic profiles on two layers with wave velocity V_1 and V_2.

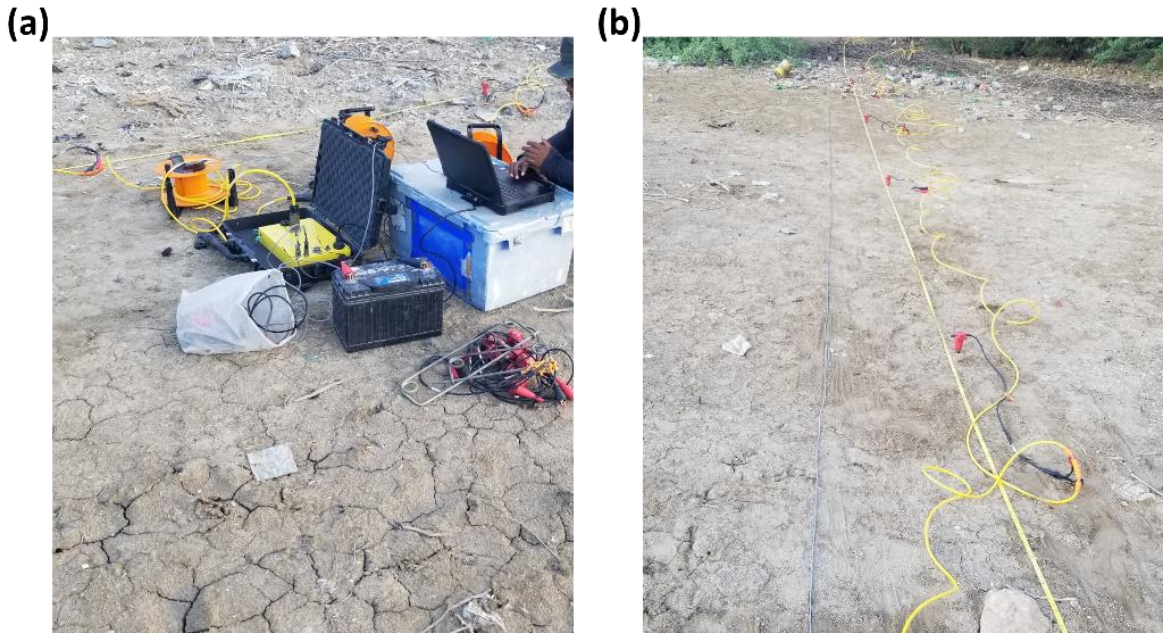

Fig. 3.6 The equipment used for the seismic profiles in Anse-à-Veau. **(a)** The DAQLink III monitored from the computer. **(b)** the geophones connected to cables along the profile.

The SRT and MASW surveys were carried out using a portable 24-channel seismograph, model DAQLink III, manufactured by the American company SEISMIC SOURCE. Equipped with a recording system 24-bit, the seismograph is controlled by computer, via an Ethernet cable, using driver software (VSCOPE™) provided by the manufacturer. A number of 24 receivers

(geophones, generally with 5 m spacing) was used. The pulse source is produced by the impact, on a rigid plastic striking plate, of a 9.1 kg (20 lb) mass equipped with a seismic trigger compatible with the seismograph.

The SRT and MASW profiles were processed with the software SeisImager, Geometrics©. The result of the SRT process consists of 2D P-waves velocity models V_P obtained by measuring the arrival times of the first seismic waves (first arrival signal pointing) and applying tomographic inversion (Fig. 3.7). The MASW procedure consists of computing a dispersion curve from the input data and creating initial S-waves velocity models by considering various layers number and thickness. The final V_S model is an inverted model obtained by iteratively minimizing the RMS (Root Mean Square) between the observed and the theoretical data (Fig. 3.8).

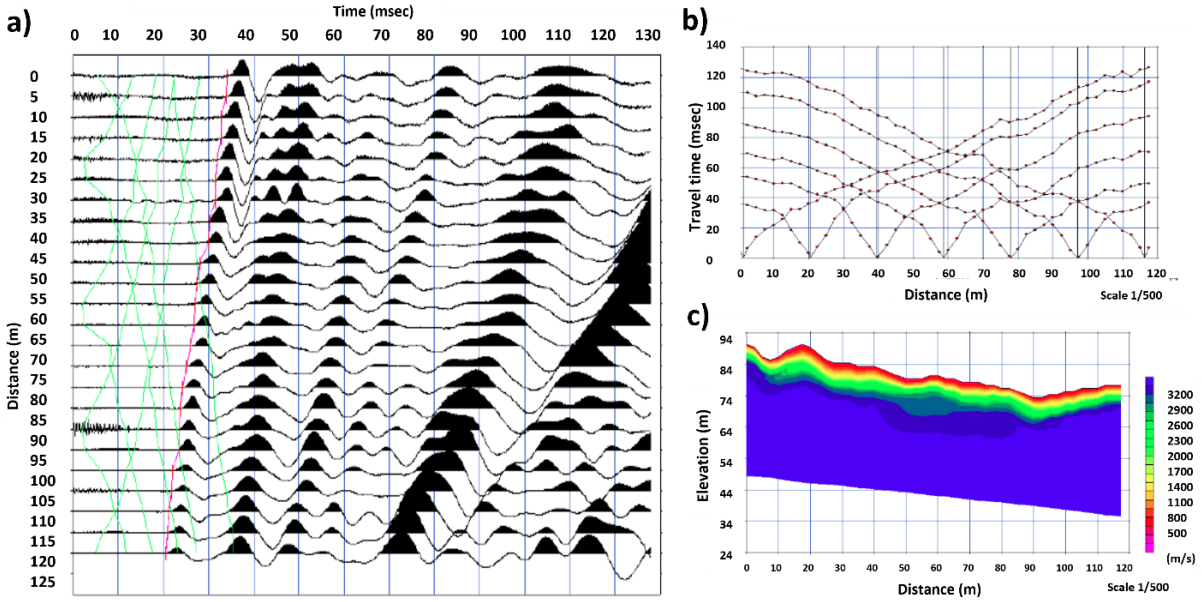

Fig. 3.7 Generation of P-wave velocity models according to the software SeisImager, Geometrics. **(a)** Time picking of the first arrival. **(b)** Travel times plotted as a function of receiver distance. **(c)** Result of P-waves velocity model V_P from tomographic inversion.

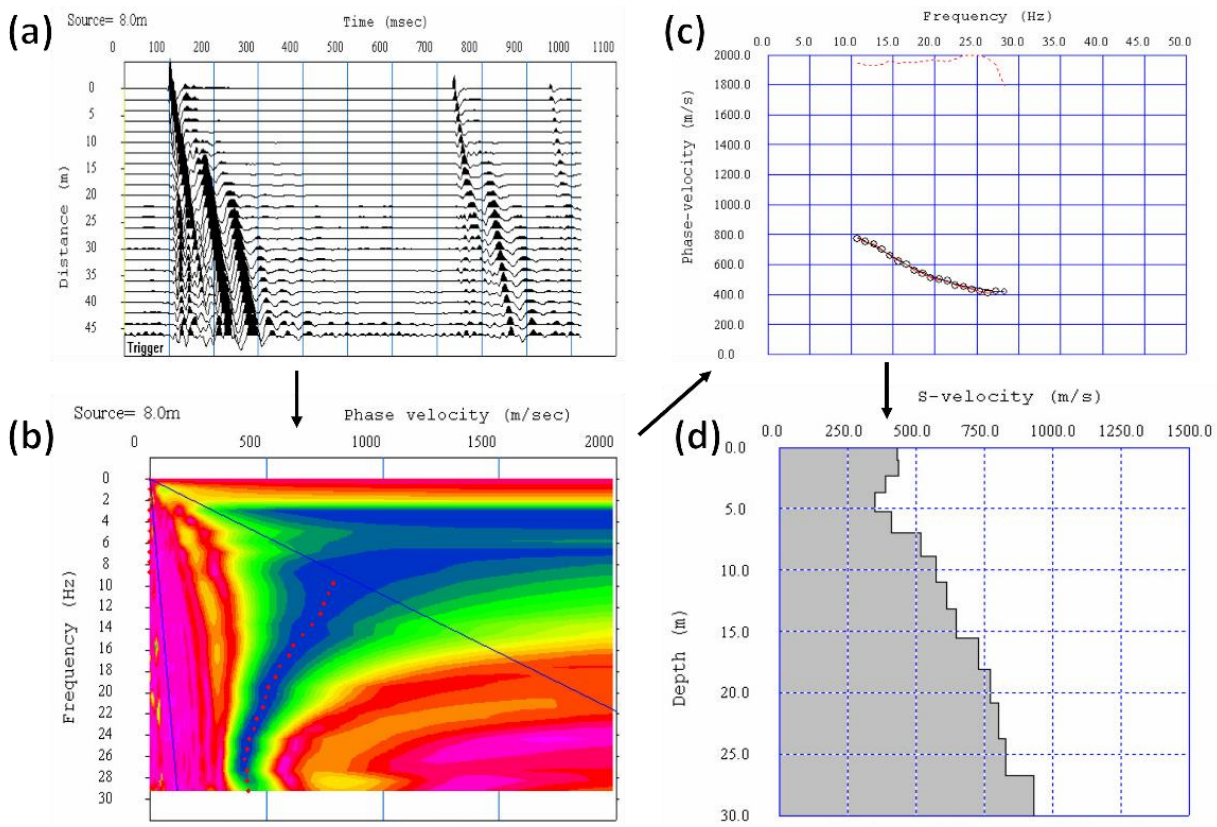

Fig. 3.8 Generation of S-wave velocity profiles according to the software SeisImager, Geometrics. **(a)** The input data. **(b)** Representation of the phase velocity. **(c)** The dispersion curve extracted. **(d)** The results of the S-wave velocity V_S.

3.1.4 Electric profiles

The electrical method used is the electrical resistivity tomography (ERT), which allows to obtain an electrical image of the subsoil, e.g. a section of the resistivity as a function of depth by measuring the resistance profile for different combinations of electrodes and potential. The resistivity model allows, in site amplification assessment, to refine and complete the subsurface structure and to remove certain uncertainties related to the interpretation of the other geophysical data.

The present method is based on Ohm's law and consists in injecting a direct current into the ground using 4 electrodes (2 current electrodes C1 and C2, 2 potential electrodes P1 and P2, see Fig. 3.9) in order to measure the intensity and study the distribution of the potential in the surrounding space (Loke 2018). From this distribution of the potential, it is then possible to deduce a distribution of the resistivity in the subsoil. In the case of a homogeneous and isotropic medium, this resistivity corresponds to the true resistivity. For a heterogeneous medium, the concept of apparent resistivity is used: ratio of the potential measured in the field to that calculated theoretically under the same conditions (same geometry of the electrodes, same intensity of injected current) on a homogeneous medium of resistivity 1. The apparent resistivity ρ_a is related to the injecting current I and the

resulting potential $\Delta\phi$ by the following equation (with k, a geometric factor that depends on the arrangement of the 4 electrodes):

$$\rho_a = k\frac{\Delta\phi}{I} \tag{3.5}$$

The first step in the method consists of carrying out a series of individual measurements using metal electrodes driven into the ground, generally along a profile (2D in our case). These measurements are carried out according to a predefined sequence. The apparent resistivity values obtained for each of the measurement quadrupoles are reported in a vertical plane called pseudo-section. In order to calculate the true or interpreted resistivity of the subsoil at each point of the vertical plane, the apparent resistivity values must be reversed (Reynolds 1997). Mathematically, the objective of the inversion is to minimize the difference (which is expressed by the RMS function: Root Mean Square) between the values of the calculated pseudo-section for the soil model and those of the measured pseudo-section. The electrical resistivity model obtained at the end of the inversion constitutes a solution, which is not unique regarding the values of the true or interpreted resistivities of the subsoil (Oldenburg and Li 1994).

Depending on the different configurations, the current is injected via two injection electrodes, and the potential difference is measured between two other (measuring) electrodes. Among the configurations (Wenner, Schlumberger, Dipole-dipole, etc.) conventionally used, the Wenner configuration is more sensitive to a vertical variation of the resistivity, whereas the dipole-dipole configuration is influenced by a horizontal variation (Dahlin and Zhou 2004).

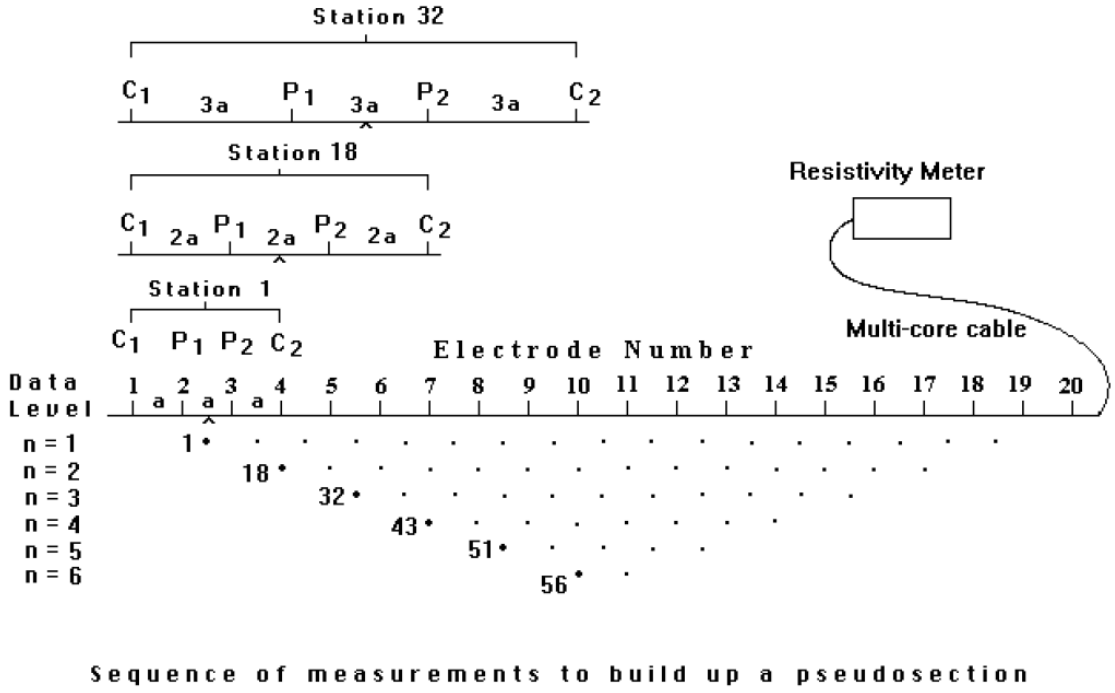

Fig. 3.9 Example of electrodes configuration for a 2D electrical surveys and the measurement sequence to construct a pseudo section (after Loke and Barker 1996).

The equipment used to perform the ERT measurements in Anse-à-Veau (Fig. 3.10) is the Terrameter SAS system from ABEM. It consists of a basic unit called Terrameter SAS 1000/ 4000 which can be supplemented as desired with accessories such as the ABEM LUND electrode systems and the ABEM SAS LOG borehole logging unit. The Wenner configuration (Dahlin and Zhou 2004) was mostly used during these surveys.

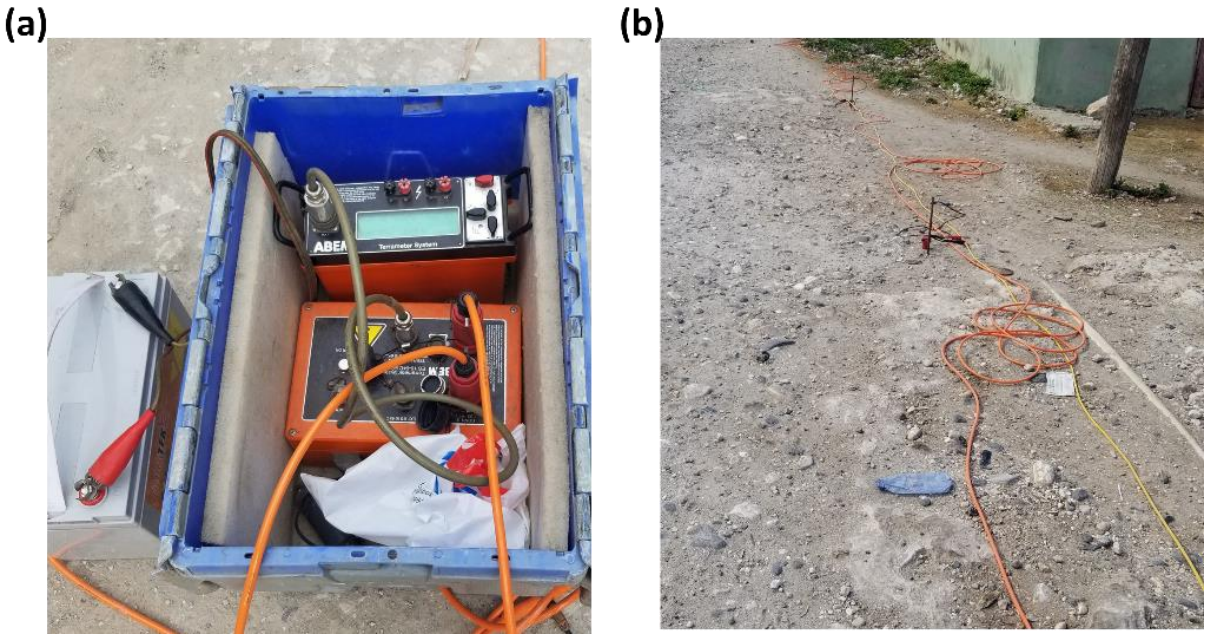

Fig. 3.10 The equipment used for the electrical survey in Anse-à-Veau. **(a)** the terrameter system. **(b)** the electrodes connected to cables along the profile.

The ERT profiles were processed with the software RES2DINV (Loke and Barker 1996) using a generalized least squares optimisation method to automatically determine a (2D) subsurface resistivity model for the input data. The pseudo-section obtained with the input data is divided into several rectangular blocks (with an apparent resistivity value for each block) whose size increases with depth. Iteratively, RES2DINV attempts to minimize the difference between the calculated and measured apparent resistivity values (see example of processing step results in Fig. 3.11).

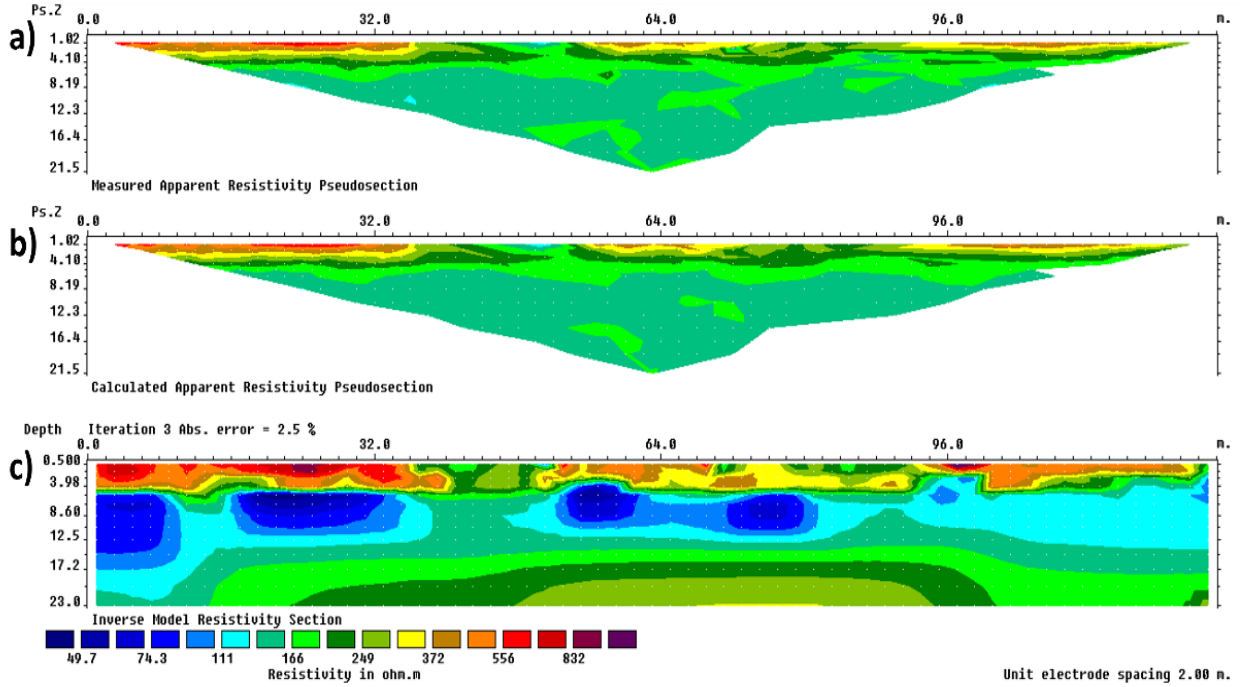

Fig. 3.11 Schematic representation of the ERT processing in RES2DINV 2D. **(a)** The raw values of apparent resistivities measured in the field. **(b)** The effect that the calculated model would produce if it were measured. **(c)** The final result of the inversion process representing the model calculated in resistivity and depths.

Note that these surveys carried out in the region of Anse-à-Veau (study area 1) in the frame of the thesis did not include geotechnical investigations such as boreholes drilling (it was not possible to reach the study area with geotechnical equipment during the surveys period). The data processing and analysis (for study area 1) in the chapter 4 also relies on field observations made during the surveys.

The surveys completed in the frame of the seismic microzonation of Cap-Haitien (study area 2) include borehole drilling completed by small scale geological mapping, seismic profiles and ambient noise recordings; but no earthquake recordings or electrical resistivity profiles. We directly analysed the final data (for study area 2) since the raw data were already processed in the microzonation reports.

3.2 Geostatistical, geomodelling and dynamic modelling methods

3.2.1 Geostatistical analysis

Geostatistical methods were initially developed to analyse geological data in the mining sector (Matheron 1970; Armstrong and Carignan 1997) but can be applied to any natural phenomenon that presents a spatial distribution according to a certain structure (Chauvet 1999). The methods have become very popular over the past 20 years in general geosciences and have various applications, such as interpolation between scalar values, stress ellipticity (Mukul 1998), soil properties (Bourennane 1997) or geophysical prospecting (Bourges et al. 2012).

The geostatistical analysis was performed using R Statistical Software (R Core Team 2024), which is an interpreted programming language that is widely used in data analysis and statistics. R allows for the processing and organization of large amounts of data for descriptive statistics, statistical testing, and graphical representation of data. It is a language based on the concept of vectors, which simplifies mathematical calculations and significantly reduces the use of iterative structures.

3.2.1.1 Fundamentals of the geostatistical theory

The geostatistical theory is based on the concept of the regionalized variable $z(x)$ interpreted as the realisation of a random function $Z(x)$. The regionalized variable $z(x)$ is a function defined in the geographic space that is generally irregular and exhibits two complementary aspects: a random aspect that explains local irregularities and a structured aspect that reflects the large-scale trends of the studied phenomenon. The random function $Z(x)$ is defined in the geographic and probabilistic space. The regionalized variable may be a wave velocity of a soil layer, a permeability, a geological facies, etc.

The random function *Z(x)* has no real statistical meaning a priori since we cannot reconstruct the probability law of *Z(x)* from a single realization *z(x)* of *Z(x)*. For statistical inference to be possible (and therefore for the probabilistic hypothesis to have any real meaning), geostatistics introduces the stationary hypothesis which suppose that the law of the random function *Z(x)* is invariant by translation. For the first two moments, we get the following relationships called weak or second-order stationarity:

- The expectation of $Z(x)$ is constant:

$$\boldsymbol{E[Z(x)] = m(x) = m} \tag{3.6}$$

- The covariance function between two points x and $x+h$ depends only on the vector h:

$$\boldsymbol{E[(Z(x) - m)(Z(x+h) - m)] = C[Z(x),\ Z(x+h)] = C(h)} \tag{3.7}$$

For $h=0$, $C(0) = E[(Z(x) - m)(Z(x+0) - m)] = E[(Z(x-m))^2] = Var[Z(x)]$ must also be constant. The stationarity then assumes the existence of a finite variance: $Var[Z(x)] = C(0)$. However, there are numerous phenomena that have an unlimited capacity of dispersion and cannot be correctly described if they are attributed a finite variance (Matheron 1970). This leads to

replacing the stationary hypothesis by a weaker hypothesis, but of analogous significance: the intrinsic hypothesis.

The intrinsic hypothesis assumes that the increments of the random function $Z(x)$ satisfy the second-order stationary hypothesis:

$$\begin{cases} \boldsymbol{E[Z(x+h)-Z(x)]=0} \\ \boldsymbol{Var[Z(x+h)-Z(x)]=2\gamma(h)} \end{cases} \quad (3.8)$$

In non-stationary geostatistics, the expected value $E[Z(x+h)-Z(x)]$ is equal to a certain function $m(h)$ called drift. The function $\gamma(h)$, called semi-variogram or simply variogram, is the basic tool for geostatistical analysis. If *Z(x)* is stationary, there is equivalence between the variogram $\gamma(h)$ and the covariance $C(h)$: $\gamma(h) = C(0) - C(h)$. A stationary random function *Z(x)* is also intrinsic, but the reciprocal is not always true (Armstrong and Carignan 1997).

The variogram is an increasing function of h. In stationary cases, $\gamma(h)$ increases to a certain limit called sill (variance of *Z(x)* in a large domain) and then remains constant (variogram with a sill or bounded variogram). The distance h at which $\gamma(h)$ reaches its sill is called range. In strictly intrinsic cases, $\gamma(h)$ increases indefinitely (variogram without a sill or unbounded variogram).

The class of variogram models that can be used for geostatistical analysis is richer than that of covariances. It includes bounded variogram models with associated covariances in the stationary model and other unbounded variogram models without associated covariances in the strictly intrinsic model (Fig. 3.12). The use of the variogram is always privileged in geostatistical modelling.

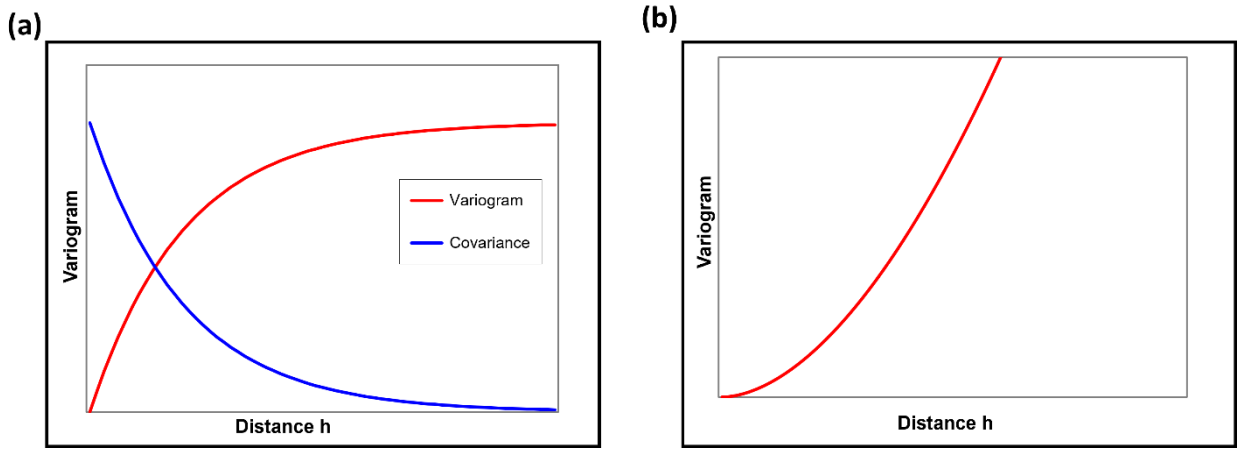

Fig. 3.12 (a) Example of bounded variogram with associated covariance (stationary model) and **(b)** unbounded variogram (strictly intrinsic model).

3.2.1.2 Variographic analysis

The variographic analysis (or structural analysis) corresponds to the calculations and modelling of variograms. Firstly, an exploratory study is carried out in order to evaluate the spatial distribution

of the spatial data, understand their degree of homogeneity, and search for atypical observations; secondly, an experimental variogram based on the available data is computed using the following expression:

$$\boldsymbol{\gamma^*(h) = \frac{1}{2N(h)} \sum_{i=1}^{N(h)} (Z(x_i + h) - Z(x_i))^2} \quad (3.9)$$

x_i and $x_i + h$ are the locations of the data points,

$N(h)$ is the number of pairs of data points separated by the distance h.

The more continuous behaviour of the experimental variogram in a specific spatial direction is called anisotropy. The purpose of the variographic analysis is to find a class of theoretical variogram models that best fit the experimental variogram since the variogram function must satisfy some very specific mathematical properties such as the conditional negativity property (Armstrong and Carignan 1997).

The variographic analysis with R is carried out using the gstat package (Gräler et al. 2016) which supports univariate and multivariate data and provides flexible tools for variogram modelling and spatial interpolation. The analysis with the gstat package follows the typical workflow usually performed in geostatistical analysis:

- Exploratory data analysis (EDA): understand the spatial data distribution and trends,
- Variogram estimation: compute the experimental variogram to quantify the spatial correlation,
- Variogram modelling: choose existing theoretical variogram models (such as spherical, exponential, gaussian, …) to fit the experimental variogram,
- Kriging: predict values at unsampled locations using the fitted variogram,
- Validation: assess the accuracy of the predictions by statistical technique such as the cross-validation,
- Visualization: maps of predictions and uncertainty.

The variographic analysis usually ends after the variogram modelling which is a subjective process since there is no true model. In practice, the main characteristics of the experimental variogram, such as behaviour at small distance, the existence of a sill and anisotropy, must be respected by the model. Generally, the modelling uses the linear regionalisation model which consists of the superposition of several basic theoretical models.

The calculation of the experimental variogram is performed based on key parameters such as:

- Calculation step: each experimental variogram is computed for distances that are multiples of a fundamental distance unit referred to as the lag step h,
- Calculation direction: the modelling is based on one or more experimental directional variograms which are related to the anisotropy of the phenomenon. These directions can be identified using the variogram map.

When the available data locations are irregular, tolerances are used on the distances and angles to regularise the experimental variogram. Improper use of these parameters can result in artifacts unrelated to the phenomenon being studied, which could negatively impact the modelling and its subsequent outputs.

3.2.1.3 The theory and basic application of kriging

Kriging is a geostatistical estimation method based on the variogram. It is the unbiased linear estimator that ensures the minimum estimation variance. Depending on the model, kriging can be simple, ordinary, universal, etc., but we can say that there is a unique kriging in the sense that there is a unique geostatistical way of approaching a local estimation problem.

Let $Z^*(V)$ be the estimator of the mean $Z(V)$ of $Z(x)$ in a spatial cell (or block) V:

$$\begin{cases} \boldsymbol{Z(V) = \frac{1}{[V]} \int Z(x) dx} \\ \boldsymbol{Z^*(V) = \sum_i \lambda_i Z(x_i)} \end{cases} \tag{3.10}$$

The kriging aims at assessing $Z(V)$ by the weighted average $\sum_i \lambda_i Z(x_i)$ by minimizing the variance $Var[Z^*(V) - Z(V)]$.

$[V]$ is the measure of the cell V which can be a point,

The $Z(x_i)$ are the known values of $Z(x)$ at n point locations x_i,

The λ_i are the unknowns of the problem.

The Ordinary Kriging (OK) is the most used in environmental and geoscientific applications. It corresponds to a stationary model with unknown but constant mean m (or an intrinsic model without drift). The Ordinary Kriging system and variance are defined by the following expressions:

$$\begin{cases} \boldsymbol{\sum_j \lambda_j \gamma(x_i, x_j) - \mu = \bar{\gamma}(x_i, V), \quad i = 1, \quad \dots, n} \\ \boldsymbol{\sum_j \lambda_j = 1} \end{cases} \tag{3.11}$$

$$\boldsymbol{\sigma_{OK}^2 = \sum_i \lambda_i \bar{\gamma}(x_i, V) - \bar{\gamma}(V, V) - \mu} \tag{3.12}$$

$\bar{\gamma}(x_i, V)$ is the average variogram between x_i and the spatial cell V,

$\bar{\gamma}(V, V)$ is the average variogram for all pairs of points that can be formed within the spatial cell V,
μ is a Lagrange parameter used in the minimization process.

Kriging is an exact interpolator: the estimate at a known location x_i gives the measured value $Z(x_i)$. The kriging variance in x_i is then zero.

When the mean m varies spatially, the stationary hypothesis cannot be applied. The random function $Z(x)$ can be considered as the superposition of two components:

$$\boldsymbol{Z(x) = Y(x) + m(x)} \quad (3.13)$$

$m(x)$ is the drift, $Y(x)$ is a residue which has the status of a random function with the second order stationarity hypothesis. The kriging that can be applied to these models is called Universal Kriging (Chauvet 1999). Another approach can be considered by assuming that higher order difference of the random function satisfies the stationarity hypothesis. $Z(x)$ is then an intrinsic random function of order *k* (IRF-k) and the non-stationarity is resolved in the generalized covariance (Myers 1989; Chauvet 1999).

The gstat package provides functionality to execute the kriging process. The function is applied to a predefined grid (a set of regularly spaced locations) over the area of interest. A set of arguments of the same function permits to define the type of kriging according to the model used and the fitted variogram. The quality of the kriging model and the fitted variogram is evaluated by the cross-validation method which consists in removing one data point, predicting it by the remaining points, and repeating the process for all points.

The output of the kriging function is the interpolated values at the prediction grid points and the prediction variance that quantifies the uncertainty. Higher variance implies higher uncertainty.

3.2.1.4 Cokriging: multivariate geostatistics

Cokriging is the extension of the kriging technique to multivariate cases. It involves the sampling of an auxiliary variable (or co-variable), besides the target variable, to be used when predicting the target variable at unsampled locations. The information carried by the co-variable improves the precision of the prediction of the target variable; this can be decisive when the co-variable is easier and cheaper to measure, and so more densely sampled, than the target variable. The superiority of cokriging over kriging in minimizing estimation variance is amply demonstrated when the secondary variables are highly correlated with primary variables (Wu et al. 2009; Emery 2012).

The structural analysis of multivariate models describes not only the spatial organization of each of the variables but also their joint organization: their coregionalization. The random function *Z(x)* then becomes a set of *N* random functions defined in the geographic and the probability space. The spatial structure of the studied phenomenon is described by both the simple variogram or covariance (between the same variables) and the cross-variogram or cross-covariance (between the target and co-variables).

Let $i = 1,..,N$ be the index of the variables Z_i, and $Z_i(x_\alpha)$ the known values of Z_i at the sampled points $\alpha = 1,..,n_i$. The estimator of $Z_{i_0}(V)$ is the following linear combination (with i_0: target variable):

$$\boldsymbol{Z^*_{i_0}(V) = \sum_{i=1}^{N} \sum_{\alpha=1}^{n_i} \lambda^i_\alpha Z_i(x_\alpha)} \quad (3.14)$$

The variographic analysis according to the linear coregionalization model assumes that simple and cross variograms are linear combinations of the same base structures (basic variogram models):

$$\boldsymbol{\gamma_{ij}(h) = \sum_{u=1}^{S} b_{ij}^{u} \varphi_u(h) \quad i,j = 1,..,N} \tag{3.15}$$

$[\gamma_{ij}(h)]$ is the matrix of the simple and cross-variograms, symmetrical of positive type,

$[b_{ij}^{u}(h)]$ are the matrices of the coregionalization, symmetrical of positive type,

$\varphi_u(h)$ are the basic variogram models (base structure).

In the bivariate case (a target variable with one co-variable, *N*=2), the modelling process involves first selecting the base structures that will be included in the bivariate model. Then, the simple variograms are fitted; finally, the cross-variogram is fitted using, for each base structure, a sill that verifies the Schwarz inequality $|b_{12}^{u}| \leq \sqrt{b_{11}^{u} b_{22}^{u}}$.

Cokriging necessitates that both the target variable and the co-variable be spatially autocorrelated individually, as well as spatially cross-correlated. Like univariate cases, the R gstat package provides functions to perform the variographic analysis. While the focus is on the target variable, the co-variable is also estimated using the full sample data, ensuring that both predictions are informed by the same underlying structure. The quality of the cokriging model can also be evaluated using the cross-validation technique.

3.2.1.5 Conditional simulation

The kriging (or cokriging) method allows performing geostatistical modelling by estimating a variable at unsampled point from the value of this variable at sampled points but smooths the variability of the studied phenomenon. The simulation methods are necessary when we want to obtain a spatial model that has the same variability characteristics as the real phenomenon. Appropriate methods are developed in nonlinear geostatistics but, unlike the simulation methods, they do not allow estimation when the criteria are complicated, nor to quantify the confidence in the estimators.

The conditional simulations are commonly used to generate multiple realizations of spatial fields, which are consistent with observed data and satisfy known constraints, such as geological boundaries or other geosciences data (Journel and Huijbregts 1978; Isaaks and Srivastava 1989). They provide a means to understand the variability of spatial processes by accounting for both the spatial continuity of the variable and the local conditions at the sampling points (Chiles and Delfiner 2012; Cressie 2015).

The simulations are constructed within a probabilistic framework where a more complete notation $Z_\omega(x)$ is considered for the random function (with $\omega \in \Omega$, the set of all possible realisation of Z). The regionalized variable z corresponds to the specific realization associated with a particular outcome $\omega_0 \in \Omega$ (then $z = Z_{\omega_0}$). Any realization Z_ω are considered as unconditional simulations; the ones that satisfy the constraint $Z_\omega(x_\alpha)$, with $\alpha = 1, \ldots, N$ the observed data at the sampled locations, are considered as conditional simulations.

The Sequential Gaussian Simulation (SGS) is one of the most used simulation methods in geostatistics and environmental science (Verly 1993; Bai and Tahmasebi 2022). It provides a way to generate realistic spatial fields that honour the data (conditional simulation) and spatial correlation while also capturing uncertainty by combining local kriging with stochastic sampling. Unlike the kriging method, which produces a single smooth estimate, SGS produces multiple conditional realizations. It is considered as a sequential simulation method in the sense that it simulates values at one location at a time and progressively builds up a realization of the field.

The main steps in the application of the SGS:

- Transform the dataset to a normal distribution if necessary,
- Create a simulation grid covering the area of interest,
- Predict the local conditional distribution (mean and variance) for each node in the simulation grid using kriging,
- Draw a random value from that distribution,
- Add the simulated value to the conditioning data for subsequent steps,
- Back-transform the realization to the original variable space if a normal transformation was applied.

The R gstat package provides the same set of objects and functions (as in the kriging case) to perform the conditional simulation. Once the variogram model is fitted, a gstat object is constructed for the simulation by specifying the model, the formula (for the type of kriging) and the number of nearest neighbours used for the local kriging estimates. The number of simulations to generate is also specified. Finally, a function is used to perform the simulations by incorporating both the trend and the spatial structure defined by the variogram. The output is a set of realizations of the variable allowing to compute conditional statistics such as mean, variance and probability maps at unsampled locations. Each realization is a possible spatial distribution of the variable constrained by both the observed data and the spatial correlation.

The present study remains within the framework of the two-point geostatistics method. Indeed, the variogram tool used here define the dissimilarity between two points, by opposite to new method called multi-point statistics (MPS) technique (Mirowski et al. 2008; Avalos and Ortiz 2020). However, the latter uses a structural tool called training image (the equivalent of the variogram in the MPS) which is too subjective and very complex in 3D modelling with fewer robust tools available for practical application.

Fig. 3.13 illustrates a geostatistical modelling performed by Sgobba et al. (2024) to identify dependencies between empirical amplification functions of sites in central Italy and the main geological and geophysical characteristics of the region.

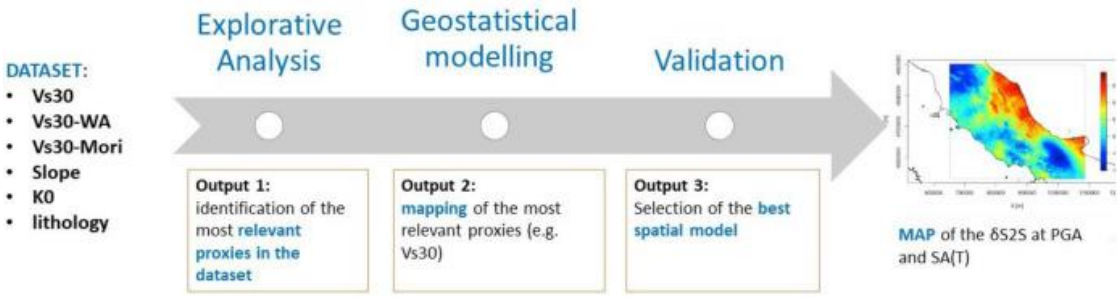

Fig. 3.13 Example of a workflow adopted in geostatistical analysis of local site amplification (after Sgobba et al. 2024).

3.2.2 Geomodelling

The use of 3D modelling has become widespread across a range of disciplines, from general geological and structural modelling (Caumon et al. 2009; Natali et al. 2013), to geothermal exploration (O'Sullivan et al. 2001; Sausse et al. 2010; Alcaraz et al. 2011) and groundwater exploration (Yongbin and Yitang 2007; Lerch and Hoppe 2007). The 3D models (or geomodels) constructed in the present study refer to a digital representation of the study areas using Leapfrog Works, a software developed by Seequent Ltd. ©, which employs implicit modelling techniques to generate geologically realistic surfaces and volumes based on available spatial data.

Geomodelling enables the integration of multiple data types into a spatially coherent framework, unlike traditional 2D cross-sections. It facilitates more robust visualization, hypothesis testing and quantitative extraction of volumes, thicknesses and spatial relationships. The implicit modelling method used in Leapfrog employs optimized radial basis functions techniques (FastRBF) to interpolate surfaces rapidly and dynamically as new data are integrated. This approach allows for automated update, consistency and rapid scenario testing (Calcagno et al. 2008; Guillen et al. 2008). The explicit modelling approach is not suitable for automated update or rapid scenario testing as it based on surfaces and volumes manually constructed from discrete points and interpreted boundaries.

3.2.2.1 Structural control and domain rules

The implicit modelling considers the lithological contacts (geological boundaries) as isosurfaces of scalar field, commonly referred to as potential field (Calcagno et al. 2008). A geological boundary is defined as the set of points where the scalar field:

$$\boldsymbol{f(x) = c} \tag{3.16}$$

With x, the spatial coordinates and c, a constant often chosen as zero for simplicity. $f(x)$ varies smoothly in space, and geological units are distinguished by these simple criteria: $f(x) < c$, inside one geological domain; $f(x) > c$, inside another geological domain.

The scalar fields are interpolated from discrete control points derived from boreholes intervals, surface mapping and structural measurements. Nevertheless, in regions affected by deformation, it is insufficient to simply interpolate from these points without accounting for structural controls, such as dip and dip azimuth of geological units.

Leapfrog allows the geomodeller to define a structural trend field, which governs the orientation of the interpolated surfaces. This trend field can be estimated from structural data and guides the interpolation of surfaces to align with the observed geological trends. Generally, the gradient of the scalar field is oriented along the structural trend, so that surfaces are generated perpendicular to this this direction, following the behaviour of real geological strata.

In addition to structural controls, Leapfrog incorporates a powerful domain logic system which allows the geomodeller to encode geological relationships that are not typically defined by data points. From a computational perspective, domain rules act as conditional constraints on the topology of the geomodel. Instead of solving a single unconstrained interpolation of all surfaces, Leapfrog resolves a system of surfaces that obey the data-derived constraints and the logic-based relationships. This approach reduces the risk of surfaces crossing illogically, units overlapping improperly or volumes appearing in unintended locations.

In many cases, Leapfrog implicit modelling technique can build accurate geological models directly from the data. However, in more geologically complex settings, the geomodeller is often required to guide the modelling process manually. Leapfrog provides several tools to support this kind of user control:

- Polylines that can be drawn along mapped contacts or interpreted structures to influence surface geometry,
- Structural trends that can be applied to specific areas to guide how layers are oriented during interpolation,
- Bounding envelopes that restrict surface generation to known geological limits,
- Surface editing tools that allow direct adjustments to surface shapes where needed.

3.2.2.2 Geomodelling workflow

The geomodelling process in Leapfrog generally follows a structured yet flexible workflow that reflects the software implicit modelling capabilities and the nature of geological modelling. The workflow follows a general sequence of steps that build from raw data toward a fully interpreted and functional geomodel.

The first step involves importing and organizing the data, which includes drilling data (from boreholes), surface mapping, structural measurements, topography and geophysical interpretations. Leapfrog provides intuitive data management tools that allow the geomodeller to link, clean and visualize the data, and define lithological and structural contacts based on logged intervals, mapping and interpreted sections. These contacts serve as control points for the implicit

interpolation process which uses radial basis functions to generate continuous surfaces representing geological boundaries.

In the second step, structural trends can be introduced to constraint the interpolation of surfaces, particularly in areas with sparse data or where bedding orientations influence unit geometry. These trends may be derived directly from drilling data (or other field data) or interpreted based on broader geological understanding. A key part of the workflow involves the definition of geological domains, which represent individual units or broader volumes of interest.

Finally, the completed geomodel can be used as a foundation to further analysis such as volume calculations, resource estimation, hydrogeological simulations or geotechnical design. Leapfrog also supports the export of models to other platforms, ensuring interoperability within multidisciplinary workflows.

The following figures (Figs. 3.14 and 3.15) illustrated two geomodels constructed with the software Leapfrog. The 3D models in Fig. 3.14 are the results of the geomodelling of the Balta rockslide (in the seismic region of Vrancea-Buzau, Romanian Carpathian Mountains) by Mreyen et al. (2021). HVSR data from ambient noise measurements combined with average S-wave velocity values from MASW measurements were used to estimate the thickness of the fractured debris materials (green colour in Fig. 3.14) according to the equation 3.1 (see section 3.1.1). The depth to the shearing horizon is inferred from the thickness value calculated for the fractured debris material, subtracted from the surface elevation value at the measurement points.

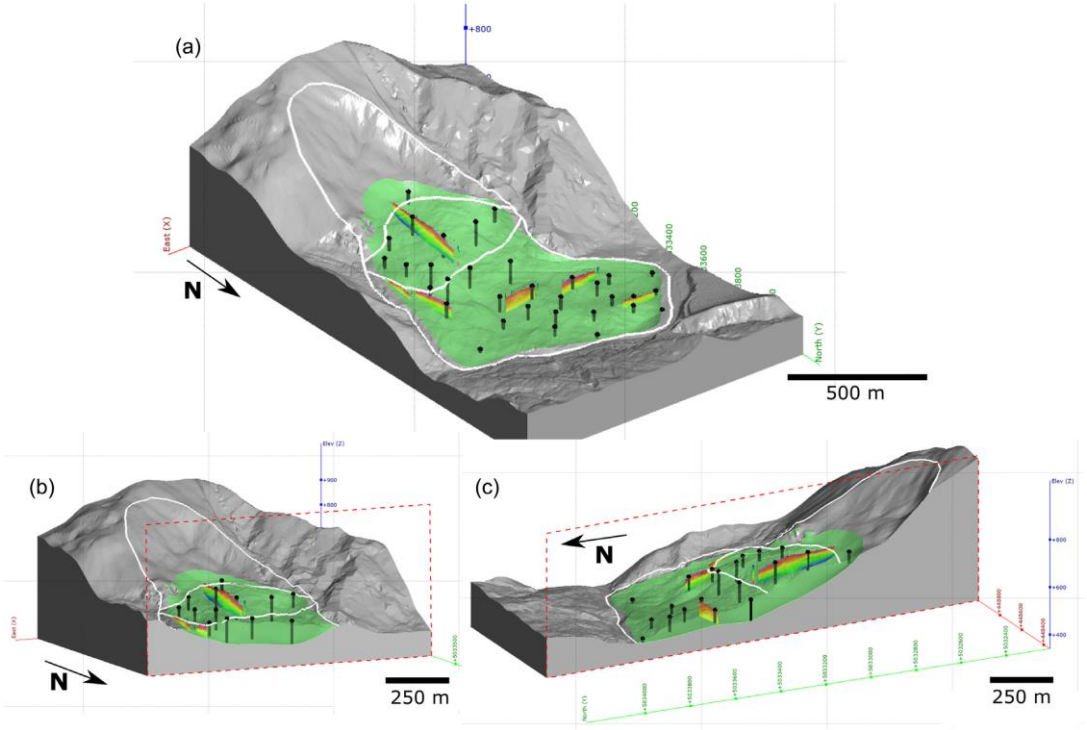

Fig. 3.14 Results of geomodelling of the Balta rockslide (in the seismic region of Vrancea-Buzau, Romanian Carpathian Mountains) with volume of rockslide debris (after Mreyen et al. 2021).

The 3D geomodel in Fig. 3.15 was constructed by Hakimov et al. (2024) to support seismic microzonation in the city of Dushanbe, Tajikistan. They integrated multiple datasets including HVSR measurements, SRT profiles, MAM surveys and boreholes to generate the geomodel with the software Leapfrog. Like in the previous case (in Fig. 3.14), the thickness of the near-surface layer was estimated using the relationship between the fundamental resonance frequency (from HVSR) and the average S-wave velocity value according to the equation 3.1.

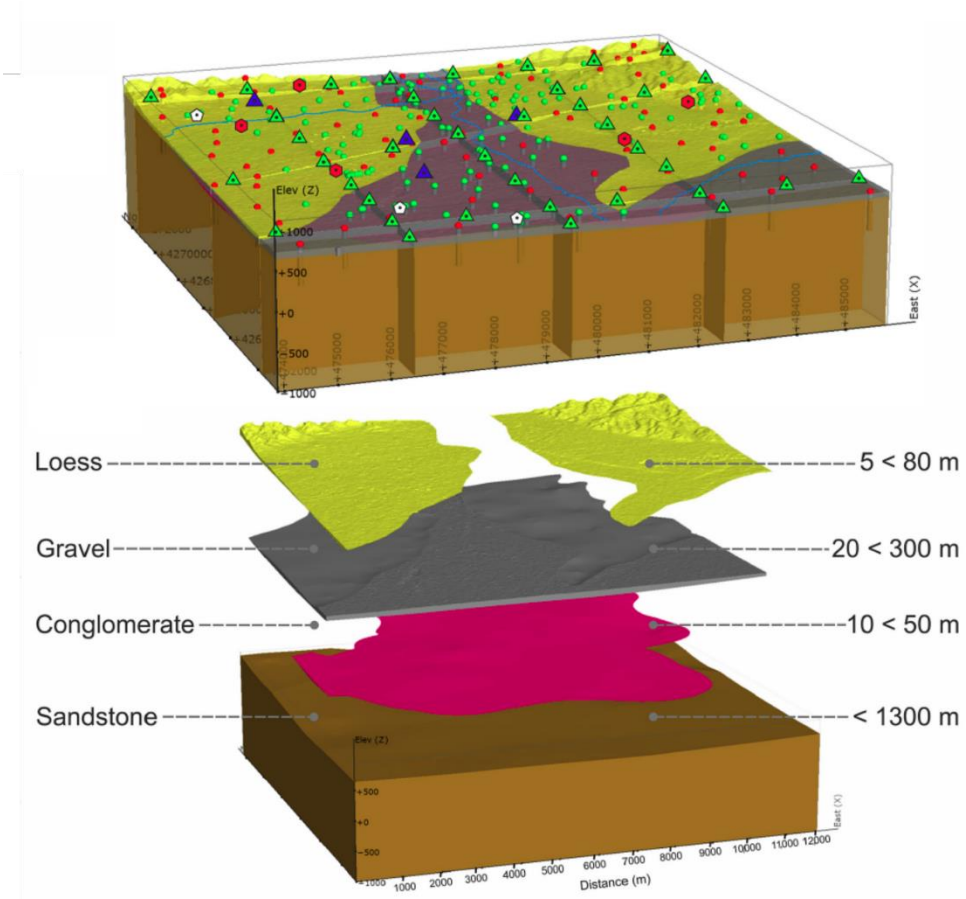

Fig. 3.15 Three-dimensional geomodel constructed by Hakimov et al. (2024) to support seismic microzonation of Dushanbe City, Tajikistan.

3.2.3 2D dynamic modelling

The 2D dynamic modelling used in the present study is based on the distinct elements method (DEM), initially developed to model jointed rock masses. The modelling process is carried out in UDEC (Universal Distinct Element Code), a numerical modelling software developed by Itasca Consulting Group ©. The software is designed to integrate the modelling of both rigid and deformable blocks, separated by joints or discontinuities, into a single computational framework.

The application of distinct element modelling to jointed rock problems has been investigated by many researchers including Cundall (1974), Bardet and Scott (1985) and Butkovich et al. (1988). The rock mass is modelled as a collection of discrete blocks; the joints between these blocks are

treated as interfaces. The contact forces and displacements at the interfaces are determined by tracking the motion of each block overt time. These motions are driven by disturbances, such as external loads or body forces, which propagate through the block system. The rate at which disturbances travel depends on the material and mechanical properties of the block system.

The methodology for dynamic modelling in UDEC (Itasca Consulting Group 2014) are:

- The model setup by defining the model geometry to which and assigning the material and joint properties,
- The static analysis by applying the initial stresses (or gravity) following the boundary conditions,
- The dynamic analysis by applying the dynamic loading and solving the dynamic simulation.

The results to analyse are mainly the displacement, velocity and acceleration over time which can be exported as history data for post-processing.

3.2.3.1 Model setup

The model setup involves defining the geometry of the domain, creating the block structure and selecting the appropriate constitutive models (such as elastic isotropic or anisotropic, Mohr-Coulomb plasticity, etc) for both the block material and the interfaces. The blocks can be modelled either as rigid or deformable; however, for more advanced simulations, it is essential to model the blocks as deformable by subdividing them into finite-difference zones. In UDEC, this is done using triangular zoning with a defined edge length.

The elastic model is one of the fundamental constitutive models used in UDEC to simulate the behaviour of rock masses or materials before yielding occurs. It assumes that the material of each block behaves according to the principles of linear elasticity as described by Hooke law. The material properties that are necessary to model elastic behaviour in UDEC are the density ρ along with the bulk modulus K and the shear modulus G. The elastic moduli modulus K and G are directly related to the Young modulus E and the Poisson ratio ν which are often used interchangeably depending on the available data. In practice, these parameters can be derived from the P-wave and S-wave velocities (V_P and V_S) measured in the soil or rock mass according to the following relations:

- The bulk modulus

$$\boldsymbol{K = \rho {V_P}^2 - \frac{4}{3}\rho {V_S}^2} \tag{3.17}$$

- The shear modulus

$$\boldsymbol{G = \rho {V_S}^2} \tag{3.18}$$

- The Poisson ratio

$$\boldsymbol{\nu = \frac{V_P{}^2 - 2V_S{}^2}{2(V_P{}^2 - V_S{}^2)}} \tag{3.19}$$

- The Young modulus

$$\boldsymbol{E = \frac{V_P{}^2 \rho(1+\nu)(1-2\nu)}{1-\nu}} \tag{3.20}$$

The elastic model is particularly advantageous due to its computational efficiency and simplicity. However, it is best suited for modelling materials that behave elastically under the applied load conditions and serves as a useful tool for preliminary stress analysis.

For the interfaces between the blocks, the Coulomb-slip failure joint model that is a generalized implementation of the classical Coulomb friction law is widely used in UDEC. These interfaces (or discontinuities) are characterized by a set of mechanical properties including the normal stiffness JK_N, shear stiffness JK_S, friction angle φ, cohesion c, tensile strength t and joint dilatation angle. The model accounts for both the shear and tensile failure mechanisms which are governed by the following expressions:

$$\boldsymbol{F^S_{max} = cA_C + F^n tan\varphi} \tag{3.21}$$

$$\boldsymbol{T_{max} = -TA_c} \tag{3.22}$$

F^S_{max}: the maximum shear force,

A_C: the area of the interfaces (or joints),

F^n: the normal force to the interfaces,

T_{max}: the maximum tensile force an intact joint,

T: the joint tensile strength.

3.2.3.2 Static analysis

The static analysis provides the essential baseline for dynamic analysis by establishing an initial equilibrium state. To complete the static analysis, boundary conditions are applied within the modelled domain. Displacement boundaries are defined by restricting movement along the axes, effectively preventing deformation at the base and sides of the model. A dynamic free field is also implemented to enable 1D finite difference calculations, allowing for the simulation of seismic wave propagation and vertical shear wave transmission along the boundaries. The number of nodes along the edge of the finite difference zone defines the extent of the free field boundaries.

The characteristics of static analysis are mainly the geometry of the model, the material properties and the boundary conditions. An automatic Rayleigh damping coefficient is used to stabilize the model by absorbing vibrational energy. Mechanical iterations continue until a static equilibrium is

reached, which is confirmed when the ratio of the unbalanced to applied mechanical forces falls below a specified threshold.

3.2.3.3 Dynamic analysis

The dynamic analysis aims at simulating the model response to dynamic loads that generate and dissipate kinetic energy over a short duration and at high frequencies, such as those caused by seismic or explosive events. To ensure accurate wave propagation through the medium, the size of the finite-difference (FD) elements is determined based on the criterion established by Kuhlemeyer and Lysmer (1973):

$$\boldsymbol{\Delta l \leq \frac{\lambda}{10}} \tag{3.23}$$

Δl : the size of the finite-difference (FD) spatial element,

λ : the wavelength associated with the highest frequency component of the input wave.

Two types of boundary conditions (BC) are used in UDEC for dynamic modelling: viscous and free-field. The viscous boundary condition, developed by Lysmer and kuhlemeyer (1969), works as a non-reflecting boundary by placing energy-absorbing points along the model edges, thereby minimizing the reflection of outgoing seismic waves back into the model. In contrast, the free-field boundary condition, introduced by Cundall et al. (1980), applies only to the lateral boundaries. It simulates an infinite domain by incorporating free-field motion without imposing lateral constraints, allowing upward-propagating seismic waves to travel as plane waves without being absorbed at the boundaries.

When free-field BC are applied at the sides, the model base is typically constrained using viscous BC. However, applying a velocity history at the bottom (as in earthquake simulations) can introduce distortions. To address the problem, a more accurate method involves applying wave energy at the model base in the form of a stress history rather than a velocity record according to the following relations:

$$\boldsymbol{\sigma_n = 2(\rho V_P)\upsilon_n} \tag{3.24}$$

$$\boldsymbol{\sigma_s = 2(\rho V_S)\upsilon_s} \tag{3.25}$$

σ_n and σ_s: the applied normal and shear stress,

ρ , V_P and V_S: the mass density, the P-wave and S-wave propagation through the medium, respectively,

υ_n and υ_s: the input normal and shear wave velocity, respectively.

The energy dissipation that naturally occurs in the ground during dynamic loading is represented by mechanical damping. For natural material such as soils and rocks, this damping is generally

considered frequency-independent and is best described as hysteretic (Cundall 1976). Rayleigh damping provides a numerical approximation to model this behaviour, offering a near-hysteretic response over a specified frequency range.

The computational efficiency of UDEC is specifically optimized for 2D simulations, thereby enabling faster and more resource-efficient analysis compared to 3D models that require significantly greater computational power.

An example of 2D dynamical modelling is presented in Fig. 3.16. The section is extracted from the geomodel in Fig. 3.15. The 2D dynamic model incorporates geotechnical parameters that describe both the block material and mechanical behaviour of joints. These include Young's modulus (E), bulk modulus (K), shear modulus (G), dry density (ρ), Poisson's ratio (v), normal and shear joint stiffness (*jkn* and *jks*), joint tensile strength (*jtens*), and cohesive forces (*jcoh*) at contacts. The values of K and G were calculated from P and S-wave velocities from seismic profiling, using standard elastic wave equations.

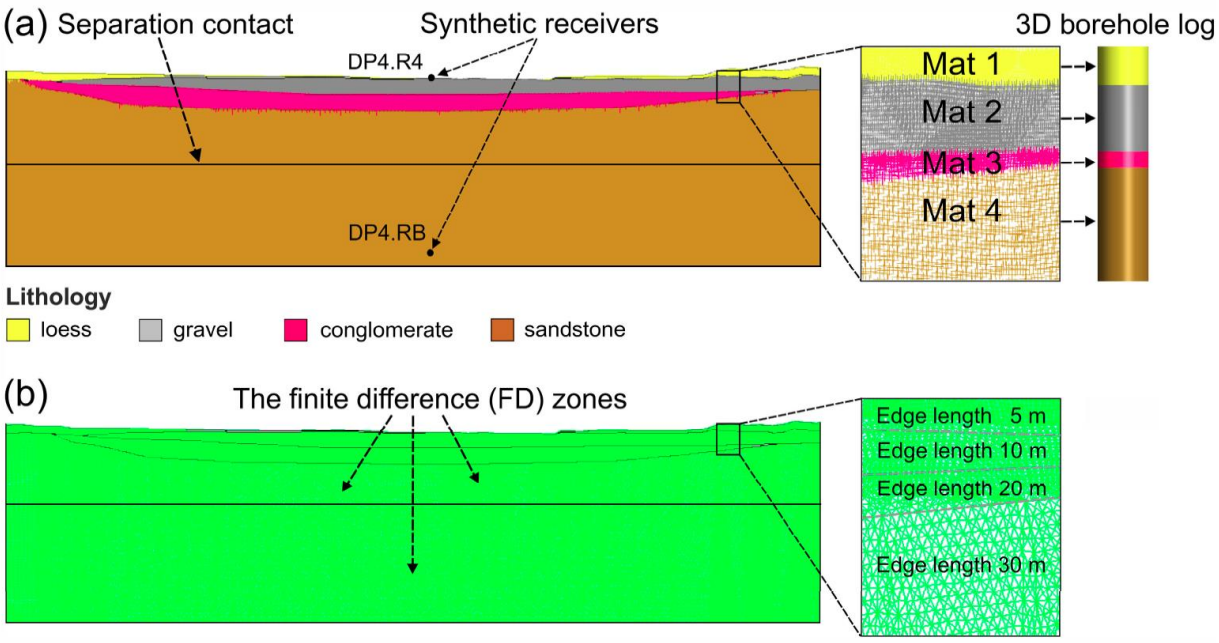

Fig. 3.16 Example of 2D dynamical modelling carried out by Hakimov et al. (2024) to support seismic microzonation of Dushanbe City, Tajikistan.

Fig. 3.17 shows results from 2D dynamic modelling by Daneels et al. (2008) for unstable slopes in Kainama, Kyrgyzstan. They obtained spectral amplifications at the surface (of the numerical model) by dividing the Fourier amplitude spectra of the computed horizontal motions by that of the reference horizontal input motion (which had its amplitudes doubled to represent rock-site ground motions). The resulting amplifications are presented at the bottom of Fig. 3.17, with strong and weak horizontal amplification shown in red and blue, respectively.

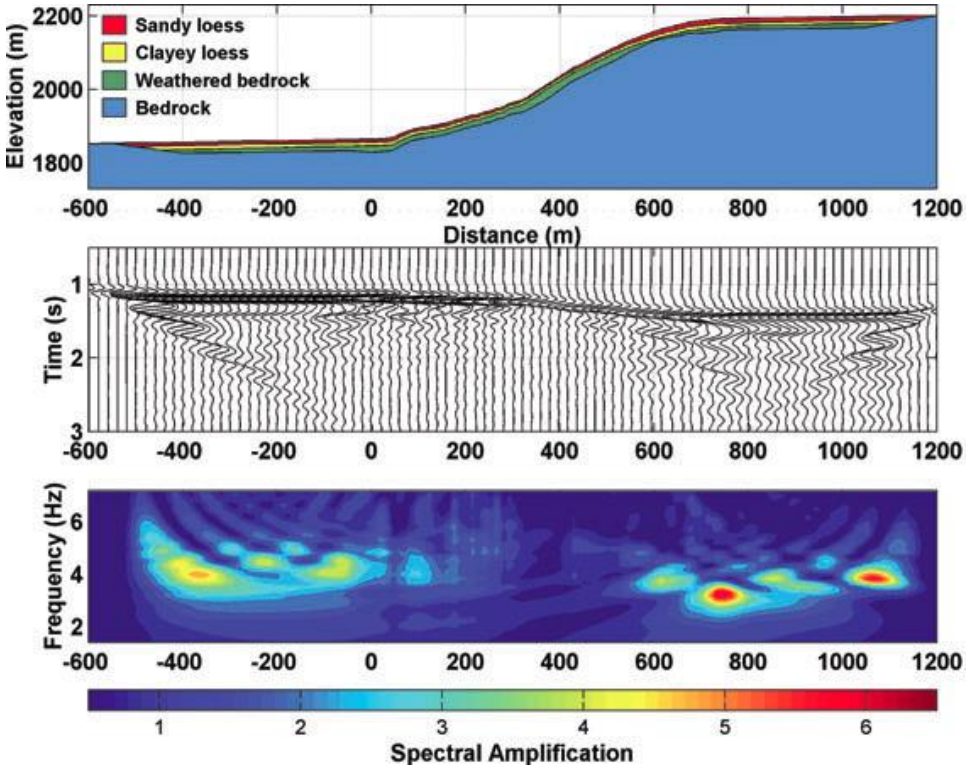

Fig. 3.17 Schematic representation of the topography and the geology of Kainama slope (after Daneels et al. (2008)). In the middle: horizontal accelerations computed every 20 m along the ground surface. At the bottom: spectral horizontal amplifications computed along the ground surface.

4 Data processing and results

4.1 Data processing and results for study area 1 (Anse-à-Veau)

The surveys carried out for study area 1 (Anse-à-Veau) include more than 150 H/V measurements, 8 ERT profiles, 22 SRT-MASW profiles and the earthquake recordings from two broadband seismometers at Anse-à-Veau, and two other ones at Miragoane and Fond des Nègres, in the vicinity of the Enriquillo Plantain Garden Fault (EPGF). The results presented in the current section (4.1) were published by Dorival et al. (2025).

4.1.1 HVSR results

The HVSR (H/V spectral ratio) data consist of ambient noise recordings of 20 to 30 min with a rate of 128 samples per second processed by the Geopsy software (Wathelet et al. 2020). The analysis is made in the frequency range 0.25-25 Hz.

In Fig 4.1, we present an example of HVSR processing for the study area. The measurement was carried out in *La Basse Ville* (at P5). As presented in Fig. 4.1a, the process starts by the selection of the most stable windows from the ambient noise recording. The selection of the windows was made according to the criteria presented in section 3.1.1 to avoid transient noise. The final result is an average applied to each selected window. Fig. 4.1b illustrates the H/V curves as a function of the frequency. The grey bar indicates the fundamental resonance frequency f_0. The corresponding value of f_0 in the vertical axis is the relative amplitude A_0. The graphs in Fig. 4.1c represent the direction of polarisation of the waves at the resonance frequency f_0. This direction is illustrated by the black arrow (N160°).

The measurements were performed across distinct environmental zones including the urban area of the town, coastal zones near the sea, and several isolated areas. Fig. 4.2 presents the spatial distribution of measurement points, the corresponding fundamental frequencies, and selected examples of H/V curves across the town of Anse-à-Veau. Fig. 4.3 illustrates representative H/V curves obtained from areas situated outside the town, particularly in the southern part of the study region, where geological and morphological conditions may differ from those within the urban setting.

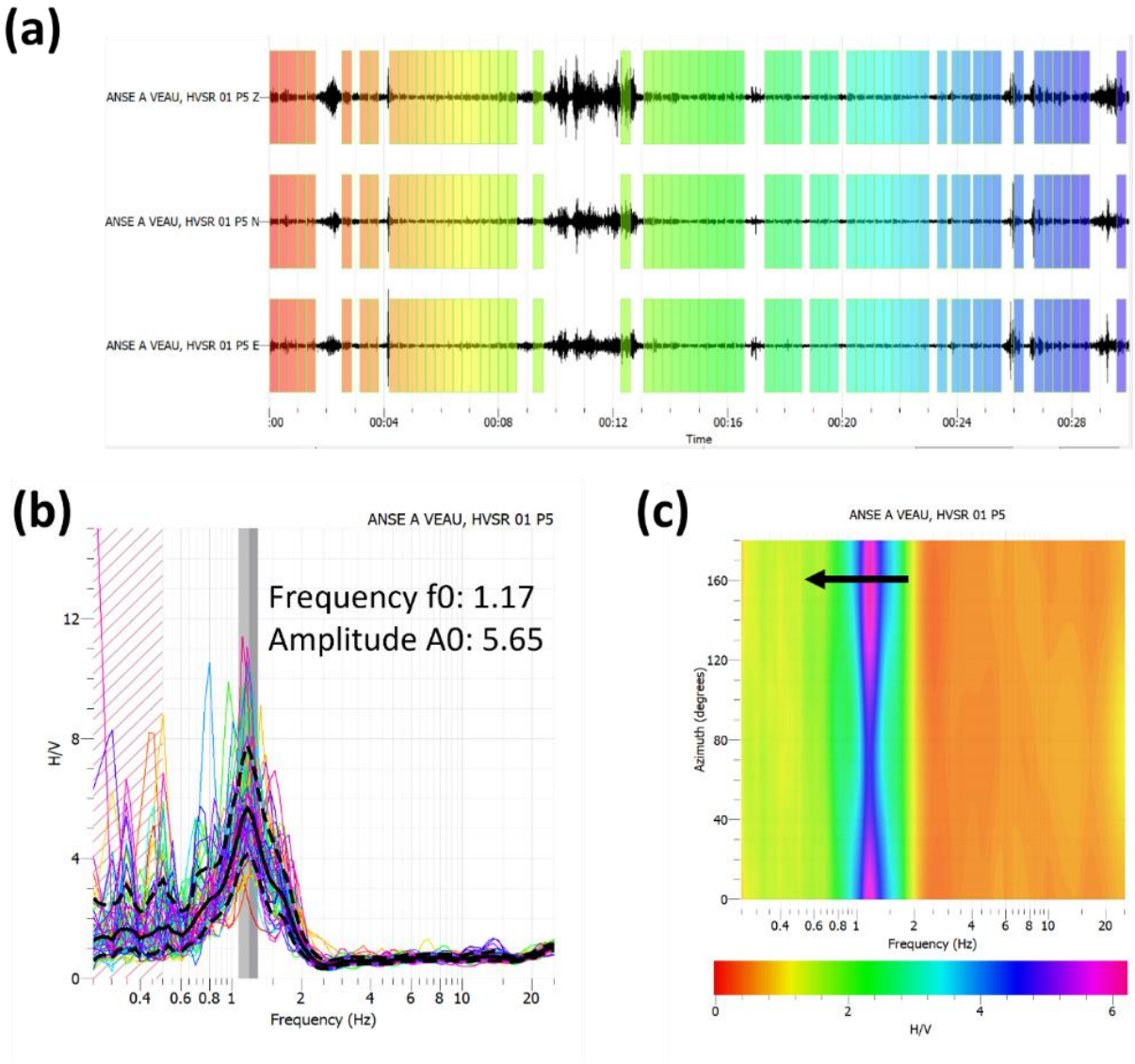

Fig. 4.1 Schematic representation of the HVSR processing workflow according to the software Geopsy.

The results show that the flat curves are observed at *La Haute Ville* where the subsurface is composed of Quaternary reef limestone. This geological unit appears to produce minimal amplification of seismic waves. From the south of *La Haute Ville* toward the transition zone between the Quaternary reef limestone and the pelagic massive limestone of the adjacent mountainous area, the H/V curves exhibit a progressive change in shape. In this contact zone (mainly characterized by marly limestone), the H/V curves become less flat and display low amplitude peaks. In certain localized sectors of this transition area, the marly limestone is covered by lateritic soils where the H/V curves show two peaks: the first, typically at lower frequency, is associated with the marly limestone, while the second, occurring at higher frequency and amplitude, likely corresponds to the shallow lateritic deposits.

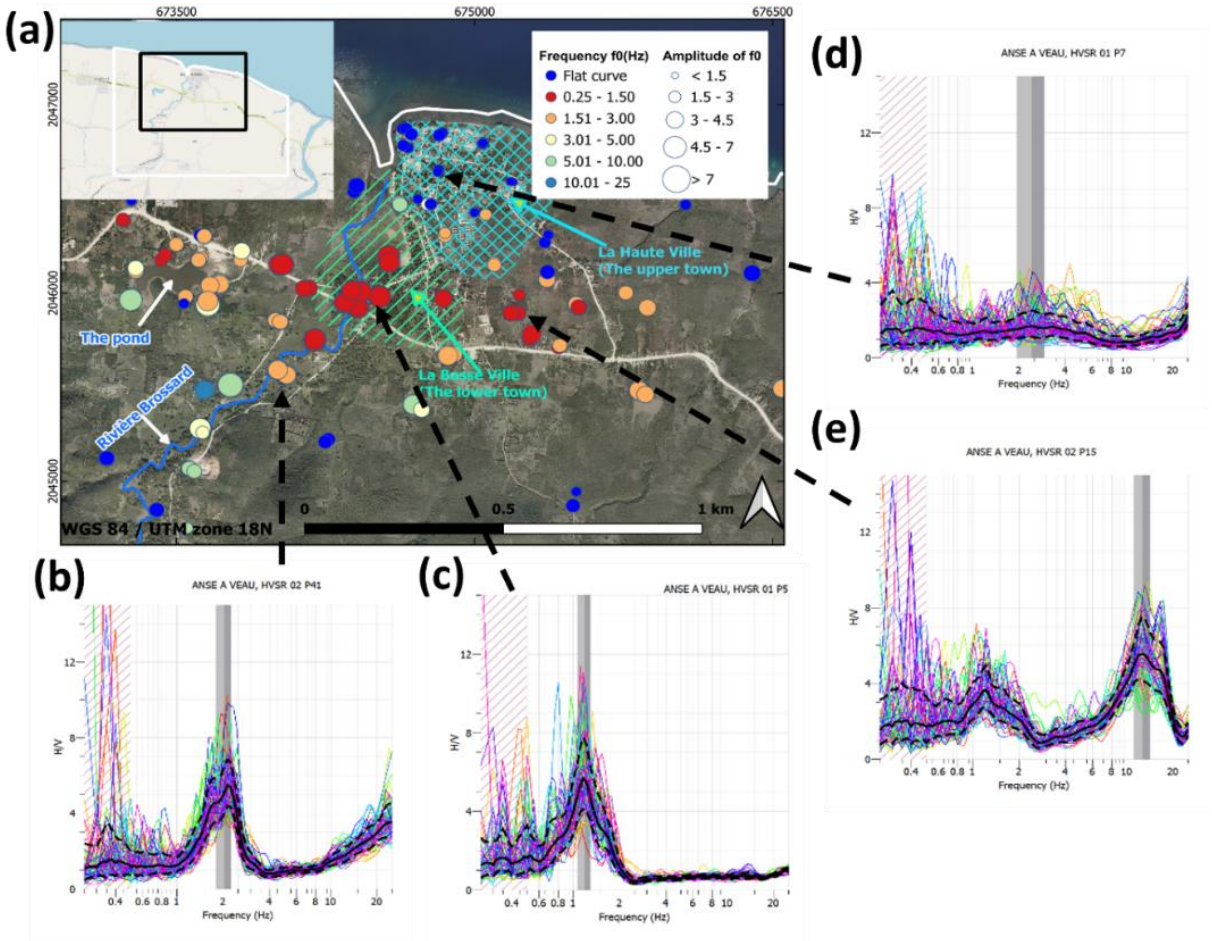

Fig. 4.2 **(a)** Location of H/V measurements near and across the town of Anse-à-Veau. Colour of circle on the map indicates the fundamental resonance frequency f_0; size of circle indicates the relative amplitude of the f_0 peak. **(b)** and **(c)** Example of H/V curves obtained near and within *La Basse Ville* (the lower town). **(d)** Example of flat H/V curves obtained in *La Haute Ville* (the upper town). **(e)** Example of H/V curves with two peaks obtained in the south of *La Haute Ville*.

The H/V curves obtained in *La Basse Ville* are characterized by low fundamental frequencies combined with high amplitude peaks, a pattern commonly associated with unconsolidated sedimentary deposits that tend to amplify seismic ground motion. This behaviour suggests that *La Basse Ville* built on alluvium may experience stronger shaking during seismic events compared to the more elevated and geologically stable zones of the study area. In Fig. 4.3, high amplitude peaks are observed near the municipality of Arnaud (southwestern corner of the map). Unlike those in *La Basse Ville*, these peaks generally occur at higher frequencies and may be associated with thinner sedimentary cover or stiffer near-surface materials. This distinction suggests that while both areas show evidence of site amplification, the underlying causes and resonance characteristics differ due to local lithological variations.

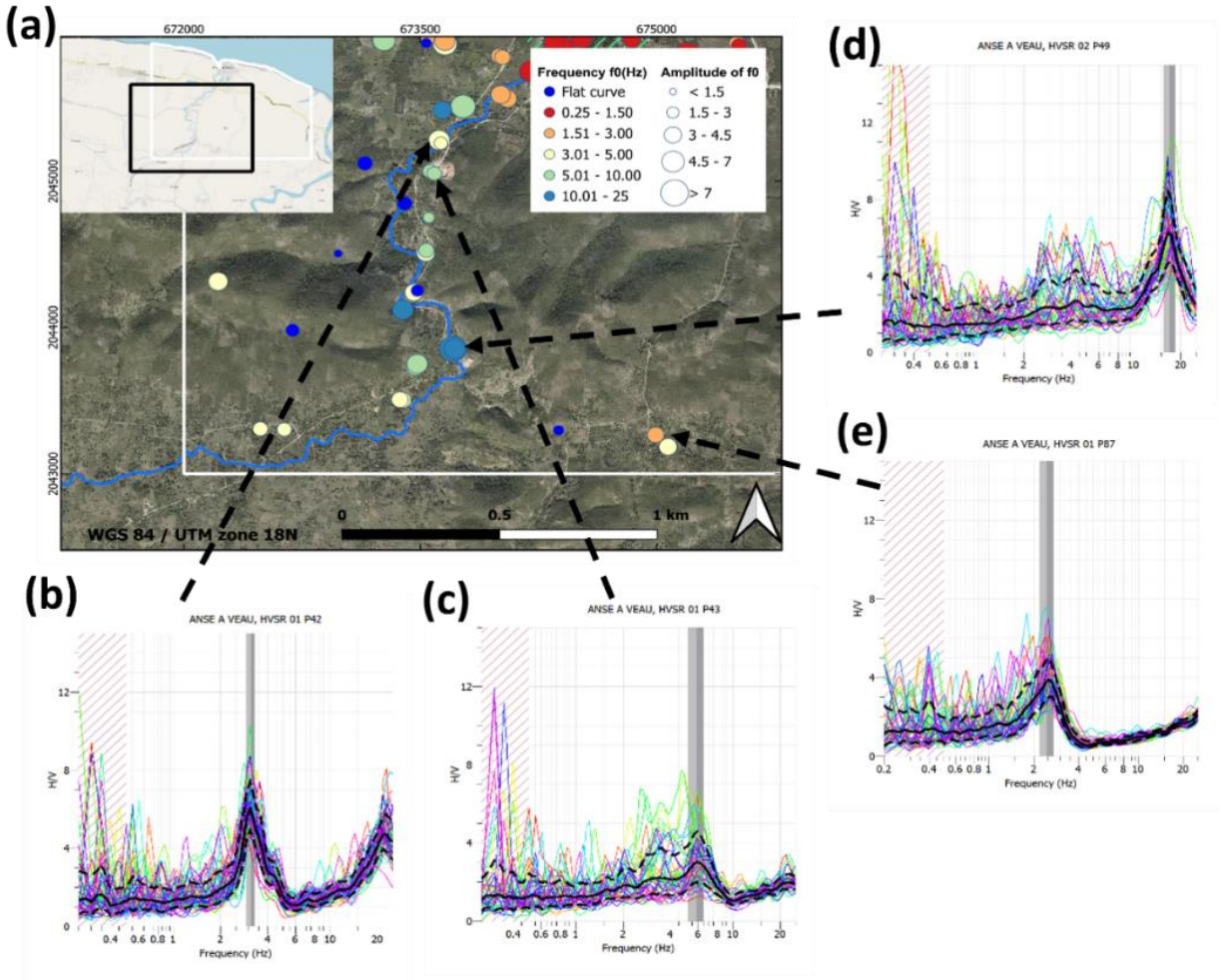

Fig. 4.3 (a) Location of H/V measurements outside the town of Anse-à-Veau. Colour of circle on the map indicates the fundamental resonance frequency f_0; size of circle indicates the relative amplitude of the f_0 peak. **(b-e)** Examples of H/V curves obtained outside the town of Anse-à-Veau, in the south of the study area.

The azimuth analysis according to the H/V processing from Geopsy is shown in Figs. 4.4 and 4.5. It indicates that the shallow layer has been deposited following a trend roughly parallel to the direction of the mountain (~N110°). The shallow layer becomes thicker at *La Basse Ville* and towards the pond according to the peak at lower frequency but with Quaternary alluvium. The polarisation is orthogonal to the mountain near the coast at *La Basse Ville* (the direction of the river seems to influence the alluvium deposit near the coast), but it is roughly parallel to the direction of the mountain in the contact zone between the Quaternary reef limestone and the pelagic massive limestone of the mountain (the direction of the mountain seems to influence the sedimentary deposit in this contact zone).

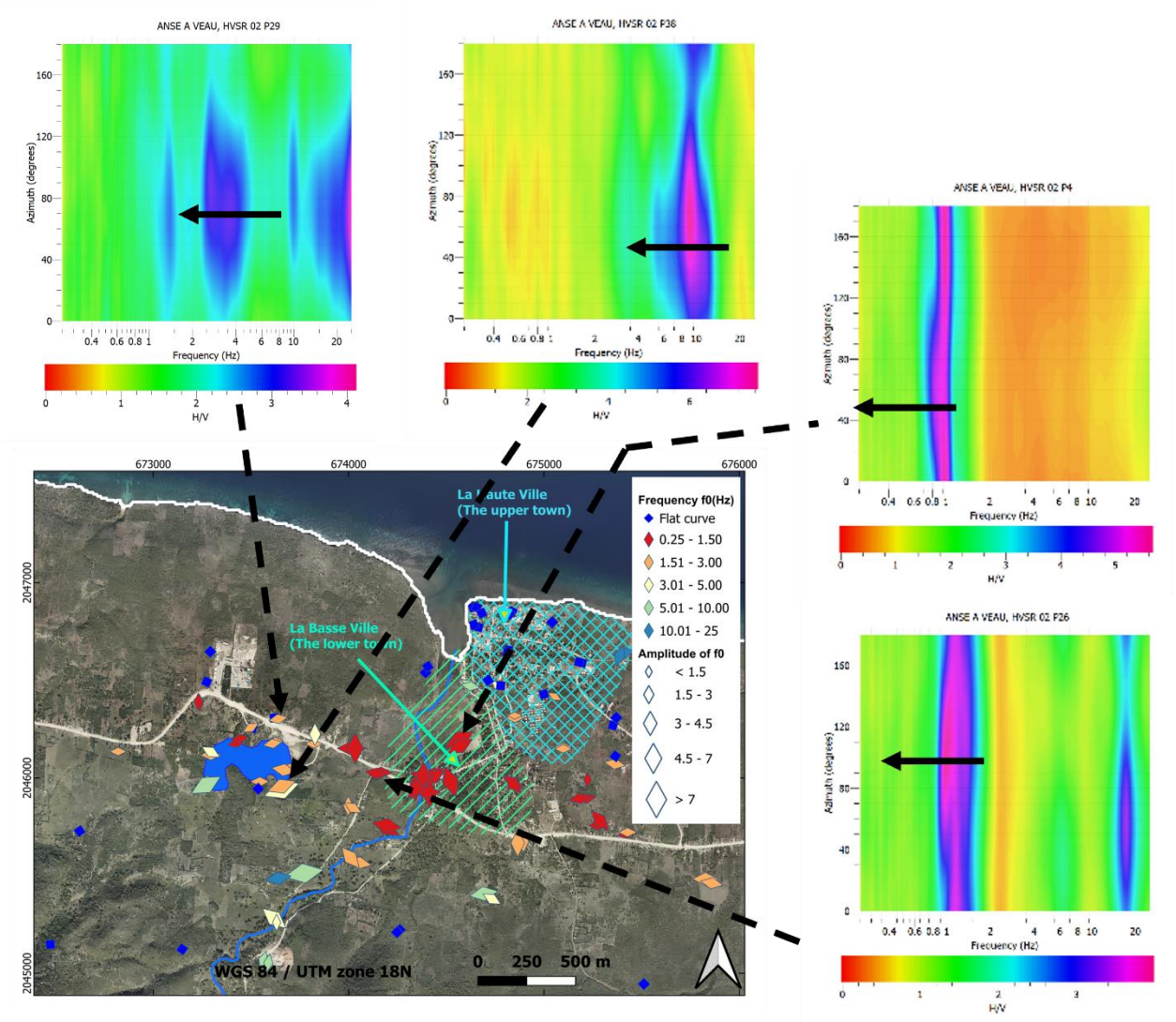

Fig. 4.4 Azimuth analysis of the ambient noise HVSR measurements near and across the town of Anse-à-Veau. The orientation of the diamonds long diagonals represents the direction of the wave polarisation. Colour of diamond symbol on the map indicates the fundamental resonance frequency f_0; size of diamond indicates the relative amplitude of the f_0 peak.

4.1.2 MASW results

The MASW method was mostly performed on profiles of 115 m (24 geophones, 5 m spacing) and processed using the software SeisImager ®. From the input data (Fig. 4.6a), we compute a dispersion curve (Fig. 4.6b), then, the dispersion curve is extracted considering the signal-to-noise ratio (Fig. 4.6c) to establish the initial S-waves velocity model (Fig. 4.6d). The grey areas in the profiles are computed from the data; the lower areas are interpolated by the processing software to represent the deeper parts. The red curves represent the experimental dispersion curves; the black ones are the theoretical curves from the inversion process. The parameter V_{S30} is also deduced for every V_S profile.

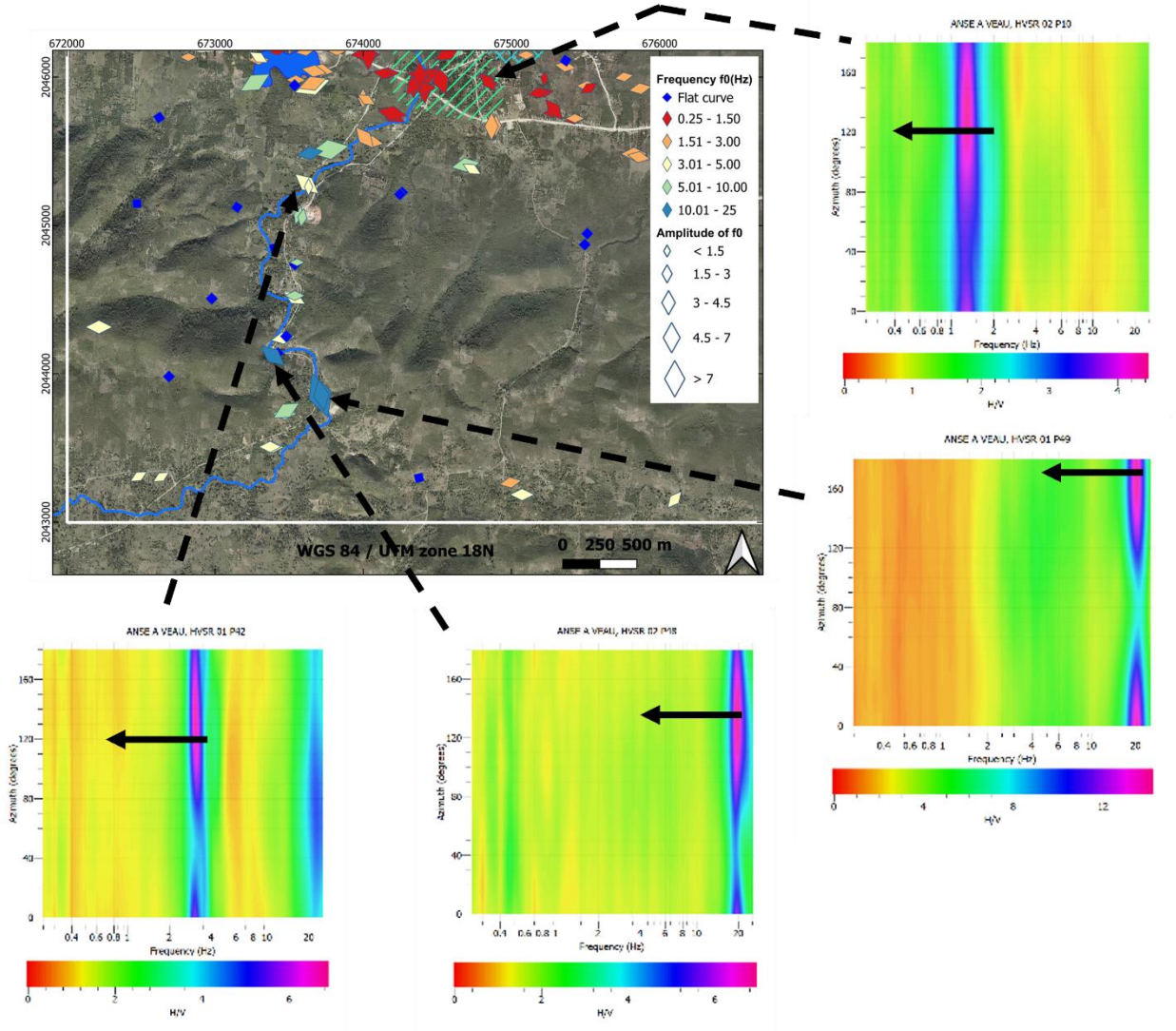

Fig. 4.5 Azimuth analysis of the ambient noise HVSR measurements outside the town of Anse-à-Veau. The orientation of the diamonds long diagonals represents the direction of the wave polarisation. Colour of diamond symbol on the map indicates the fundamental resonance frequency f_0; size of diamond indicates the relative amplitude of the f_0 peak.

The results obtained for some the sites within and outside the town of Anse-à-Veau are presented in Figs. 4.7 and 4.8, respectively. The models obtained for *La Basse Ville* are combination of two dispersion curves. One is from the common active MASW method described in the methodology; the other one is from passive MASW technique using ambient noise. Indeed, the energy generated by the shots in the active method, differently from the energy from ambient seismic noise, could not reach the deeper parts of the very soft layers at *La Basse Ville*. The combined dispersion curves are slightly smoothed while merging the two individual curves (from active and passive sources). Then, the contrasts are not clear in the V_S profiles for *La Basse Ville* despite that we observed clear peak in the HVSR curves.

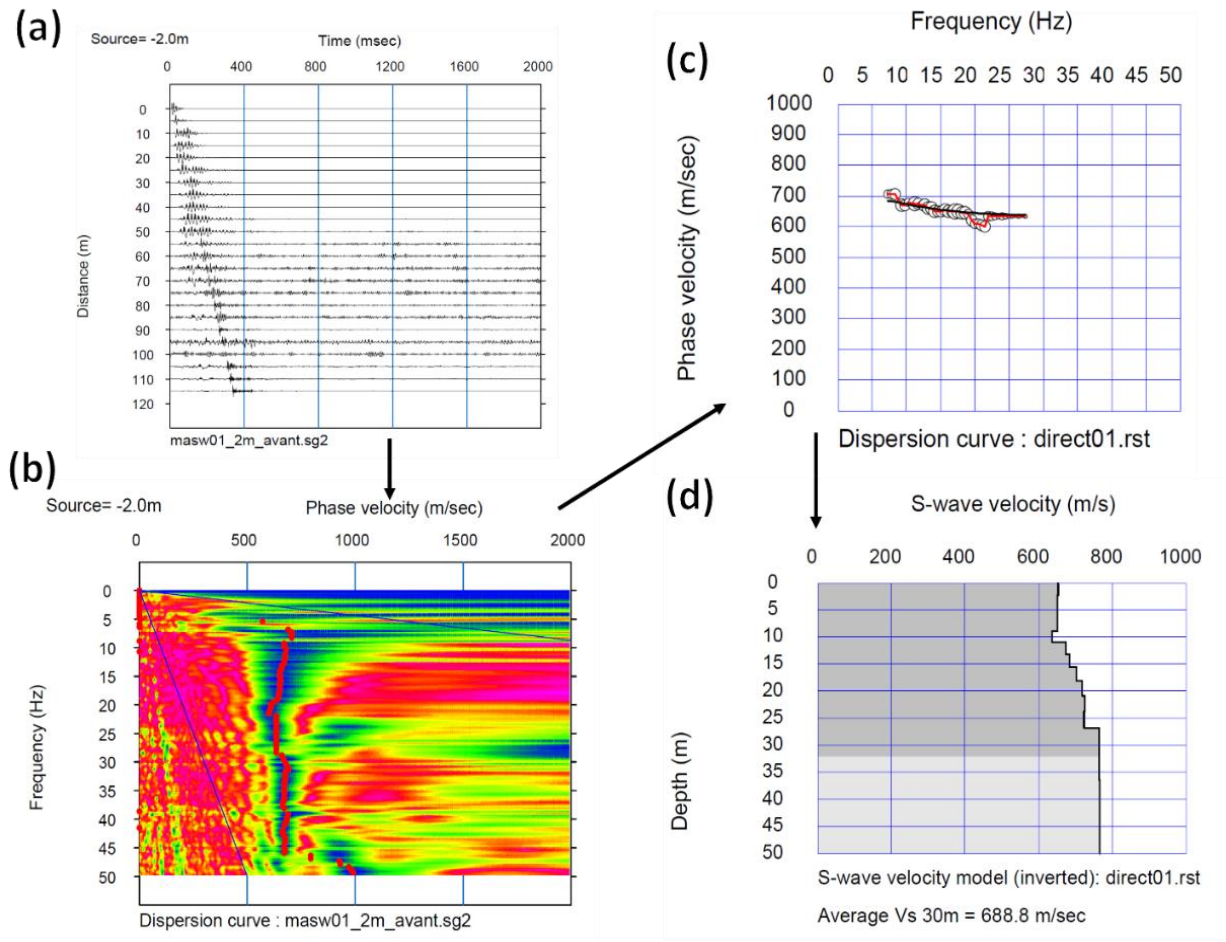

Fig. 4.6 Example of MASW profiles processing in a site (P1) at *La Haute Ville* in Anse-à-Veau. **(a)** The input data. **(b)** Representation of the phase velocity. **(c)** The dispersion curve extracted. **(d)** The results of the S-wave velocity V_S.

The highest V_S values (>600 m/s) are observed in *La Haute Ville* on the Quaternary reef limestone where the soils are mechanically competent and interpreted as minimal potential for ground motion amplification. These V_S values are consistent with the flat and low amplitude H/V curves identified and confirm the relatively rigid seismic response of this sector. In contrast, the lowest V_S values (100-250 m/s) are measured in *La Basse Ville* on the Quaternary alluvium. These unconsolidated sediments contribute to the significantly reduced S-waves and high potential for seismic amplification observed in this area.

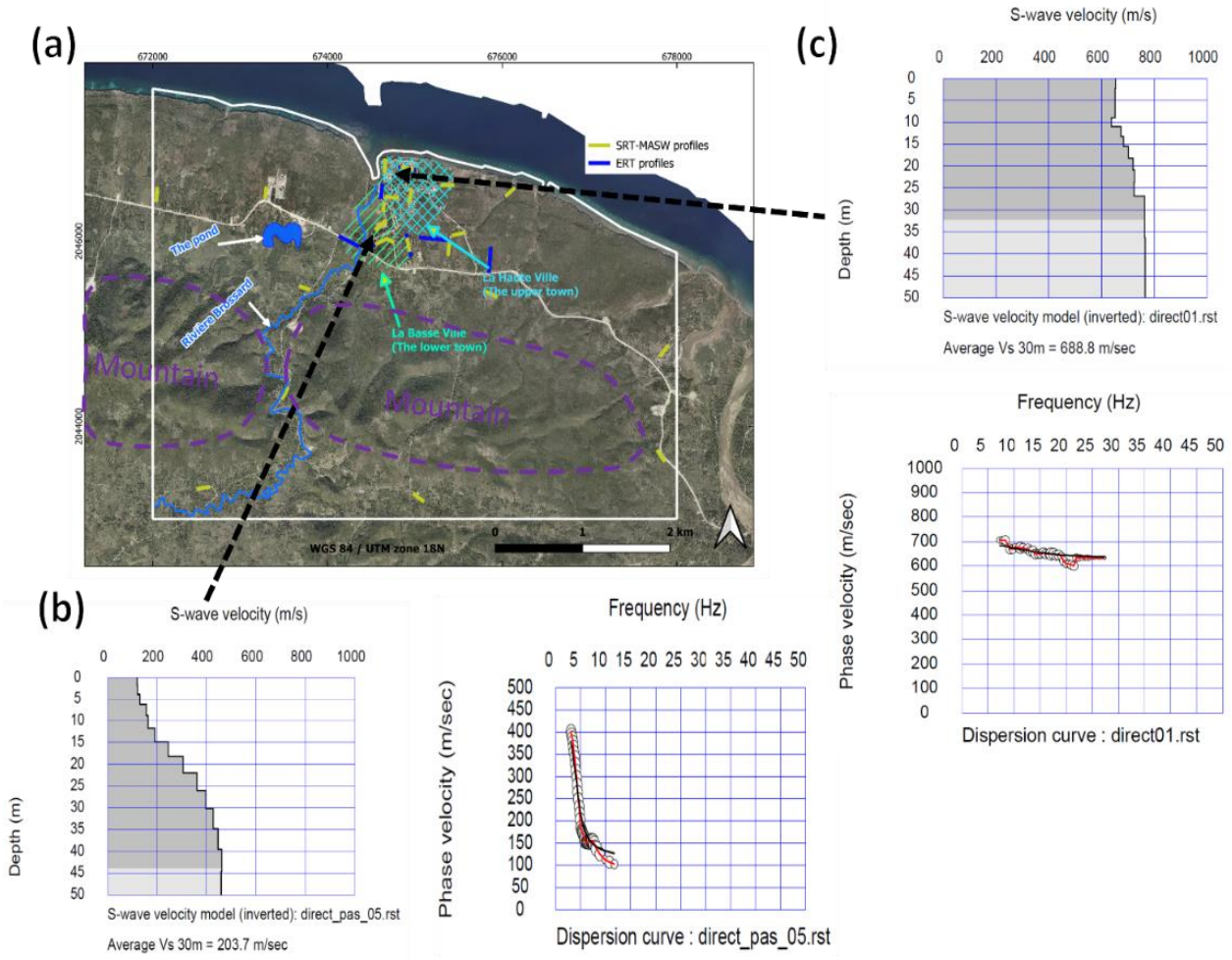

Fig. 4.7 (a) Location of seismic profiles MASW carried out in Anse-à-Veau. **(b)** S-waves velocity profile (V_S) and dispersion curve obtained in *La Basse Ville*. **(c)** S-waves velocity profile (V_S) and dispersion curve obtained in *La Haute Ville*.

The sites located on the other side of the mountain in the southern part of the study area (Fig. 4.8), are characterized by intermediate V_S values (400-500 m/s) in the west (Fig. 4.8b) and V_S values (220-380 m/s) in the east (Fig. 4.8c). The corresponding H/V curves in these areas display features that are intermediate between the clear, pronounced peaks observed in the softer alluvium and the flat curves of the reef limestones.

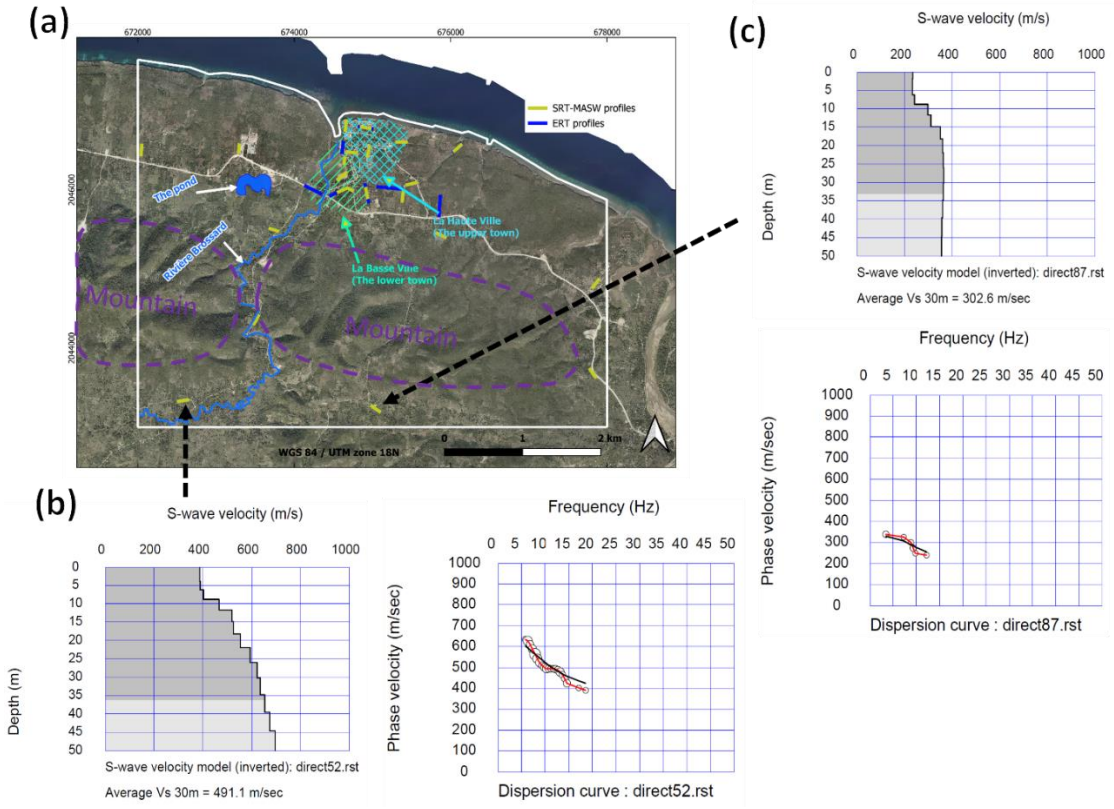

Fig. 4.8 (a) Location of seismic profiles MASW carried out in Anse-à-Veau. **(b)** and **(c)** Examples of S-waves velocity profile (V_S) and dispersion curve obtained outside the town of Anse-à-Veau, on the other sides of the mountain, southern part of the study area.

4.1.3 SRT results

The SRT profiles, carried out with the same configuration as the MASW, were also processed with the software SeisImager ®. An example of SRT processing for a site (P10) in Anse-à-Veau is presented in Fig. 4.9. The result consists of 2D P-waves (Fig. 4.9a) velocity models V_P obtained by calculating travel time curves (Fig. 4.9b) and applying tomographic inversion.

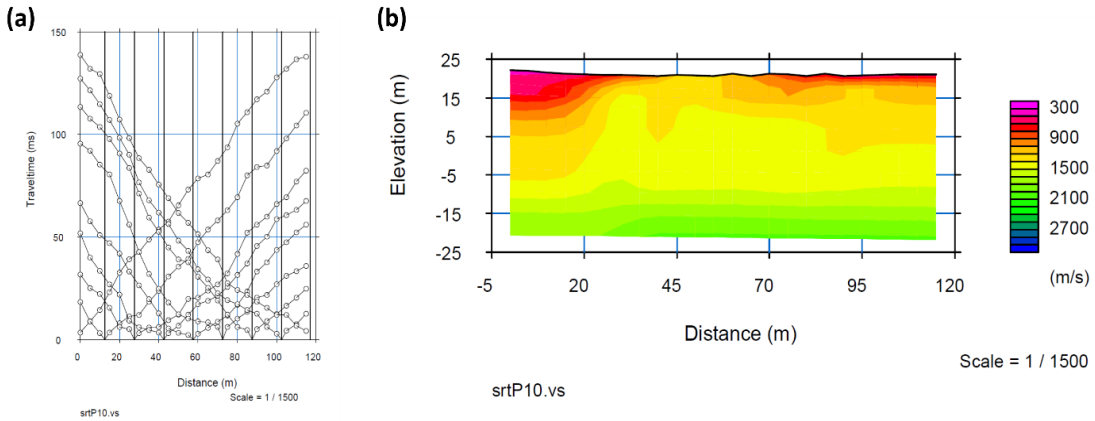

Fig. 4.9 Example of SRT profiles processing in a site (P10) in Anse-à-Veau. **(a)** Travel times plotted as a function of receiver distance. **(b)** Result of P-waves velocity model V_P from tomographic inversion.

The SRT results obtained for selected sites in Anse-à-Veau are presented in Fig. 4.10. The V_P values display a wide range varying from approximately 300 m/s for the superficial soft layer to about 3000 m/s for the underlying hard rock formations. This variation reflects the strong contrast in lithological and mechanical properties across the study area, which directly influences the seismic response of the different geological units. The low V_P correspond to unconsolidated shallow materials and the alluvium of *La Basse Ville* while the high velocities confirm the presence of dense material at greater depths and the reef limestone of *La Haute Ville*.

In addition to *La Basse Ville*, some sites located in the eastern and southern parts of the study area characterized by low to intermediate V_P values. These sites may represent regions with mixed lithological compositions such as the marly limestone or partially compacted alluvial materials which contribute to moderate seismic velocities.

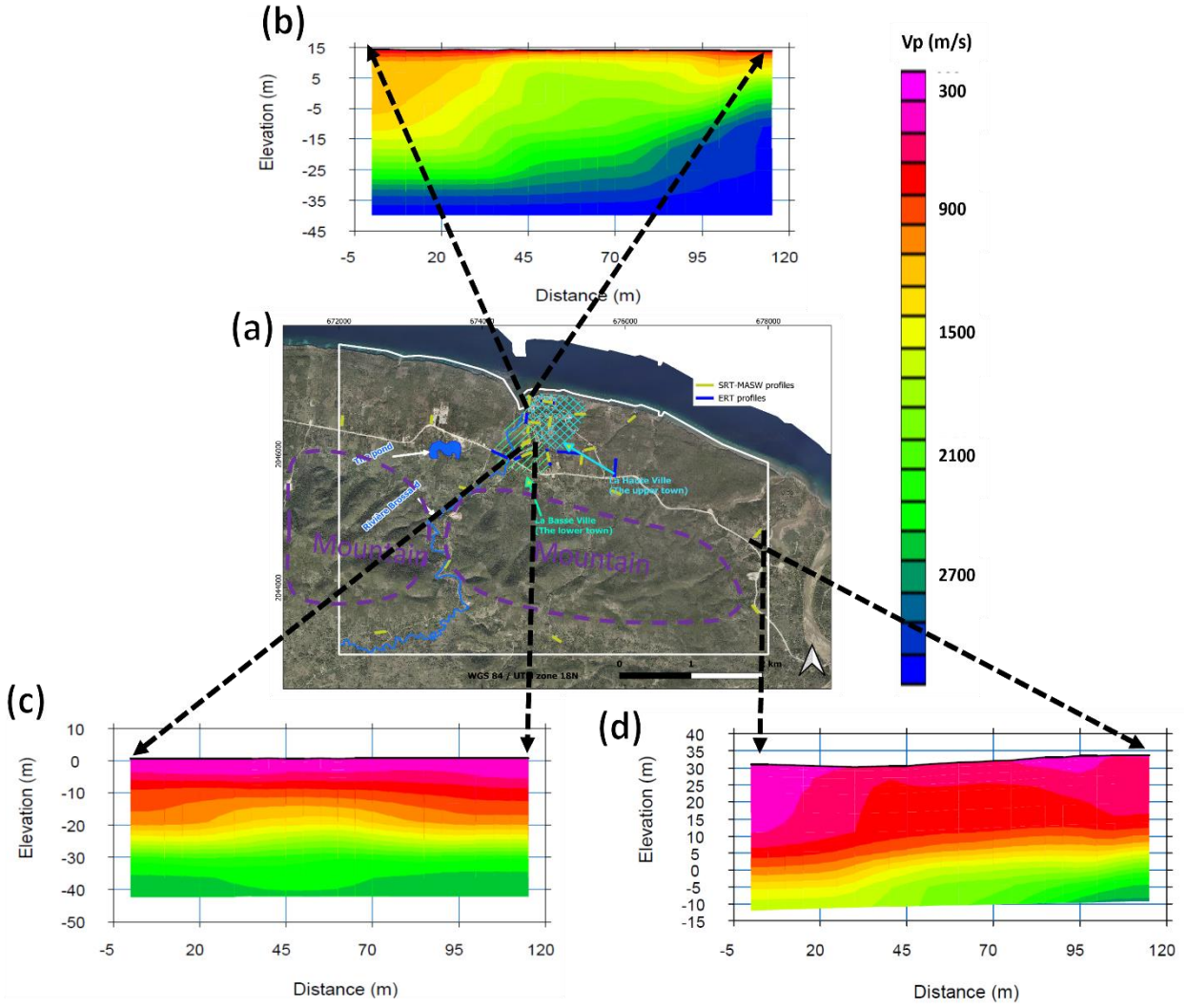

Fig. 4.10 (a) Location of seismic profiles SRT carried out in Anse-à-Veau. **(b)** Example of P-waves velocity profile (V_P) obtained in *La Haute Ville*. **(c)** Example of P-waves velocity profile (V_P) obtained in *La Basse Ville*. **(d)** Example of P-waves velocity profile (V_P) obtained outside of the town of Anse-à-Veau, western part of the study area.

4.1.4 ERT results

The ERT profiles were processed with the software RES2DINV (Loke and Barker 1996). The electrical resistivity values obtained from the ERT profiles exhibit significant spatial variability, ranging from 0.1 to 3000 ohm.m across the investigated depths. This wide range reflects the diverse lithological and hydrogeological conditions within the study area. In general, the low resistivity values are associated with soft and fine-grained soils, whereas higher resistivity values correspond to coarse-grained, granular materials and hard rock formations. However, saturated or saline materials tend to reduce resistivity values even in granular materials or hard rock formations. This phenomenon is illustrated in the resistivity section shown in Fig. 4.11b, where the observed distribution of resistivity suggests the influence of sea water infiltration.

The ERT profiles reveal that the layers with the lowest resistivity are predominantly situated in *La Basse Ville* on the Quaternary alluvial deposits characterized by high moisture content and fine-grained sediments. Similarly, low resistivities zones are also identified in the transitional area between *La Haute Ville* and the mountain, corresponding to region where marly limestone and weathered materials are present. These findings are consistent with the seismic results, which also indicate soft and unconsolidated soils in these sites.

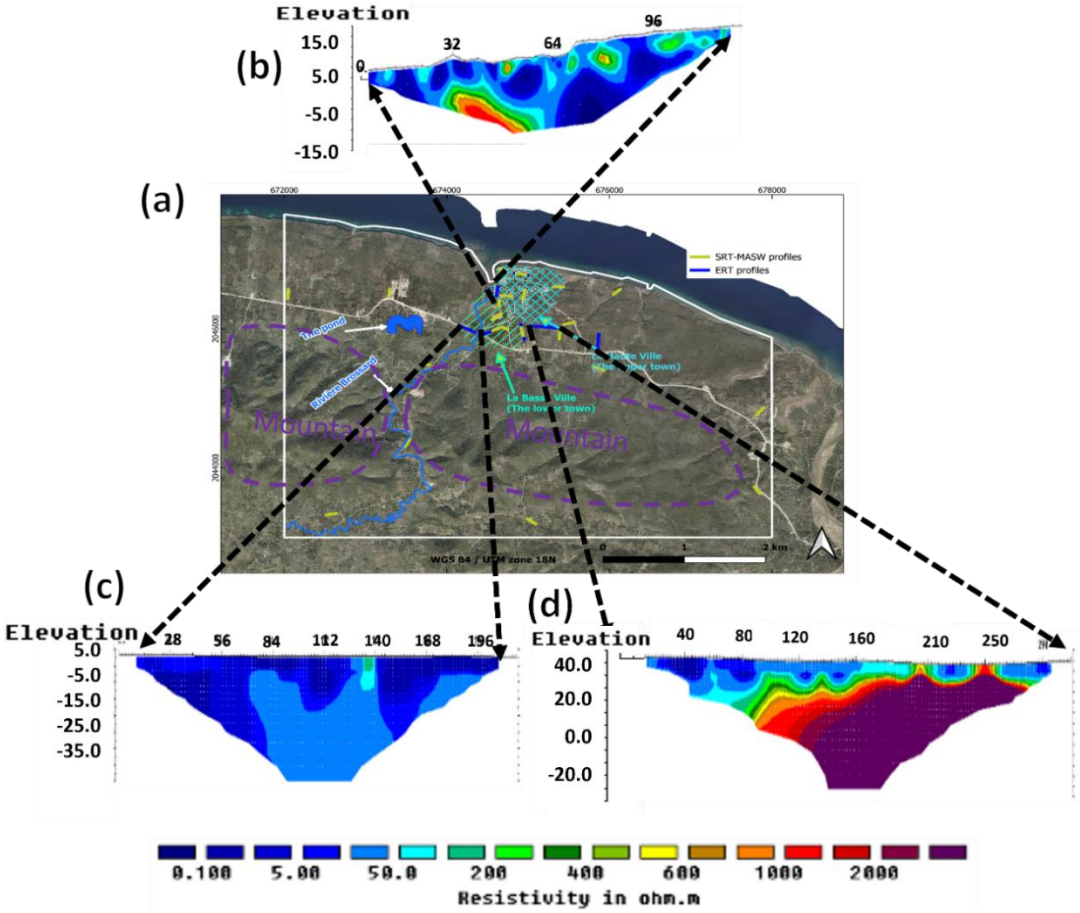

Fig. 4.11 (a) Location of electric profiles ERT carried out in Anse-à-Veau. **(b)** Example of resistivity section obtained in a transition zone between *La Basse Ville* and *La Haute Ville*. **(c)** Example of resistivity section obtained in *La Basse Ville*. **(d)** Example of ERT obtained in the south of *La Haute Ville*.

4.1.5 SSR results

4.1.5.1 The reference seismic station

The implementation of the SSR technique necessitates the establishment of at least one reference station located on a site with characteristics of a bedrock, and one or more additional stations positioned at target sites where seismic amplifications is expected. The geophysical characteristics of the reference site used in the present study are illustrated in Fig. 4.12. The reference site is located in the *La Haute Ville* part, where the subsurface is primarily composed of reef limestone (Fig. 4.12a). The geological and geophysical evidence confirms that this location represents a competent and stable foundation, making it suitable for used as a reference in the SSR analysis.

The H/V curves obtained at the reference site (Fig. 4.12b and c) are notably flat with very low amplification across the frequency spectrum. This behaviour is typical of hard rock or highly consolidated formations that transmit seismic waves without significant resonance or site effects. The MASW profile (Fig. 4.12d) reveals values of V_S below 760 m/s in the upper 5 m, which then progressively increase with depth. This gradient reflects the transition from a thin weathered layer near the surface to the denser, unweathered reef limestone at greater depths. Similarly, the SRT profile (Fig. 4.12e) indicate that the V_P values increase rapidly below 5 m of depth (>1000 m/s). The combined results from the H/V, MASW and SRT analysis confirm the presence of a stiff, competent geological unit at shallow depth.

The seismic station at the reference site in *La Haute Ville* (the upper town of Anse-à-Veau), the one at the target site in *La Basse Ville* (the lower town) as well as the two others in Miragoane and Fonds des Negres along the EPGF continuously recorded ground motion data, including natural seismic events and background ambient noise. The identification of seismic events was not performed through independent computation of earthquake parameters for the present study. Indeed, the location and the magnitude of the recorded earthquakes were obtained directly from the platform Ayiti Séismes (https://ayiti.unice.fr/ayiti-seismes/) and from the Technical Unit of Seismology (UTS-BME, Haiti). This approach ensured that each recorded event could be accurately correlated with officially documented seismic occurrences. For instance, in the case of the earthquake EQ 005 presented in Fig. 4.13a, the seismogram is from the reference station (UR02) located in *La Haute Ville*, but the location and the magnitude were retrieved from the aforementioned databases by matching the precise date and time of recording. The time axis displayed in the seismogram is expressed in Universal Time Coordinated (UTC) for consistency with seismic catalogues. The earthquakes EQ 005 (as well as the other ones occurred at the beginning of January 2022) has been considered as a possible aftershock of the 14 August 2021 earthquake. Their locations are shown on the map in Fig. 4.14.

The H/V curves derived from both the earthquake recording (HVEQ) and the ambient noise measurement (HVSR) at the reference station are displayed in Fig. 4.13b and 4.13c, respectively. Both curves exhibit a flat shape with low amplitudes, a characteristic signature of sites underlain by competent bedrock with negligible site effects.

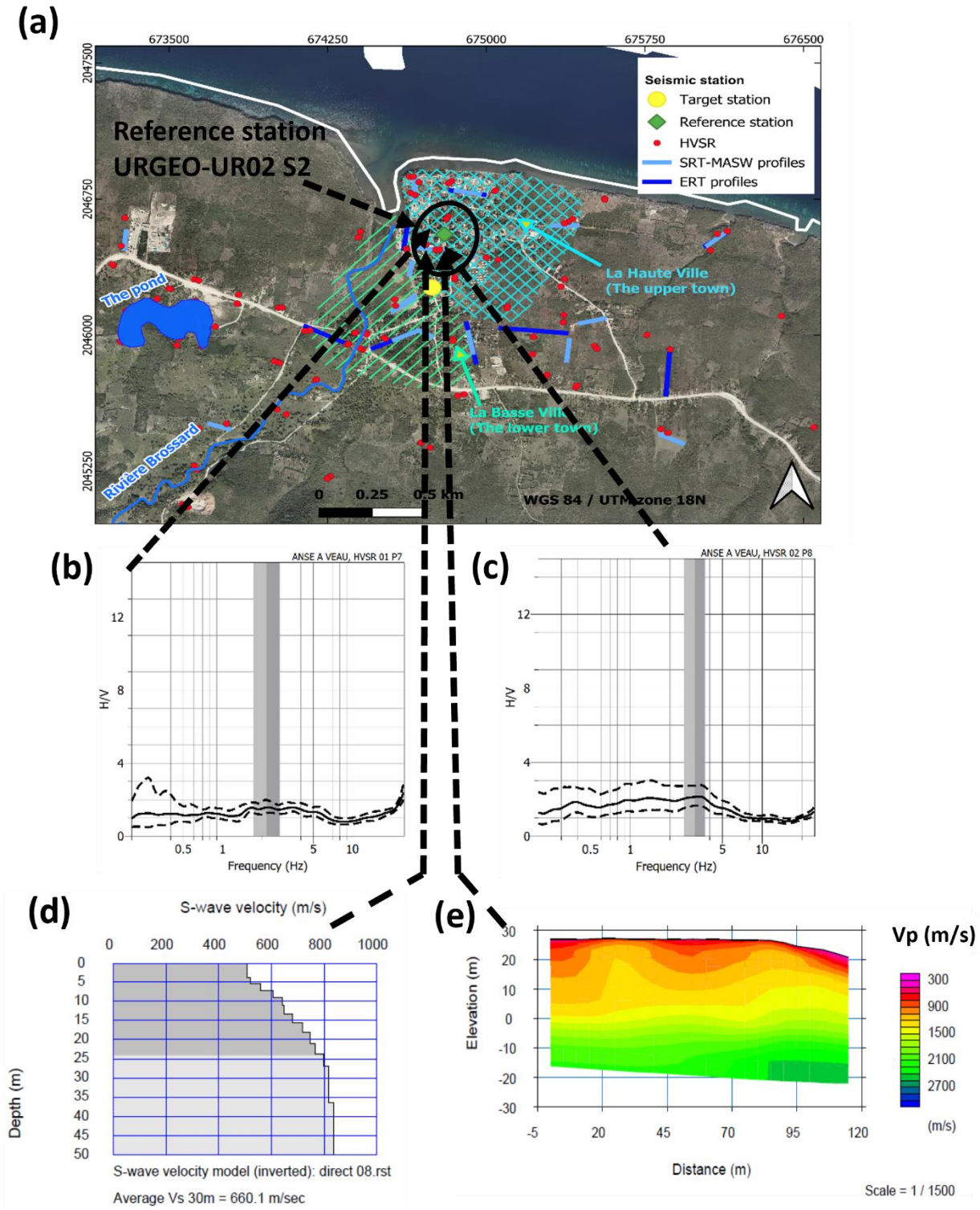

Fig. 4.12 Presentation of the reference site for the study area of Anse-à-Veau (from Dorival et al. 2025). **(a)** Location of the reference station UR02 S2 in *La Haute Ville* on the reef limestone. (**b)** and **(c)** Flat H/V curves obtained from ambient noise recorded at the site by the Tromino (section 3.1). The dashed black lines represent the standard deviation estimated for H/V curves calculated from 20 to 30 individual time windows. **(d)** Seismic profile V_S from MASW method. **(e)** SRT profile (P-wave velocities).

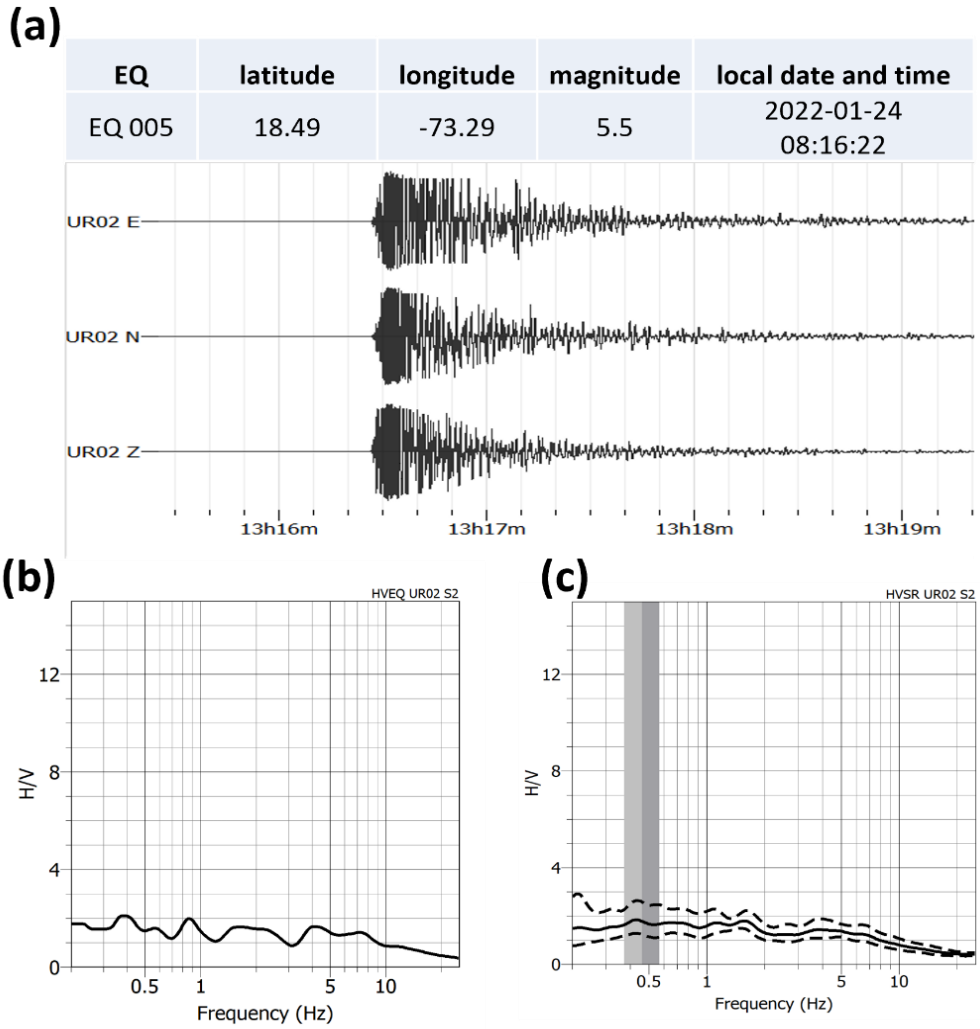

Fig. 4.13 (a) Earthquake recorded by the reference station UR02 S2 (from Dorival et al. 2025). **(b)** H/V of the earthquake recorded by the reference station. **(c)** H/V of ambient noise recorded by the reference station. The dashed black lines represent the standard deviation estimated for H/V curves calculated from 20 to 30 individual time windows.

4.1.5.2 The SSR in the target site

The SSR analysis was applied to the earthquakes listed in Table 4.1 and illustrated in Fig. 4.14. The target seismic station used for the analysis is located in *La Basse Ville* (within the black ellipse in Fig. 4.15a), an area known for its pronounced site effects. This location has consistently demonstrated significant seismic wave amplification during recent (like the 2021 Nippes earthquake) and historical seismic events.

For a selected earthquake, the Fourier spectrum of each horizontal component recorded at the target station (in *La Basse Ville*) was computed and subsequently divided by the corresponding spectra obtained from the reference station in *La Haute Ville*. The SSR calculation was performed on the S-wave coda (as the seismometers used are very sensitive and the first arrivals are often

saturated in the recorded seismograms). The earthquakes were classified into three distinct groups based on their location with respect to the target station: GNE for events originating from the north-east, GE for those from the east and GSE for those from the south-east (as shown in Fig. 4.14). The SSR results presented in Fig. 4.15b-c and Fig. 4.16 include representative SSR curves for one of the analysed earthquakes (EQ006), SSR curves for each group, as well as the average SSR curves computed across all selected earthquakes.

Table 4.1 Summary of the earthquakes (EQ) selected for the application of the SSR method

EQ	latitude	longitude	depth (km)	Magnitude (Mw)	local date and time
EQ 005	18.54	-73.29	2.5	5.5	2022-01-24 08:16:22
EQ 006	18.49	-73.29	8.5	3.7	2022-01-24 08:21:26
EQ 007	18.55	-73.31	4.5	4.6	2022-01-24 08:43:16
EQ 008	18.55	-73.3	1.5	5.4	2022-01-24 09:06:41
EQ 010	18.54	-73.29	3.5	4.2	2022-01-24 09:14:30
EQ 011	18.49	-73.27	6	4.3	2022-01-24 10:08:30
EQ 012	18.45	-73.25	7	3.6	2022-01-24 13:32:23
EQ 015	18.48	-73.29	10	4.5	2022-01-24 15:01:45
EQ 018	18.42	-73.19	7	4.3	2022-01-24 18:26:46
EQ 020	18.45	-73.24	10	4.2	2022-01-24 21:27:29
EQ 021	18.44	-73.26	11	4	2022-01-25 01:06:05
EQ 023	18.48	-73.25	8.5	3.7	2022-01-25 11:51:33
EQ 024	18.56	-73.33	17.5	4.6	2022-01-25 13:50:57
EQ 025	18.53	-73.34	3	4.6	2022-01-25 20:14:28
EQ 031	18.44	-73.27	11.5	3.9	2022-01-26 13:05:22
EQ 035	18.55	-73.25	4.5	4.3	2022-01-28 16:50:26
EQ 039	18.44	-73.28	13	4.3	2022-01-30 04:22:29
EQ 046	18.48	-73.49	7	4.3	2022-05-02 10:41:16
EQ 047	18.47	-73.31	7	3.6	2022-05-06 22:13:06
EQ 048	18.39	-73.45	9	3.6	2022-05-08 19:27:12
EQ 049	18.48	-73.58	9	4.4	2022-05-09 12:45:53

The SSR curves for the single earthquake EQ006 reveal distinct frequency-dependent amplification patterns. As illustrated Fig. 4.15b-c, the results for this event exhibit two noticeable peaks on the E-W component, occurring at approximately 2 Hz and 6 Hz. However, the peak at ~2 Hz is less clear on the E-W component for the SSR curves (Fig. 4.16a, c and e) computed for all the distinct groups of earthquakes (GNE, GE and GSE; see Fig. 4.14). In the average SSR curve for the E-W component (Fig. 4.16g), a more consistent and pronounced amplification peak emerges at approximately 3 Hz (while it is less evident on the SSR curves of the respective earthquakes groups, or on the single SSR curve of EQ006, see Fig. 4.15b). The peaks at approximately 3 Hz and 6 Hz of frequency are also observed on the N-S component for the average SSR curve (Fig. 4.16h), the respective earthquake groups (Fig. 4.16b, d and f) and the single EQ006 event (Fig. 4.15c). The H/V curve obtained for the selected earthquake (EQ006) is characterized by weakly pronounced peaks at approximately 2 Hz and 3 Hz.

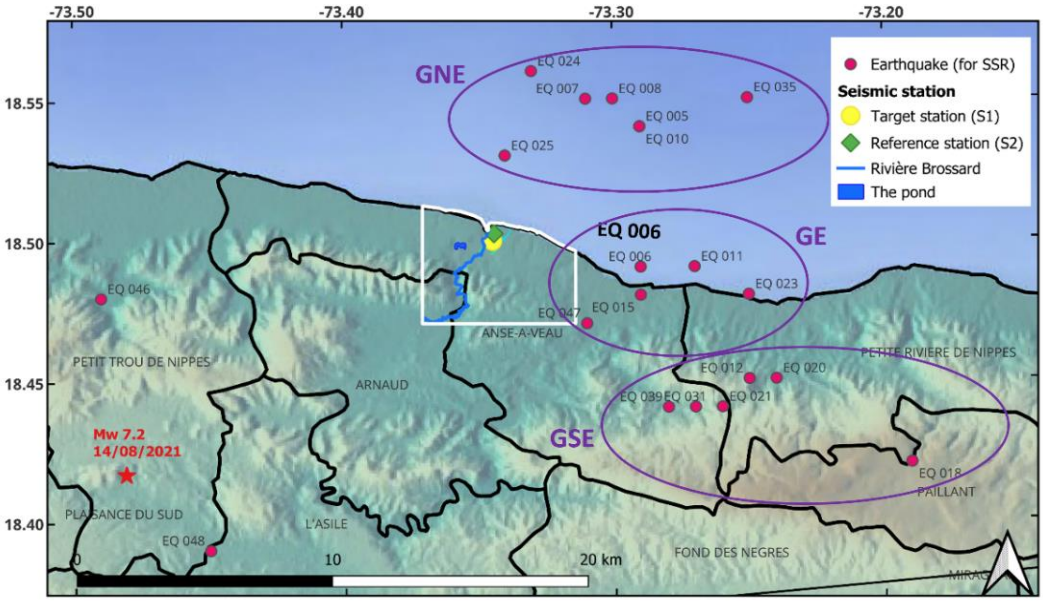

Fig. 4.14 Locations of the earthquakes (EQ) selected for the application of the SSR method (from Dorival et al. 2025). They are separated into three groups based on their location with respect to the target station: GNE in the north-east, GE in the east and GSE in the south-east. The study area is delimited by the white polygon. The distance between the target station (S1, the yellow circle) and the reference station (S2, the green diamond) is very small with respect to the distance to the earthquakes epicentre. The red star indicated the location of the 14 August 2021 earthquake.

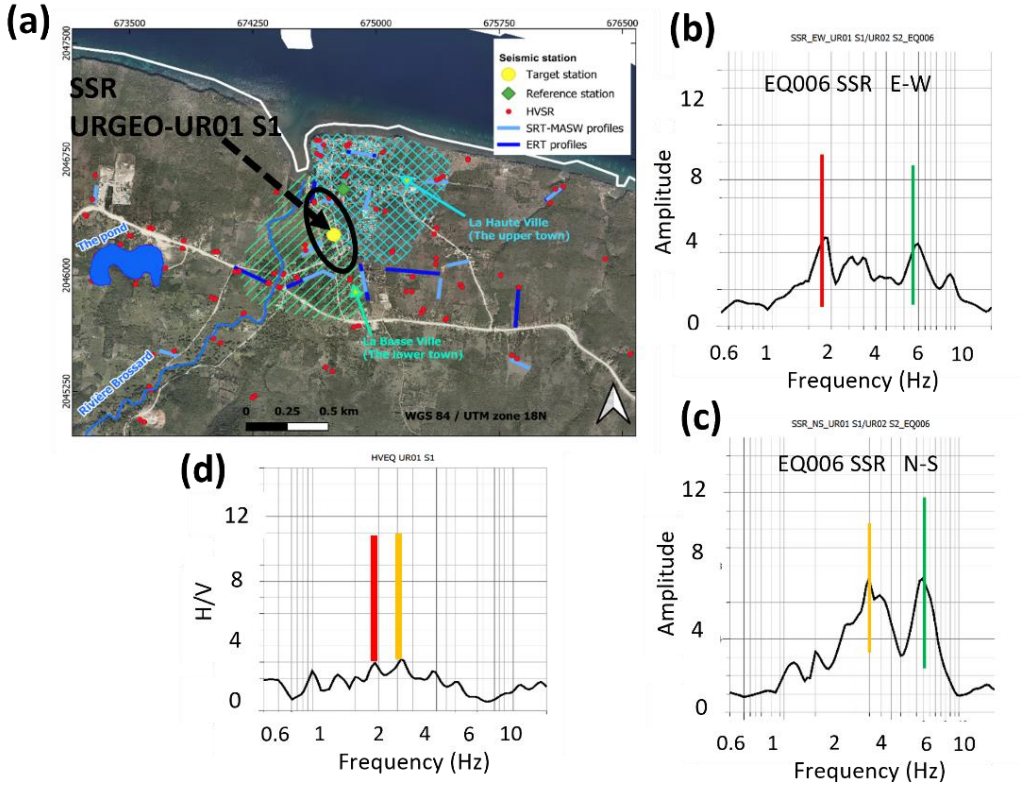

Fig. 4.15 **(a)** Location of the target station UR01 S1 in La Basse Ville on the Quaternary alluvium (from Dorival et al. 2025). **(b)** SSR in the E-W direction for the earthquake EQ006 (see Fig. 10) at the target station UR01 S1 with respect to the reference station UR02 S2 for two of the recorded earthquakes. **(c)** SSR for the same event in the N-S direction. **(d)** H/V curves from an earthquake recorded by the target station.

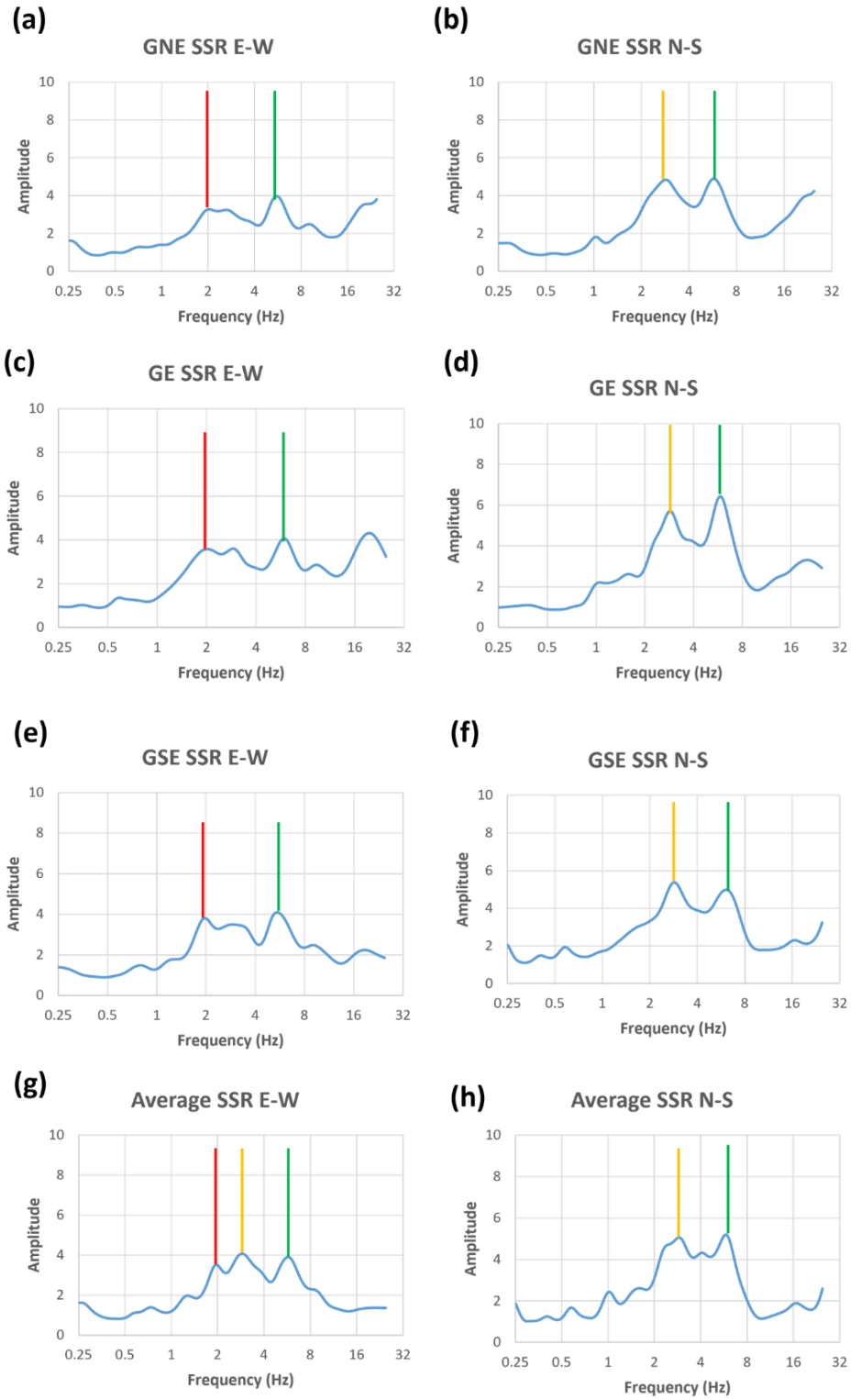

Fig. 4.16 Results of the SSR method applied at the target station UR01 S1 with respect to the reference station UR02 S2 for the selected earthquakes in Table 5.1 and Fig. 5.7 (from Dorival et al. 2025). **(a)** and **(b)** SSR curves in E-W and N-S components for the earthquakes in the group GNE. **(c)** and **(d)** SSR curves in E-W and N-S components for the earthquakes in the group GE. **(e)** and **(f)** SSR curves in E-W and N-S components for the earthquakes in the group GSE. **(g)** and **(h)** SSR curves in E-W and N-S components for all the earthquakes.

The lithological conditions at the target station appear to be particularly complex as the site is located near the boundary of the alluvial deposit. This transitional position between the soft Quaternary alluvium of *La Basse Ville* and the more compact material of *La Haute Ville* likely gives the rise to heterogeneous subsurface layering and lateral variations in stiffness. Such geological complexity can significantly influence the recorded seismic response, as evidenced by the multiple peaks and directional differences observed in the SSR analysis.

The peak observed at approximately 6 Hz in the two components (E-W and N-S) for all the SSR curves (single, group and total average) likely reflects the response of a relatively simple superficial deposit. In contrast, the peaks observed at lower frequency (around 2 Hz and 3 Hz) are more indicative of deeper or more complex subsurface structures. The presence of the first one in only the E-W component (and the second one in the N-S component) suggests that the site is affected by anisotropy or lateral heterogeneity in the sedimentary layers near the edge of the alluvial deposit. These differences likely result from variations in layer thickness or boundary geometry between the alluvium and the underlying bedrock.

The higher amplitude associated with the 3Hz peak in the N-S components could be explained by the wave polarisation effects in the same direction. This interpretation is supported by the azimuthal analysis of the ambient noise H/V near the target site (see Fig. 4.4). Moreover, the SSR results obtained for the three earthquake groups (GNE, GE and GSE) show that the directional distribution of seismic sources does not significantly influence the amplitude differences observed between the E-W and N-S components.

4.1.6 Discussion (study area 1)

The analysis and interpretation of data in the Anse-à-Veau region provides a typical example of an approach that only uses geophysical investigations for site characterisation. This is a methodology based on ambient noise measurements (HVSR) and S-wave inversion (MASW) completed by Seismic Refraction Tomography (SRT), Electrical Resistivity Tomography (ERT) and Standard Spectral Ratio (SRT). These methods, particularly the ambient noise measurements, anchored in the HVSR approach reported in the literature (Nakamura 1989; Nakamura and Saito 1983; Bard 1999; SESAME 2004).

Similar techniques have been adopted in Haitian studies. For example, Ulysse et al. (2018, 2021) used H/V ambient noise analysis in Port-au-Prince and (Fonds Parisien, 37 km to east of Port-au-Prince) for site amplification assessment in complement to other geophysical and geotechnical data. St-Fleur et al. (2016) analysed spectral ratios in Port-au-Prince and compared them with numerical simulations.

The present approach is consistent with several other studies (Bonnefoy-Claudet et al. 2006; Chatelain et al. 2008) that reveals some the limitations and conditions under which H/V works best. Chatelain et al. (2008) evaluated how measurement setup such as duration, instrument and noise window selection can influence H/V curves.

The analysis of these geophysical data for the region of Anse-à-Veau is a valuable baseline that helps illustrate how ambient noise and surface wave analysis can delineate zones of low frequency amplification in soft sediments in opposite to higher and stiffer zones. The degree to which these zones correlate with damage patterns may help validate or refine the inferred fundamental resonance frequencies. A simplified geological section inferred from the combined results of the geophysical data is shown in Fig. 4.17.

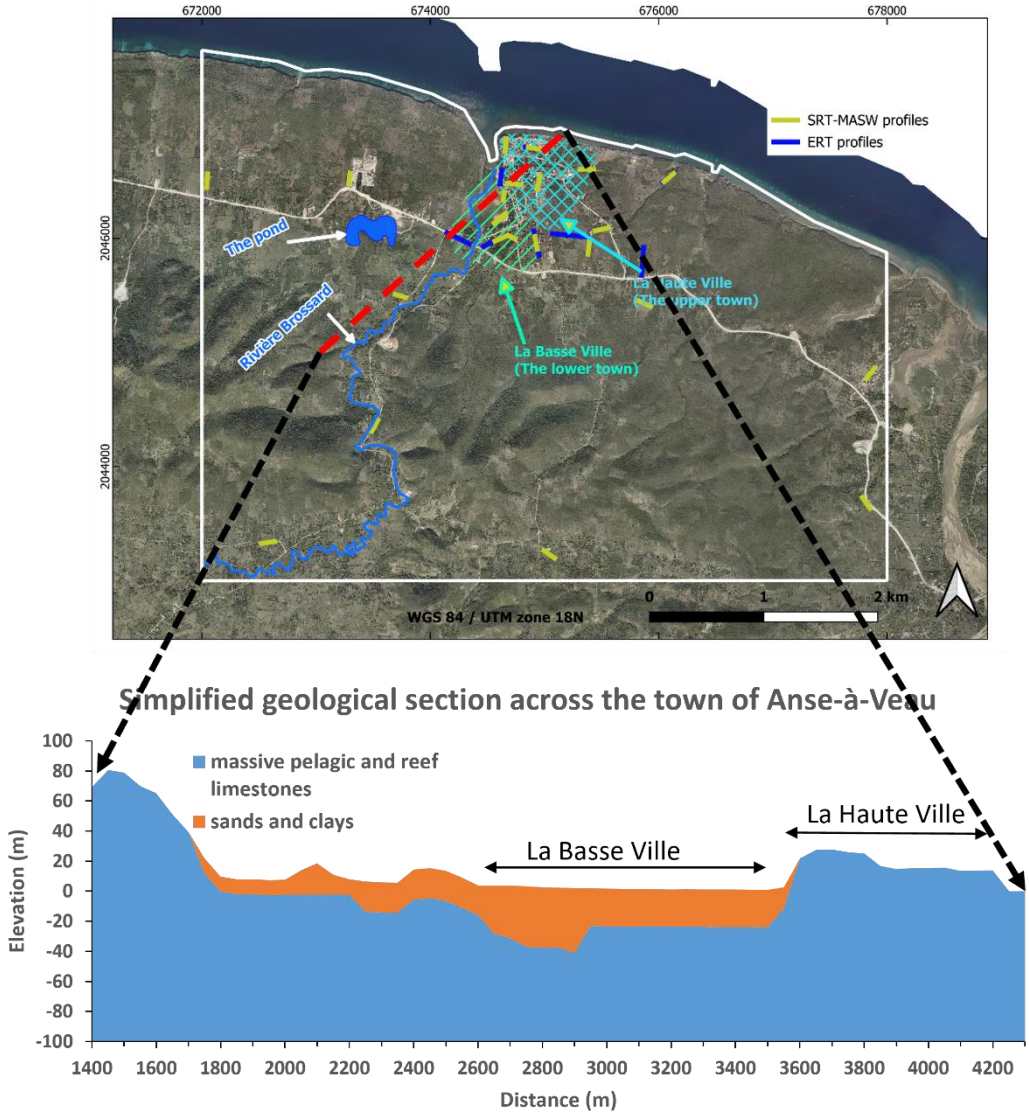

Fig. 4.17 Simplified geological section across the town of Anse-à-Veau.

4.2 Data analysis for study area 2 (Cap-Haitien)

The seismic microzonation of Cap-Haitien (Roullé et al. 2013; Bertil et al. 2014; Bertil et al. 2014a) includes ambient noise recordings processed by HVSR method, seismic profiles by MASW, and boreholes (BH) drilling with standard penetration test (or cone penetration test). In the present analysis, we only selected the usable data located inside study area 2. Part of the data (particularly the boreholes data) were available before the seismic microzonation since they were collected from geotechnical investigations carried out by the LNBTP (or the private geotechnical company Geotechsol).

The data compiled for study area 2 include 61 HVSR, 21 MASW, and 21 boreholes (BH) with standard penetration test (SPT) or cone penetration test (CPT) as well as the geological map carried out during the microzonation (Monthel et al. 2013). The results are directly presented here for analysis and interpretation since they have been already processed.

4.2.1 HVSR data analysis

The HVSR results are divided into 6 groups according to their locations and the H/V curves characteristics. The groups I, II and III (Fig. 4.18) are located in the north of the study area (the main part of the city of Cap-Haitien); the groups IV, V and VI (Fig. 4.19) are in the south of the study area (the alluvial plain that includes the international airport of Cap-Haitien). Each group reflects different subsurface conditions and geological settings across the study area. The interpretation of these curves, in combination with azimuthal analysis, provides insight into the spatial variability of site effects and their possible structural controls.

According to the seismic microzonation reports (Roullé et al. 2014; Bertil et al. 2014), The H/V data were processed using the Nakamura (1989) technique implemented in the software Geopsy (as in the Anse-à-Veau case). The horizontal components were averaged, and the H/V ratio were computed over windows of stationary noise. The azimuth analysis to further investigate potential directional effects and to verify the anisotropy of the resonance peak was performed in framework of the present work.

The H/V curves of group I (Fig. 4.18b) are characterized by H/V peaks at approximately 3 Hz. These measurements were predominantly recorded along the coastal line in the alluvial plain and embankment layers where soft sediments are widespread. The azimuth analysis, represented by the orientation of the diamonds long diagonal, suggests a clear directional dependence which appears to be influenced by the direction of the coastline. The nature of the H/V peaks in this group, coupled with the soft superficial deposits, suggests a high potential for seismic amplification in these areas.

For group II (Fig. 4.18c), the H/V curves reveal pronounced peaks around 4.5 Hz, indicative of stiffer and shallower subsurface materials compared to group I. They are located on the colluvial deposit near the coast. The azimuth analysis shows a more complex pattern of directional effects in this group. While some sites display directional trends that align with the coastline (suggesting

an influence from sedimentary layering or coastal geomorphology), others deviate significantly. These differences may be related to subsurface structural features, such as the contact zone between the colluvial units and the volcano-sedimentary facies, which could create lateral impedance contrasts or irregularities in wave propagation. Similar to group I, these areas can be characterized by high potential for site amplification though with greater spatial variability due to more complex subsurface structure.

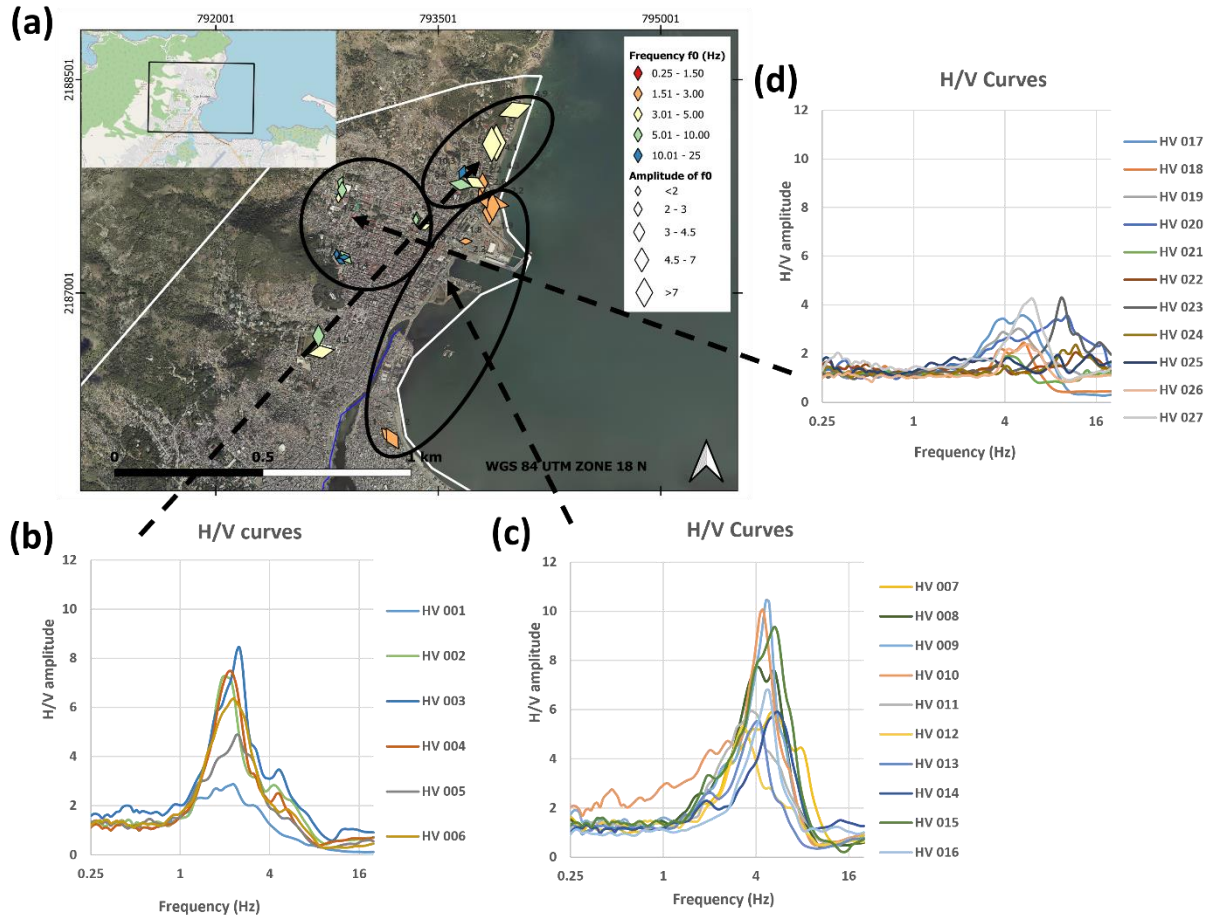

Fig. 4.18 HVSR results obtained from the ambient noise measurements in the main part of the city of Cap-Haitien. **(a)** The orientation of the diamonds long diagonals represents the direction of the wave polarisation from azimuth analysis. The colour indicates the fundamental resonance frequency f_0; the size indicates the relative amplitude of the f_0 peak. **(b)** HVSR curves obtained for the group I. **(c)** HVSR curves for group II. **(d)** HVSR curves for group III.

The group III (Fig. 4.18d) are marked by H/V curves that are either flat or exhibit poorly defined peaks at high frequencies (generally above 6 Hz). These sites are located further inland, predominantly on the volcano-sedimentary facies and older colluvial surfaces, where the materials are significantly more compacted. The lack of pronounced H/V peaks suggests either a low impedance contrast between surface and subsurface layers, or that the resonance frequencies are

beyond the range of interest due to presence of very stiff soils or shallow bedrock. The potential for site amplification in these locations is considered very low, making them less critical in terms of seismic risk.

The H/V curves in the other part of the study area (including the airport of Cap-Haitien) are also divided in 3 groups for analysis and interpretations. They are presented in Fig. 4.19 with group IV, V and VI in Fig. 4.19b, 4.19c and 4.19d respectively. The curves were identified based on their distinct H/V spectral characteristics, despite most of them being located within the coastal alluvial plain. The differences reflect the variability in sediment thickness, material stiffness and local geomorphological context. The azimuth analysis provides further insight into the directional characteristics of ground motion amplification.

The group IV sites (Fig. 4.19b) are characterized by well-defined H/V peaks at low frequencies (<1 Hz). They are located within the deepest sections of the alluvial plain in areas where fine-grained, unconsolidated sediments, such as clay and silt, have accumulated to substantial thicknesses. The soft sediments overlying stiffer material at depth results in a strong impedance contrast, producing a clear resonance at low frequencies. The azimuth analysis for this group consistently shows an orientation of maximum H/V amplitude in the direction N140-160, suggesting a polarisation of wave in a preferred direction. The low frequencies with their relative amplitude imply that these areas are particularly susceptible to significant seismic amplification.

The group V (Fig. 4.19c) includes sites with H/V peaks between 1 and 2 Hz with high amplitude. Some of the measurements are located near marshy areas in the alluvial plain and areas with embankments layer in the Cap-Haitien airport. The subsurface conditions here are likely more variable and include a mix of saturated clays, silts and anthropogenic fill. The azimuth analysis reveals mixed directional patterns. At some sites, the orientation of the maximum H/V amplitude appears to follow the marsh edge, suggesting the presence of elongated sedimentary features that influence wave propagation. In other locations, the patterns appear less coherent likely due to local fill or shallow heterogeneities with no consistent directional control. This suggests that both natural depositional processes and human modification are influencing the site response in this group.

The group VI (Fig. 4.19d) is composed of sites distinct resonance peaks at higher frequencies, typically between 3 and 8 Hz, with relatively moderate to high amplitudes. These sites are located at the margins of the alluvial plain and extend further onto the areas of colluvial deposits and the volcano-sedimentary units. The broad range of resonance frequencies across this group suggests considerable variation in subsurface conditions, both laterally and vertically. In some cases, the higher frequency peaks (6-8 Hz) likely reflect the shallow layers, possibly thin soil cover overlying bedrock or cemented colluvium. In other cases, the lower frequency peak (~3 Hz) may be associated with thicker or less compacted colluvial units or transition zones between softer alluvium and stiffer colluvium or volcanic-sedimentary material. The azimuth analysis reveals weak to moderate directional dependence with no clear regional trend.

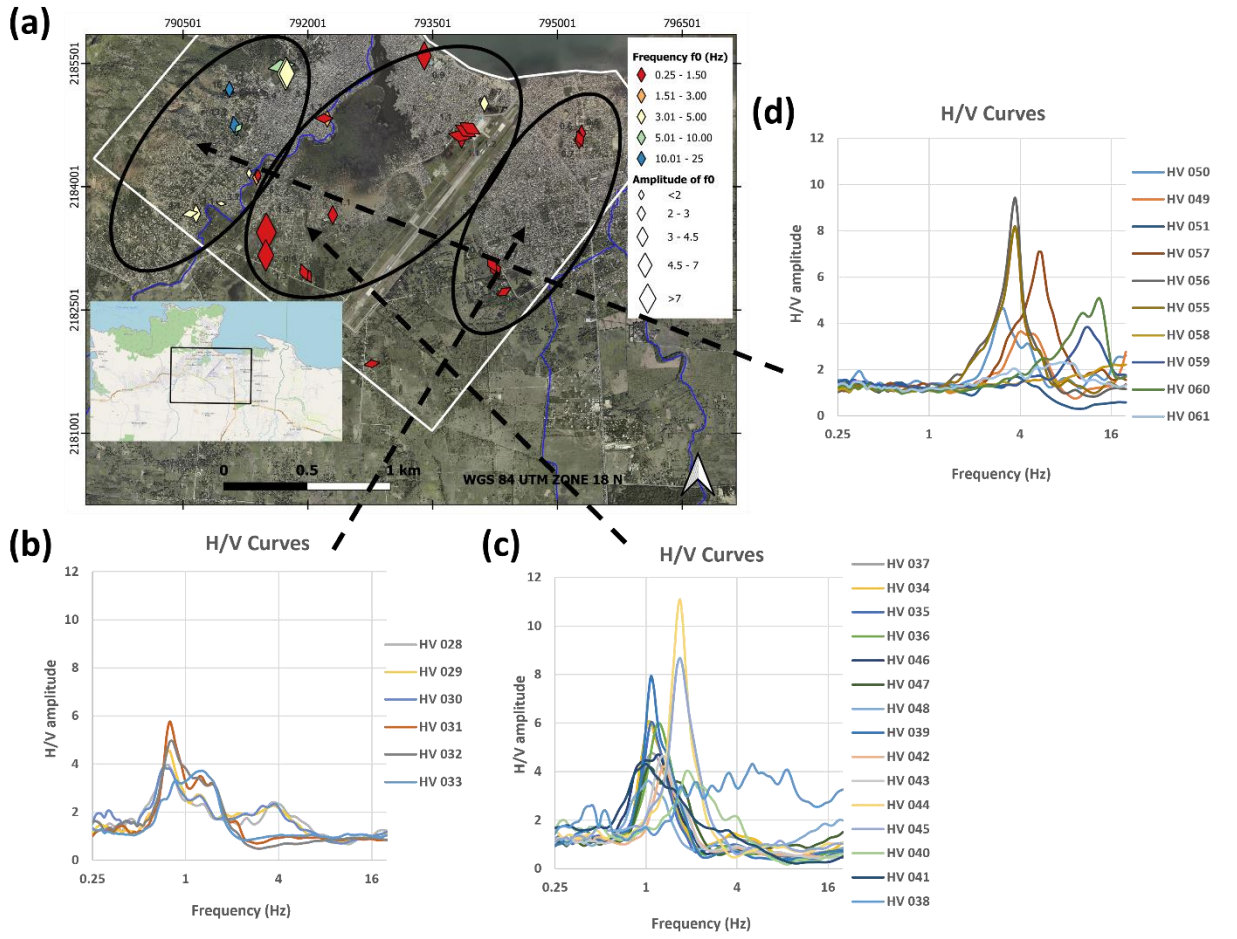

Fig. 4.19 HVSR results obtained from the ambient noise measurements in the alluvial plain (including the Cap-Haitien international airport). **(a)** The orientation of the diamonds long diagonals represents the direction of the wave polarisation from azimuth analysis. The colour indicates the fundamental resonance frequency f_0; the size indicates the relative amplitude of the f_0 peak. **(b)** HVSR curves obtained for the group IV. **(c)** HVSR curves for group V. **(d)** HVSR curves for group VI.

4.2.2 MASW data analysis

The MASW results are divided into 3 groups (I, II and II) according to their characteristics and their locations across the study area. The locations and the profiles of group I are shown in Fig. 4.20a and 4.20b. The locations of group II and III are indicated in Fig. 4.21a, their profiles are respectively presented in Fig. 4.21b and Fig. 4.21c.

The MASW of group I (Fig. 4.20) were carried out across the alluvial plain and along the immediate coastal margin, particularly in zones where thick unconsolidated sediments are known to accumulate. The resulting V_S profiles reveal low to moderate S-wave velocities, generally ranging from 150 to 400 m/s in the investigated depths. This velocity range is related to the unconsolidated or poorly consolidated Quaternary sediments, such as clay, silt, fine sand and anthropogenic deposits present in this part of Cap-Haitien.

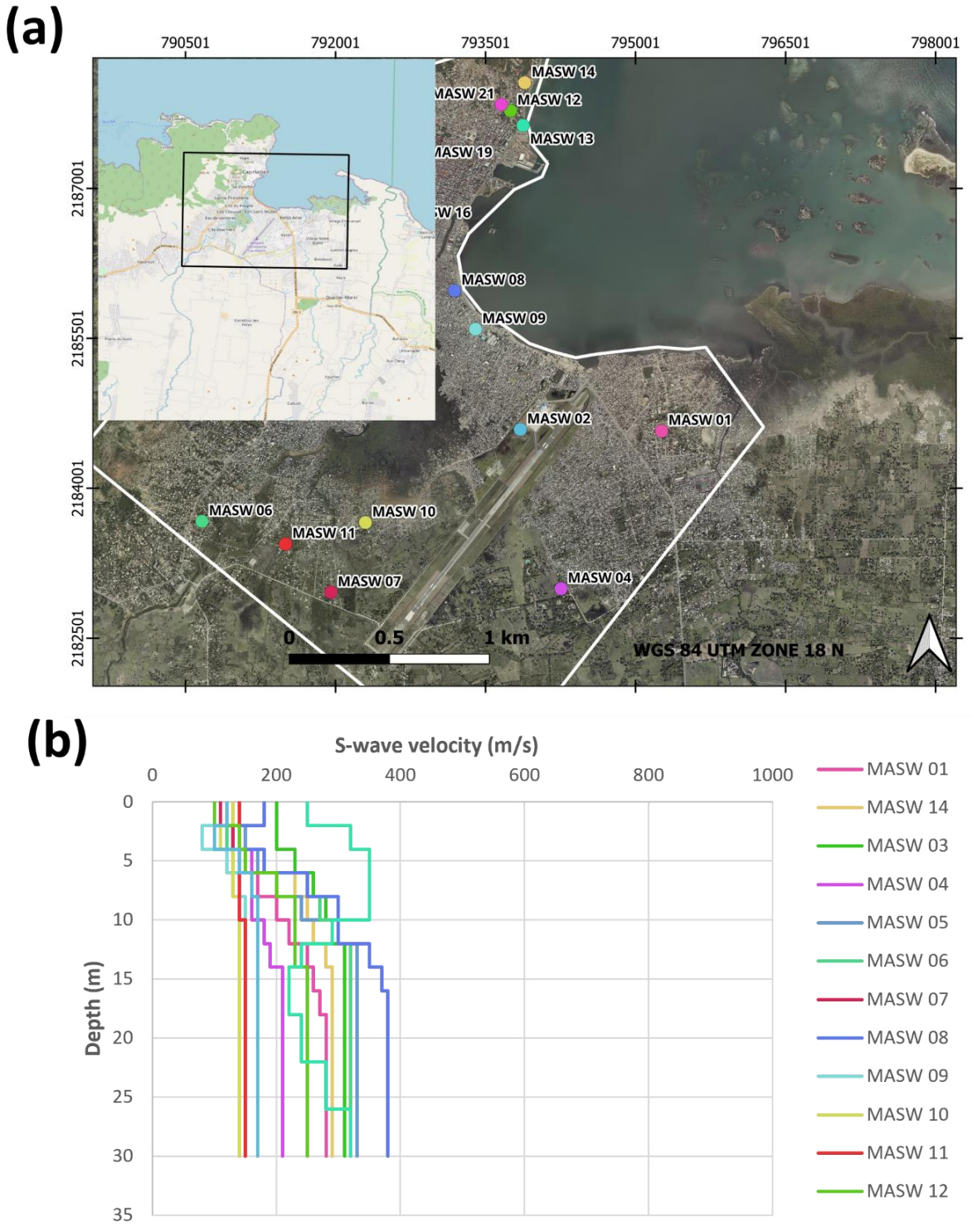

Fig. 4.20 The seismic tests (MASW) carried out in the alluvial plain and along the coastline of Cap-Haitien. **(a)** The locations of the MASW tests. **(b)** The S-wave velocities profiles from the MASW on the map.

The profiles in the central part of the alluvial plain (around the marshy area between the river and the airport) tend to exhibit the lowest V_S values, below 200 m/s in the investigated depths. These

low velocities correspond to soft, saturated sediments, which are commonly found in former river channels and marshy areas. In contrast, the profiles located on slightly elevated ground or closer the coastal embankments show a progressive increase in V_S values, with layers reaching 300-400 m/s. This increase may reflect more compacted sandy deposits, or thinner sediment package overlying stiffer material, especially in areas that have been subject to urban development.

For the profiles located in the transition zone between the alluvial plain and the colluvial the deposit, and near the coastline, a slightly faster layer appears at 10 m depth. That could correspond to gravelly horizons or buried coastal fill formed during older shoreline processes.

According to soil classification from the International Building Code (IBC), the standardized geomechanical parameter V_{S30} for the profiles of group I corresponds to sites of classes E and D which imply high susceptibility to seismic amplification. In the sites where the V_{S30} value is consistently below 200 m/s (in the central part of the alluvial plain between the river and the airport), the ground motion amplification is expected to be strong during seismic events, especially at low frequencies.

The other groups of MASW profiles (group II and III) have been carried out on sites underlying by colluvial deposits, volcanic and volcano-sedimentary facies which are topographically elevated and geologically more consolidated than the alluvial plain. The group II and III are presented in Fig. 4.21b and 4.21c respectively.

The S-wave velocities in group II and III show a notable increase compared to the ones in group I. The surface layers appear relatively loose or weathered, but stiffness increases rapidly in depth, with V_S values generally between 500 and 700 m/s from 10 m depth for group II (Fig. 4.21b), and V_S values between 600 and 900 m/s from 5 m depth for group III (Fig. 4.21c). Unlike the gradual transitions observed in the profiles of group I (Fig. 4.20b), the profiles of group II and III show discrete velocity contrast, likely marking the boundary between loose superficial layers and more indurated older deposits or even shallow bedrock. The sharp velocity gradients observed at shallow depths may correspond to weathering layers where the upper few meters have been mechanically or chemically altered but quickly transition to intact bedrock below.

The parameter V_{S30} values are in the range 400-600 m/s for group II (Fig. 4.21b), and 600-800 m/s for group III (Fig. 4.21c). The soil classifications according to the International Building Code (IBC) are site of class C for group II, and class C and B for group III. These velocities suggest a reduced potential for site amplification compared to the soft alluvium although the topographic setting and lateral velocity variations in the colluvial deposits could still lead to complex seismic response in certain locations. The volcanic and volcano-sedimentary units are the stiffest and most seismically stable ground conditions observed in the study area and are expected to produce minimal amplification of the input ground motion.

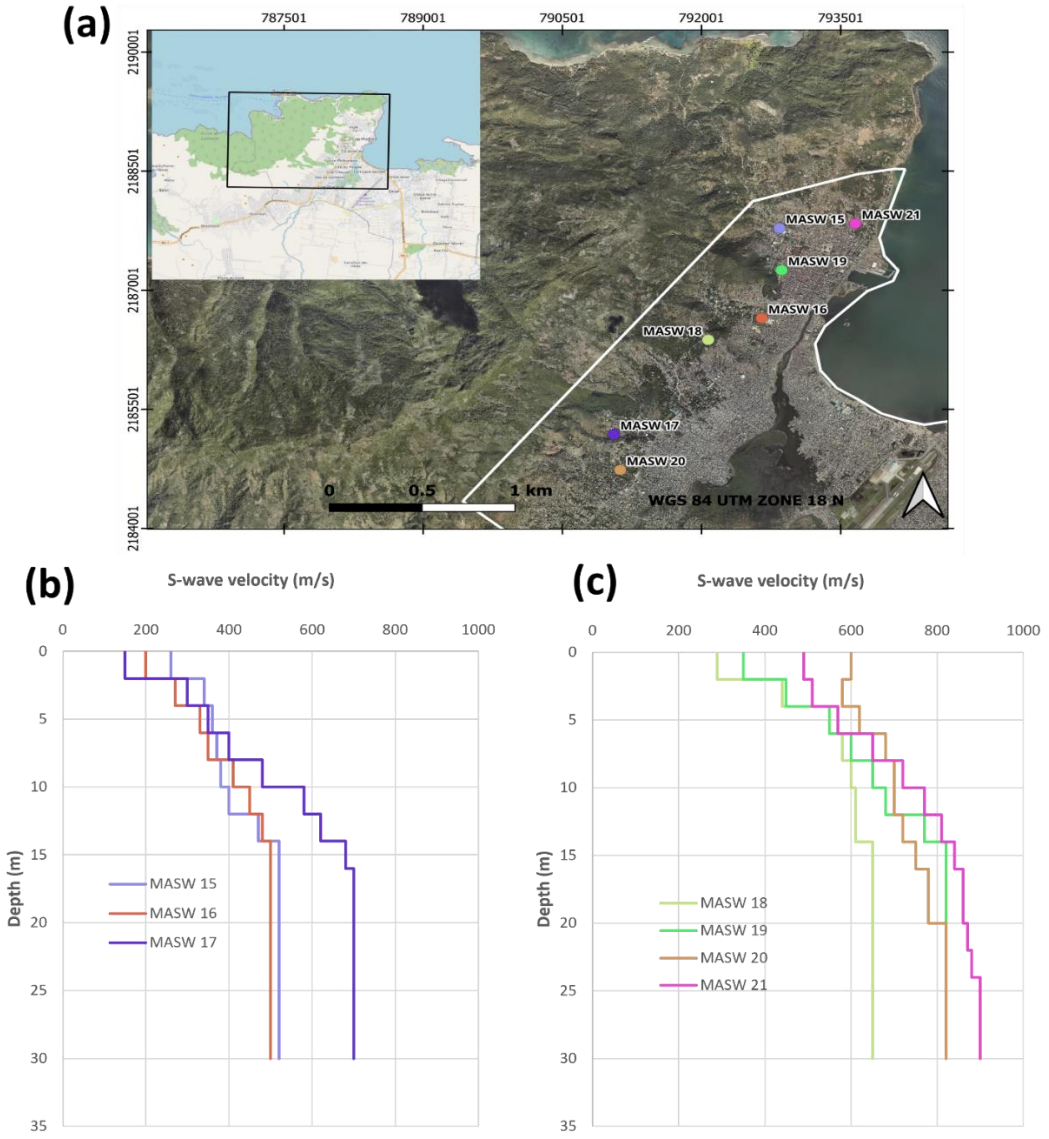

Fig. 4.21 The seismic tests (MASW) carried out on the colluvial deposits and the volcano-sedimentary facies. **(a)** The locations of the MASW tests. **(b)** The S-wave velocities profiles from the MASW in the colluvium formations. **(c)** The S-wave velocities profiles from the MASW in the volcano-sedimentary facies.

The V_S profiles show a progressive increase in subsurface compactness from group I to group III. The sites of group I are located in the softest zones concentrated in the alluvial and coastal plain composed of unconsolidated clays, silts and fine sands, often saturated, that correspond to low seismic velocities and high amplification potential. The sites of group II and III are located on intermediate to hard layers with minimal overlying weathered and unconsolidated material. The profiles are generally uniform with little vertical variation beyond the weathering layers. This clear velocity gradient across the three groups aligns with the broader geological setting of Cap-Haitien, from the soft alluvial coastal plain to the harder volcanic and volcano-sedimentary units in the mountain (*Morne du Cap*).

4.2.3 Boreholes data analysis

The geotechnical boreholes with SPT (or CPT) carried out to complement the geophysical investigations (MASW and HVSR) are divided into 2 groups according to their location across the study area. They are presented in Fig. 4.22 and Table 4.2 for group I, and in Fig. 4.23 and Table 4.3 for group II. These boreholes provide direct insight into soil strength, stiffness and layering, and allow the estimation of S-wave velocity (V_S) based on empirical correlations.

For the boreholes with SPT-N values, the S-wave velocities (V_S) were computed (estimated) using the following empirical relationships (based on new data and existing correlation between V_S and N in the literature):

- From Daag et al. (2022) for all soils

$$\boldsymbol{V_S = 56.82N^{0.4861}} \tag{4.1}$$

- From Thokchom et al. (2017) for all soils

$$\boldsymbol{V_S = 3.311N + 160.5} \tag{4.2}$$

- From Kirar et al. (2016) for all soils

$$\boldsymbol{V_S = 99.5N^{0.345}} \tag{4.3}$$

For the boreholes with CPT data (q_c: cone tip resistance, f_s: sleeve friction resistance), the S-wave velocities (V_S) were estimated using the following empirical relationships:

- From Hegazy and Mayne (1995) for all soils

$$\boldsymbol{V_S = (10.1\log(q_c) - 11.4)^{1.67}(100\, f_s/q_c)^{0.3}} \tag{4.4}$$

- From Mayne (2006) for all soils

$$\boldsymbol{V_S = 118.8\log(f_s) + 18.5} \tag{4.5}$$

The group I (Fig. 4.22 and Table 4.2) located in the main part of the city (on the colluvium and the volcano-sedimentary units) provide higher geotechnical resistance values. The SPT-N values range from 5 to >50 in the upper 10-20 m (although there are SPT-N values <5 in some superficial layers). The refusal (N>50) is reached at shallow depths in several boreholes, particularly where hard rock is encountered. For the CPT, q_c and f_s have average values of 1600 kPa and 127 kPa respectively in the upper 5 m. These values correspond to medium-dense to very dense soils including gravelly colluvium, silty-sandstone turbidites and karstified limestones. The lithological description in the Table 4.2 is the field observation realized during these tests.

The high compactness of the sites of group I results in minimal amplification of seismic waves as also shown by the flat H/V curves. These areas are generally more suitable for standard foundation designs and are less susceptible to liquefaction or deep ground motion resonance.

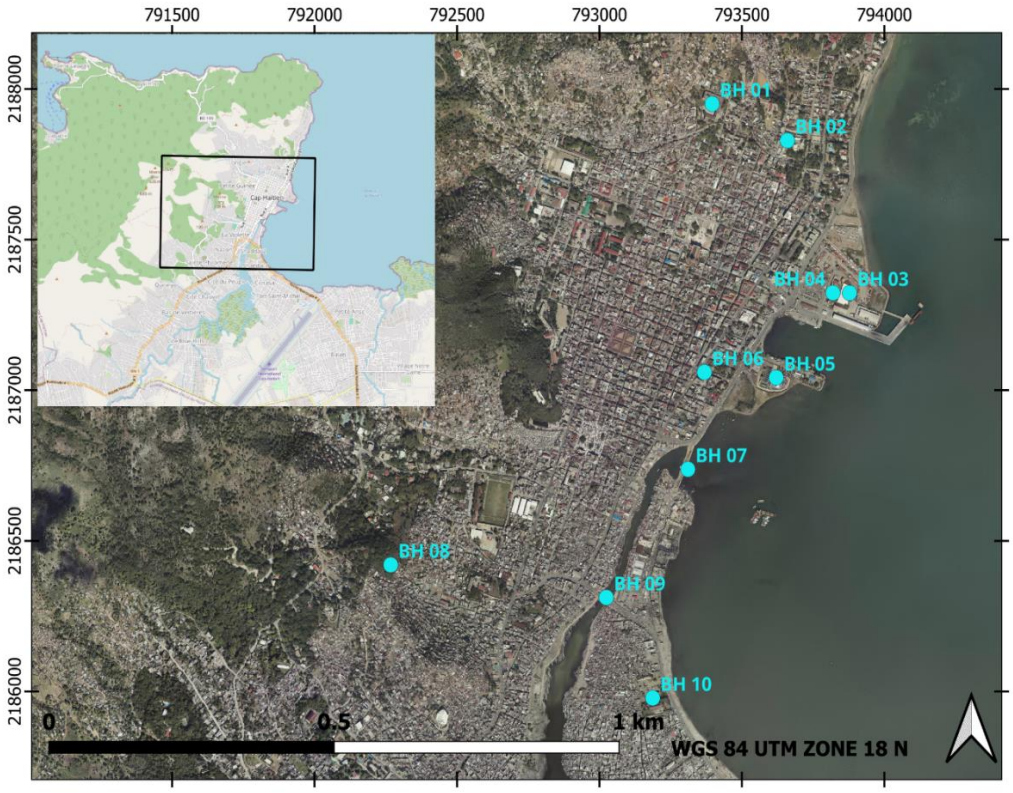

Fig. 4.22 Locations of the boreholes log with SPT (or CPT) carried out in the main part of the city of Cap-Haitien.

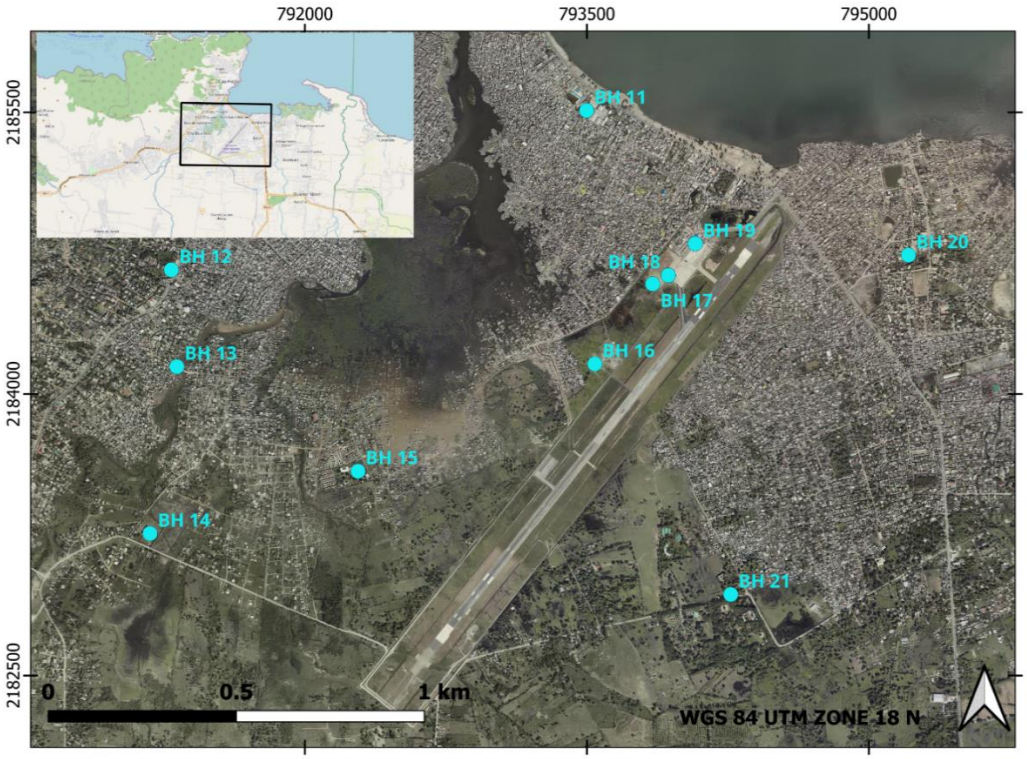

Fig. 4.23 Locations of the boreholes log with SPT (or CPT) carried out in the alluvial plain (including the Cap-Haitien international airport).

The boreholes of group II located in the alluvial plain (Fig. 4.23 and Table 4.3), that includes the marshy areas and the airport, provide low geotechnical resistance values. The SPT-N values are typically low in the upper 10-20 m depth. Some localized layers show slightly high SPT-N values due to interbedded denser layers. For the CPT, q_c and f_s have values of 1000-1100 kPa and 55-111 kPa respectively in the upper 5 m. These values correspond to soft, water-saturated sediments, often with high content of organic material or fine-grained silts and clays.

These results are in accordance with the MASW profiles carried out in the alluvial plain and coastal margin of Cap-Haitien. The soft soils are susceptible to high amplification during seismic events as confirmed by pronounced low-frequency H/V peaks in these areas.

Table 4.2 Summary of results of the boreholes log with SPT (or CPT) carried out in the main part of the city of Cap-Haitien.

Boreholes	Depth (m)		SPT	CPT		Computed V_S (m/s)	Lithological description
	From	To	N	q_c(kPa)	f_s(kPa)		
BH 01	0	6.5	12			206.2	clayey gravel
	6.5	20	50			800.0	silty gravel
BH 02	0	10	45			337.8	silty gravel
BH 03	0	3	14			218.9	gravelly sand
	3	6	1			106.7	silt
	6	15	11			196.0	sandy gravel
BH 04	0	12	6			157.8	sand
BH 05	0	7	5			154.2	silty sand
	7	15.5	13			208.0	gravelly-silty sand
BH 06	0	3.5	26			262.8	sandy-silty gravel
	3.5	9.5	6			159.1	sandy-clayey silt
	9.5	15.5	14			213.5	clayey-sandy gravel
BH 07	0	17	4			140.4	silt
	17	34	38			318.6	clayey sand
	34	37	50			363.4	clayey gravel
	37	40	39			325.7	silty sand
BH 08	0	2	50			363.4	clayey sand
	2	14	50			363.4	clayey gravel
BH 09	0	15	6			158.3	silty sand
	15	27	39			324.7	clayey sand and gravel
	27	40	38			318.3	clayey sand
BH 10	0	5		1600	127	241.6	silt and sand

Table 4.3 Summary of results of the boreholes log with SPT (or CPT) carried out in the alluvial plain (including the Cap-Haitien international airport).

Boreholes	Depth (m)		SPT	CPT		Computed V_S (m/s)	Lithological description
	From	To	N	q_c(kPa)	f_s(kPa)		
BH 11	0	5		1100	111.2	250.1	silt and sand
BH 12	0	3.5	15			223.8	clayey silt
	3.5	6.5	32			298.3	clayey gravel
	6.5	20	50			800.0	clayey and silty sand
BH 13	0	11	24			263.3	silty sand
	11	25	33			299.7	silty-clayey sand
	25	40	46			347.7	silty-clayey gravel
BH 14	0	3	6			159.8	silty-clayey sand
	3	10	13			204.5	silty sand
	10	12	5			158.2	sandy-gravelly clay
BH 15	0	30	6			155.6	clay
BH 16	0	11	11			193.7	silty sand
	11	20	5			149.9	silt
BH 17	0	3.5	2			122.1	sandy-gravelly clay
	3.5	12.5	16			225.7	silty sand
	12.5	35.5	6			163.2	silt and clay
	35.5	44.5	22			273.7	silty-clayey sand
	44.5	50	29			278.3	clayey gravel
BH 18	0	14	11			199.4	silty gravel and sand
	14	20.5	5			157.7	silt
BH 19	0	9.5	10			187.2	sand
BH 20	0	8		1000	55	191.0	silt and sand
BH 21	0	12.5	9			182.2	clay
	12.5	24.5	5			154.9	silt
	24.5	30.5	9			189.2	clay

4.2.4 Discussion (study area 2)

The Cap-Haitien approach aims for a better and stronger engineering relevance by integrating geophysical methods with geotechnical data. These observations are well highlighted in the seismic microzonation reports of Cap-Haitien (Roullé et al. 2014; Bertil et al. 2014). The present analysis adds more V_S values by adopting multiple empirical formulas (Daag et al. 2022; Kirar et al. 2016; Thokchom et al. 2017; Mayne 2006; Hegazy and Mayne 1995) and comparing the V_S from different sources.

The results in Cap-Haitien are consistent with broad patterns observed in other cities built on thick sediments like Mexico City (Bard et al. 1988; Bard and Bouchon 1980). The multiple datasets allow more precise site characterisation than is typically possible in purely geophysical studies (like in the Anse-à-Veau case).

A similar contrast is observed in the study area of Anse-à-Veau: the low frequency peaks from HVSR results are found in the alluvial deposits (at *La Basse Ville*, along *Riviere Brossard* and

around the pond). The elevated zones (at *La Haute Ville* and in the mountains) composed of limestones are characterized by flat curves or high frequency peaks. In Cap-Haitien, the H/V curves in the alluvial plain show well defined low frequency peaks with high amplitudes; the ones in the volcanic and colluvial areas tend to be flat or characterized by high frequency peaks with low amplitudes, indicative of shallow and stiff layers.

The MASW profiles for S-wave velocity (V_S) models were performed in both regions. The results show strong correlation with the H/V analysis with low V_S values in soft sediments areas and high V_S values in limestones, colluvial or volcanic terrains. The V_S profiles in Cap-Haitien are supported by empirical V_S estimated from SPT and CPT, which significantly enhances the confidence in the analysis and interpretations. Fig. 4.24 shows a simplified geological section inferred from the combined results of the geophysical and geotechnical data.

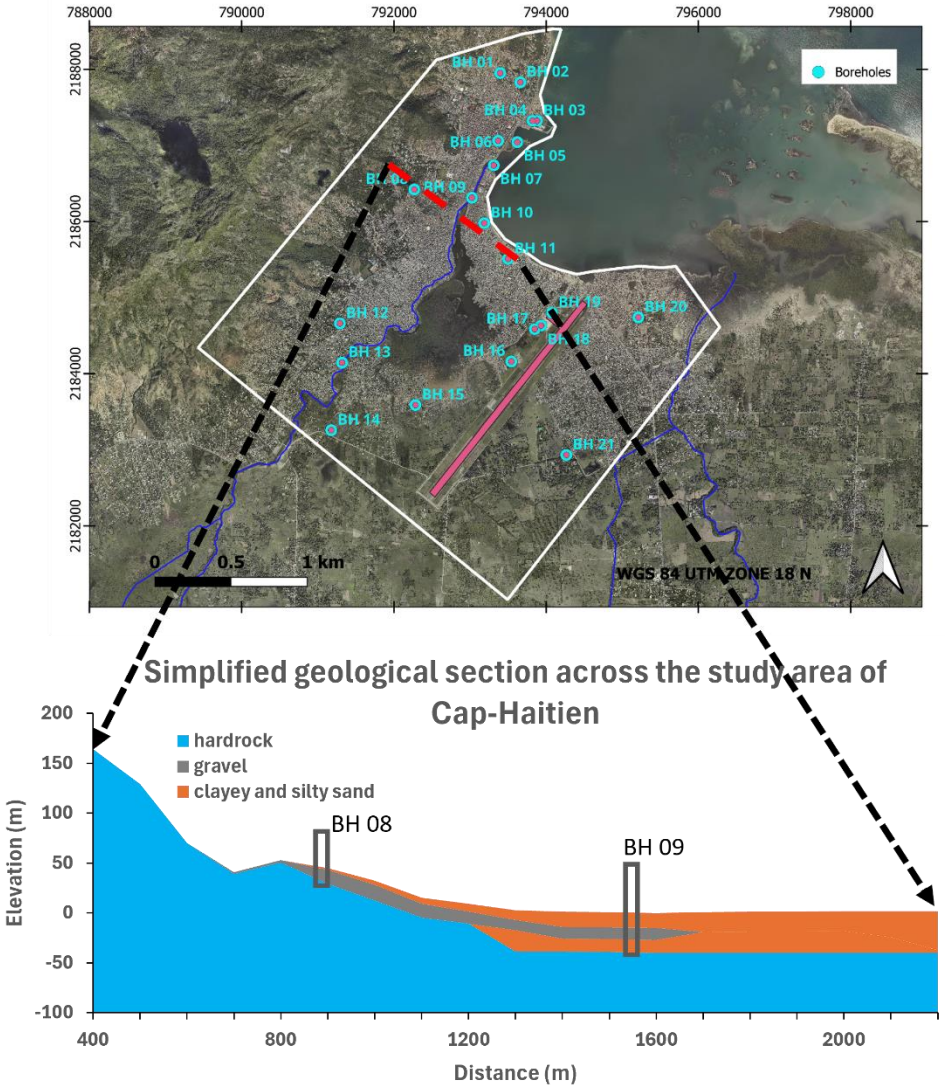

Fig. 4.24 Example of a simplified geological section across the study area of Cap-Haitien.

5 Site characterisation and local ground motion mapping

This chapter presents the site characterisation and local ground motion mapping from the geostatistical analysis of geophysical and geotechnical data. The data are first analysed using detailed geostatistical methods and then submitted to interpolations technique to produce the site characterization maps. The same procedures are followed for the study areas (Anse-à-Veau and Cap-Haitien). Empirical relationships are used to establish the local ground motion maps.

5.1 Study area 1: Anse-à-Veau

5.1.1 Exploratory data analysis (Anse-à-Veau)

The exploratory data analysis (EDA) involves a series of descriptive and graphical analysis to better understand the structure, trends and spatial variability of the geophysical-seismological data. The variables to analyse include the fundamental frequency (f_0) and amplitude (A_0) from the HVSR results, and the S-wave velocities (V_{S30}) derived from the MASW profiles. The accurate spatial prediction and quantification of uncertainty associated with these variables are essential for the development of reliable site characterisation maps.

The geophysical parameters f_0, A_0 and V_{S30} usually exhibit non-normal distributions, non-stationarity spatial behaviour, and cross-correlation driven by geological layering and lateral variations. The classical deterministic interpolation methods such as the inverse distance weighting (IDW) and the spline methods fail to represent spatial continuity, ignore cross-dependencies, and provide no measure of uncertainty. For these reasons, geostatistics offer a more robust framework.

The histograms and basic statistics of f_0 and A_0 (Figs. 5.1 and 5.2) show that the variables depart substantially from any normal distribution. The frequency values are marked by wide variations, from as low as 0.56 Hz to more than 22 Hz, with a distinctly long tail toward higher frequencies. This small cluster of very high resonance peaks is detrimental to the statistical homogeneity of the dataset and reflects the abrupt geological contrasts in the study area. The pronounced skewness (2.59) and the high kurtosis (6.24) confirm that a few stiff or shallow-bedrock sites dominate the upper part of the distribution.

The amplitude A_0 (Fig. 5.2) behaves more moderately but still shows a noticeable positive skew. Although its tail is not extreme as that of f_0, the amplitude remains heavily influenced by the contrast between soft alluvial deposits and stiffer limestone units. In both cases, the raw data reflect the geological patchwork of the study area: thick alluvial layers along the river and in *La Basse Ville*, reef limestones in *La Haute Ville*, and massive pelagic limestones and marly formations toward the mountains.

The V_{S30} values, on the other hand, have a nearly symmetrical distribution (Fig. 5.3). The skewness and the kurtosis are close to zero, and the histogram shows a broad but more balanced range between about 100 and 800 m/s. While the V_{S30} is statistically more well behaved than the HVSR parameters, its spatial pattern reflects the geological zonation observed in the HVSR cases.

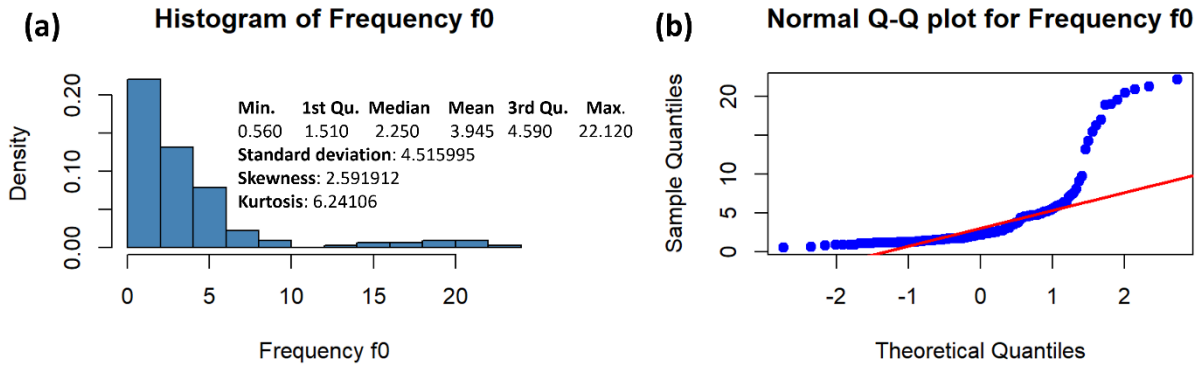

Fig. 5.1 **(a)** Histogram and descriptive statistics of the fundamental resonance frequency (f_0) from the HVSR data in Anse-à-Veau. **(b)** Normal Q-Qplot of f_0. The sample points (in blue) are not aligned with the normal line (in red).

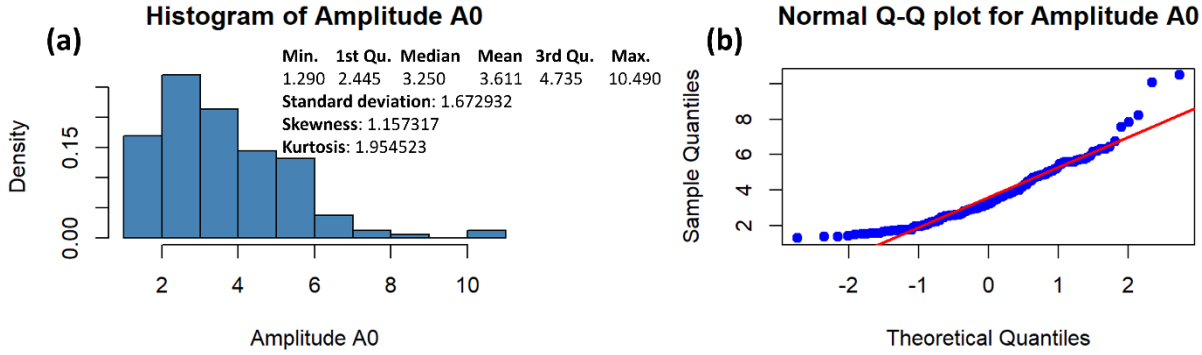

Fig. 5.2 **(a)** Histogram and descriptive statistics of the amplitude (A_0) from the HVSR data in Anse-à-Veau. **(b)** Normal QQplot of A_0. The sample points (in blue) are not aligned with the normal line (in red).

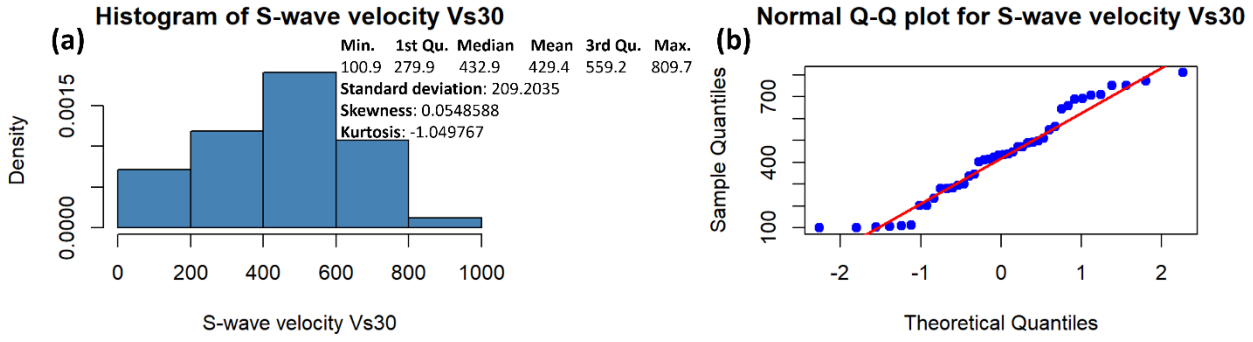

Fig. 5.3 **(a)** Histogram and descriptive statistics of the S-wave velocities (V_{S30}) derived from the MASW profiles in Anse-à-Veau. **(b)** Normal Q-Qplot of V_{S30}. The sample points (in blue) are closer to the normal line (in red) than for the HVSR cases.

Because the geostatistical methods such as kriging and sequential Gaussian simulation (SGS) rely on an underlying normal (Gaussian) distribution, the raw HVSR data cannot be used directly. A normalizing transformation was therefore applied.

After the transformation, the three variables almost exhibit symmetric distributions:

- f_0 is centred with negligible skewness (0.0003) and near-zero kurtosis (-0.15),
- A_0 shows a very good reduction in asymmetry, with its histogram becoming much more balanced,
- V_{S30}, already close to Gaussian, becomes even more stable and compact.

The histograms and Q-Q plots of the transformed data (Figs. 5.4, 5.5 and 5.6) illustrate this improvement. Most of the points are close to the normal line (the red line in the figures), with only slight deviations at the extremes. This transformation step allows the variables to be treated as Gaussian fields and provides a basis for the construction of stationary variogram models. Small deviations at the extremes are common and expected in natural geological datasets, especially when the underlying lithology changes abruptly over short distances.

The normal transformation does not remove spatial trends but only corrects the distributional shape. Thus, even after the transformation, the data still contain large-scale gradients identified earlier. These must be removed through detrending before the residuals can be considered stationary.

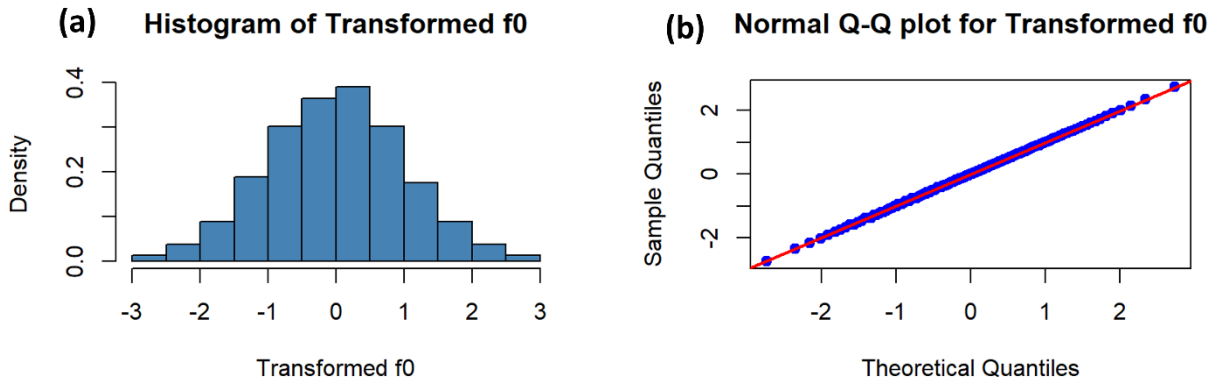

Fig. 5.4 **(a)** Histogram and descriptive statistics of the transform fundamental resonance frequency (f_0) from the HVSR data in Anse-à-Veau. **(b)** Normal Q-Qplot of the transformed f_0.

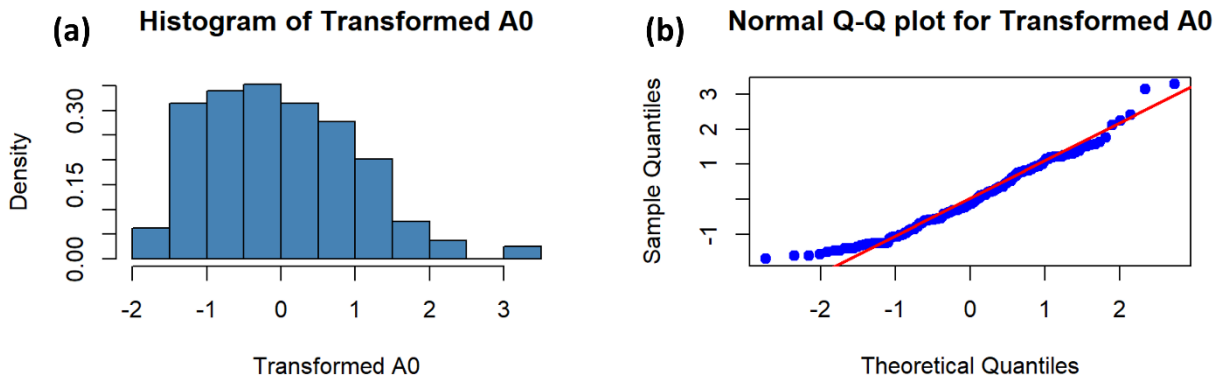

Fig. 5.5 (a) Histogram and descriptive statistics of the transformed amplitude (A_0) from the HVSR data in Anse-à-Veau. **(b)** Normal Q-Qplot of the transformed A_0.

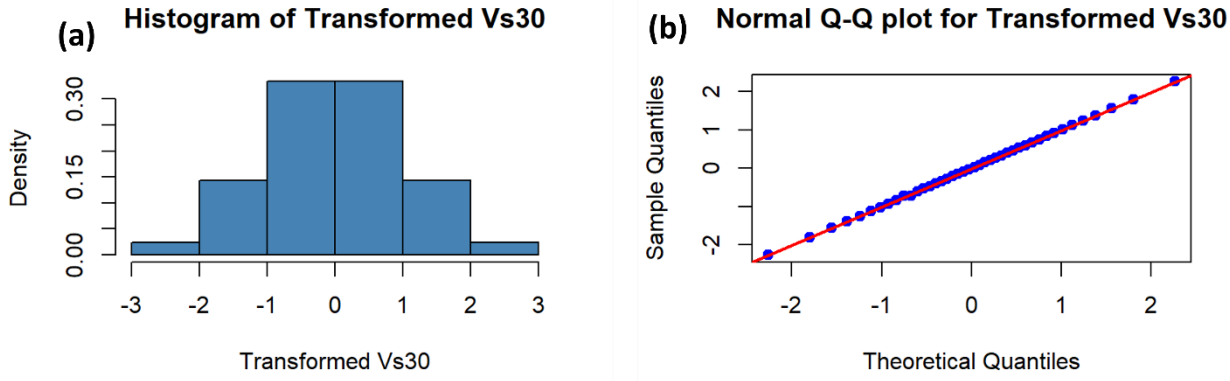

Fig. 5.6 (a) Histogram and descriptive statistics of the transformed S-wave velocities (V_{S30}) derived from the MASW profiles in Anse-à-Veau. **(b)** Normal Q-Qplot of the transformed V_{S30}.

The spatial distribution (provided in Appendix A5) indicates how the variables evolve across the landscape. The fundamental frequency f_0 increases as one move away from *La Basse Ville* and the pond area, where the sedimentary cover is thickest. The amplitude A_0 shows the opposite trend, with higher values concentrated in the zones dominated by the alluvial soft deposits and a clear decline toward the stiffer limestones units.

These patterns make physical sense: thicker and softer sediments tend to generate low resonance frequencies with high amplification, while stiff or shallow bedrock leads to the opposite behaviour. The V_{S30} follows a similar logic, rising steadily toward rock outcrops and high relief areas. These observations confirm that the datasets contain large-scale geological trends and justify the use of universal kriging, multivariate cokriging, and sequential Gaussian simulation.

5.1.2 Variogram modelling (Anse-à-Veau)

The variogram captures the degree of dissimilarity between observations as a function of distance and direction, reflecting both geological structure and measurement uncertainty. In this section, the complete variogram analysis is presented for the three principal variables: the fundamental resonance frequency f_0 (Fig. 5.7), the amplitude A_0 (Fig.5.8), and the S-wave velocities V_{S30} (Fig. 5.9). The methodology follows the standard geostatistical sequence: construction of experimental variograms, assessment of anisotropy, model selection, parameter estimation and geological interpretation. These steps are essential for ensuring that the spatial modelling reflects the real subsurface processes that control the seismic site response.

To construct the experimental variograms, the dataset was pairwise differenced over a series of distance classes (lags). The choice of lag width and maximum distance is always a balance between resolution and stability. The smaller lags offer fine detail but may result in noisy estimates if the data pairs are sparse. The larger lags produce smoother curves but risk masking important short-scale variability. For the present dataset, the lag widths were chosen to ensure a sufficient number of data pairs while preserving sensitivity to geological variations. The maximum distance was set to approximately half of the maximum spatial extent of the study area, as in common practice.

The resulting experimental variograms displayed the classical features expected in geological environments: an initial rapid increase in variance at short lags that corresponds to local heterogeneity, followed by a slower, more gradual rise that reflects broad geological structures, and a stabilisation around a sill at longer distances. These features confirm that, after detrending, the variables are stationary for the variogram modelling.

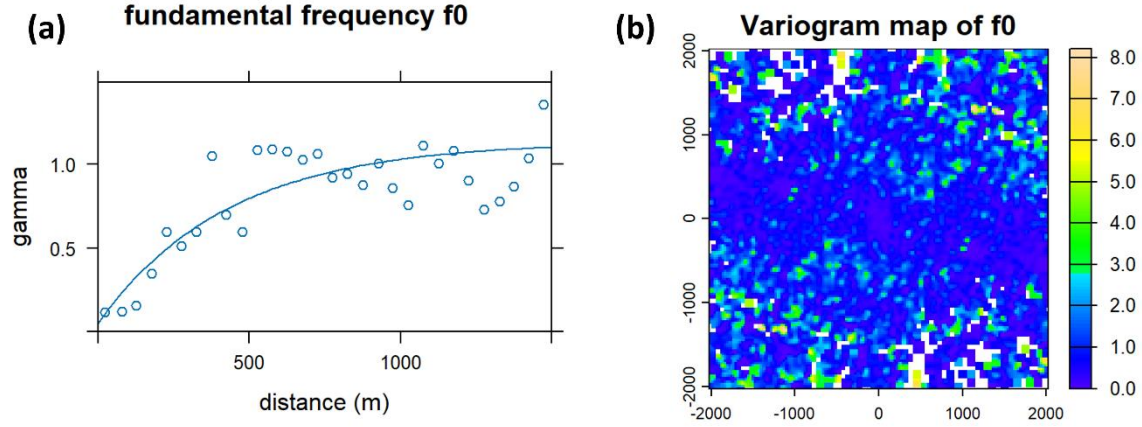

Fig. 5.7 (a) Variogram model and **(b)** variogram map of the fundamental resonance frequency (f_0) from the HVSR data in Anse-à-Veau.

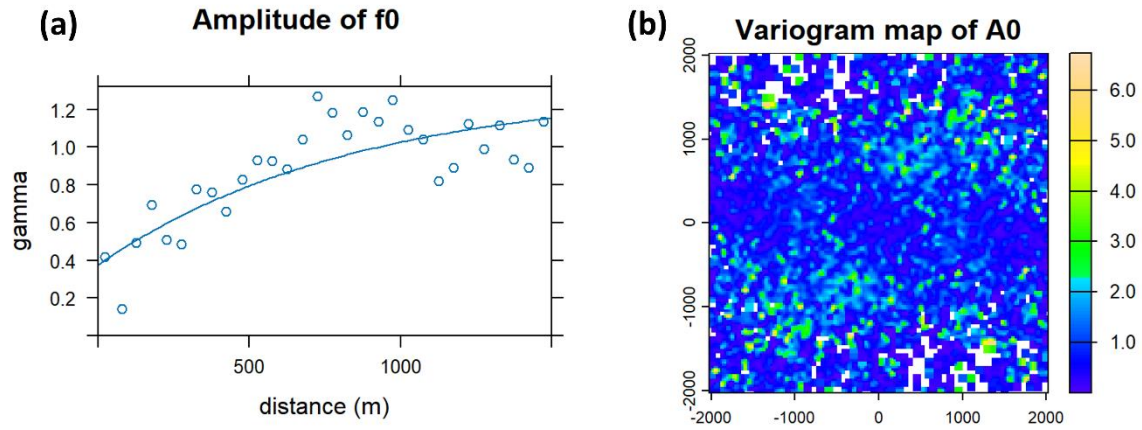

Fig. 5.8 **(a)** Variogram model and **(b)** variogram map of the amplitude (A_0) from the HVSR data in Anse-à-Veau.

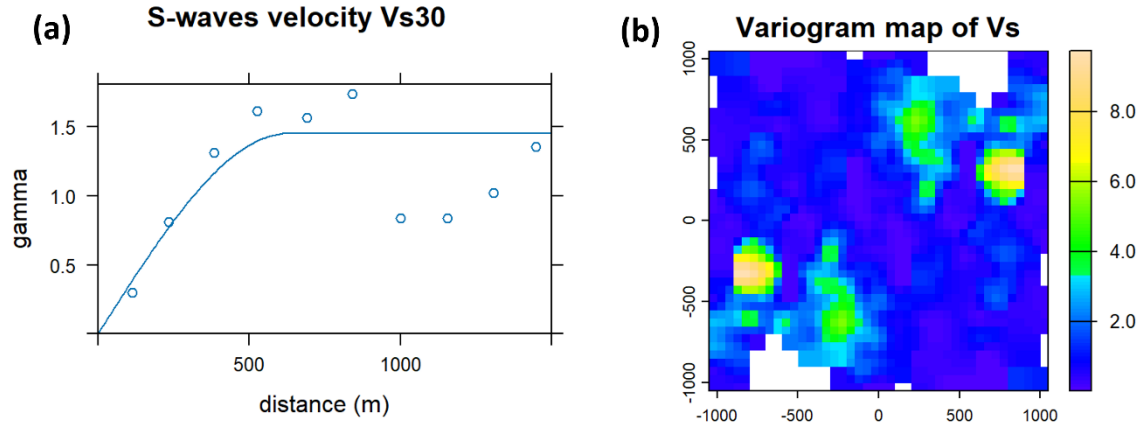

Fig. 5.9 **(a)** Variogram model and **(b)** variogram map of the S-wave velocities (V_{S30}) derived from the MASW profiles in Anse-à-Veau.

The variogram maps represent the spatial variability in two dimensions and allow to identify the anisotropy related to geological structures or topographic trends. The HVSR results (f_0 and A_0) displayed a clear anisotropic pattern aligned approximately along azimuths N100-110. This direction corresponds closely to the structure of the transition zone between *La Haute Ville* and the mountains. In such settings, the sediment thickness and impedance contrasts vary more rapidly perpendicular to the sedimentary deposit axis than along it, which naturally produces anisotropic spatial continuity in the HVSR parameters.

The S-wave velocities (V_{S30}) display an anisotropy oriented along N130-140, slightly rotated relative to the HVSR parameters. This direction is controlled by lithological and geomorphological gradients at different scales than the HVSR parameters, and the observed anisotropy reflects the gradual stiffening of the materials toward the mountain ranges. The persistence of anisotropy in V_{S30} indicates that the spatial continuity of the stiffness is governed by different geological mechanisms than the site response parameters.

The variogram models presented in Figs. 5.7, 5.8 and 5.9 are omnidirectional (ignoring the anisotropy). This allows the selection of an appropriate model.

For the fundamental resonance frequency (f_0), we have:

- Nugget: 0.0508
- Structure: Exponential
- Partial sill: 1.0819
- Range: 428 m

For the amplitude (A_0):

- Nugget: 0.3760
- Structure: Exponential
- Partial sill: 0.9334
- Range: 839 m

For the S-wave velocities (V_{S30}):

- Nugget: 0.0000
- Structure: Spherical
- Partial sill: 1.4528
- Range: 629 m

The differences in the model type (exponential for f_0 and A_0 but spherical for V_{S30}) already suggest fundamental distinctions in the underlying spatial processes. The exponential variogram captures the sharp local variability of f_0, which is influenced by abrupt changes in sediment thickness and impedance contrast. An exponential rise at short lag distances reflects the heterogeneous nature of the sedimentary column. The amplitude A_0 shares the same spatial controls with f_0 but with smoother transitions across the geological units. The exponential structure captures these properties. The V_{S30} is smoother because it represents a depth-averaged velocity.

For the fundamental frequency f_0, the nugget is relatively small, indicating that measurement noise is limited and that the acquisition process is generally stable. However, the presence of a non-zero nugget may also indicate the existence of real micro-scale heterogeneity in sediment thickness and impedance properties.

The amplitude A_0 displays a larger nugget value. The higher nugget is consistent with the greater susceptibility of amplitude measurements to environmental noise, site coupling conditions, and short-scale variations in damping or impedance contrast. Unlike the frequency, which is often more robust to environmental perturbations, the amplitude can vary over very small distances due to changes in the local geometry of the sediment-bedrock transition or due to the presence of anthropogenic features at the surface. This larger nugget therefore reflects the variability related to the measurements and the intrinsic small-scale amplification differences.

For the V_{S30}, the nugget is essentially zero, which is a noteworthy contrast to the HVSR parameters. This behaviour is consistent with the physical nature of V_{S30} as a depth-averaged property, which smooths out small-scale heterogeneities. Moreover, the acquisition protocol for MASW surveys tends to produce stable estimates with strong signal penetration and low susceptibility to shallow perturbations. The near-zero nugget therefore reinforces the interpretation of the V_{S30} as a smoother, more continuous geophysical variable compared to the HVSR data in the study area 1.

The range of the f_0 variogram (~428 m) corresponds closely to the lateral extent of the sediment compartments within the alluvial deposit. This indicates that the spatial continuity of the resonance frequency is governed primarily by the geometry of the sedimentary basin and by the distribution of soft Quaternary deposits. The relatively moderate range reflects the degree to which sediment thickness changes across the plain, transitioning from deep accumulations near the river to thinner layers toward the limestone margins.

The range of A_0 (~839 m) is larger, implying that site amplification effects are coherent over a broader spatial domain. This difference arises because amplitude is influenced by the impedance contrasts and basin geometry, which tend to vary more smoothly across the study area. The amplitude therefore integrates the effects of geological layering over wider areas, resulting in longer-range spatial correlation.

For the V_{S30}, the range of approximately 629 m aligns well with the width of the soft lithological units of the study area (see geological context in section 2.2.2). Unlike the HVSR parameters, the V_{S30} captures more integrated structural properties, which naturally extend over larger distances. The range therefore reflects the continuity of near-surface stiffness across geological units characterized by gradual transitions rather than abrupt changes.

The sills of the variograms correspond to the total variance and provide an indication of the intensity of small to medium scale heterogeneity. The results show that the datasets are adapted for geostatistical modelling, as the sills represent genuine spatial variability rather than artifacts of non-stationarity. The ranges and sills encapsulate the fundamental geological structure of the study area, revealing a coherent relationship between spatial continuity and the underlying lithological setting.

5.1.3 Site characterisation maps (Anse-à-Veau)

The site characterisation maps are produced from the spatial interpolation and multivariate prediction results obtained for the three geophysical variables investigated in the study area: the fundamental resonance frequency f_0, the relative amplitude A_0, and the S-wave velocity V_{S30}.

The analytical workflow follows directly from the exploratory analysis and variogram modelling described in the previous sections. Because these variables were shown to be non-stationary, universal kriging (UK) was first applied in the normal-score space to obtain unbiased local predictions. For multivariate enhancement, two additional approaches were tested: traditional cokriging (CK) through a fitted linear model of coregionalization, and regression kriging (RK, to

validate the cokriging, because the MASW data are limited) exploiting the partial functional dependence between the V_{S30} and the HVSR parameters. For the regression kriging, an ordinary kriging is applied to the residuals obtained from the deterministic relationship between V_{S30} and f_0. The cross-validation technique provides a Root Mean Square Error (RMSE) of 0.1662. The RMSE for the cokriging is 0.1591.

The spatial continuity of the three variables reflects the variogram models described previously. For f_0 and A_0, an exponential variogram was fitted with anisotropy along N100-110, while V_{S30} was modelled with a spherical variogram along N130-140. The ranges of the fitted models were approximately 428 meters for f_0, 839 meters for A_0, and 629 meters for V_{S30}, while the nugget effects were small for f_0, moderate for A_0, and essentially zero for V_{S30}. These characteristics dictated the spatial gradients, and local variability of the kriging outputs.

The kriged prediction map of f_0 (Fig. 5.10) reproduces the expected geological pattern. Low frequencies, generally below 2 Hz, dominate *La Basse Ville* (thick Quaternary alluvial deposits) and the marly limestone with high clay content, while higher frequencies, exceeding 5 Hz, occur over the stiffer limestone units in *La Haute Ville* and the mountainous ridge, reflecting stiffer bedrock conditions. The associated standard error map (Fig. 5.11) reveals that uncertainty is lowest in the Anse-à-Veau town where measurement density is relatively homogeneous, and highest in the southern and southeastern areas with sparse data and across sharp lithological transitions. The low frequencies combined with high amplitudes in *La Basse Ville* indicate strong site amplification, whereas low frequencies over *La Haute Ville*, which are associated with low amplitudes, suggest limited site effect potential. The higher prediction variance for f_0 compared to A_0 reflects both the sensitivity of f_0 to sediment thickness and the smaller nugget effect, consistent with the more rapid local variability of resonance frequencies.

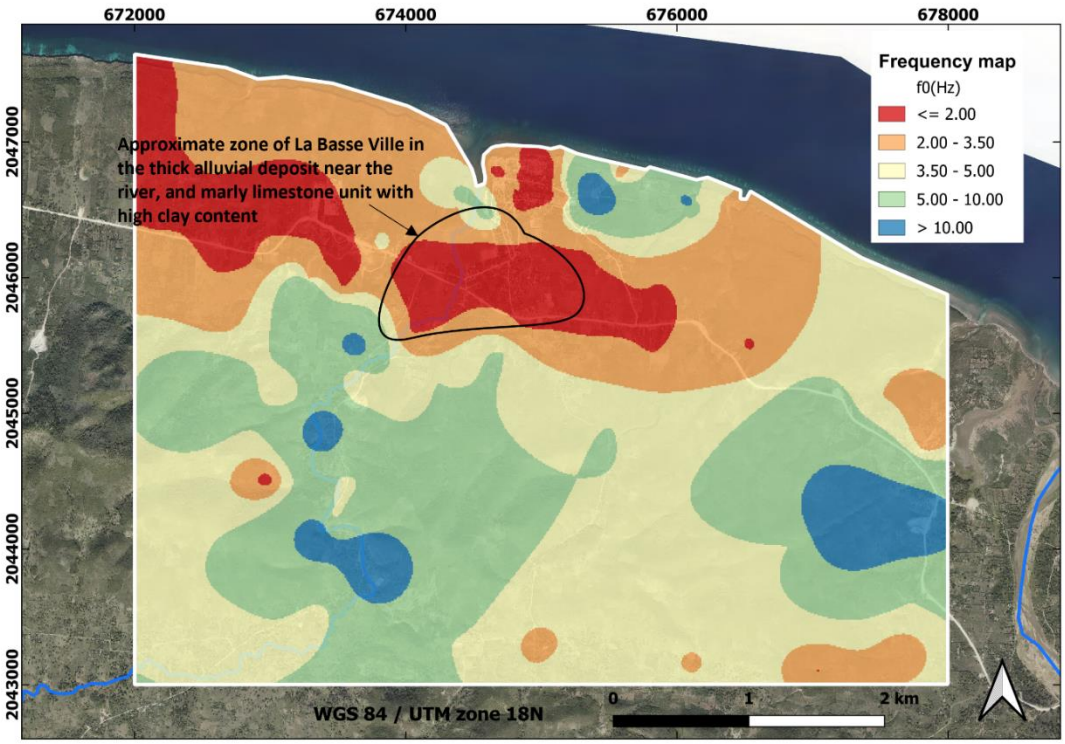

Fig. 5.10 Fundamental frequency map f_0 obtained from universal kriging of the HVSR data in Anse-à-Veau.

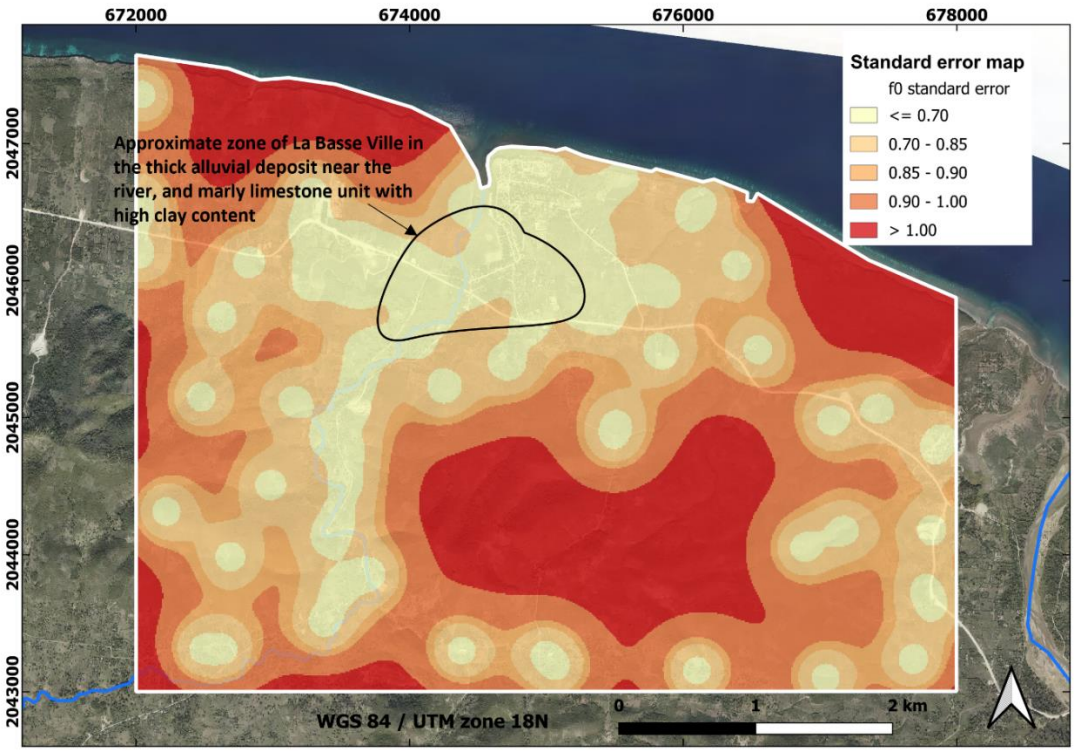

Fig. 5.11 Standard error map f_0 obtained from universal kriging of the HVSR data in Anse-à-Veau.

The amplitude A_0 exhibits a smoother spatial pattern due to its longer variogram range (~839 m). High amplitude values, generally exceeding 4.5, are concentrated in *La Basse Ville* and along the basin margins, reflecting soft sediments with strong impedance contrasts. Intermediate amplitudes dominate the marly limestone area, whereas low amplitudes map the compact limestone and mountainous regions. The kriged prediction map of A_0 (Fig. 5.12) highlights these patterns, while the associated standard error map (Fig. 5.13) shows lower uncertainty than f_0, particularly in regions with dense HVSR measurements. In the southern area, relatively high amplitudes coincide with higher frequencies; although these areas display amplification, the higher frequencies reduce their significance for site effect potential. The weaker variation in A_0 compared to f_0 explains the more homogeneous spatial distribution and lower prediction errors.

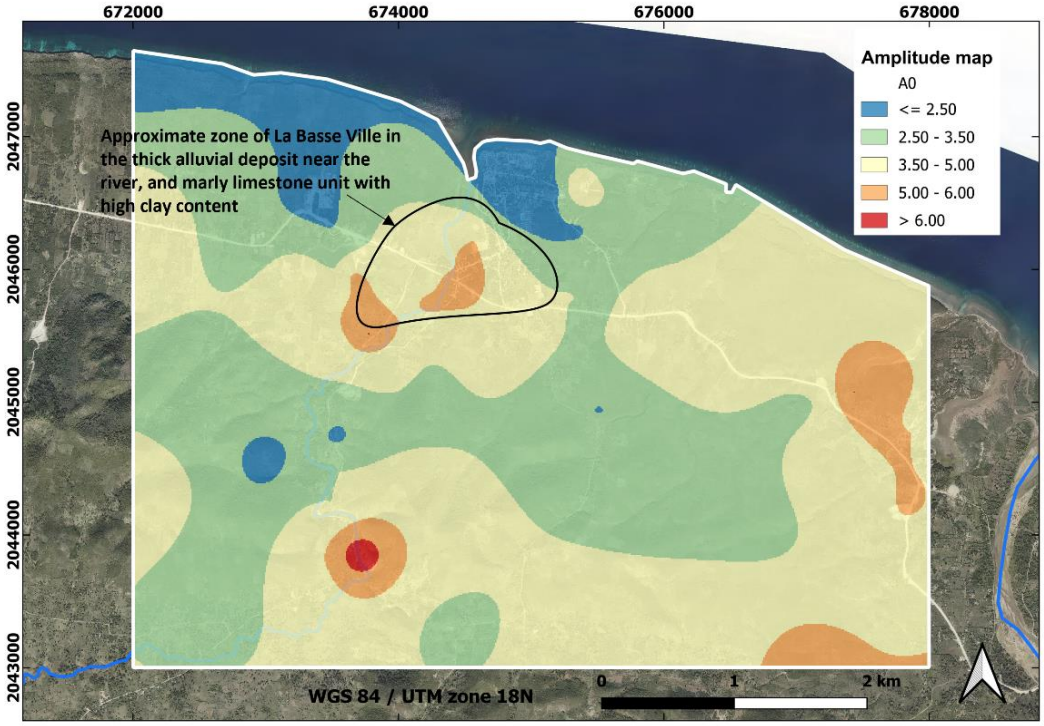

Fig. 5.12 Amplitude map A_0 obtained from universal kriging of the HVSR data in Anse-à-Veau.

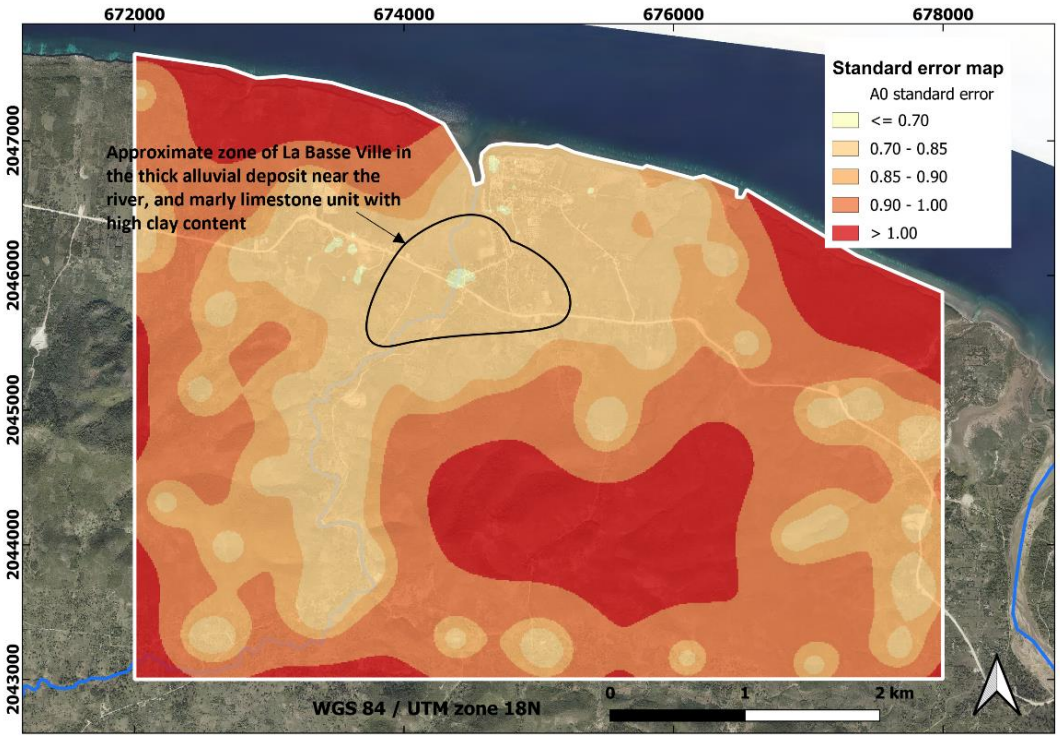

Fig. 5.13 Standard error map A_0 obtained from universal kriging of the HVSR data in Anse-à-Veau.

The MASW results are combined with the H/V results to produce a map of the parameter V_{S30}. The amount of the H/V data allows to take advantage of the cokriging technique and give more coherence to the final V_{S30} map since the H/V and the MASW results are correlated. The simple variograms (for each dataset) and cross-variogram (between the H/V and MASW data) were modelled together, since there are mathematical restrictions between them (Emery 2012). The linear model of co-regionalisation used assumes that simple and cross-variograms are linear combinations of the same theoretical basic models.

The V_{S30} map, presented in Fig. 5.14, is the smoothest among the three variables, with high values in the limestone mountainous ridge (600-800 m/s) and low values in the Quaternary alluvial plain (100-250 m/s). The corresponding standard error map (Fig. 5.15) indicates minimal uncertainty across most of the study area, particularly where MASW measurements and HVSR data are dense.

From a geological and seismic hazard perspective, the integrated analysis of f_0, A_0 and V_{S30} allows the identification of zones with high site effect potential. The areas with low f_0 and high A_0, such as *La Basse Ville*, correspond to strong amplification, whereas higher frequencies with high amplitudes in the southern area produce localized amplification but with reduced seismic significance. Low f_0 and low A_0 in *La Haute Ville* suggest minimal site effect potential. The spatial patterns of the standard errors reflect both measurement density and local heterogeneity, with lower uncertainties in homogeneous urban zones and higher uncertainties in geologically complex or sparsely sampled regions. The orientation of anisotropy in all three variables is consistent with

the strike of sedimentary and structural units, confirming that kriging and cokriging outputs capture the main geological trends.

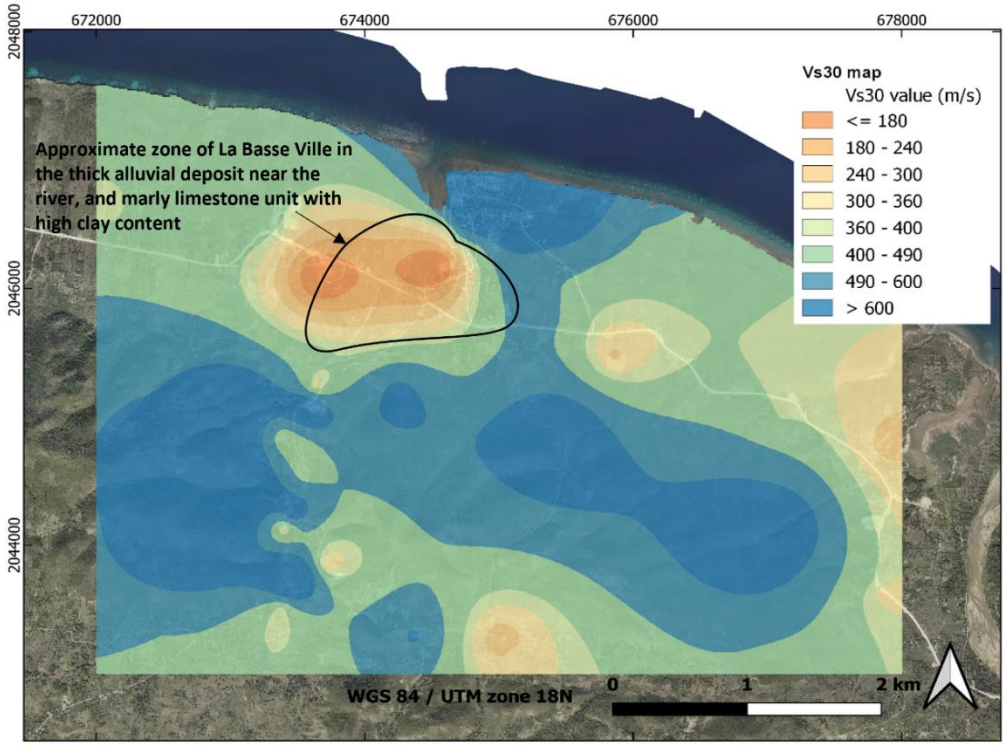

Fig. 5.14 V_{S30} map obtained by applying the cokriging technique between the MASW and the H/V results.

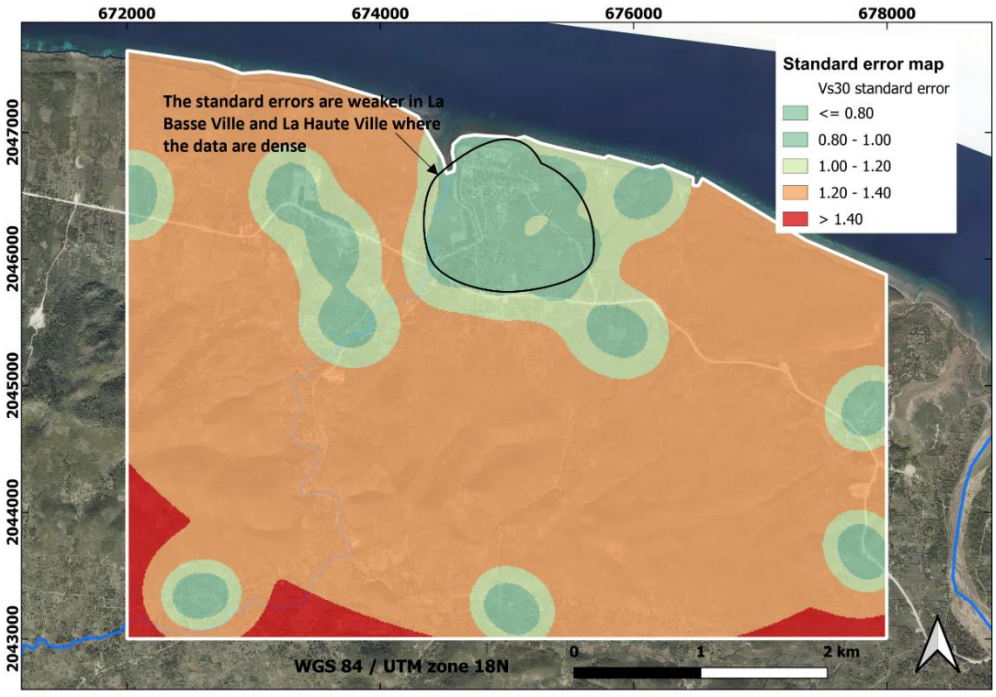

Fig. 5.15 Standard error map of V_{S30} from the cokriging technique between the MASW and the H/V results.

In summary, the universal kriging captured the spatial structure of f_0 and A_0 while the cokriging enhanced the V_{S30} predictions in the alluvial deposits. The combination of prediction maps (Figs. 5.10, 5.12, 5.14) and associated standard error maps (Figs. 5.11, 5.13, 5.15) provides a comprehensive understanding of site amplification potential, lithological variations, and the spatial uncertainty of geophysical estimates across the study area.

A map of site effect index (Fig. 5.16) was computed by combining the all the above parameters. The methodology used to define the index is described in Ulysse et al. (2021) for the area of Fonds-Parisien, 37 km to the east of Port-au-Prince, Haiti.

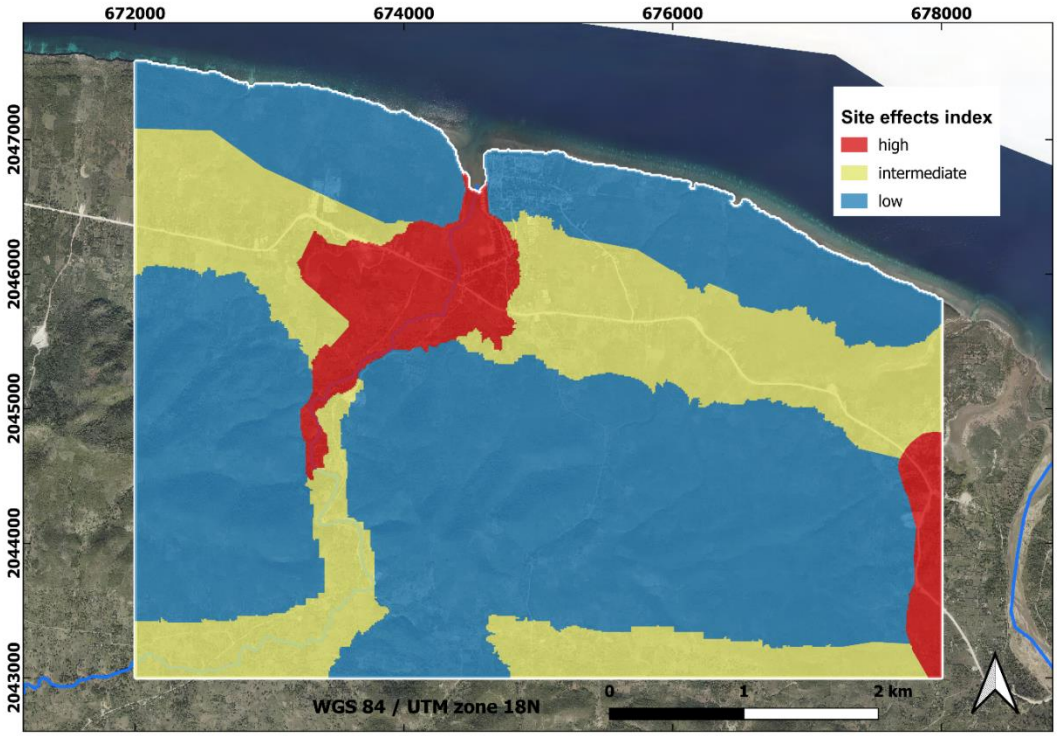

Fig. 5.16 Map of site effect index for the study area of Anse-à-Veau.

5.1.4 Local ground motion maps (Anse-à-Veau)

The spatially based methods for local ground motion assessment provide an indispensable complement to numerical modelling approaches. Whereas deterministic or probabilistic numerical simulations often require substantial computational resources and rely on predefined structural, geological, and source parameters (each associated with inherent uncertainties) spatial methods enable the integration of empirical field measurements with regional seismic hazard information at fine spatial resolutions. This makes them particularly well suited for heterogeneous geological settings such as coastal alluvial basins, where site effects exert a dominant influence on surface ground motion (Joyner and Boore 1993; Atkinson and Boore 2003).

These spatial methods operate by explicitly mapping the small-scale geomorphological variability that controls wave propagation in the near-surface layers. High-resolution surveys (typically involving geophysical techniques such as the ones in the present study) are combined with geomorphological mapping to characterize the sediment thickness, stiffness contrasts, and lateral facies changes that modulate seismic amplification. The resulting spatial datasets can then be coupled with empirical or semi-empirical site amplification models to generate continuous maps of ground motion parameters. Borcherdt (1994) demonstrated that proxy variables such as the V_{S30} are particularly effective in describing soil-induced amplification when integrated at the regional scale. The approach adopted in this study follows this philosophy by using interpolated V_{S30} to directly inform local ground motion estimates.

The current seismic hazard maps for Haiti by Frankel et al. (2011) had been established by using the probabilistic method and the next generation attenuation (NGA) laws (Boore and Atkinson 2008; Campbell and Bozorgnia 2008; Chiou and Youngs 2008) for the crustal faults. Besides the magnitude and distance terms, these attenuation laws include a site amplification term via the parameter V_{S30}. Frankel et al. (2011) calculated the magnitude and distance terms for each NGA separately, but they used the site amplification formula from Boore and Atkinson (2008) NGA for all of them. The latter is a function of V_{S30}, period, and the calculated Peak Ground Acceleration (PGA) for a rock site.

In the present study, we adopt the updated attenuation relations developed by Boore et al. (2014), which extend the earlier NGA formulation by introducing a depth-dependent site term in addition to V_{S30}. This represents a significant advancement for the local ground motion prediction, as it partially accounts for the effects of sediment thickness and the depth to high-velocity bedrock.

To supply the required V_{S30} values, we use the spatially interpolated map constructed from MASW measurements, further refined by cokriging using HVSR data. This multivariate geostatistical approach is particularly effective in the study area, where the V_{S30} are spatially correlated with the resonance frequency due to the variable sensitivity to sediment thickness and stiffness. The resulting V_{S30} map captures the subtle but important lateral variations in shallow lithology across *La Basse Ville*, the marly-limestone transition zone, and the limestone plateau of *La Haute Ville*.

The ground motion assessment is based on two sets of attenuation relationship that compute the Peak Ground Acceleration (PGA) for the southern peninsula with no site effects and for the study area with the site effects. The first attenuation equation is from Boore and Atkinson (2008) of the Next Generation Attenuation (NGA) and was used in the seismic hazard maps for Haiti by Frankel et al. (2011). The second equation is from Boore et al. (2014) and can be seen as an update version of the first one.

The results presented in Fig. 5.17 are the potential PGA generated by the 14 August 2021 earthquake for a uniform firm rock site with a V_{S30} of 760 m/s across the southern peninsula. In Fig. 5.18, we present a map of PGA estimated from ground shaking with data compiled by US Geological Survey (https://earthquake.usgs.gov/earthquakes/eventpage/us6000f65h/shakemap/analysis).

The maps computed from the NGA (Fig. 5.17) show high PGA values (>0.5 g) concentrated along the fault segment involved in the M 7.2 Nippes 2021 earthquake that are rapidly attenuated with the distance. The estimated PGA map (Fig. 5.18) from ground shaking show high values (>0.5 g) around the epicentre (and the other end of the segment fault) that are more gently attenuated with distance.

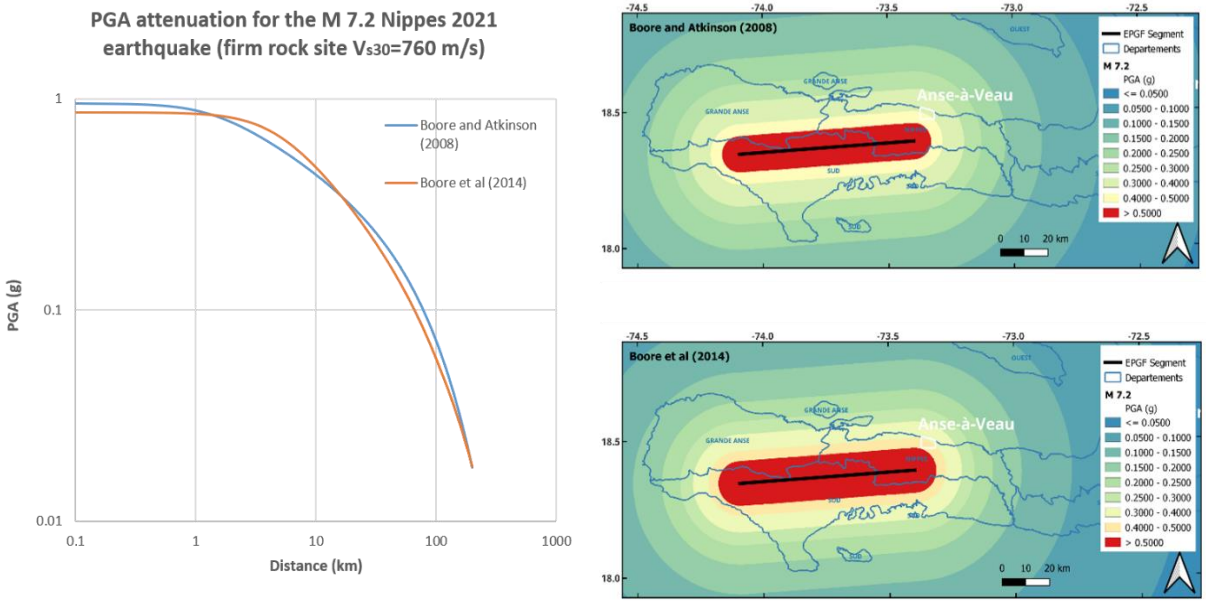

Fig. 5.17 Results of the seismic scenario for the M 7.2 Nippes 2021 earthquake. The maps (after Dorival et al. 2025) are computed for a uniform firm rock site of V_{S30}=760 m/s across the southern peninsula.

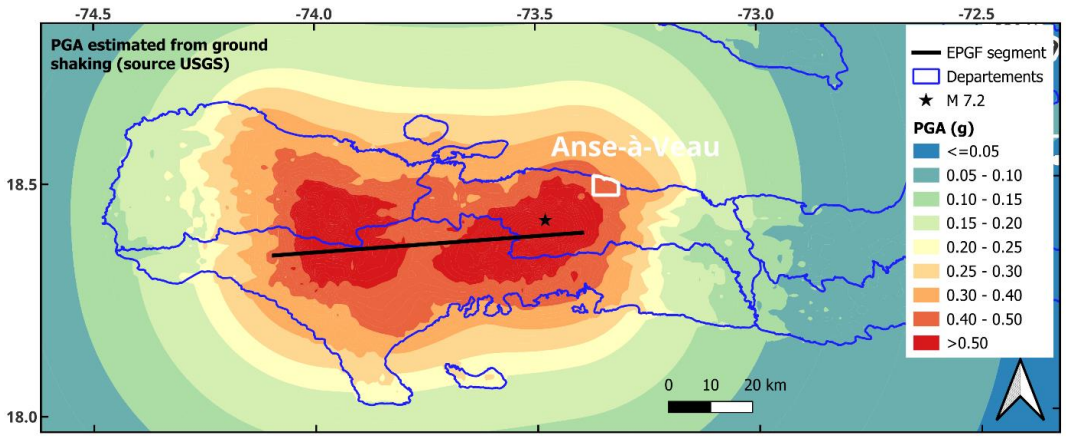

Fig. 5.18 Map of PGA (after Dorival et al. 2025) of the southern peninsula for the M 7.2 Nippes 2021 earthquake estimated from ground shaking with data compiled by the US Geological Survey.

For the study area, we use the NGA from Boore et al. (2014) to calculate the site amplification term with the V_{S30} from the MASW. The maps presented in Fig. 5.19 are constructed by

considering the linear site amplification term (Fig. 5.19a) and both (linear and nonlinear) site amplification (Fig. 5.19b). The value of the PGA is higher in the area with low V_{S30} value when considering only the linear site amplification term. When including the non-linear term, the PGA still increases when V_{S30} value decreases; however, below 360 m/s, the inverse phenomenon is observed. The latter could correspond to attenuation related to non-linearity behaviour of the soft layers below 360 m/s.

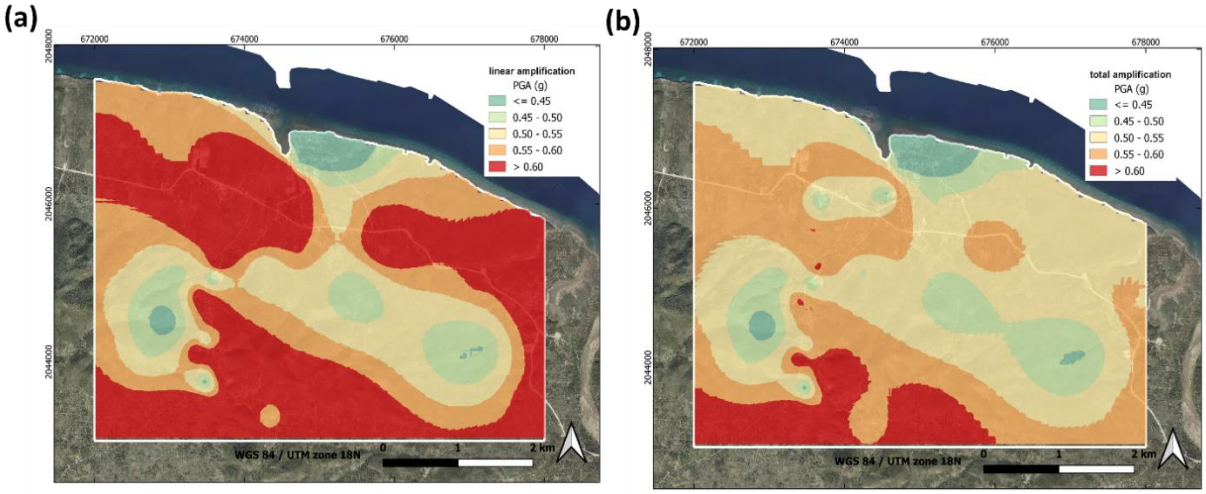

Fig. 5.19 PGA distribution maps (after Dorival et al. 2025) for the area of Anse-à-Veau from the NGA (Boore et al. 2014). **(a)** The PGA with linear site amplification. **(b)** The PGA with total (both linear and nonlinear) site amplification.

5.1.5 Discussion (study area 1)

5.1.5.1 Exploratory data analysis and geological interpretation

The EDA results revealed that raw HVSR parameters exhibit strong non-normality and spatial non-stationarity. The heavy-tailed distributions and strong skewness in f_0 and A_0 reflect the mixed sampling of very soft alluvium and stiffer marly limestones. High f_0 values correspond to shallow limestone outcrops, while low f_0 in the alluvial deposits relate to thick unconsolidated sediments.

The spatial gradients in f_0 and A_0, and their opposite trends (increasing f_0 and decreasing A_0 with distance from the river), provide evidence of large-scale geological controls, specifically sediment thinning toward the limestone plateau. The normal-score transformation successfully restored approximate normality and weak stationarity, in line with geostatistical recommendations for non-Gaussian geophysical data, enabling variogram modelling and kriging.

5.1.5.2 Variogram structure and geological controls

The fitted variogram models closely reflect the geological structure of the basin. The exponential models for f_0 and A_0, and anisotropy along N100-110, indicate rapid lateral changes and direction-

dependent continuity. The small to moderate nugget values represents measurement variability and local-scale heterogeneity.

For the V_{S30}, the spherical model with near-zero nugget and anisotropy along N130-140 reflects the smooth behaviour of MASW derived S-wave velocity and the coherent lithological deposits in the study area. The variogram analysis captured both measurement characteristics and geological structure, an essential prerequisite for reliable kriging.

5.1.5.3 Kriging, cokriging and spatial prediction

The kriged f_0 values delineate the sedimentary basin with low frequencies in the alluvial plain (*La Basse Ville*) and high frequencies over the limestone formations. This spatial pattern is consistent with classical 1D resonance theory. The standard error map shows increased uncertainty along geological boundaries and in areas with sparse sampling.

The A_0 displays smoother spatial variability and lower kriging variance, consistent with its longer variogram range. The presence of high amplitudes over soft alluvium confirms strong impedance contrasts, while low amplitudes over limestone indicate limited site effects. This agrees with established relationships between A_0 and V_{S30} impedance contrasts.

The V_{S30} results distinguish alluvial sediment (<250 m/s), marly limestones transitions (300-450 m/s), and limestone bedrock (>600 m/s). The cokriging approach proved especially useful in areas with sparse MASW data, enhancing spatial coherence without artificial smoothing.

5.1.5.4 Local ground motion assessment

Integrating the geostatistical V_{S30} model with the Boore et al. (2014) NGA relations provided a detailed assessment of the local ground motion:

- Under linear site amplification, PGA increases monotonically with decreasing V_{S30},
- Under nonlinear amplification, PGA decreases below V_{S30}=360 m/s due to soil softening at strong shaking levels.

The results demonstrate how combining HVSR, MASW, and advanced geostatistics with modern attenuation relations produces realistic, spatially resolved and physically interpretable local ground motion maps.

5.2 Study area 2: Cap-Haitien

5.2.1 Exploratory data analysis (Cap-Haitien)

The descriptive statistics and histograms of the fundamental frequency f_0 (Fig. 5.20a) indicate that the dataset strongly departs from a Gaussian distribution. The frequency values span a wide interval, from about 0.60 Hz up to nearly 16 Hz, with a long and pronounced tail toward higher frequencies. This behaviour is reflected quantitatively by the marked positive skewness (1.55) and elevated kurtosis (1.76). These metrics show that a relatively small group of sites with very high resonance peaks dominates the upper end of the distribution. The Q-Q plot (Fig. 5.20b) further confirms that f_0 is strongly non-Gaussian, with substantial departures from the normal line (in red) at both distribution extremes.

The amplitude A_0 displays a more moderate but still important asymmetry. Its histogram (Fig. 5.21a) shows values ranging from 1.7 to 11, with a recognizable tail toward large amplifications. The positive skewness (0.71) highlights the influence of soft sedimentary environments (marsh deposits, recent alluvium, and abandoned meanders in the study area) where amplification is naturally stronger. The Q-Q plot (Fig. 5.21b) shows systematic deviations from normality, particularly in the upper tail, confirming that A_0 is also unsuitable for Gaussian based geostatistical methods in its raw form.

The V_{S30} distribution is significantly less Gaussian than that HVSR cases. The histogram (Fig. 5.22a) reveals a strongly right-skewed distribution, with values concentrated between 150 and 300 m/s, despite the presence of a long upper tail extending to 716 m/s. The skewness (1.38) and positive kurtosis (0.99) confirm this imbalance. The Q-Q plot (Fig. 5.22b) shows pronounced deviations from the normal line not only in the upper and lower tails but also across the central quantiles, indicating that the V_{S30} is far from normally distributed. This behaviour reflects the geological organization of the study area: extensive soft alluvial cover in the plain contrasts sharply with stiff volcanic and limestone outcrops on the slopes of *Morne du Cap*, producing a clear separation between low-velocity and high-velocity.

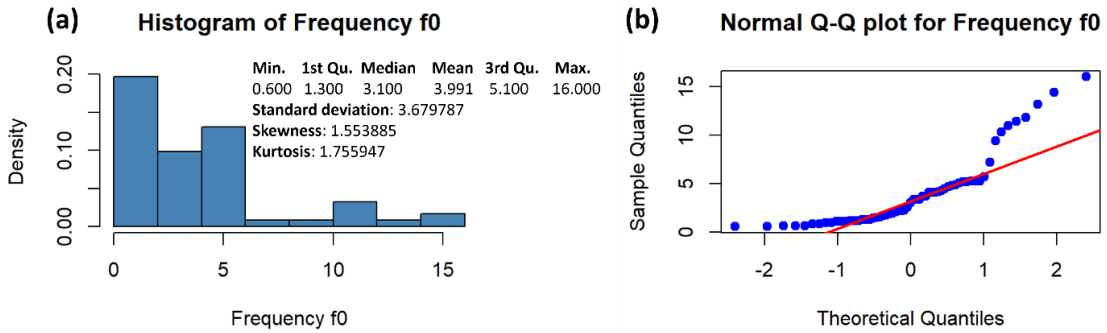

Fig. 5.20 **(a)** Histogram and descriptive statistics of the fundamental resonance frequency (f_0) from the HVSR data in Cap-Haitien. **(b)** Normal Q-Qplot of f_0. The sample points (in blue) are not aligned with the normal line (in red).

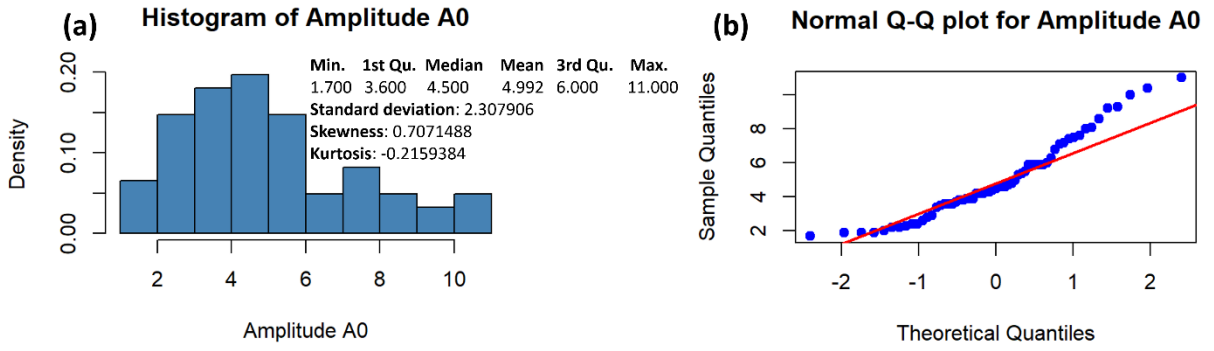

Fig. 5.21 (a) Histogram and descriptive statistics of the amplitude (A_0) from the HVSR data in Cap-Haitien. **(b)** Normal Q-Qplot of A_0. The sample points (in blue) are not aligned with the normal line (in red).

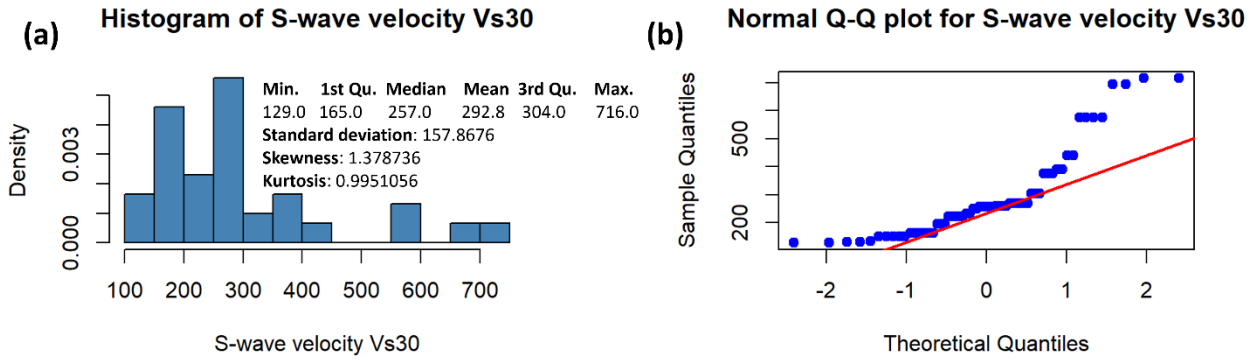

Fig. 5.22 (a) Histogram and descriptive statistics of the S-wave velocities (V_{S30}) derived from the MASW profiles in Cap-Haitien. **(b)** Normal Q-Qplot of V_{S30}.

Like in the previous case, the three parameters (f_0, A_0 and V_{S30}) were transformed using a monotonic normalizing transformation. The transformed histograms (provided in Appendix B3) demonstrate a substantial improvement in symmetry and variance homogeneity for all variables.

The transformation of the fundamental frequency f_0 produces a clear enhancement in statistical behaviour. The transformed values now range from -2.13 to 2.40, with a mean very close to zero (0.002) and a standard deviation of approximately 0.99. The skewness (0.035) is nearly zero, indicating an almost perfectly symmetric distribution, while the kurtosis (-0.40) suggests only a slight flattening relative to a Gaussian curve. The Q-Q plot confirms this improvement, with most points falling closely along the normal line. Small departures remain in the upper tail, which is typical of variables influenced by strong geological contrasts between sedimentary basins and shallow bedrock conditions.

The transformation of A_0 is also successful. Among the three variables, the V_{S30} exhibits the strongest improvement following the normal transformation. The raw distribution was heavily skewed, but the transformed histogram (Appendix B3) becomes well centred and symmetric. The spatial distribution (also provided in Appendix B3) illustrate how the three variables reflect the geological structure of the study area. These spatial patterns reveal that the dataset contains important large-scale geological trends, implying that the stationarity assumption (constant mean) is violated. As a result, subsequent geostatistical modelling requires methods adapted to non-stationary contexts such as universal kriging.

5.2.2 Variogram modelling (Cap-Haitien)

The variogram analysis is presented for the fundamental resonance frequency f_0 (Fig. 5.23). The other are provided in Appendix B3. Like in the case of Anse-à-Veau, the methodology follows the standard geostatistical workflow: construction of experimental variograms, assessment of anisotropy, model fitting, parameter estimation and geological interpretation.

The resulting experimental variograms display the expected features for heterogeneous geological environments: a rapid rise in variance at short lags, corresponding to local heterogeneity; a more gradual increase at intermediate lags, reflecting broader geological structures; and stabilization around a sill at longer distances. These patterns confirm that, after detrending, the variables exhibit enough stationarity for variogram modelling.

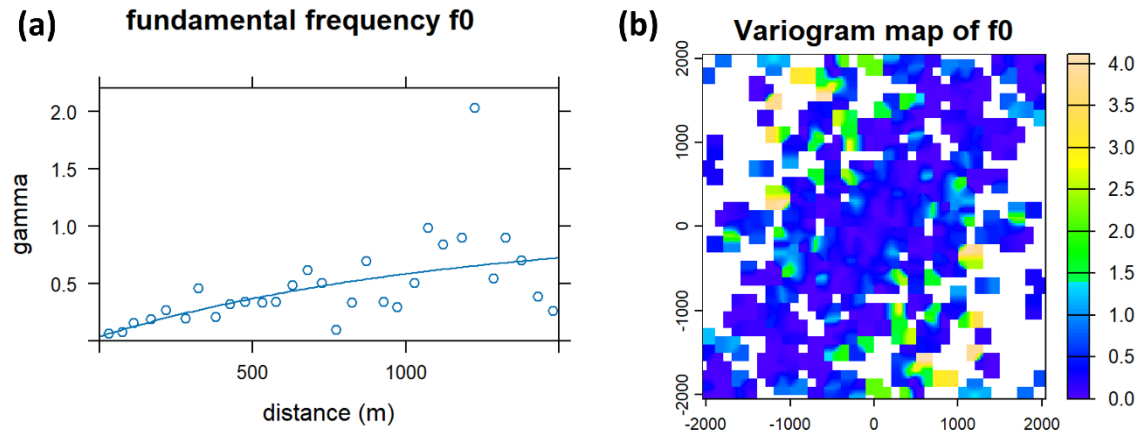

Fig. 5.23 (a) Variogram model and **(b)** variogram map of the fundamental resonance frequency (f_0) from the HVSR data in Cap-Haitien.

The fundamental frequency f_0 shows a clear anisotropic pattern oriented approximately N45 (Fig. 5.23b) broadly aligned with both the *Morne du Cap* mountain range and the *Riviere du Haut du Cap* (see the geological context in section 2.3.2).

For model selection, the experimental variograms were considered in an omnidirectional sense to identify the general spatial structure.

For the fundamental resonance frequency (f_0), we have:

- Nugget: 0.0411
- Structure: Exponential
- Partial sill: 0.9375
- Range: 1149 m

For the amplitude (A_0):

- Nugget: 0.2014
- Structure: Exponential
- Partial sill: 1.5778
- Range: 889 m

For the S-wave velocities (V_{S30}):

- Nugget: 0.0008
- Structure: Spherical
- Partial sill: 0.6357
- Range: 279.7 m

For the fundamental frequency f_0, the nugget is modest (0.0411), suggesting that acquisition is stable, while fine-scale heterogeneity in sediment thickness or impedance contrasts contributes to small-scale variability. For A_0, the higher nugget (0.2014) reflects both environmental noise and intrinsic small-scale differences in amplification caused by local geometry or anthropogenic effects in the study area. For V_{S30}, the near-zero nugget (0.0008) confirms that MASW derived velocities are smooth and robust, weakly affected by shallow heterogeneities.

The fundamental frequency f_0 exhibits a range of 1149 m, corresponding to the lateral extent of soft sediment compartments within the study area. This indicates that resonance frequency is primarily governed by basin geometry and the distribution of soft Quaternary deposits.

The variogram analysis provides direct insight into the geological controls on seismic site response. The long-range correlation of f_0 corresponds to sediment thickness variations across the alluvial plain. The anisotropy along N45 corresponds to the regional orientation of the *Morne du Cap* and the river direction, highlighting the influence of topography and depositional trends on the resonance frequency and the S-wave velocity.

5.2.3 Site characterisation maps (Cap-Haitien)

The site characterisation maps were generated from the spatial interpolation of the fundamental resonance frequency f_0 and the S-wave velocity V_{S30}. The spatial continuity of these variables was modelled using universal kriging for f_0 and cokriging for V_{S30}, taking advantage of the correlation between H/V and MASW datasets. The regression kriging is also tested to validate the cokriging between the MASW and HVSR data. The RMSE provided by the cross-validation for the regression kriging and the cokriging are respectively 0.2892 and 0.2784.

The kriged map of the fundamental frequency f_0 (Fig. 5.24) reveals a spatial pattern controlled by the sediment thickness and the lithology of the Quaternary deposits. Low frequencies (<2 Hz) dominate the alluvial plain, particularly near the river and the marshy zones where thick, unconsolidated sediments accumulate. These low frequencies reflect resonance conditions characteristic of deep sedimentary layers. High frequencies (>5 Hz) appear along the slopes of *Morne du Cap*, where the shallow, stiff volcanic and carbonate bedrock limits the development of long-period resonance. These areas correspond to andesites, volcanites, and limestone scree. The standard error map (Fig. 5.25) shows low uncertainty in the densely sampled plain and higher uncertainty where the data coverage is more limited and the geological transitions are sharper.

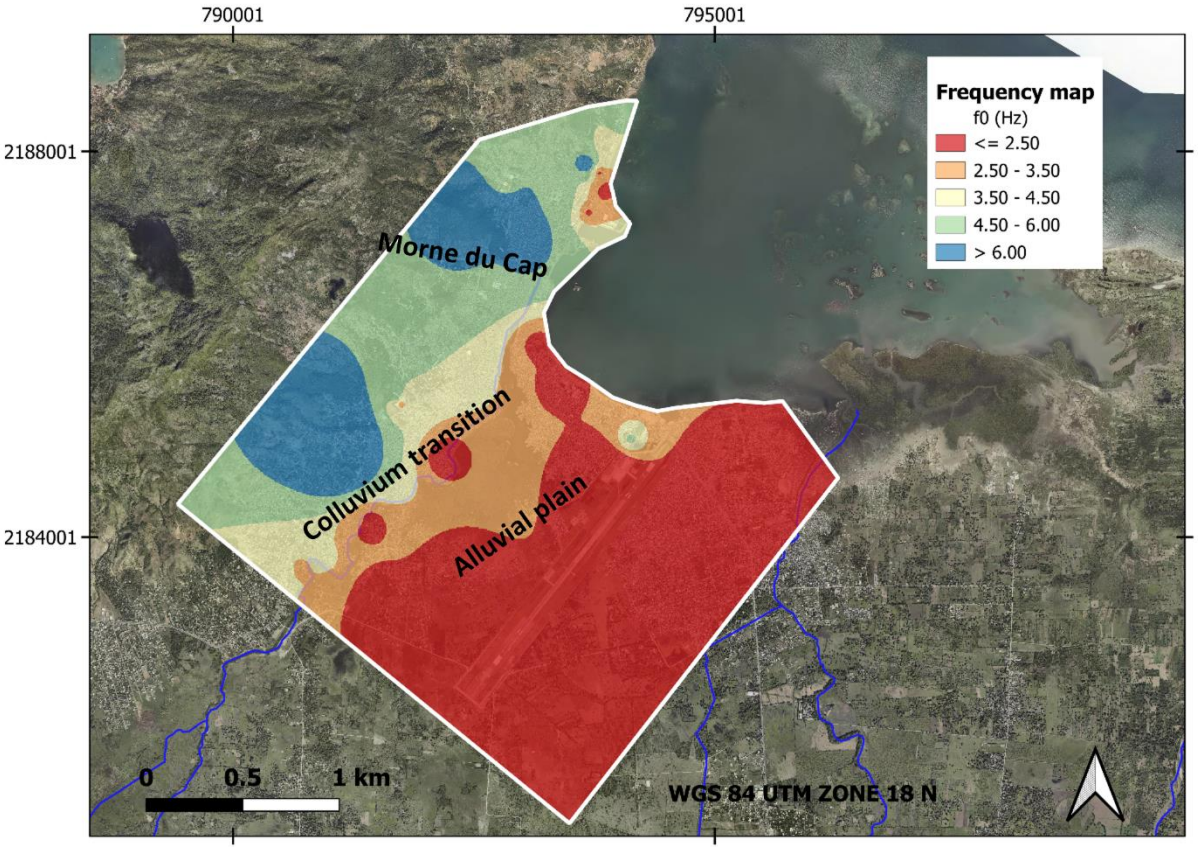

Fig. 5.24 Fundamental frequency map f_0 obtained from universal kriging of the HVSR data in Cap-Haitien.

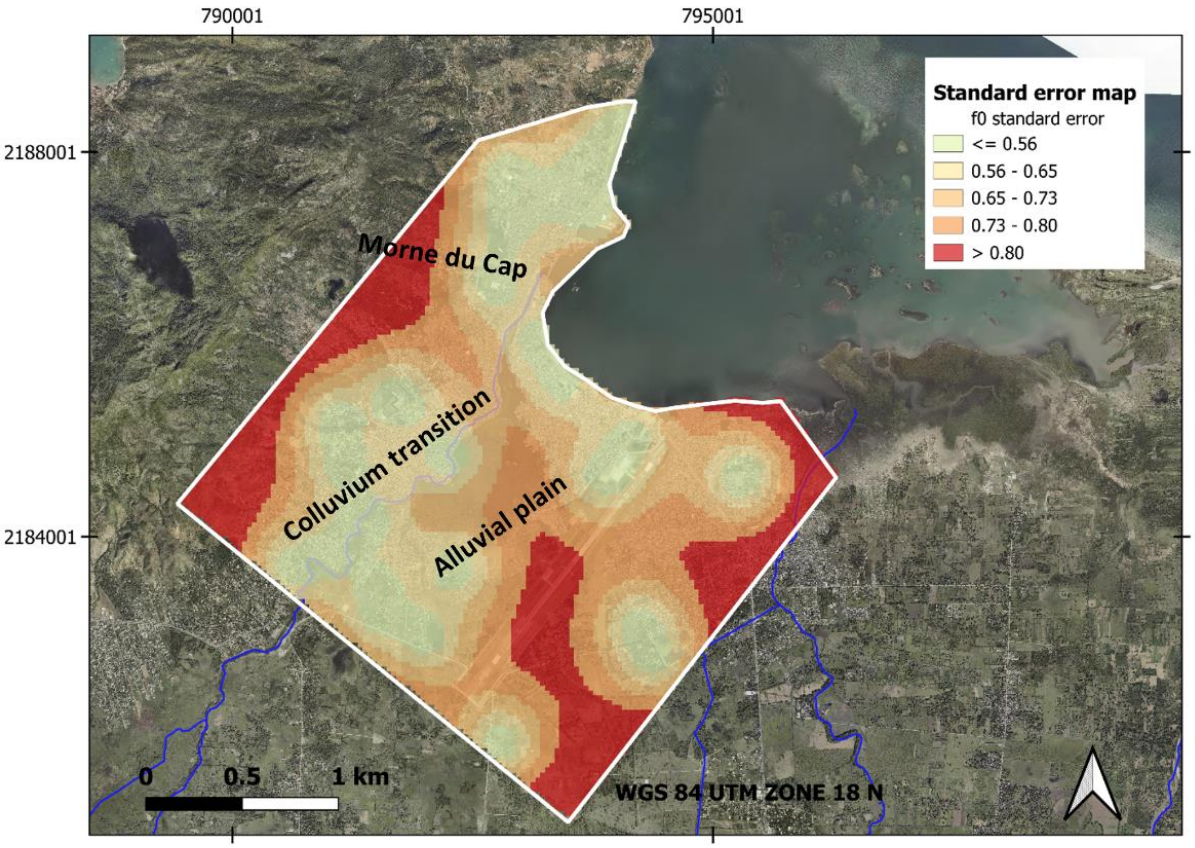

Fig. 5.25 Standard error map f_0 obtained from universal kriging of the HVSR data in Cap-Haitien.

The V_{S30} map derived from cokriging (Fig. 5.26) provides the characteristics of the near-surface stiffness across the geological formations. The high V_{S30} values (>560 m/s) characterise the volcano-sedimentary terrains of *Morne du Cap*, where andesites, volcanites, karstified limestones, and granitoids dominate. These units exhibit high shear-wave velocities due to their consolidated nature and minimal weathering. The low V_{S30} values (100-250 m/s) occur in the Quaternary alluvial plain, particularly within marshy zones and abandoned channels composed of soft silts, sands, gravels, and organic material. The intermediate V_{S30} values (250-400 m/s) extend across colluvial zones where heterogeneity increases due to mixtures of silts, gravels, and fractured blocks.

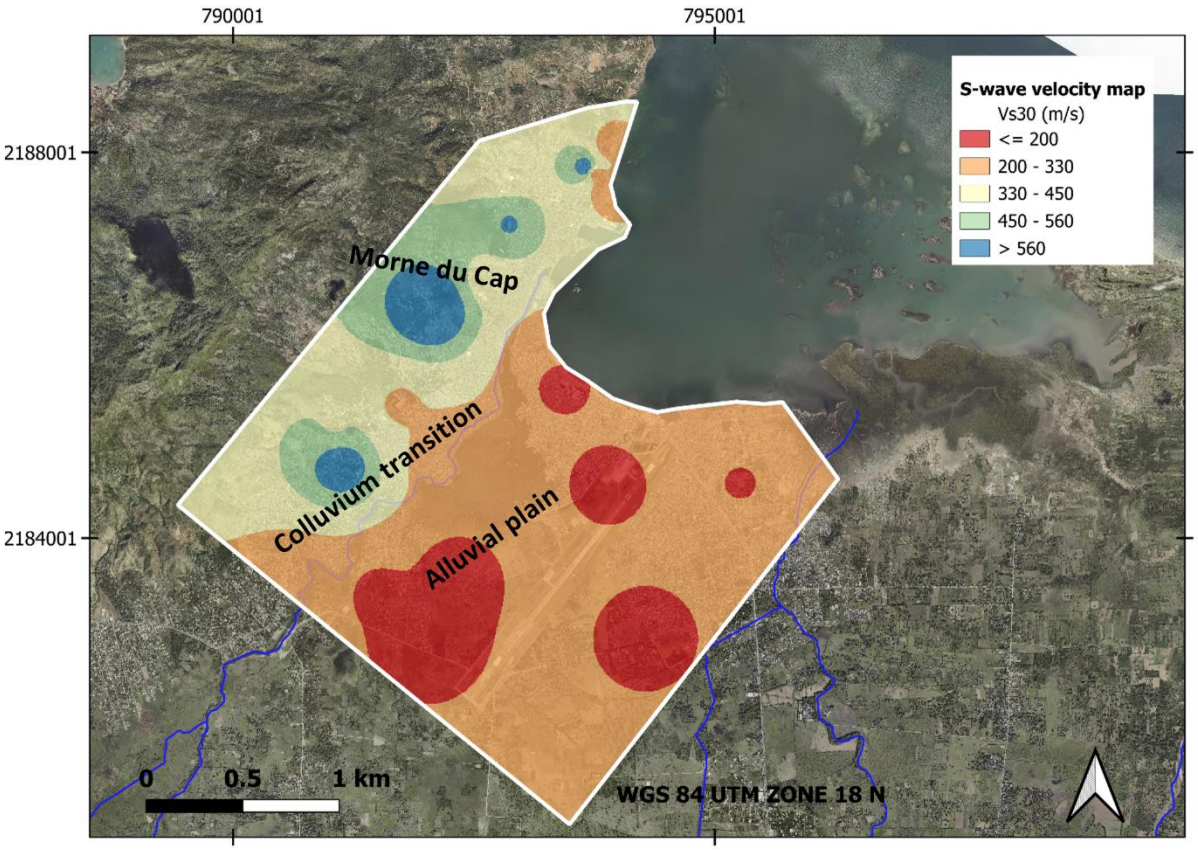

Fig. 5.26 V_{S30} map obtained by applying the cokriging technique between the MASW and the H/V results.

The combined interpretation of the H/V and MASW data reveals zones of potential seismic amplification. High site effect potential occurs over the soft Quaternary alluvium. Moderate amplification occurs in the sediment-bedrock transition zones characterised by the colluvial deposits, where impedance contrasts are still present but less pronounced. Low site effect potential characterizes the stiff volcanic and the limestone formations of *Morne du Cap*.

This integrated analysis provides a clear delineation of areas susceptible to seismic site effects, consistent with the geological framework. The map of site effect index in Fig. 5.27 is constructed following the same methodology used by Ulysse et al. (2021) for the area of Fonds-Parisien, 37 km to the west of Port-au-Prince.

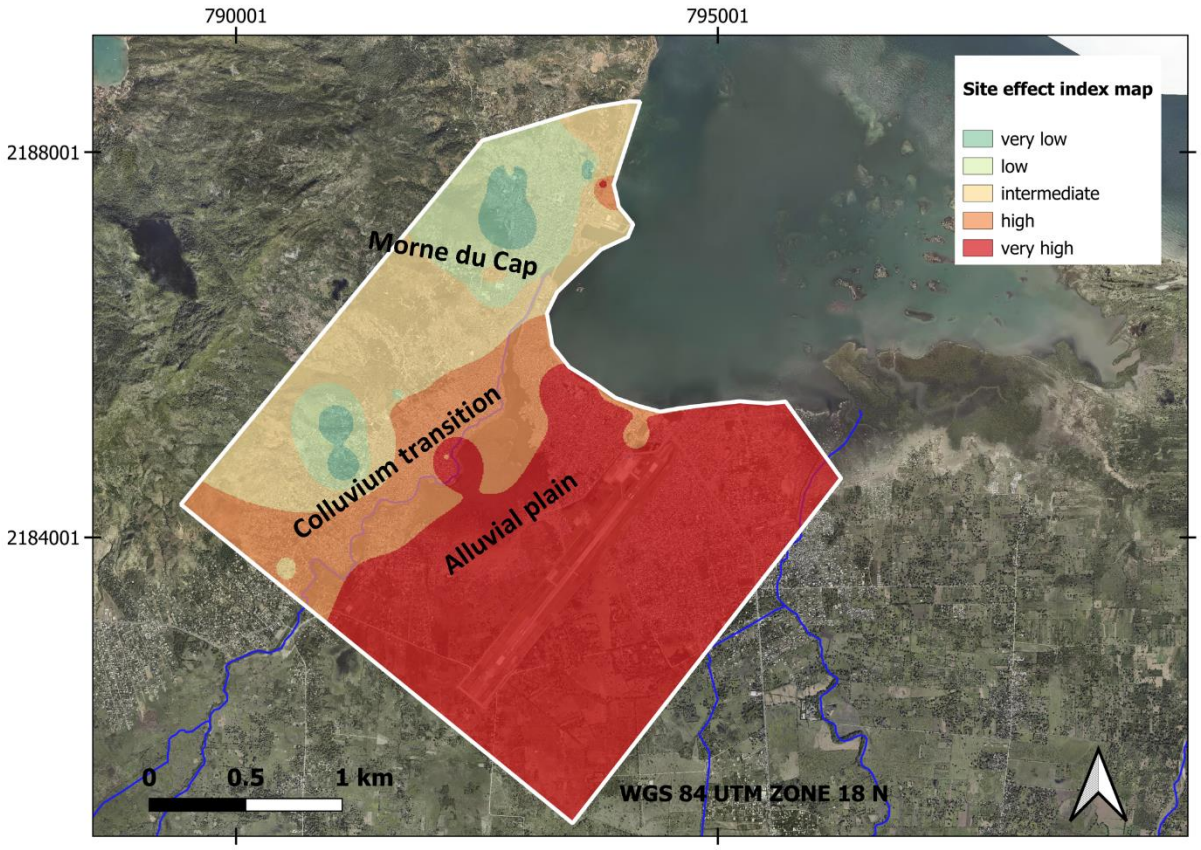

Fig. 5.27 Map of site effect index for the study area of Cap-Haitien.

5.2.4 Discussion (study area 2)

5.2.4.1 Exploratory data analysis and geological interpretation

The exploratory data analysis (EDA) revealed that the raw HVSR parameters (f_0 and A_0) as well as V_{S30} display strong non-normality and evident spatial non-stationarity. Low f_0 values correspond to thick alluvial sediments located in the river areas and the marshy zones, where fine grained silts and sands accumulate. High f_0 values occur over the andesitic-volcanic units and karstified limestone surrounding *Morne du Cap* and its southeastern slope, where shallow bedrock generates short-period resonance.

The V_{S30} displayed extreme deviations from normality in its raw form due to the abrupt contrast between soft alluvium (<250 m/s) and stiff volcanic-limestone terrains (>560 m/s), but its transformed form behaved closely to Gaussian.

5.2.4.2 Variogram structure and geological controls

The experimental variogram of f_0 revealed an anisotropy oriented to N45, matching both the orientation of *Morne du Cap* and the direction of the *Riviere du Haut du Cap*. This directionality suggests that sediment thickness and impedance contrast vary more gradually along the structural ridge and more abruptly perpendicular to it. The fitted model comprises a nugget (0.04) and an

exponential structure with a range 1149 m, indicating rapid changes at short distances (heterogeneous alluvium) combined with smoother large-scale geological control.

The V_{S30} variogram displays an anisotropy also aligned with N45, consistent with the geometry of lithological belts transitioning from the soft alluvium of the plain to the stiff andesites and limestones of *Morne du Cap*. The fitted structure is spherical, with an almost zero nugget (0.0008) and a range of 280 m, which matches the short to medium scale variations in near-surface stiffness and the coherent behaviour of the S-wave velocities in Cap-Haitien.

5.2.4.3 Kriging, cokriging and spatial prediction

The universal kriging results for f_0 and the cokriging results for V_{S30} produced spatially coherent maps that closely match the known geology.

The kriged f_0 map delineates the Quaternary alluvial plain deposits:

- Low frequencies (<2 Hz) occur over the marshy zones and thick alluvial pockets, especially near the river and abandoned meanders,
- Intermediate to high frequencies (3-6 Hz) correspond to the colluvial slopes where the sediment is thinner,
- High frequencies (>6 Hz) are found over the andesitic-volcanic ridge and karstified limestone of *Morne du Cap*.

The V_{S30} map separates the geological units with:

- <250 m/s in the soft alluvial plain deposits,
- 300-450 m/s in the colluvial deposits marking the transition to stiffer rocks,
- >560 m/s in andesites, volcanites, granitic intrusions, and karstified limestones of the southeastern slope.

The cokriging improves prediction in zones with limited MASW coverage by exploiting the correlation with the HVSR parameters. Unlike simple kriging, it enhances spatial coherence without smoothing out true geological contrasts.

The maps in the present chapter were produced on the basis of the kriging and cokriging technique according to a classical geostatistical analysis. The conditional simulation (SGS) will be used in the next chapter to generate the contact surface between the layers in the geomodels.

6 Geomodelling

This chapter presents the geomodelling workflow, results and interpretation applied to the two distinct study areas (Anse-à-Veau and Cap-Haitien). The data were first analysed and standardized using R, ensuring consistent quality control and reproducibility across both study areas. The results from the software R/RStudio were then imported into the software Leapfrog Works (Seequent Ltd. ©), where a series of geological surfaces, volumes, and structural frameworks were constructed. The chapter outlines the modelling strategy, including data conditioning, interpolation choices, and validation steps.

6.1 Study area 1 (Anse-à-Veau)

6.1.1 Data preparation and integration

The foundation of most geomodels in Leapfrog is borehole data, which provide the only direct observations of lithological and structural units at depth. The data must include collar coordinates, downhole orientation measurements, and coded lithological or geotechnical intervals. Where available, continuous geochemical or geophysical logs offer additional quantitative descriptors that enhance the definition of lithological domains. In addition to the borehole information, raster datasets such as surface geological maps and digital elevation models (DEMs) play a central role in guiding the geometry and continuity of geological units, provide spatial context and help define major structural features.

Leapfrog incorporates a variety of GIS derived inputs that support both geological and engineering interpretations. The DEMs are essential for establishing the topographic surface, which forms the upper boundary of all geological volumes. The software applies a radial basis function (RBF) interpolation to generate smooth, geologically consistent boundaries while honouring borehole data and structural trends. The combination of direct observational data, surface mapping and geophysical constraints ensures that the resulting geomodel captures both local detail and regional geological structure.

The surveys carried out in Anse-à-Veau did not include any geotechnical investigations (it was not possible to reach the study area with geotechnical equipment in the frame of the thesis). Therefore, to produce the input data, the H/V measurements and MASW profiles were incorporated into the software Leapfrog by representing each site as a pseudo-borehole whose depth corresponds to the thickness of the surficial sedimentary layer. These depths were derived following a two-step procedure that exploits the spatial correlation between the two datasets (HVSR and MASW). Because the number of H/V measurement sites (providing fundamental frequency, f_0) exceeded the number of MASW profiles (providing S-wave velocity, V_S), the cokriging approach was adopted to allow the estimation of V_S at locations where only f_0 measurements were available. Once the V_S values were estimated at the H/V locations, the sediment thickness h, for the sites where the H/V curves are not flat, was calculated using the classical relationship $h = Vs/(4 \times f_0)$,

which links the fundamental resonance frequency of the soil column to its S-wave velocity and thickness (see Section 3.1.1). In Fig. 6.1, we present a couple of data (H/V and MASW) for a site in *La Basse Ville* where the H/V curve is characterised by a pronounced peak.

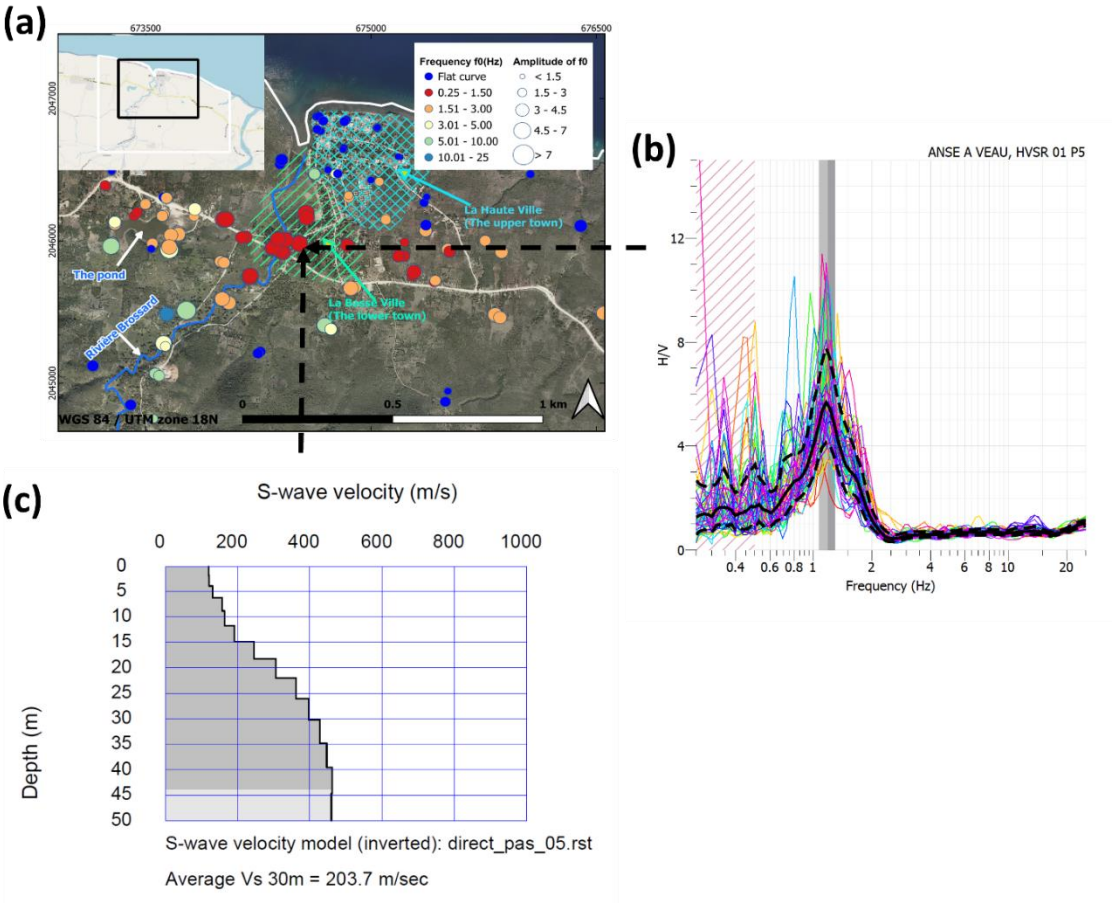

Fig. 6.1 Example of a couple of data (H/V and MASW) for a site in *La Basse Ville* where the H/V curve is characterised by a pronounced peak.

To integrate these results into the geomodel, the depth *h* was subsequently interpolated over a fine spatial grid using conditional geostatistical simulations carried out in the R/RStudio environment. The simulations were conditional in the sense that they honoured all available datasets used as constraints, including the original H/V and MASW measurements as well as additional geophysical information from SRT and ERT profiles. The methodology for the geostatistical analysis including the Sequential Gaussian Simulation (SGS) was presented in section 3.2.2. The results were interpreted as input borehole data into Leapfrog.

The topographic surface used in the geomodelling workflow was generated from a digital elevation model (DEM) with a spatial resolution of 5 m. This high-resolution DEM provides a detailed representation of the terrain, ensuring adequate precision for subsequent geological and

geophysical interpretations. All elevation data were processed and projected in the WGS 84 UTM Zone 18 coordinate reference system (CRS), which guarantees spatial consistency with the other datasets incorporated in the model. The resulting topographic surface serves as the upper boundary of the geomodel.

6.1.2 Lithological and structural control

The data generated from the SGS in the environment R/RStudio include the lithological intervals and the structural data (for orientation and constraints). The lithological units are defined according to the geological map (chapter 2), and the site characterisation maps (chapter 5). The software extracts contact points automatically at the boundaries between lithological units. These contact points act as the primary constraints for the implicit model and define where each geological contact is observed in space.

The layers that are characterized by the same lithological-geophysical properties are categorized into the same groups in order to simplify the models. For instance, the layer considered as bedrock beneath the soft sedimentary layers and the area characterized by the flat H/V curves are combined to form the lithological unit: basement. In Fig. 6.2, we show a representation of the near-surface soft layer depth logs (obtained from H/V and MASW data), and the seismic (SRT) and electric (ERT) profiles for the early stage of the models.

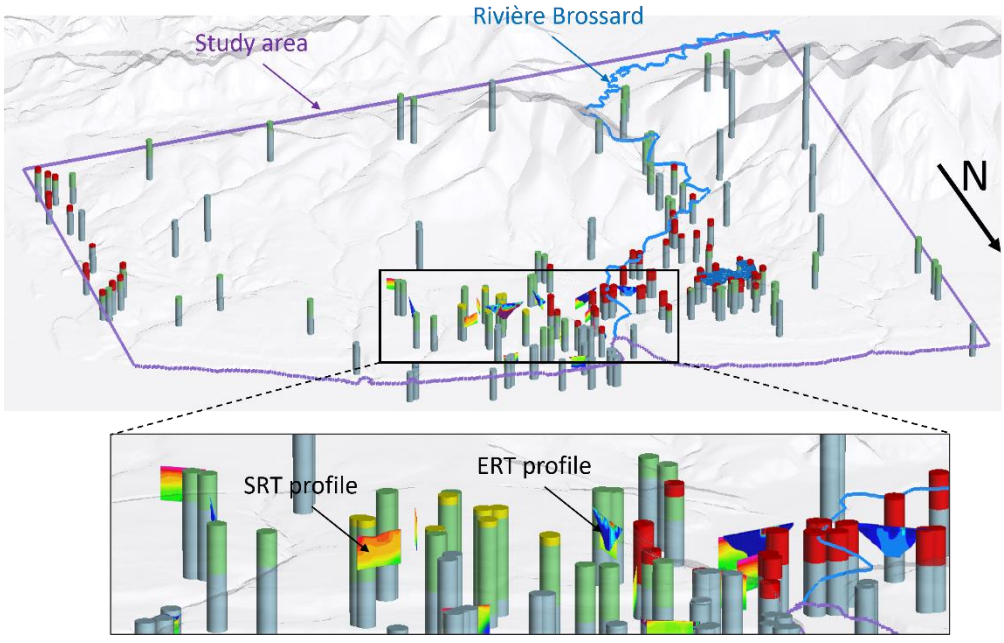

Fig. 6.2 Representation of the depth logs distributed over the Anse-à-Veau area (obtained from H/V and MASW data), and the seismic (SRT) and electric (ERT) profiles in the early stage of the models (view to the South, with Sea shore in frontal part).

The structural data are also defined according to the site characterisation maps (chapter 5) and field observations to influence the orientation of the contact surfaces by defining anisotropies in the implicit function.

6.1.3 Surfaces generation

Once lithological contacts and structural trends are defined, Leapfrog uses an implicit radial basis function (RBF) interpolator to generate the geological surfaces. The software is supposed to calculate an isosurface for each lithological boundary, producing continuous, geologically consistent surfaces across the model domain. However, in the present study, the lithological boundaries (or contact surfaces) are directly controlled by the structural data generated during the SGS in R/RStudio. The depth parameter calculated from the H/V and MASW data (and the completed by the SRT and ERT profiles) was considered as the variable in the conditional simulation. Fig. 6.3 presents an example of structural data in the study area.

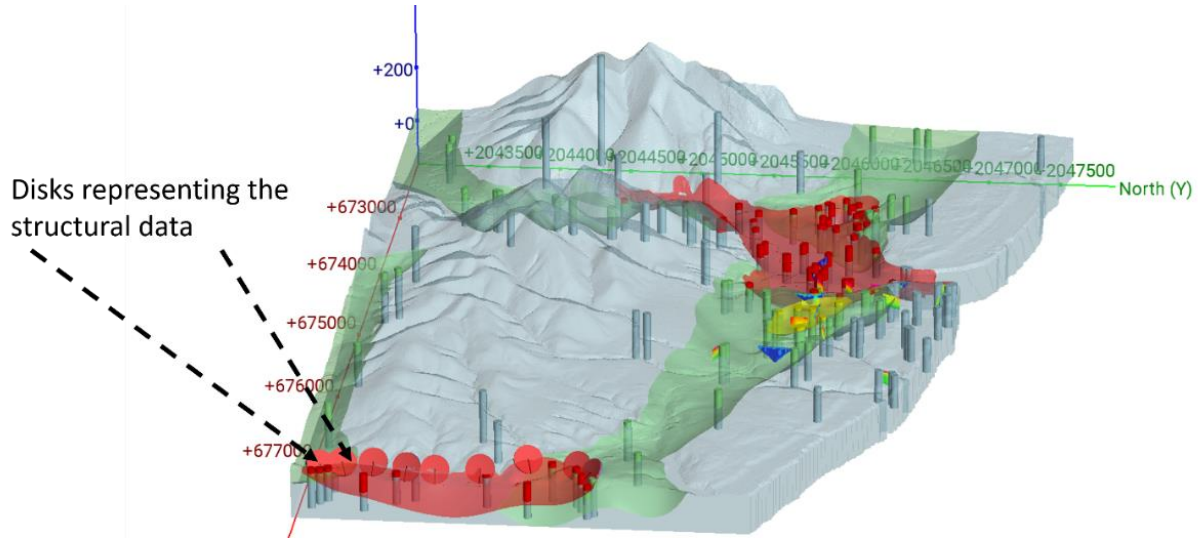

Fig. 6.3 Structural data (represented by the disks) used to constraint the boundary of an alluvial deposit in the eastern part of the study area of Anse-à-Veau (view to the West, with Sea shore in the right part).

When the surfaces honour both lithological and structural constraints, they are finalised and used to build geological volumes. These volumes form the basis for further analysis, such as property modelling.

6.1.4 3D geomodel generation

The 3D geomodel (Fig. 6.4) generated for the study area of Anse-à-Veau results from an integrated interpretation of the geophysical datasets combined with the geomorphological context of the study area. The alluvial deposits are distinguished by well-defined H/V spectral ratios, presenting

a pronounced peak at low frequencies, indicative of high lithological amplification. These formations are further characterized by low S-wave (V_S) and P-wave (V_P) velocities, consistent with unconsolidated sediments. The units classified as marly limestone occur primarily along the transitional zone separating the reef limestone of *La Haute Ville* from the pelagic massive limestone of the mountain, as well as in the southern sector of the study area. These formations display H/V curves with one or two identifiable peaks and intermediate amplification levels. In the southwestern sector, the peak occurs at higher frequencies, reflecting the presence of shallow marly limestones with elevated clay content near the river system.

A smaller unit of lateritic soil is identified within the broader marly limestone domain. This laterite formation exhibits H/V curves with two distinct peaks, capturing the contrast between the residual soil and the underlying marly substrate. The basement encompasses all formations characterized by coherent, high velocity lithologies, including the reef limestone of *La Haute Ville*, the massive pelagic limestone of the mountain, and the competent bedrock underlying the superficial deposits. These units are marked by flat H/V curves lacking significant lithological amplification, reflecting their consolidated and mechanically rigid nature. These interpreted formations provide the structural and stratigraphic framework upon which the geomodel is constructed.

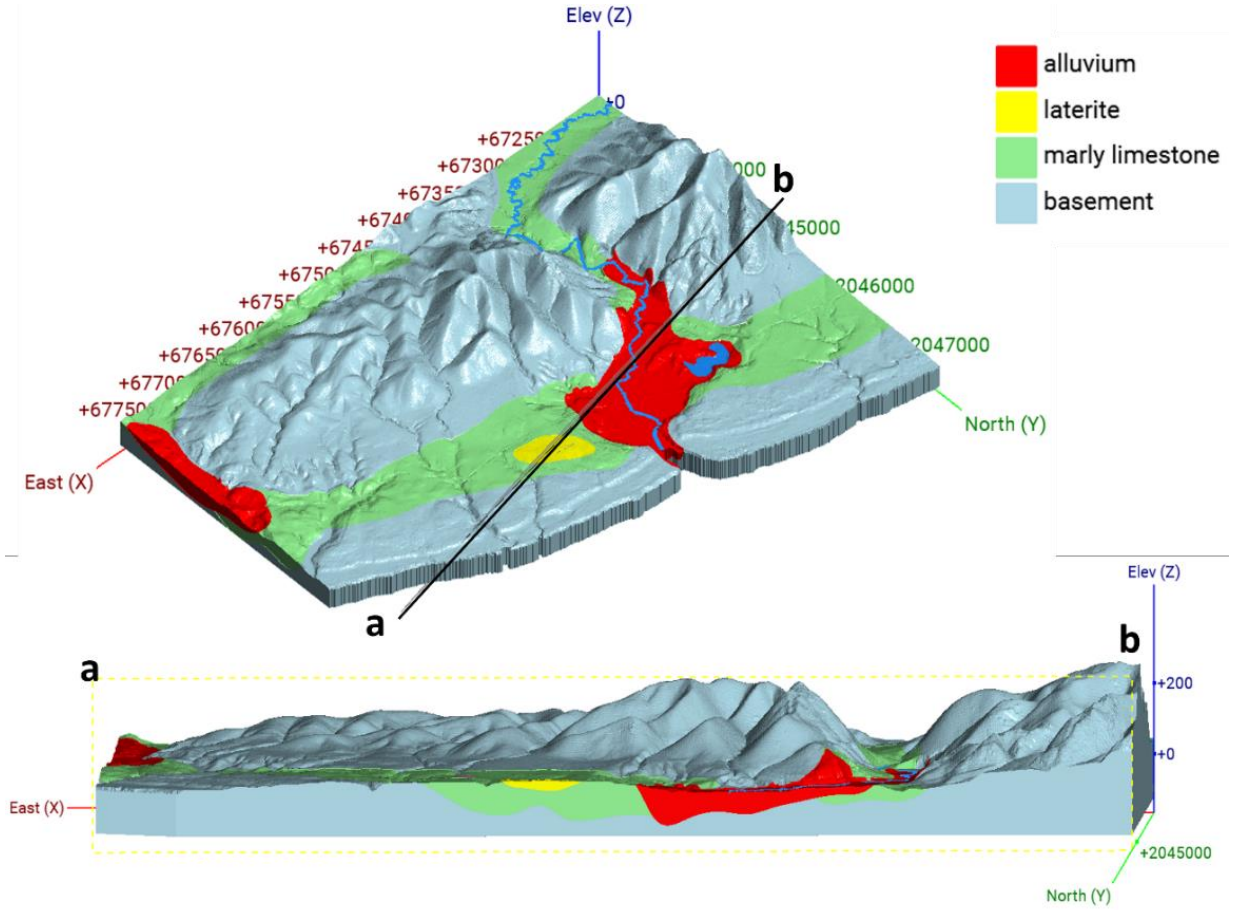

Fig. 6.4 The geomodel and related roughly E-W trending cross-section constructed in Leapfrog Works with input data obtained from geostatistical simulation in the R/RStudio environment (after Dorival et al. 2025). The topography is generated with a DEM of 5 m resolution in the WGS84 UTM Zone 18 CRS.

6.1.5 Discussion (study area 1)

The 3D geomodel provides a coherent representation of the subsurface architecture by integrating geophysical measurements with the geomorphological characteristics of the Anse-à-Veau study area. The model delineates the major lithological formations and highlights the spatial relationships between sedimentary deposits, weathered materials and competent bedrock.

The alluvial deposits are clearly distinguishable in the model due to their characteristic geophysical responses. Their well-defined H/V spectral ratios, with strong peaks at low frequencies, reflect the high impedance contrast typical of unconsolidated sediments overlying more competent bedrock. These observations are corroborated by the low V_S and V_P values obtained in this sector, confirming the presence of soft materials that are prone to significant seismic amplification.

The marly limestone units occupy transitional positions within the geomodel. Their distribution along the contact between the reef limestone of *La Haute Ville* and the pelagic massive limestone of the mountain reflects a complex depositional and erosional history. The intermediate amplification levels and the presence of one or two H/V peaks suggest heterogeneity within this formation, likely linked to variable clay content and differential weathering. This is especially evident in the southwestern part of the study area, where high-frequency peaks indicate shallow marly limestones enriched in clay near the river system. These variations highlight the sensitivity of the H/V method to subtle lithological changes and underscore the importance of integrating multiple geophysical datasets for accurate interpretation.

The lateritic unit, though limited in extent, provides further insight into the near-surface weathering processes affecting the region. The presence of two distinct H/V peaks within this material points to a significant contrast between the residual soil layer and the underlying marly limestone. The correct identification of this laterite layer enhances the resolution of the model in the weathered zone and contributes to a more accurate representation of the shallow subsurface.

The basement formations (reef limestone, pelagic limestone and competent underlying bedrock) form the structural backbone of the geomodel. Their flat H/V curves, indicative of minimal amplification, are consistent with the behaviour of consolidated lithologies. These units provide a critical reference surface for interpreting the thickness and distribution of overlying sediments. Their continuity and spatial extent in the model also validate the structural interpretation of the study area, particularly the distinction between surficial deposits and the mechanically rigid formations of *La Haute Ville* and the mountain.

The integration of geophysical data and geomorphological context in the Anse-à-Veau geomodel demonstrates the effectiveness of combining H/V spectral ratios, seismic velocities, and implicit 3D modelling techniques. The resulting framework captures both the complexity of the subsurface and the geological processes shaping the region, offering valuable insights for geotechnical assessments and seismic hazard analysis.

6.2 Study area 2 (Cap-Haitien)

6.2.1 Data preparation and integration

The surveys carried out in the frame of seismic microzonation of Cap-Haitien include H/V measurements and MASW profiles as well as boreholes drilling completed by small scale geological mapping. Therefore, to produce the input data, the data from the borehole logs were combined with the H/V measurements and MASW profiles. They were then incorporated into the software Leapfrog according to the same procedure explained for study area of Anse-à-Veau.

The topographic surface used was also derived from a 5 m resolution digital elevation model (DEM). This high-resolution dataset captures terrain features in fine detail, providing good accuracy for geological and geophysical analysis. All elevation information was processed and projected in the WGS84 UTM Zone 18 coordinate reference system (CRS) to maintain spatial compatibility with the other datasets used in the model.

6.2.2 Lithological and structural control

The datasets produced through the Sequential Gaussian Simulation (SGS) workflow in R/RStudio consist primarily of lithological intervals, and structural information which provides orientation data and geometric constraints for the modelling process. The definition of lithological units follows the classifications established in the geological maps presented in chapter 2 and the spatial analysis detailed in chapter 5. Based on these inputs, the software automatically extracts contact points at the boundaries between lithological units. These contact points form the principal set of constraints for the implicit geomodelling procedure, as they delineate the precise spatial locations where lithological contacts are observed and thus guide the interpolation of subsurface surfaces.

To enhance model clarity and manage complexity, the lithological units that show similar geological and geophysical characteristics are consolidated into broader categories. For example, the competent bedrock underlying the unconsolidated sedimentary cover, together with regions dominated by volcanic and volcano-sedimentary facies, are grouped into a single lithological unit referred to as the basement. This grouping strategy preserves the essential geological relationships while reducing unnecessary detail, thereby facilitating more efficient model construction and interpretation. Fig. 6.5 shows a representation of the near-surface soft layer depth logs (obtained from borehole, H/V and MASW data) for the early stage of the model.

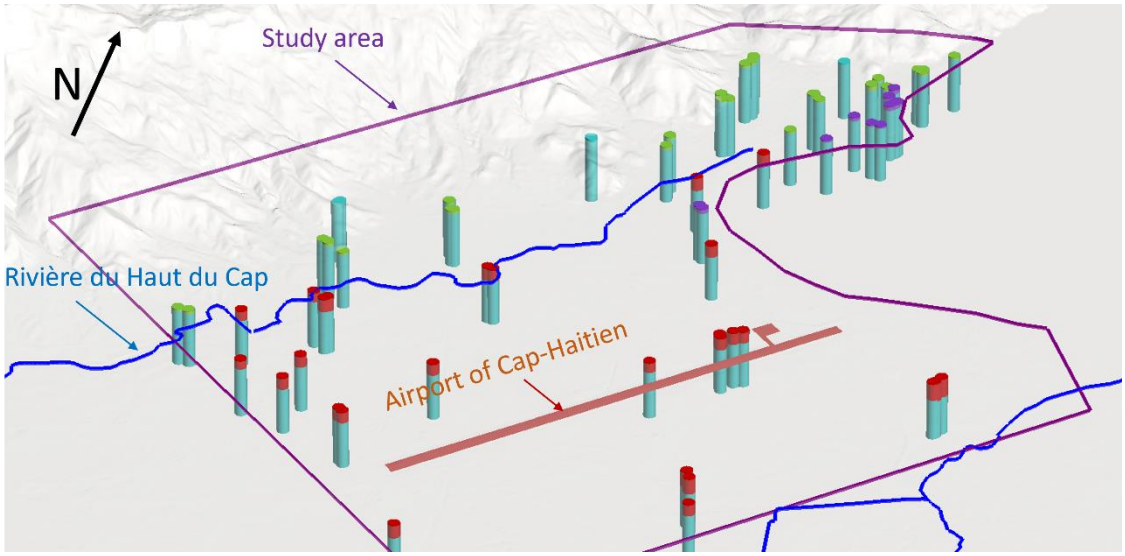

Fig. 6.5 Representation of the depth logs distributed over the study area of Cap-Haitien (obtained from borehole, H/V and MASW data) in the early stage of the model.

6.2.3 Surfaces generation

Like in study area 1, the construction of lithological boundaries (contact surfaces) is driven more explicitly by the structural information generated through the SGS procedure in R/RStudio. The depth parameter, derived from the borehole data combined with the H/V and MASW surveys, is used as the conditioning variable during simulation. This ensures that the interpolated surfaces reflect the subsurface structure inferred from multiple datasets, rather than relying solely on the spatial distribution of contact points.

Once the implicit surfaces appropriately satisfy the imposed lithological and structural constraints, they are validated and accepted as the final geological boundaries. These finalised surfaces are then used to construct 3D geological volumes, which represent the spatial extent of each defined unit within the subsurface.

6.2.4 3D geomodel generation

The 3D geomodel developed for the Cap-Haitien study area (Fig. 6.6) represents the outcome of an integrated interpretation combining geotechnical and geophysical datasets with the geomorphological characteristics of the region. Within this framework, the alluvial deposits in the coastal plain are identifiable through their distinct H/V spectral signatures, which display a pronounced low-frequency peak indicative of strong lithological amplification. These deposits are further characterised by low V_S values, consistent with unconsolidated sediments typical of the alluvial plain deposits.

The colluvial units are mainly located along the transition between the alluvial deposits and the volcanic and volcano-sedimentary formations of *Morne du Cap*. In the central urban area of Cap-Haitien, these colluvial deposits occupy the slope-break zone, reflecting their origin from downslope material accumulation.

The basement unit is formed by all the formations associated with coherent, high velocity lithologies. This includes the competent bedrock underlying the superficial deposits as well as the lithologies forming the southeastern slope of *Morne du Cap*. These units are characterised by flat H/V curves with no significant amplification, indicative of their consolidated nature.

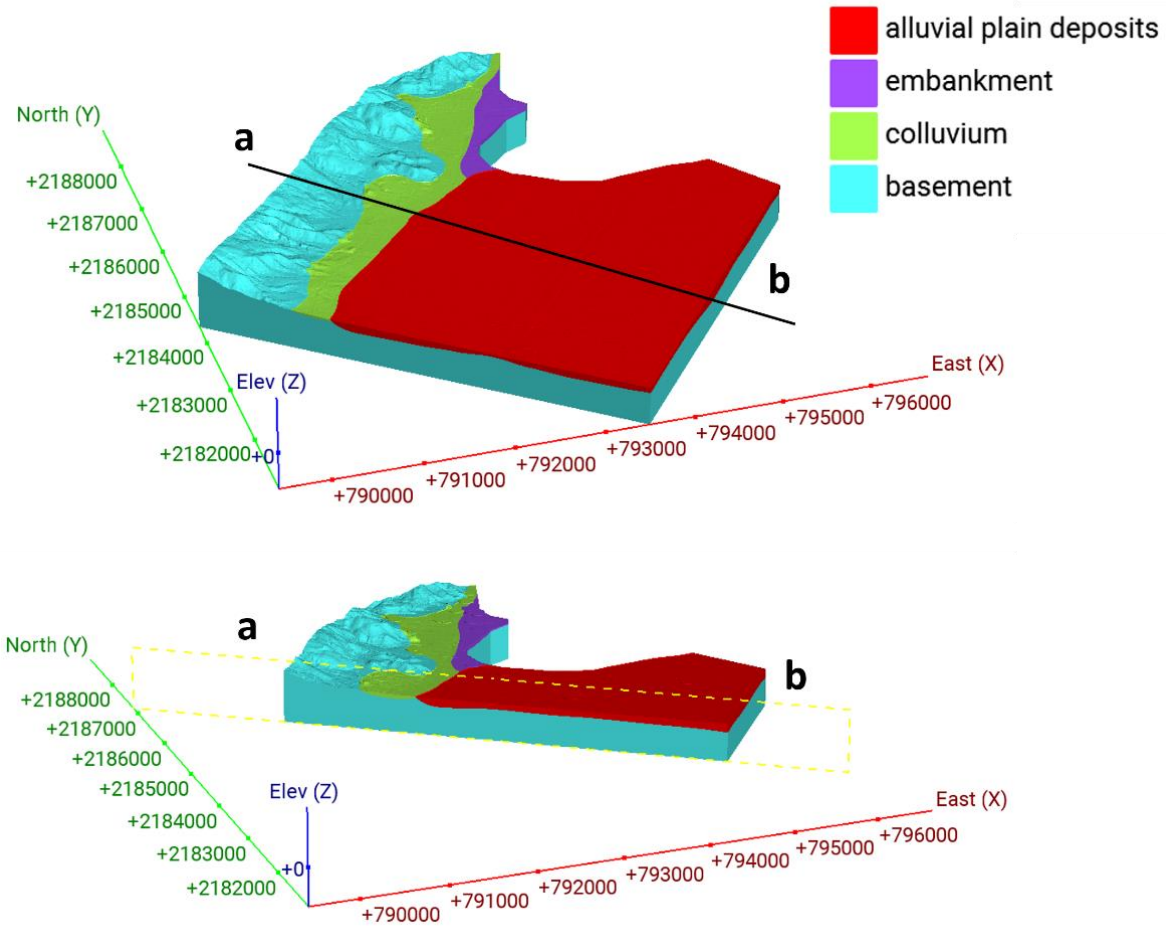

Fig. 6.6 The geomodel of study area 2 (Cap-Haitien) and related NW-SE trending cross-section constructed in Leapfrog Works with input data obtained from geostatistical simulation in the R/RStudio environment. The topography is generated with a DEM of 5 m resolution in the WGS84 UTM Zone 18 CRS.

6.2.5 Discussion (study area 2)

The 3D geomodel constructed for the Cap-Haitien study area (Fig. 6.6) provides a coherent representation of the subsurface architecture by integrating geotechnical and geophysical datasets

with the geomorphological context of the region. Through the application of implicit modelling techniques guided by lithological contacts and structural constraints derived from SGS, the model delineates the major geological units and clarifies the spatial relationships between alluvial deposits, colluvial materials, and basement formations. This structural and stratigraphic framework contributes to a more complete understanding of the subsurface conditions that influence geotechnical behaviour and geohazard susceptibility within Cap-Haitien.

The alluvial deposits in the coastal plain are distinctly expressed within the geomodel. Their identification is supported by the well-defined H/V spectral ratios that show pronounced peaks at low frequencies, reflecting the strong impedance contrast characteristic of unconsolidated sediments overlying rigid bedrock. These observations correspond with low V_S values, confirming the presence of soft, water-saturated sediments across the alluvial plain.

The colluvial units occupy an intermediate position between the alluvial plain and the volcanic and volcano-sedimentary formations of *Morne du Cap*. Their spatial distribution reflects slope processes such as erosion, sediment transfer, and the accumulation of heterogeneous material along the transitional zone at the mountain front. These deposits provide geophysical responses that fall between those of the soft alluvial sediments and the competent basement, indicating varying degrees of consolidation. This variability, combined with their geomorphological setting, suggests that the colluvium represents a zone of increased geotechnical sensitivity, particularly in urbanized areas situated along the slope break.

The basement unit forms the most mechanically rigid component of the geomodel. It encompasses the competent bedrock underlying the superficial deposits as well as the volcanic and volcano-sedimentary formations that define the southeastern slope of *Morne du Cap*. These lithologies are characterized by flat H/V curves that lack significant amplification, consistent with the behaviour of consolidated, high-velocity materials. The basement surface establishes a key reference horizon within the model and governs both the geometry and thickness of the overlying deposits.

The Cap-Haitien geomodel provides a good representation of the subsurface conditions and offers a strong foundation for applications such as seismic hazard assessment, geotechnical evaluation and urban development planning.

7 Dynamic modelling

This chapter presents the development of the 2D dynamic numerical models derived from the 3D geomodels constructed in chapter 6. The geological surfaces and formation boundaries provide the geometric framework from which representative cross-sections are extracted for numerical analysis. The Universal Distinct Element Code (UDEC) is employed to simulate the dynamic behaviour of the subsurface under seismic loading. Material properties, boundary conditions and discontinuity patterns are assigned based on the interpreted formations, ensuring that the models reflect realistic site conditions. The resulting simulations allow assessment of amplification effects, deformation mechanisms and the influence of geological heterogeneity on dynamic response. The background theory and the methodology was presented in section 3.2.3.

7.1 Study area 1 (Anse-à-Veau)

7.1.1 2D models geometry and properties

The location of the three profiles (2D cross sections) used for the 2D dynamic modelling within the study area of Anse-à-Veau is shown on the 3D geomodel in Fig. 7.1. These three 2D models (Fig. 7.2) provide a detailed representation of the subsurface geometry and the spatial distribution of the four lithological units within the study area. The profile A-A', oriented approximately north-south, crosses both the reference and target seismic stations, allowing a direct comparison of the subsurface structure beneath each site.

The profile B-B', oriented east-west, intersects all four lithological units represented in the 3D geomodel. These include the alluvial deposits, the marly limestone units, the localized lateritic soil formation, and the underlying basement. The profile C-C', also oriented east-west, crosses the southern part of the study area, where marly limestone dominates the shallow subsurface, with a small part of alluvial materials at the end the profile. The 2D models have been made deformable according to the expression $\Delta l \leq \lambda/10$ (Δl is the size of the finite-difference (FD) spatial element; λ is the wavelength associated with the highest frequency component of the input wave, see section 3.2.3). This relationship ensures accurate wave propagation through the medium.

Across all three sections, the dynamic material properties were established using geophysical parameters (P-wave velocity V_P and S-wave velocity V_S) and widely accepted empirical correlations. For each lithological unit, the selected parameters include Poisson's ratio (v), dry density (ρ), bulk modulus (K), and shear modulus (G). These values were chosen to represent the stiffness, deformability, and impedance characteristics of the subsurface materials, all of which strongly influence seismic-wave transmission and amplification. The contrast in these parameters between the soft alluvial deposits, the intermediate marly limestone units, the localized lateritic soils, and the more competent basement formations reflects the variability in their mechanical and dynamic behaviour. A complete overview of the assigned material properties is provided in Table 7.1, where each unit is associated with the corresponding physical and mechanical parameters used

in the modelling. A Rayleigh damping of 2% has been used across all the models (for geological materials, damping commonly falls in the range of 2 to 5% of critical according to the reference manuals, Itasca Consulting Group 2014).

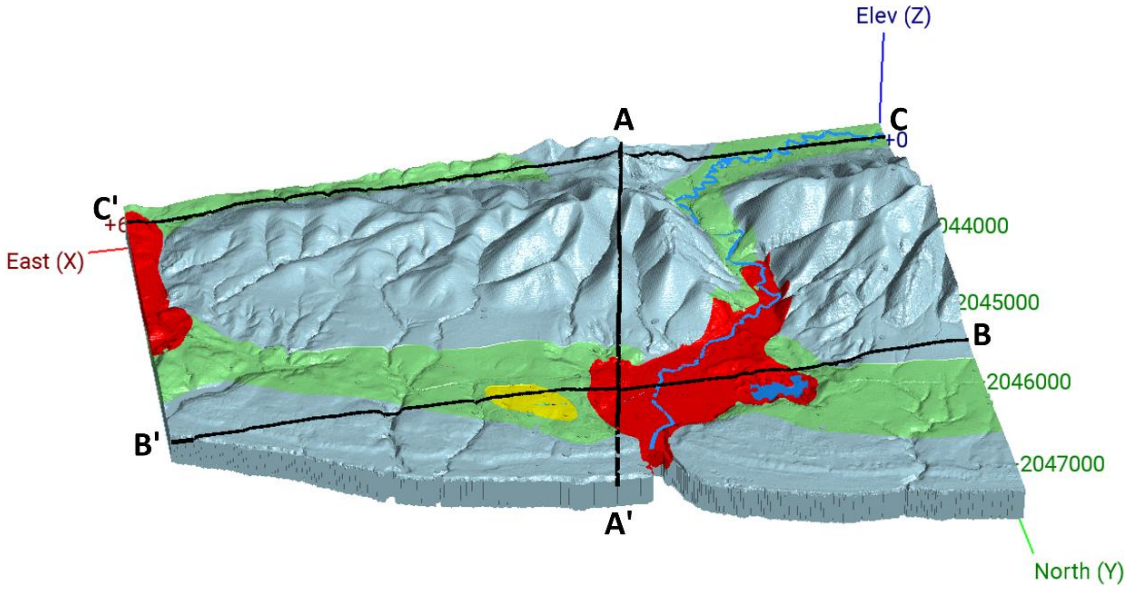

Fig. 7.1 Location of the cross-sections used for 2D dynamic modelling in the study area of Anse-à-Veau.

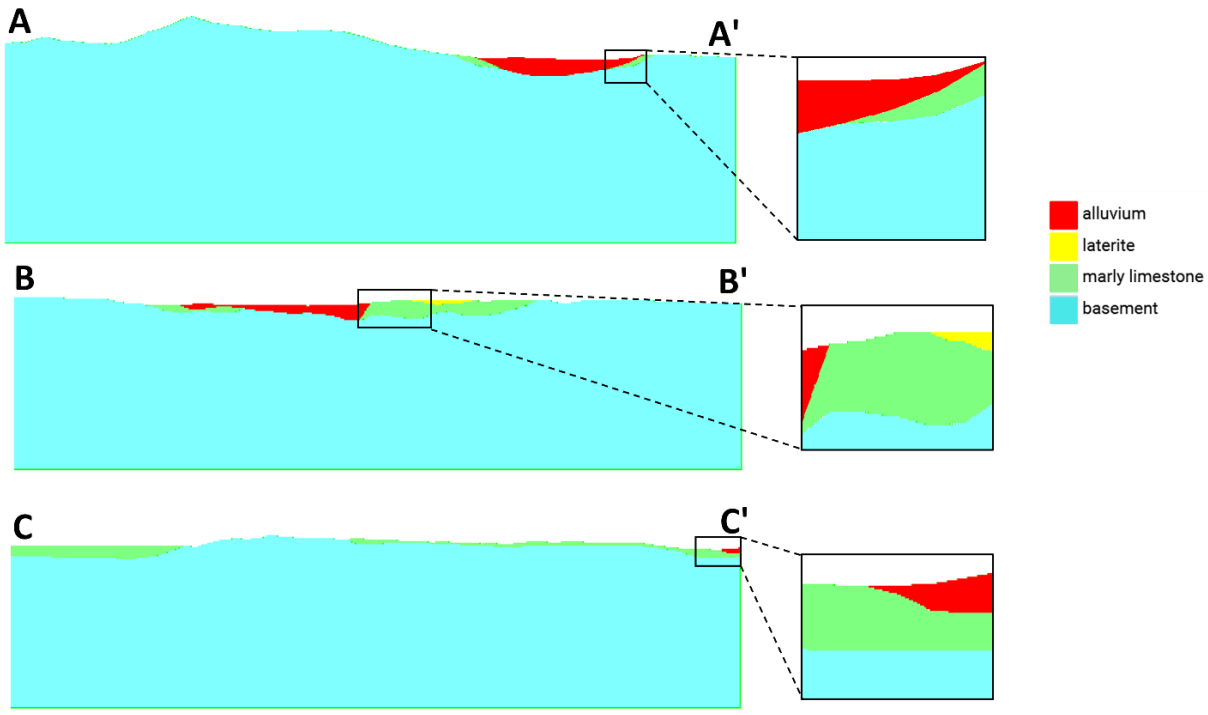

Fig. 7.2 Geometric configuration of the 3 cross-sections (AA', BB' and CC', see Fig. 7.1) used for the 2D dynamic modelling in the study area of Anse-à-Veau.

Table 7.1 Summary of material properties for the different layers across the 2D dynamic models for the study area of Anse-à-Veau. P-wave velocity V_P; S-wave velocity V_S; Poisson's ratio v; dry density ρ; bulk modulus K; shear modulus G.

Lithology	V_P (m/s)	V_S (m/s)	v	ρ (kg/m^3)	K (MPa)	G (MPa)
Alluvium	300	180	0.21	1290	60.3	41.8
Laterite	350	200	0.25	1340	92.7	53.6
Marly limestone	1000	450	0.37	1743	1272.5	353
Basement	3200	1000	0.44	2330	20766.5	2331.5

7.1.2 Static analysis

The static analysis ensures that the models are in a stable equilibrium state, free from artificial velocities or unbalanced forces that could interfere with the dynamic simulation. This step is essential because dynamic results are only meaningful if they originate from a physically realistic and mechanically consistent initial condition.

For every 2D cross-sections (section A-A', B-B' and C-C'), two models have been established: one model characterized by only one uniform layer (the basement layer) across the whole model for pure topographic effect analysis, and another one characterized by all the layers as presented in Fig. 7.2 for combined lithological and topographic effect analysis.

Proper boundary conditions have been applied by fixing the boundary edges. A gravity loading with $g = 10\ m/s^2$ was also introduced at this point to simulate the self-weight of the 2D models.

After defining the initial conditions, UDEC is cycled in a quasi-static manner to allow the system to approach the static equilibrium. During this process, an automatic Rayleigh damping coefficient is used to stabilize the model by dissipating excess vibrational energy. The mechanical cycling proceeds until the system reaches static equilibrium, which is confirmed when the ratio of unbalanced forces to applied forces falls below a specified threshold (10^{-9}, in the present case). The variation of the maximum unbalanced forces over the cycles for the 2D models are provided in Appendix A6.

7.1.3 Dynamic loading

The Ricker wavelet has been used as the dynamic loading in the present study, considering two primary frequencies: 1.4 and 3.5 Hz. This particular wavelet is widely applied in engineering seismology because its spectrum closely matches that of real seismic signals, as highlighted by Gholamy and Kreinovich (2014). The signal is symmetric, smooth, and begins and ends at zero

amplitude. This prevents the introduction of artificial trends, permanent displacements, or numerical instabilities in simulations.

The Ricker wavelet is mathematically convenient. This helps reduce computational effort and ensures that the source behaves consistently across simulations. As formulated by Ricker (1953), the Ricker wavelet can be described by:

$$\boldsymbol{A = (1 - 2\pi^2 f^2 t^2) e^{-\pi^2 f^2 t^2}} \tag{7.1}$$

Where A is the amplitude, $f(Hz)$ indicates the central frequency (1.4 and 3.5 Hz, in the present case), and $t(s)$ represents the dynamic time. The version of the Ricker wavelet employed here is shown in Fig. 7.3.

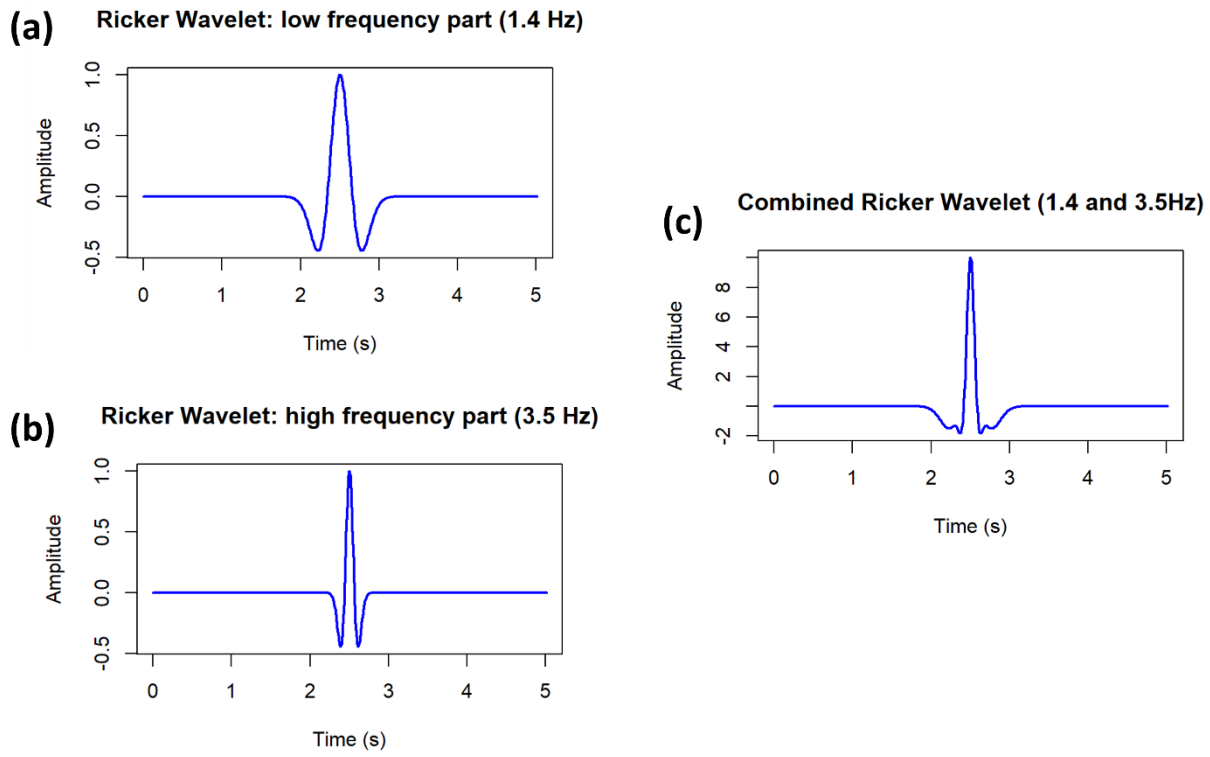

Fig. 7.3 (a) Ricker wavelet at low frequency part. **(b)** Ricker wavelet at high frequency part. **(c)** Combined Ricker wavelet from the sum of two Ricker wavelets at frequency 1.4 and 3.5 Hz.

The wavelet originates at the base of the model and travels upward along the y-axis, passing through the entire 2D model, for every cross-section or profile (A-A', B-B' and C-C'). The amplitude and duration of the dynamic load change according to the characteristics of the signal. The signal duration is predefined, and peak values are scaled using a coefficient to adjust intensity. To ensure all secondary seismic effects are captured, the dynamic simulation and data recording are carried out over a period of 15 s. This extended time frame is particularly important for models

designed to assess the cumulative influence of geological conditions and terrain, as these secondary phenomena can develop gradually.

The wave transmitted from the base of every model is first recorded at about 10 m above the bottom by a synthetic receiver considering as a reference station for the spectral amplification analysis.

7.1.4 SSR analysis at the surface receivers

The SSR analysis were carried out using the software Geopsy (Wathelet et al. 2020). All surface receiver recordings along the x-component are compared with their corresponding reference histories, which are first scaled by a factor of two and subsequently filtered. For each receiver, an artificial three-component dataset is generated. In this dataset, the surface time history is assigned to both horizontal components, while the vertical component is substituted with the corresponding reference recordings.

7.1.4.1 The profile A-A'

The cross-section A-A', roughly trending N-S, allows a detailed assessment of seismic response across the main lithological and geomorphological domains of the study area of Anse-à-Veau. The SSR analysis performed at twelve synthetic receivers placed along the surface of the model provide essential information on the relative influence of topography and near-surface stratigraphy on site amplification. The results are presented in Figs. 7.4, 7.5 and 7.6, which correspond respectively to the southern, central, and northern portions of the profile.

The southern part of the profile is entirely underlain by competent basement rocks composed of massive pelagic limestones. The synthetic receivers RAA.1 to RAA.4 are located in this domain. Fig. 7.4 shows that the SSR curves for both pure topography and combined topography with surface layers are almost identical at every receiver. This results from the absence of superficial sediments in this part of the profile. The spectral ratios remain flat throughout the analysed frequency range, indicating no significant amplification. The high seismic velocities of the basement and its consolidated nature suppress any resonance effects, and the weak topographic gradients in this area do not induce measurable topographic amplification. This response is consistent with the expected behaviour of Cretaceous pelagic limestones and with the flat H/V curves recorded at sites located on the same lithology.

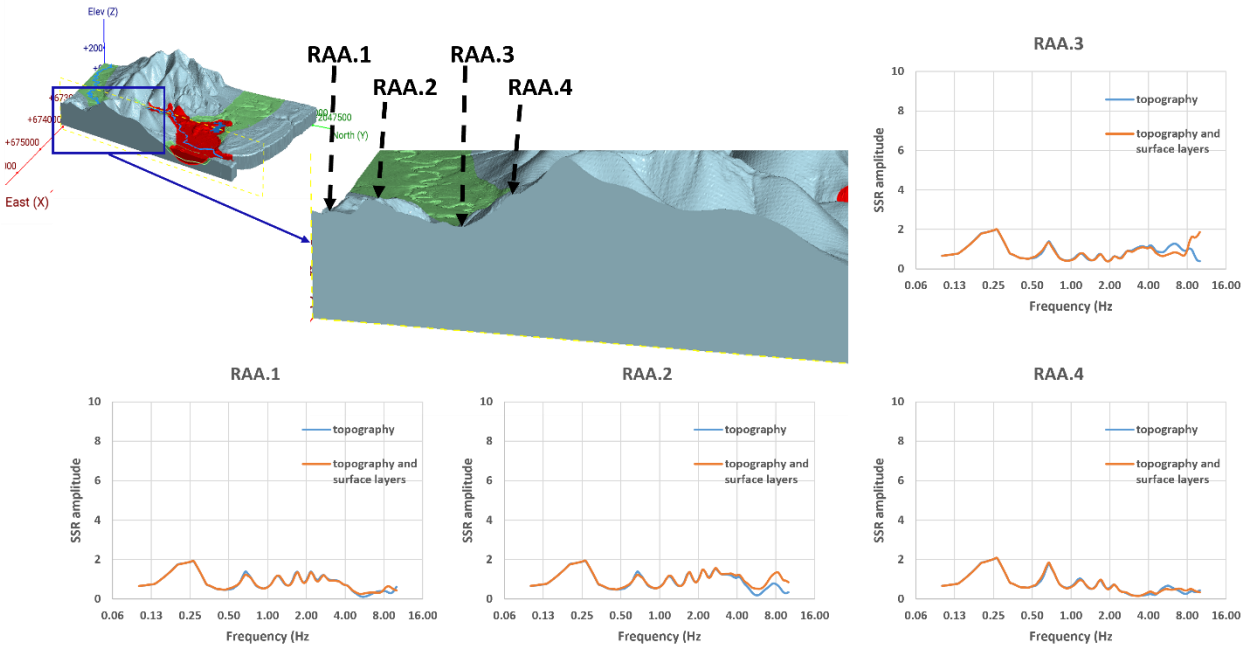

Fig. 7.4 SSR analysis at the synthetic receivers on the surface of the cross-section A-A'. The receivers RAA.1 to RAA.4 are placed in southern part of the profile.

The central portion of the profile crosses the crest of the mountain, the northern slope, the marly limestone unit at the foot of the slope, and the alluvial deposits of *La Basse Ville*. Fig. 7.5 illustrates the evolution of the SSR response as the geological conditions change.

The receivers RAA.5 and RAA.6 are situated on the top and northern flank of the mountain, both underlain by the basement formation. Their SSR curves show no significant amplification, confirming that the mechanical properties of the basement control the site response. Even though the topography becomes steeper at these locations, the dynamic simulations indicate that any potential topographic effect remains negligible at the input frequencies considered.

A clearer amplification appears at RAA.7, located in the marly limestone area near the foot of the mountain. Fig. 7.5 shows a peak of approximately 2.5 at around 4 Hz. This amplification reflects the intermediate mechanical behaviour of the marly limestones, which possess lower stiffness than the underlying basement and therefore allow frequency-dependent resonance. The peak at 4 Hz is consistent with the H/V features observed in the transitional marly units of the geomodel.

At RAA.8, which is positioned above the alluvial deposits of *La Basse Ville*, the SSR curve displays pronounced amplification over a wide frequency range. Fig. 7.5 shows values close to 4 extending from slightly below 1 Hz to above 8 Hz. This broadband amplification reflects the low seismic velocities and strong impedance contrast typical of unconsolidated alluvial materials.

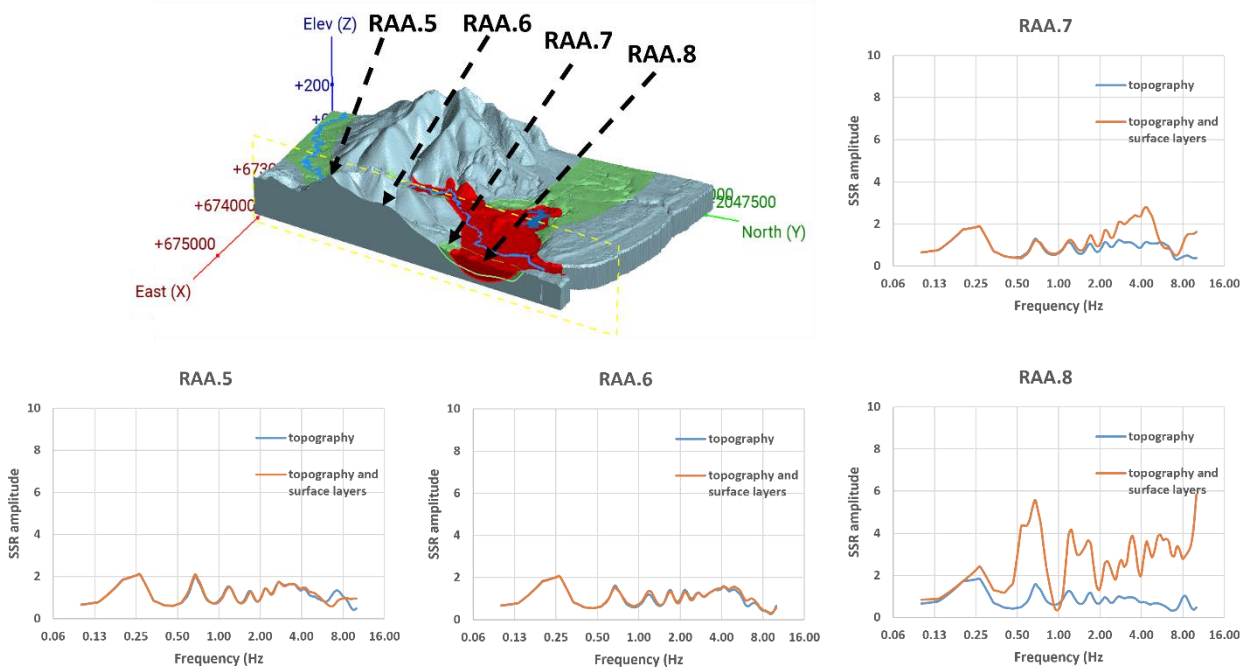

Fig. 7.5 SSR analysis at the synthetic receivers on the surface of the cross-section A-A'. The receivers RAA.5 to RAA.8 are placed in the central portion of the profile.

The northern part of the profile includes the thick alluvial deposits of *La Basse Ville*, the contact zone with the marly limestones, and the reef limestone basement of *La Haute Ville*. Fig. 7.6 presents the corresponding SSR results. This part of the profile also contains the locations of the real seismic stations UR01 S1 (target) and UR02 S2 (reference), which allows a direct comparison between synthetic and observed behaviour.

At RAA.9, placed at the same position as UR01 S1, the synthetic SSR curves reproduce the key amplification patterns observed in the field recordings. Fig. 7.6 shows amplification factors of about 3 to 4 between 1 and 2 Hz, together with values close to 6 between 4 and 6 Hz. These peaks match the resonance characteristics associated with the alluvial deposits in this area and closely correspond to the observed SSR curves of the real target station (see comparison in Fig. 7.7).

At RAA.10, located at the boundary between the alluvial deposits and the limestone units, the SSR curve displays an amplification peak of about 4 just below 8 Hz. Fig. 7.6 indicates that this high-frequency amplification is linked to the impedance contrast that develops at the transition between the soft alluvium and the stiffer limestones. The shallow depth of the marly limestone in this zone can further enhance the resonance of higher-frequency components.

The receivers RAA.11 and RAA.12 are situated on the reef limestone basement of *La Haute Ville*. Their SSR curves remain flat across all frequencies in Fig. 7.6. The absence of amplification reflects the stiff and consolidated nature of the limestone bedrock. This behaviour is consistent with the flat H/V spectral ratios previously identified in the geomodel and with the seismic response observed at the real reference station UR02 S2 (see section 4.1.5).

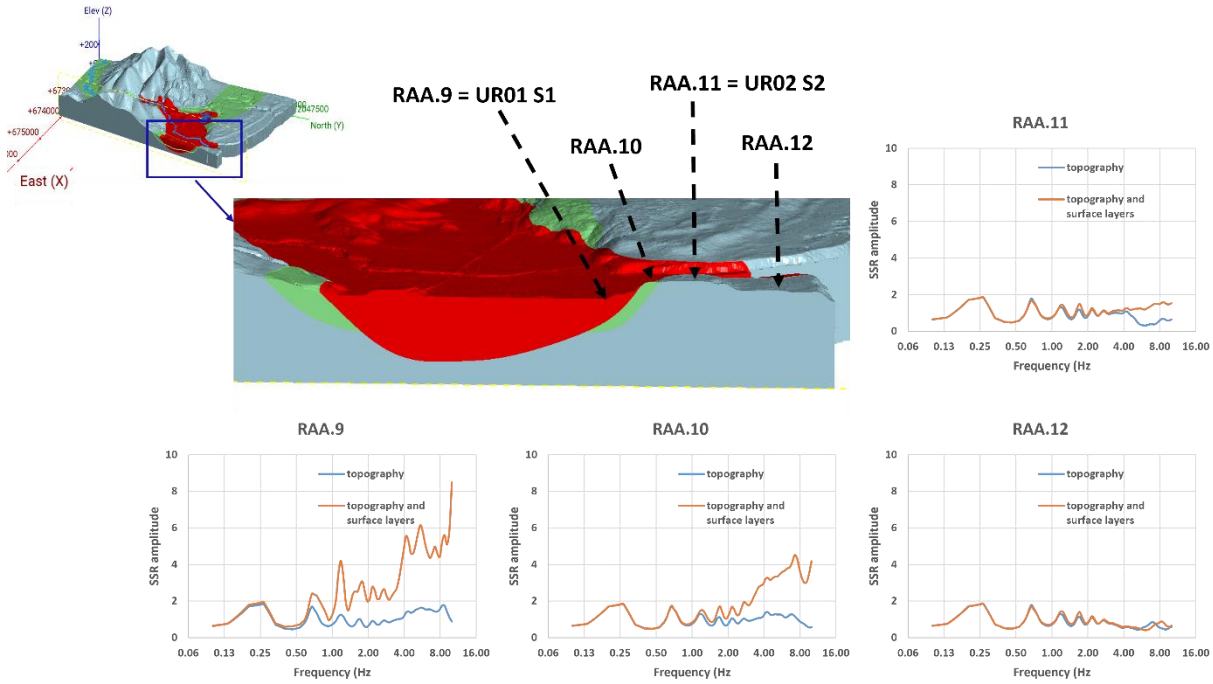

Fig. 7.6 SSR analysis at the synthetic receivers on the surface of the cross-section A-A'. The receivers RAA.9 to RAA.12 are placed at the northern part of the profile.

The comparison between the modelled SSR curve at RAA.9 and the observed SSR curves at the nearest installed station (Fig. 7.7) indicates that the numerical model reproduces the observed site response more consistently for the N-S component than for the E-W component. This preferential agreement with the N-S component can be directly related to the orientation of the profile A-A' (trending approximately in the N-S direction) used for the modelling.

The amplification at the frequencies ~1 Hz and 6 Hz in the modelled SSR correspond closely to the main peaks observed in the N-S component of the measured SSR curves for a selected earthquake (EQ 006, see Fig. 7.7b). The smaller low frequency peak is not observed in UR01 when considering the average SSR curves for multiple earthquakes in the area (see Fig. 7.7c).

The weaker correspondence between the modelled SSR and the observed SSR for the E-W component likely reflects site-response phenomena associated with lateral heterogeneities and basin-edge effects acting perpendicular to the modelled profile. The comparative analysis suggests that the modelled SSR provides a reliable representation of the site response along the N-S direction, which is consistent with the orientation of the modelled profile A-A'.

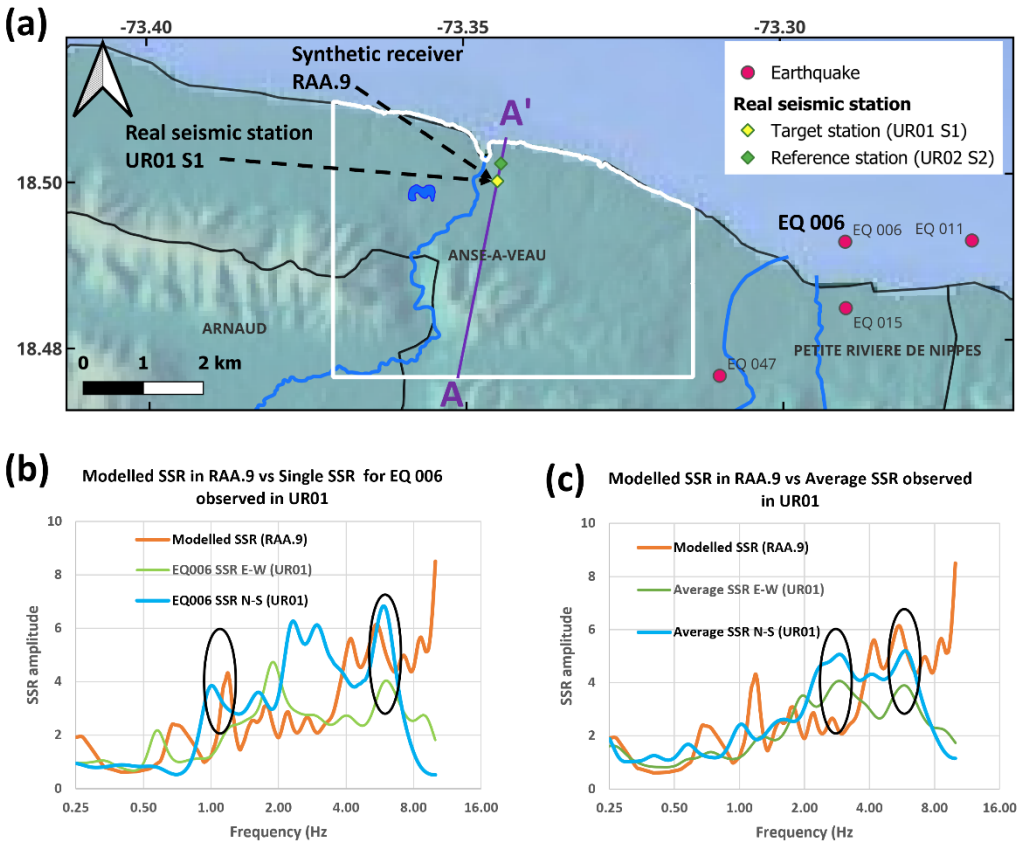

Fig. 7.7 Comparison between the modelled SSR at the synthetic receiver RAA.9 and the observed SSR at the real target seismic station UR01 S1. **(a)** Location of the synthetic and real stations, and the profile A-A' across the study area. **(b)** Modelled SSR at RAA.9 and single SSR for the earthquake EQ 006 recorded by UR01. **(c)** Modelled SSR at RAA.9 and average SSR for selected earthquakes in the region recorded by UR01 (see section 4.1.5 for the earthquakes characteristics).

The results obtained along profile A-A' highlight the strong dependence of seismic amplification on the local lithological and structural context. The basement regions characterised by pelagic and reef limestones do not generate significant amplification, even in areas with moderate topographic slopes. The marly limestone units produce moderate and frequency-specific amplification, particularly around 4 Hz. The alluvial deposits of *La Basse Ville* generate the strongest response, with amplification occurring over a wide frequency range and with peak values that match observations at the real target station. The contact zone between alluvial deposits and marly limestones also produces distinctive high-frequency amplification related to local impedance contrasts.

7.1.4.2 The section B-B'

The east-west cross-section B-B' intersects the basement unit, the marly limestone domain, the localized lateritic soil formation situated between *La Haute Ville* and the mountain range, and both

shallow and thick accumulations of alluvial deposits. Twelve synthetic receivers were positioned at the surface (RBB.1 to RBB.12), and SSR analysis were conducted for each receiver. The results are presented in Figs. 7.8, 7.9, and 7.10.

The western part of the profile begins in the basement unit, where the receivers RBB.1 and RBB.2 are located. As shown in Fig. 7.8, both receivers exhibit flat SSR curves with no meaningful amplification in either modelling configuration. This behaviour is consistent with the consolidated nature of the basement rocks, which provide high seismic velocities and weak amplification.

A change in response is observed at RBB.3, where the profile crosses the marly limestone formation. Fig. 7.8 shows amplification slightly above 2 around 2.5 Hz and again near 10 Hz. These moderate peaks are compatible with the intermediate stiffness of the marly limestone and reflect local resonance phenomena that are typical for this unit.

The most pronounced amplification (factor close to 10 at approximately 1.5 Hz) in this segment occurs at RBB.4, located on the alluvial deposits near the pond of Anse-à-Veau. The value is unexpectedly high, although the soft and saturated nature of the alluvial deposits in this sector can partially explain such behaviour. Additional amplification between 3 and 5 occurs within the broad frequency range of 2 to 8 Hz. These results indicate that the alluvium in this area exhibits strong impedance contrasts and internal layer variability, possibly accentuated by local geometry or thickness variations around the pond.

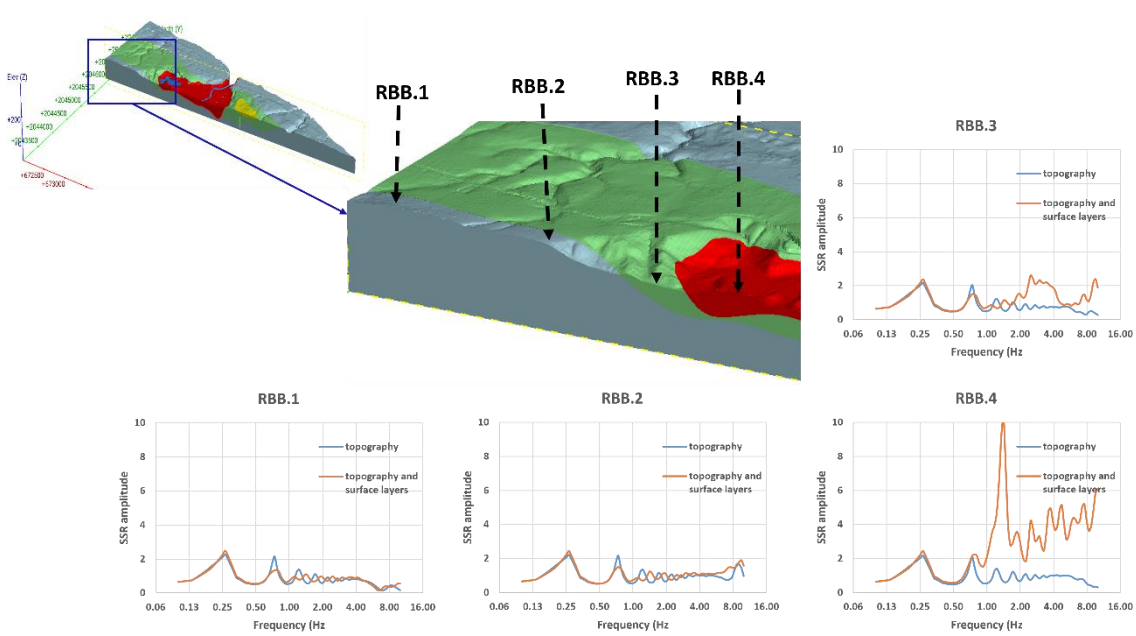

Fig. 7.8 SSR analysis at the synthetic receivers on the surface of the cross-section B-B'. The receivers RBB.1 to RBB.4 are placed at the western portion of the profile.

The receivers in the central part of the profile traverse several lithologies, beginning with shallow alluvial deposits at RBB.5. The SSR curve at this location shows amplification between 4 and 6 in the frequency band from 2 to 4 Hz, as illustrated in Fig. 7.9. These values match the expected behaviour of soft, near-surface alluvium underlain by stiffer material, where resonance typically occurs at mid to low frequencies.

The receiver RBB.6, located on thick alluvial deposits within *La Basse Ville*, shows the SSR results with one of the strongest amplifications along the profile. Fig. 7.9 shows values near 10 between 0.5 and 1 Hz, indicating a very low fundamental frequency that reflects the considerable thickness and very low seismic velocities of the sediments. A secondary amplification of approximately 2.5 appears at ~1.5 Hz. The combination of these peaks suggests a multilayered or gradually varying sedimentary structure. The magnitude of the amplification at low frequencies is higher than expected based on nearby profiles and may point to a local thickening or strong contrast at depth.

At RBB.7, the profile crosses the marly limestone formation again. The corresponding SSR curve in Fig. 7.9 shows only weak amplification, consistent with the moderate stiffness and reduced impedance contrasts typical of this unit. This behaviour fits the general trend already observed for marly limestones in profile A-A'.

The receiver RBB.8 is positioned on the localized lateritic soil formation overlying marly limestone. Fig. 7.9 shows amplification between 4 and 5 in the frequency band of 2-8 Hz. These values correspond to the typical response of lateritic soil, which often produces multiple spectral peaks due to its residual origin and its contrast with the underlying marly limestone. The broad frequency range of amplification suggests a combination of shallow impedance contrasts and internal heterogeneity within the lateritic layer.

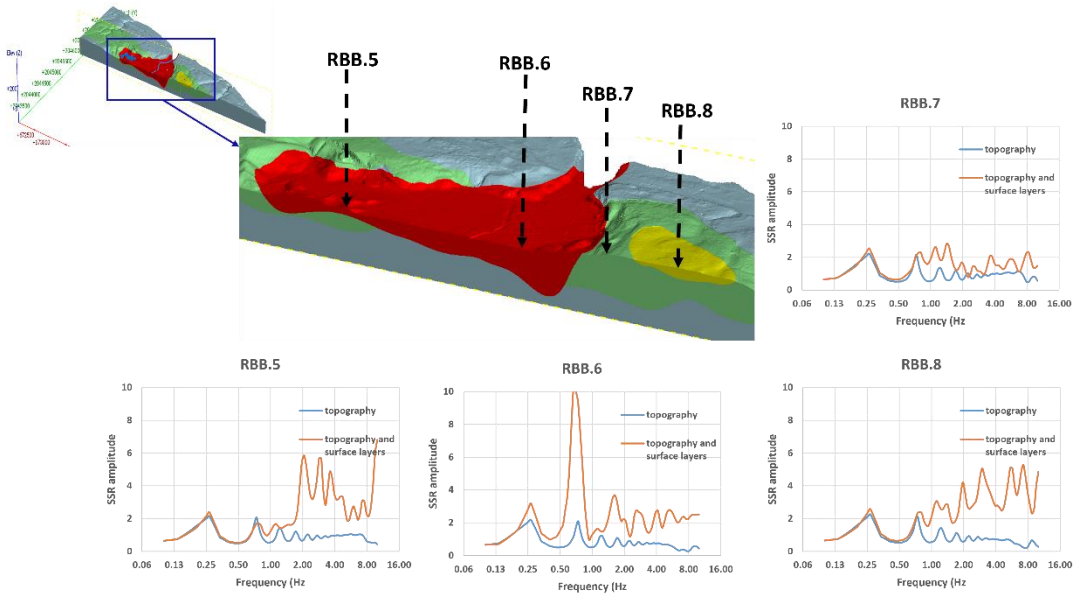

Fig. 7.9 SSR analysis at the synthetic receivers on the surface of the cross-section B-B'. The receivers RBB.5 to RBB.8 are placed at the central part of the profile.

The eastern end of the profile crosses the reef limestone basement that underlies *La Haute Ville*. The receivers RBB.9 to RBB.12 are positioned in this domain. As shown in Fig. 7.10, none of these receivers display any significant amplification. The SSR curves remain nearly flat, which confirms the absence of soft superficial materials and the dominance of high-velocity, coherent limestone. This behaviour matches the expected dynamic response of competent bedrock and reflects the absence of local seismic amplification.

The SSR results along profile B-B' highlight the influence of lithological variations on seismic amplification. The basement sections show no amplification, as expected for stiff limestone formations. The marly limestone units exhibit moderate and frequency-dependent amplification that is consistent with their intermediate mechanical properties. The localized lateritic soil formation produces broad amplification peaks, indicating significant impedance contrasts at shallow depth. The strongest amplification occurs in the alluvial deposits, particularly near the pond of Anse-à-Veau and within *La Basse Ville*, where values approaching 10 are recorded at low frequencies. Although such values are unexpectedly high compared to experimental results (H/V and MASW), they correspond to areas where the alluvial deposits are exceptionally soft or locally thickened, conditions that can significantly increase amplification. The reef limestone basement at the eastern end of the profile shows no amplification, confirming the validity of the lithological model and its representation in the dynamic modelling.

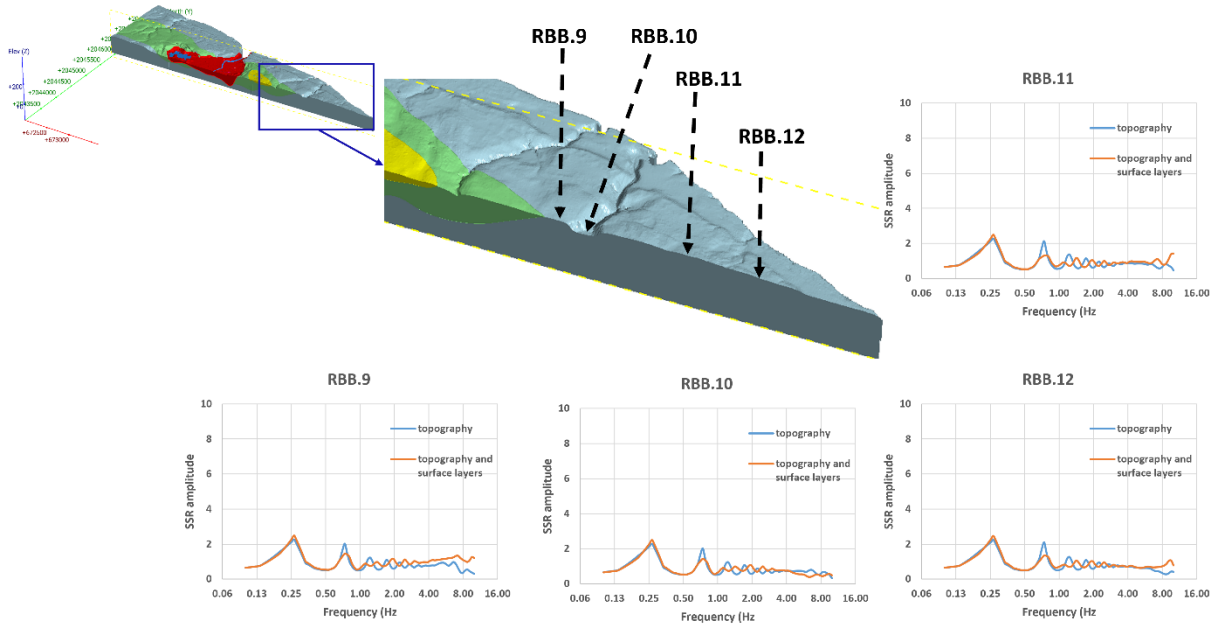

Fig. 7.10 SSR analysis at the synthetic receivers on the surface of the cross-section B-B'. The receivers RBB.9 to RBB.12 are placed at the eastern portion of the profile.

7.1.4.3 The section C-C'

The east-west cross-section C-C' provides an analysis of the dynamic behaviour across the marly limestone domain, the pelagic limestone basement, and the small unit of alluvium that occupies the eastern end of the study area. Ten synthetic receivers were placed at the surface (RCC.1 to RCC.10), and SSR analysis were performed for each of them using pure topography and combined topography with surface layers. The results are presented in Figs. 7.11 and 7.12.

The western part of the profile begins in the marly limestone unit, where RCC.1 and RCC.2 are located. Fig. 7.11 shows that both receivers exhibit an amplification close to 4 around 1.5 Hz. These peaks are consistent with the behaviour expected for marly limestones, which often produce mid-frequency resonance due to their intermediate stiffness and moderate impedance contrasts with underlying materials. The presence of shallow marly limestone in this area strengthens this frequency response by enhancing resonance effects at relatively low frequencies.

The receivers RCC.3, RCC.4, and RCC.5 are positioned within the pelagic limestone basement. Fig. 7.11 shows flat SSR curves at all three locations, indicating no significant amplification. This behaviour is typical for competent limestone formations, where high seismic velocities and strong mechanical integrity suppress resonant amplification. The similarity between the pure topography and combined-layer curves confirms that the response is dominated by the basement lithology, with minimal influence from surface geometry.

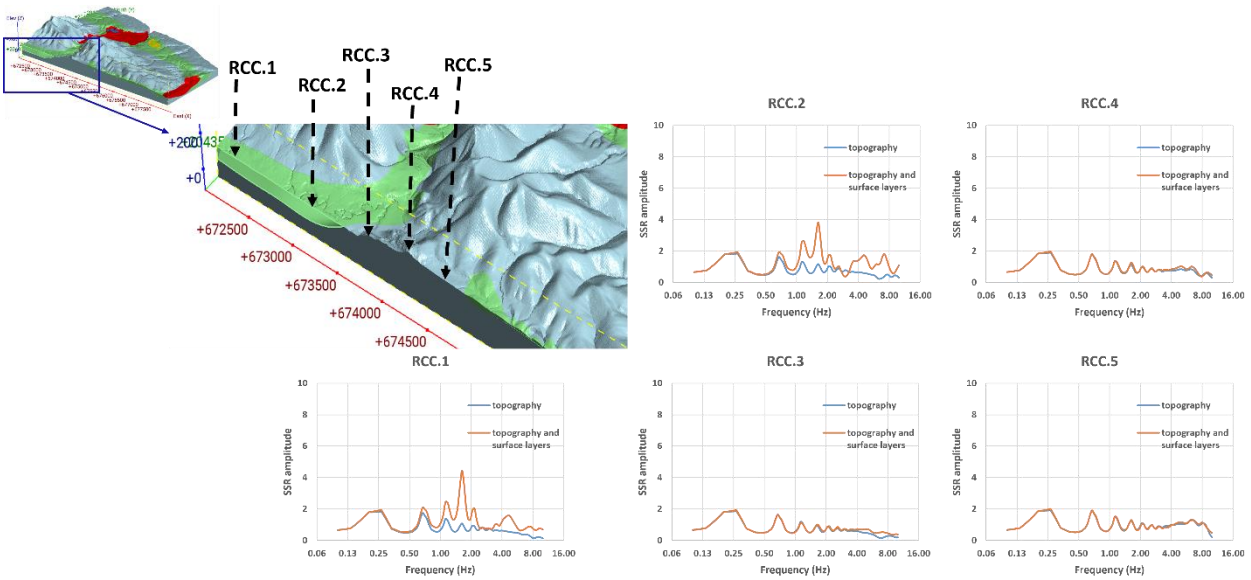

Fig. 7.11 SSR analysis at the synthetic receivers on the surface of the cross-section C-C'. The receivers RCC.1 to RCC.5 are placed at the western portion of the profile.

In the eastern segment of the profile, RCC.6, RCC.7, and RCC.8 are located on the marly limestone unit. RCC.6, situated where the marly limestone is shallow, shows no clear amplification (Fig.

7.12). This result may reflect either a limited impedance contrast at this specific location or a surface geometry that does not favour resonant amplification at the modelled frequencies.

The receivers RCC.7 and RCC.8 are positioned farther east, where the marly limestone becomes less shallow. Both receivers exhibit amplification between 2 and 3 in the frequency range from 4 to 8 Hz. The higher frequencies associated with these peaks suggest resonance driven by a greater thickness of marly limestone above the basement. These results are consistent with the behaviour already observed in the geomodel, where marly limestone units often display one or two peaks at moderate to high frequencies.

The final two receivers, RCC.9 and RCC.10, are located on the small alluvial deposit in the eastern end of the profile. RCC.9 shows a peak of approximately 3 around 2 Hz, which may correspond to a modest but clear resonance associated with the presence of a thin alluvial layer. RCC.10, which lies where the alluvial thickness increases, presents a more complex amplification pattern. Fig. 7.12 shows a pronounced peak of 6 around 1.8 Hz, as well as two additional peaks of approximately 4 near 4 Hz and 6 Hz. The first peak is likely controlled by the contrast between the soft alluvial material and the basement unit. The two higher-frequency peaks may reflect impedance contrasts between the alluvium and the underlying marly limestone, indicating a multilayer resonance consistent with the layered structure shown in the geomodel.

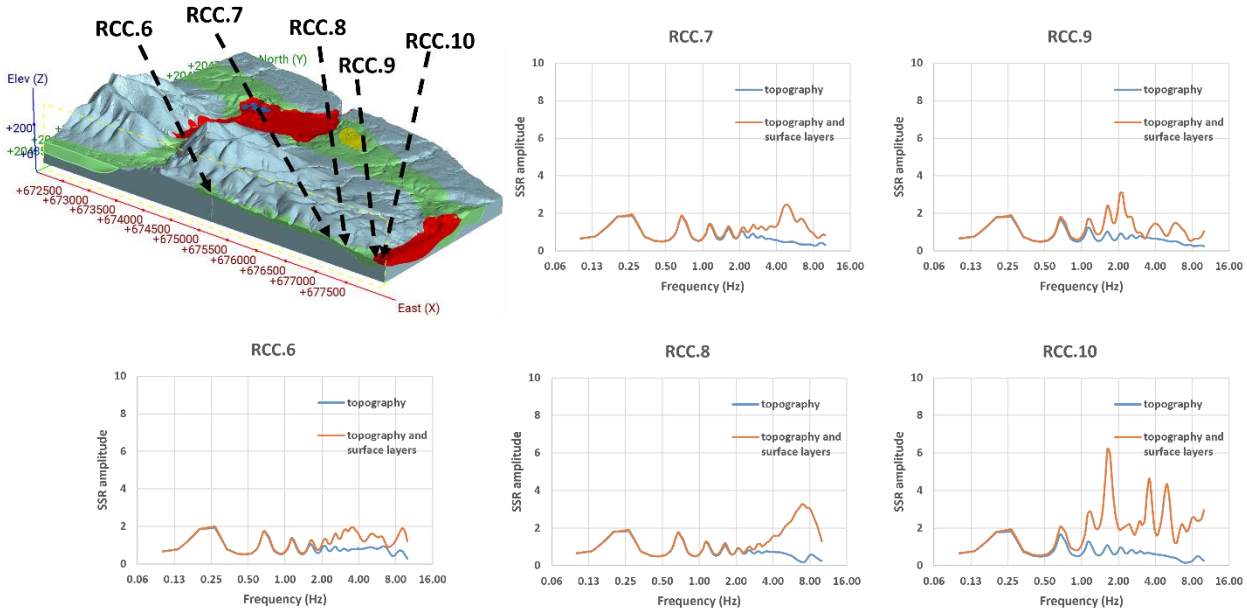

Fig. 7.12 SSR analysis at the synthetic receivers on the surface of the cross-section C-C'. The receivers RCC.6 to RCC.10 are placed at the eastern portion of the profile.

The dynamic response along profile C-C' highlights the contrasting behaviours of the lithological units present in the southern part of the study area. The pelagic limestone basement shows stable and non-amplifying behaviour, consistent with its high stiffness and consolidated nature. The

marly limestone unit produces amplification at selected frequencies, but the magnitude and frequency range vary according to the thickness and depth of the unit. The small alluvial deposit at the eastern end of the profile produces the strongest amplification, particularly at RCC.10 where the alluvium is thicker and more capable of sustaining low-frequency resonance. The presence of multiple amplification peaks at this location indicates the interaction of several impedance contrasts within a layered structure. These results confirm the sensitivity of the alluvial and marly limestone domains to local variations in thickness and lithological properties, and they match the dynamic behaviour identified in the geomodel.

7.1.5 Discussion (study area 1)

The combined analysis of the three 2D dynamic models developed for profiles A-A', B-B', and C-C' provides important insight into the site effect characteristics of the study area of Anse-à-Veau. These models allow an assessment of how lithological variability and near-surface geometry influence seismic ground motion across a complex coastal-mountainous setting. The SSR results from synthetic receivers placed across the models reveal patterns that are overall consistent with the stratigraphic framework of the 3D geomodel, the observed HVSR data and the expected seismic response of alluvial and limestone formations.

7.1.5.1 Lithological control on amplification patterns

Across all three profiles, the strongest and most consistent amplification is associated with the alluvial deposits of *La Basse Ville* and, to a lesser extent, the small alluvial unit at the eastern end of profile C-C'. These results are aligned with the geological framework of the study area, where the alluvium is characterised by low seismic velocities and significant impedance contrasts with the underlying limestone formations. The fundamental frequencies in the 1 to 2 Hz range, and higher-frequency peaks between 4 and 6 Hz, appear repeatedly in these domains. These frequency bands are comparable to what Ulysse et al. (2018a) reported for soft sediment sites in Port-au-Prince.

The marly limestone units produce moderate amplification, generally between 2 and 3, and across narrower frequency ranges. This behaviour reflects the intermediate geotechnical properties of these units, which are stiffer than the alluvium but still capable of generating resonance.

The lateritic soil formation encountered along profile B-B' exhibits a broader amplified frequency range, between 2 and 8 Hz, which is consistent with its residual soil structure and the impedance contrasts with the underlying marly limestone. The presence of multiple peaks is a typical indicator of multilayer or gradational contrast within near-surface weathered horizons. Similar behaviour was documented in the loess formations described by Hakimov et al. (2024), where multiple narrow-band peaks are associated with depositional history and heterogeneity.

The basement formations (pelagic and reef limestones) show flat SSR curves in all models, as expected for competent high-velocity bedrock. This behaviour mirrors the flat H/V spectral ratios acquired in the field and serves as an internal validation of the numerical models. Such stability in the dynamic response is also consistent with the findings of Ulysse et al. (2018a) at the Gros-Morne (Port-au-Prince) reference stations.

7.1.5.2 Topographic amplification and interaction with surface layers

The topographic effects in the study area appear to be limited compared to lithological effects, especially in profiles A-A' and C-C', which include sections of steep mountain slopes. The modelled responses show that the slopes and hilltops do not generate significant amplification at the tested excitation frequencies, except in isolated cases where local focusing effects may occur. The absence of strong topographic peaks in the purely topographic models also suggests that the terrain morphology is not sufficiently sharp or ridge-like (as there are no ridges between high and steep slopes) to generate polarised topographic resonance at the dominant frequencies of 1.4 and 3.5 Hz used for the Ricker wavelet loading.

7.1.5.3 Comparison between synthetic and experimental SSR

One of the strengths of the modelling approach is the ability to compare synthetic SSR results with empirical data, particularly along the A-A' profile where real stations UR01 (target) and UR02 (reference) are located. The comparison between the modelled SSR curve along profile A-A' and the observed SSR curves at the real target station indicates that the numerical model reproduces the observed site response, and more consistently for the N-S component than for the E-W component. Indeed, the agreement with the N-S component can be directly related to the orientation of the profile A-A' (trending approximately in the N-S direction).

The synthetic SSR curves approximately reproduce the main amplification bands observed at UR01 (mostly for the N-S component). This confirms that the geomodel captures the geometry and mechanical properties of the alluvial basin. The agreement is consistent with the kind of model-to-data alignment reported by Ulysse et al. (2018a) for the Gros-Morne area (Port-au-Prince), where numerical SSR results reproduced the primary observed amplification peaks.

7.2 Study area 2 (Cap-Haitien)

7.2.1 2D model geometry and properties

A single profile (2D cross section) trending NW-SE is used for the 2D dynamic modelling within the study area of Cap-Haitien as showed on the 3D geomodel in Fig. 7.13. The 2D model provides a simple representation of the subsurface geometry and the spatial distribution of the lithological units within the study area. It has been made deformable according to the expression $\Delta l \leq \lambda/10$ (Δl is the size of the finite-difference (FD) spatial element; λ is the wavelength associated with the highest frequency component of the input wave, see section 3.2.3). This relationship ensures accurate wave propagation through the medium.

The dynamic material properties (Table 7.2) were established using geotechnical and geophysical parameters (P-wave velocity V_P and S-wave velocity V_S) provided by the seismic microzonation reports of Cap-Haitien (Bertil et al. 2014; Roullé et al. 2014). For each lithological unit, the selected parameters include Poisson's ratio (v), dry density (ρ), bulk modulus (K), and shear modulus (G). These values were chosen to represent the stiffness, deformability, and impedance characteristics geological units defined in the 3D geomodel. Indeed, for simplicity, we did not include all the small layers characterized by the borehole (surface layer depth) logs; the layers with almost similar characteristics were grouped together and average values were considered within the 3D geomodel and the resulting 2D model. A Rayleigh damping of 2% has been used across all the models (for geological materials, damping commonly falls in the range of 2 to 5% of critical according to the reference manuals, Itasca Consulting Group 2014).

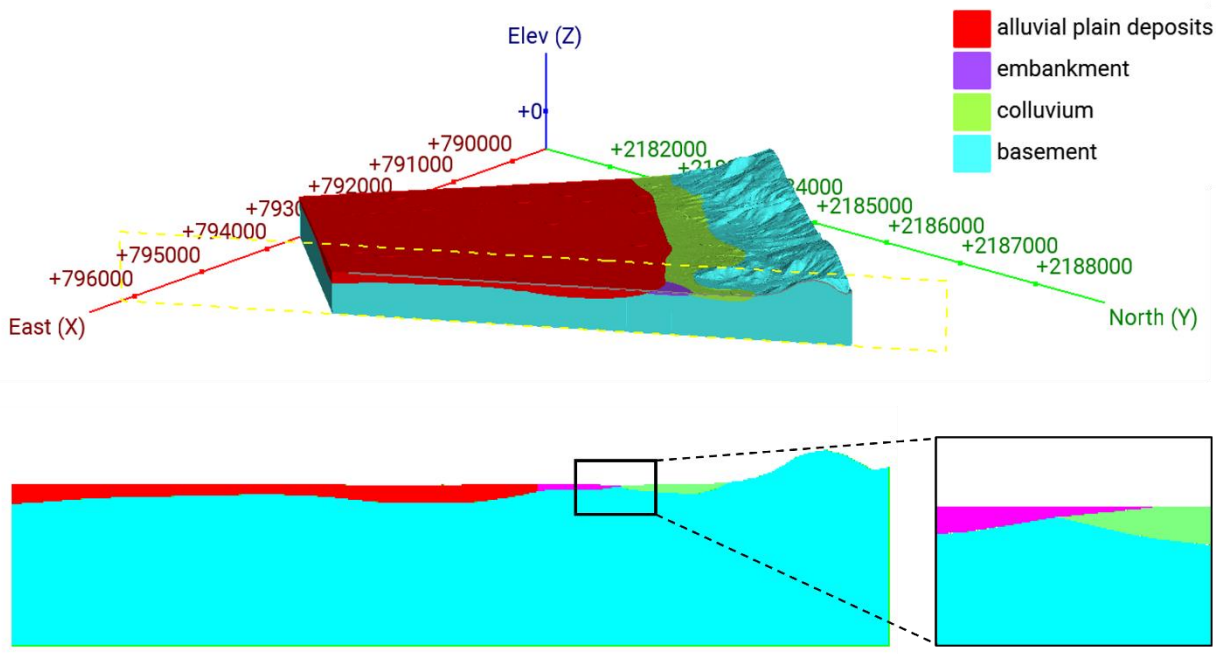

Fig. 7.13 Location of and geometric configuration of the cross-section used for 2D dynamic modelling in the study area of Cap-Haitien.

Table 7.2 Summary of material properties for the different layers across the 2D dynamic models for the study area of Cap-Haitien. P-wave velocity V_P; S-wave velocity V_S; Poisson's ratio v; dry density ρ; bulk modulus K; shear modulus G.

Lithology	V_P (m/s)	V_S (m/s)	v	ρ (kg/m^3)	K (MPa)	G (MPa)
Alluvial plain deposits	800	180	0.47	1650	990	53.4
Embankment	900	220	0.46	1700	1280	82.3
Colluvium	1100	400	0.42	1800	1940	280
Basement	2800	800	0.45	2250	15400	1440

7.2.2 Static analysis

Two models have been established: one model characterized by only one uniform layer (the basement layer) across the whole model for pure topographic effect analysis, and another one characterized by all the layers as presented in Fig. 7.13 for combined lithological and topographic effect analysis. As in the case of Anse-à-Veau, proper boundary conditions have been applied by fixing the boundary edges. A gravity loading with $g = 10\ m/s^2$ was also introduced to simulate the self-weight of the 2D models.

The mechanical cycling proceeds until the system reaches static equilibrium, which is confirmed when the ratio of unbalanced forces to applied forces falls below a specified threshold (10^{-9}, in the present case). The variation of the maximum unbalanced forces over the cycles for the model is provided in Appendix B4.

7.2.3 Dynamic loading

The Ricker wavelet has been also used as the dynamic loading for the study area of Cap-Haitien, considering two primary frequencies: 1.4 and 3.5 Hz. This helps reduce computational effort and ensures that the source behaves consistently across simulations.

The wavelet originates at the base of the model and travels upward along the y-axis, passing through the entire 2D model. The dynamic simulation and data recording are carried out over a period of 15 s. The wave transmitted from the base of every model is first recorded at about 10 m above the bottom by a synthetic receiver considering as a reference station for the spectral amplification analysis.

7.2.4 SSR analysis at the surface receivers

The SSR analysis were performed using the Geopsy software package (Wathelet et al., 2020). For each surface receiver, the x-component recordings were compared with their corresponding reference traces, which were first amplified by a factor of two and then filtered. An artificial three-component dataset was subsequently created for every receiver: the surface time history was assigned to both horizontal components, while the vertical component was replaced by the corresponding reference recording.

The 2D dynamic modelling was performed using twelve synthetic receivers placed on the surface of the profile crossing the study area of Cap-Haitien. The SSR results derived from both pure topography and combined topography-surface layer simulations highlight patterns that are coherent with the 3D geomodel, the distribution of superficial formations, and the expected impedance contrasts between the soft sediments and the competent basement lithologies.

The southeastern portion of the profile (Fig. 7.14) is entirely located within the alluvial plain, where unconsolidated sands and silts are expected to generate notable amplification due to low seismic velocities. Despite this expectation, the SSR response at RCH.1 does not exhibit any significant amplification peaks. This behaviour is consistent with the known spatial variability of the alluvial deposits in Cap-Haitien, where a previous microzonation study (Bertil et al. 2014) identified a relatively stiffer sector within the eastern alluvial plain. RCH.1 likely corresponds to this less compressible domain, which reduces the impedance contrast with the substratum.

In contrast, receivers RCH.2 to RCH.4 display a clear low-frequency peak, with amplification factors between 4 and 6 around 0.6 Hz. This resonance is characteristic of thick, soft alluvial sequences and is consistent with their HVSR signatures, which generally show strong low-frequency amplification. A second, much weaker peak is observed near 2 Hz, suggesting either a thinner surficial layer or an internal stratification within the alluvial deposits. The consistency of these peaks across multiple receivers reinforces the interpretation of a laterally continuous sedimentary basin with variable but overall significant thickness in this part of the coastal plain.

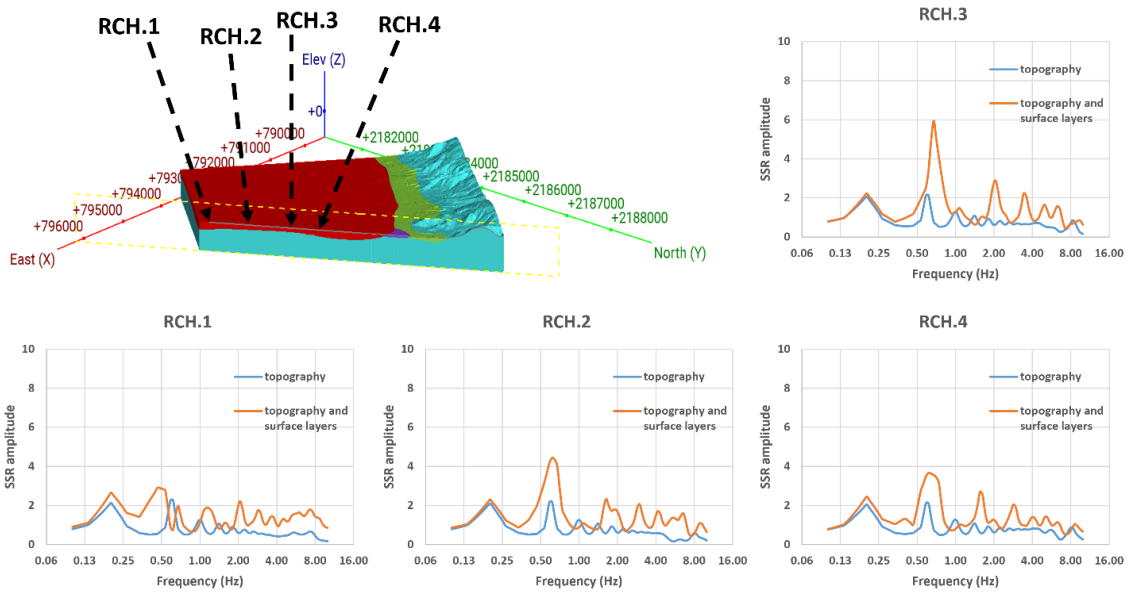

Fig. 7.14 SSR analysis at the synthetic receivers on the surface of the profile of Cap-Haitien. The receivers RCH.1 to RCH.4 are placed at the southeastern portion of the profile.

The central portion of the profile (Fig. 7.15) includes a complex arrangement of alluvium, river-mouth embankments, and colluvial deposits. The receivers RCH.5 and RCH.6, located near the mouth of *Rivière du Haut du Cap*, show amplification at very low frequencies. This behaviour suggests the presence of particularly thick or water-saturated alluvial and deltaic deposits, consistent with their depositional environment and with previous studies that have identified deep soft soils in the western part of the urban plain. The strong low-frequency resonance in this sector may contribute to long-period ground motion amplification during large earthquakes.

At RCH.7, which corresponds to the artificial embankment zone near the coastline and river mouth, the SSR results show a notable amplification peak of around 4 just below 2 Hz. This frequency range is consistent with shallow but relatively soft man-made fill materials, which tend to exhibit resonance at slightly higher frequencies than natural alluvium. The result confirms the mechanical distinctiveness of embankment materials relative to the surrounding natural formations.

The receiver RCH.8, located on the colluvial unit marking the transition between the alluvial plain and the volcanic bedrock, shows very weak or no meaningful amplification. The colluvial deposits often contain heterogeneous mixtures of silts, gravels, blocks, and reworked soil, but their overall seismic stiffness is generally higher than that of alluvial sands and silts. The absence of a strong resonance peak indicates limited impedance contrast with the underlying basement units, and it confirms that the colluvial apron acts as a transition zone with reduced site response.

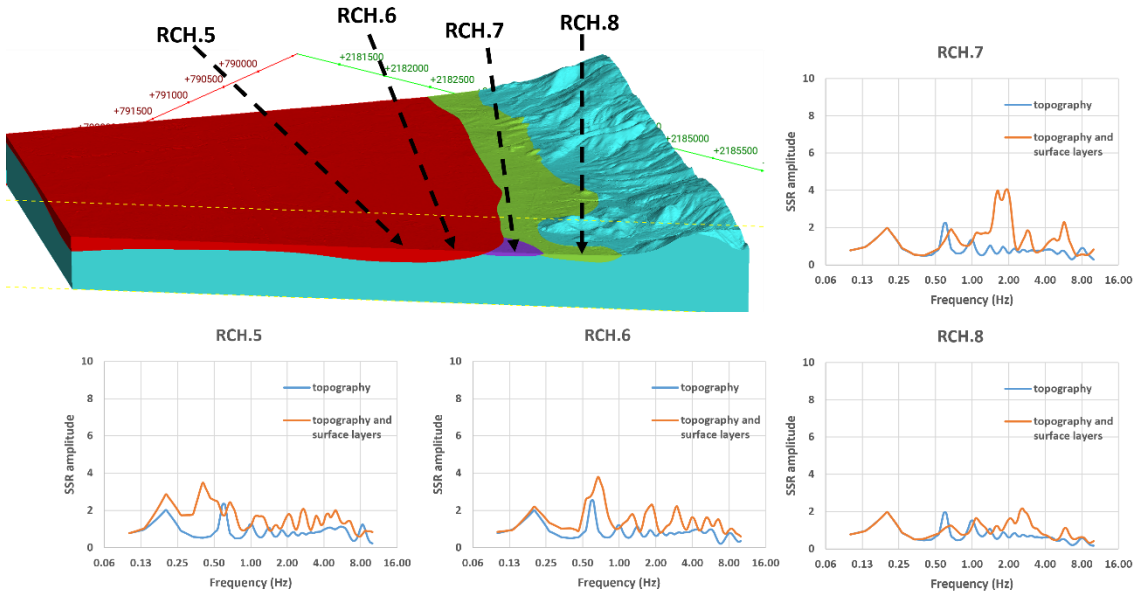

Fig. 7.15 SSR analysis at the synthetic receivers on the surface of the profile of Cap-Haitien. The receivers RCH.5 to RCH.8 are placed at the central part of the profile.

The northwestern end of the profile (Fig. 7.16) crosses the colluvial deposits at the foot of *Morne du Cap* before entering the competent volcanic and volcano-sedimentary basement. The receiver RCH.9, positioned in the colluvial zone, shows no clear amplification, which is consistent with the behaviour observed at RCH.8 and reinforces the interpretation that the colluvial units are too stiff and too thin to produce significant resonance.

The receivers RCH.10 to RCH.12, located on the volcanic basement from the flank to the summit of *Morne du Cap*, mostly exhibit flat SSR curves, as expected for high-velocity materials. However, a small amplification of 2-3 is observed around 0.6 Hz. This peak likely reflects a modest topographic effect associated with the relief of *Morne du Cap*. The presence of similar low-frequency slope-related amplification in purely topographic simulations suggests that geometry, rather than shallow stratigraphy, controls this behaviour.

The simple Cap-Haitien profile demonstrates the dominant influence of the soft alluvial sediments on seismic amplification, with strong low-frequency peaks in the central and southeastern portions of the profile. The embankment materials show distinct resonance at slightly higher frequencies, while colluvial units display weak responses due to their comparatively high stiffness. The volcanic basement exhibits limited amplification, except for minor topographic effects. These results are consistent with the expected geological behaviour and provide a good basis for understanding the spatial distribution of seismic site effects in the Cap-Haitien plain.

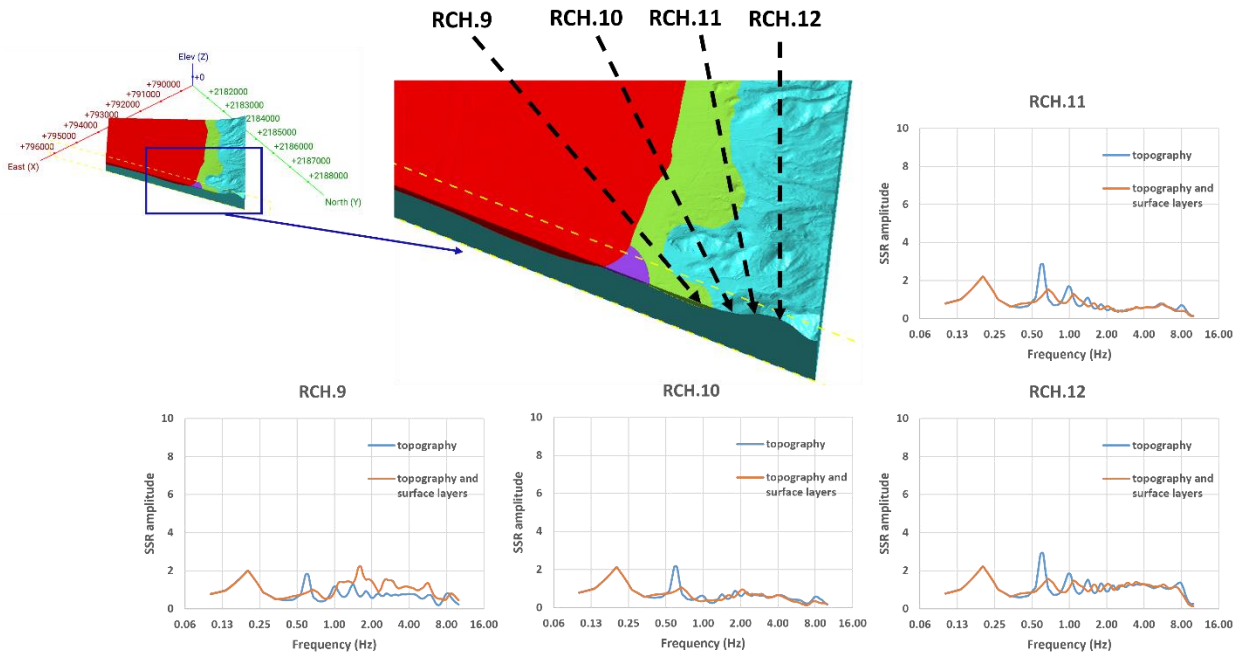

Fig. 7.16 SSR analysis at the synthetic receivers on the surface of the profile of Cap-Haitien. The receivers RCH.9 to RCH.12 are placed at the northwestern portion of the profile.

7.2.5 Discussion (study area 2)

The SSR modelling along the Cap-Haitien profile highlights the strong control exerted by the geological framework on seismic site response. The southeastern and central parts of the section, which overlie the thick alluvial deposits of the coastal plain, show the highest amplification. The receivers RCH.2 to RCH.6 display clear low frequency peaks around 0.6 Hz and secondary peaks near 2 Hz. These patterns are typical of very soft alluvial sediments with high impedance contrasts and are consistent with the broad constant-acceleration domain described by Bertil et al. (2014a).

The embankment unit at RCH.7 shows a peak close to 2 Hz, confirming its distinct response relative to natural alluvium. The colluvial units at RCH.8 and RCH.9 exhibit very weak amplification, which reflects their intermediate stiffness and heterogeneous composition. These results are coherent with the gradual increase in soil stiffness observed in the transitional Classes 3 to 5 defined in the framework of the microzonation of Cap-Haitien by Bertil et al. (2014a).

The receivers placed on the volcanic basement of Morne du Cap show flat SSR curves with small low-frequency peaks of 2 to 3. These values are attributed to topographic effects related to the slope geometry rather than to lithological contrasts.

8 Discussion

The investigations conducted in Anse-à-Veau and Cap-Haitien illustrate two complementary scales of seismic site characterisation. Anse-à-Veau represents a context where absence of geotechnical data requires a reliance on non-invasive geophysical methods. Cap-Haitien reflects a more advanced framework where geophysical investigations are supported by geotechnical data. The two study areas highlight the strengths and limitations of different methodological approaches and show how integrated analysis supports reliable microzonation.

The combined application of geophysical methods, geomodelling and numerical simulations has been developed in previous works (Ulysse et al. 2018; 2021) for site effects assessment in the eastern zone of the Enriquillo Plantain Garden fault (Port-au-Prince region and Fonds Parisien), but the present study is carried out in a coastal setting characterized by a more complex geological context, including alluvial formations and river mouth environments. Such conditions introduce strong spatial heterogeneity that was not fully considered in earlier studies carried out in more uniform settings. This work also applies geostatistical analysis to better capture spatial variability and uncertainty in the data. The use of these methods reduces interpolation errors in both the maps of the site characterisation and the 3D geomodels.

8.1 Geophysical-seismological data analysis across the study areas

The methodology used in Anse-à-Veau is shaped by data scarcity. Ambient noise recordings, surface wave inversion, seismic refraction, electrical resistivity imaging, and standard spectral ratio techniques constitute the primary tools for defining subsurface conditions. HVSR is the leading method in this workflow, and its role aligns with numerous international and Haitian studies (Hakimov et al. 2021, 2024; Ulysse et al. 2018, 2021). The method is sensitive to impedance contrasts and provides reliable estimates of fundamental frequency when significant velocity differences exist between superficial materials and the bedrock. MASW complements HVSR by capturing the depth-dependent evolution of S-wave velocity, which is critical for estimating V_{S30} and for constraining the geometry of sedimentary layers. The SRT and ERT profiles, respectively, provide P-wave velocity and electrical resistivity distribution related to the properties of the surface layers, which allow to represent the subsurface and support local seismic amplification assessment.

The geophysical data of Cap-Haitien did not include SRT and ERT data but were completed by borehole drilling with SPT. The availability of borehole with SPT logs allows V_S to be estimated using several empirical formulas and complete the MASW data. This set of independent estimates strengthens the confidence in the derived velocity structure. The region of Cap-Haitien also has a history of previous microzonation work, which provides both geological and engineering context.

Although the two regions have different levels of data density, the patterns revealed by HVSR and MASW data analysis are consistent across both. For Anse-à-Veau, the low resonance frequencies

with high spectral amplitudes and low velocity wave occur in soft and unconsolidated sediments in *La Basse Ville*. The more compact soils in *La Haute Ville* and the mountain ranges exhibit low spectral amplitude and high velocity wave. The transition zone between the reef limestone of *La Haute Ville* and the pelagic limestone of the mountains (marked as marly limestone) is characterized by intermediate values of fundamental frequency, amplitude and velocity.

For the study area of Cap-Haitien, the low resonance frequencies with high spectral amplitudes and low velocity wave occur in soft and unconsolidated sediments in the coastal alluvial plain deposits (that include the airport of Cap-Haitien). The more compact soils and volcano-sedimentary facies in *Morne du Cap* exhibit low spectral amplitude and high velocity wave. The colluvial deposits (in transition between the coastal plain and the very compact formations of the mountains) are characterised by intermediate values of amplitude and velocity.

8.2 Exploratory data analysis of HVSR and velocity parameters

The exploratory data analysis (EDA) of the HVSR parameters f_0 and A_0 as well as V_{S30} shows that seismic indicators do not behave as simple Gaussian variables in either region. The raw distributions exhibit strong skewness and heavy tails. This behaviour reflects the stark contrast between soft alluvium and competent bedrock. Low f_0 values cluster near thick sedimentary pockets while high f_0 values cluster near shallow limestone outcrops. The same pattern appears in the amplitude, where high A_0 values indicate a strong impedance contrast and often correlate with sites where the underlying bedrock is deep.

Normal-score transformation helps overcome these statistical challenges (the non-normality). The transformation produces distributions that approach a Gaussian form and allows variograms to be fitted without violating geostatistical assumptions. This transformation was particularly important for the V_{S30} in Cap-Haitien. The raw V_{S30} values range from extremely soft soils to stiff volcanic formations, producing highly skewed distributions with multiple modes. In this context the transformation serves as a necessary step to ensure stable spatial interpolation.

The spatial patterns observed in the exploratory analysis confirm the geological structure. In Anse-à-Veau, f_0 and A_0 transition from low frequency and high amplitude in the alluvial deposits to high frequency and low amplitude in the compact limestones. In Cap-Haitien, the lowest frequencies are mainly observed the coastal plain. The spatial gradients reflect the thickness of sediments, the underlying lithology, and the directional nature of sedimentary deposition.

8.3 Variogram structure and geological control of spatial continuity

The variogram results reveal the spatial logic that governs resonance frequency, amplitude and S-wave velocity. In both regions, the principal directions of continuity reflect the geometry of the geological structures. In Anse-à-Veau, the orientation of the variograms corresponds to the alignment of the sediment deposits with respect to the surrounding limestone ridges. This

arrangement suggests that the primary factor controlling frequency variability is the progressive thickening and thinning of sediments. A similar behaviour appears in Cap-Haitien where the strongest spatial continuity occurs along the slope of *Morne du Cap*.

The nugget values provide information about small-scale variability. Moderate nugget values in f_0 and A_0 suggest that near-surface heterogeneity and measurement conditions influence the results. The nugget for V_{S30} is almost negligible in Cap-Haitien, which indicates that seismic velocities derived from MASW (completed by the V_S determined empirically by SPT values) show strong internal consistency. This result is reasonable because surface wave inversions tend to produce smoothly varying profiles that reflect broader geological contrasts.

The fitted ranges reflect the scale of geological features. Short ranges indicate rapid changes in sediment thickness and characterize deposits with frequent lateral transitions. Longer ranges correspond to consolidated materials where changes occur more gradually. These patterns suggest that the variogram is sensitive to both the mechanical properties of materials and the geomorphological processes that formed the landscape. The variogram maps show direction of anisotropy of the surface layers related to direction of polarisation revealed by the azimuth analysis of the ambient noise HVSR data.

8.4 Spatial prediction through kriging and cokriging

The kriging and cokriging provide detailed interpolations that integrate the spatial structure captured by the variograms. In Anse-à-Veau, the kriged f_0 successfully delineates the basin geometry, with low frequencies marking thicker sediment and higher frequencies tracking limestone outcrops. The kriging variance (via the standard error maps) highlights zones of uncertainty at geological boundaries and in areas with sparse sampling. The A_0 surface reveals the highest amplification in soft deposits and smoother transitions toward the limestone units.

The V_{S30} map produced from cokriging identifies soft sediments, transitional marly units, and limestone formations with clear boundaries. Cokriging is particularly advantageous where MASW coverage is limited, since the method incorporates the correlation between V_{S30} and HVSR data, ensuring better predictions in poorly sampled sector.

In Cap-Haitien, the interpolated maps reproduce the broad alluvial plain, the colluvial belt, and the stiff basement. The f_0 map captures the progressive shift from low frequencies in the sediments to high frequencies along the volcanic ridge. The V_{S30} map identifies soft soils, intermediate colluvial zones, and stiff volcanic or limestone units. The improved resolution gained by combining HVSR and MASW with cokriging highlights the benefit of multivariate geostatistics.

8.5 Three-dimensional geomodel interpretation

The 3D geomodel developed for Anse-à-Veau provides an integrated representation of the subsurface architecture. The alluvial deposits form a distinct unit characterized by soft materials, high amplification, and strong impedance contrasts. These sediments occupy low-lying areas along the river in *La Basse Ville* and near the pond. The marly limestones form a transitional zone between the soft alluvium and the hard limestones. The lateritic soils represent thin weathered layers near the surface that nonetheless influence the local spectral response. The massive limestone units form the structural base of the model and define the limits of sedimentary accumulation.

In Cap-Haitien, the 3D geomodel displays a more complex set of units. The largest deposits correspond to the coastal alluvial plain and are characterised by soft and water-saturated materials. The colluvial deposits occupy the intermediate slopes and exhibit variable stiffness that depends on their origin and degree of consolidation. The volcanic and limestone basement unit forms the most stable part of the model. The combination of SGS simulations with implicit modelling techniques creates a coherent subsurface geometry that supports seismic hazard assessment.

Both geomodels reveal the strong influence of depositional history on the seismic response. The 3D models also provide the necessary structural context for the dynamic modelling.

8.6 Dynamic modelling and interpretation

The synthetic SSR simulations in Anse-à-Veau highlight the distinct responses of each lithological unit. The alluvial deposits produce the strongest amplification with clear peaks near 1 to 2 Hz and additional peaks at higher frequencies. The marly limestones respond with intermediate amplification, and lateritic soils generate multiple frequency peaks due to internal layering. The limestone bedrock produces little to no amplification.

The comparison between modelled SSR and observed SSR results is particularly valuable along profile A-A' where the numerical model reproduces the observed site response (more consistently for the N-S component than for the E-W component). This preferential agreement with the N-S component can be directly related to the orientation of the profile A-A' (trending approximately in the N-S direction). The weaker correspondence between the modelled SSR and the observed SSR for the E-W component likely reflects site-response phenomena associated with lateral heterogeneities and basin-edge effects acting perpendicular to the modelled profile. The comparative analysis suggests that the modelled SSR provides a reliable representation of the site response along the N-S direction, consistent with the orientation of the modelled profile A-A'.

The agreement between modelled peaks and those recorded by UR01 validates the geometry and velocity structure of the model. This confirmation demonstrates that geophysical data combined with implicit geological modelling can produce realistic dynamic behaviour. The agreement is consistent with the kind of model-to-data alignment reported by Ulysse et al. (2018a) for the Gros-

Morne area (Port-au-Prince), where numerical SSR results reproduced the primary observed amplification peaks.

In Cap-Haitien, the dynamic simulations reveal a strong low-frequency amplification around 0.6 Hz throughout the central part of the plain. This signature corresponds to very soft soils with large thicknesses. Secondary peaks near 2 Hz reflect the variable layering within the sediments. The transition zones display reduced amplification. The volcanic slopes produce flat spectral ratios with minor low-frequency peaks, which are more consistent with geometric effects than with lithological contrasts.

The V_{S30} maps computed from the cokriging method (and the related estimation variance) as well as the simulated contact surfaces between the basement and the soft sedimentary layers influence directly the computed SSR. A variation in the spatial distribution of the V_{S30} would change the impedance contrast and then the amplitude observed in the computed SSR. For a given V_S value, a change observed in the surface layers thickness will directly affect the fundamental frequencies observed in the computed SSR.

8.7 Implications for microzonation and seismic risk

The combined results from geophysical data processing, geostatistical analysis, geomodelling, and numerical modelling emphasize the value of integrated approaches for seismic microzonation. The different results for the two study areas (Anse-à-Veau and Cap-Haitien) show good agreements between the applied geophysical methods. The zones characterised by the highest seismic velocities are those where the flat H/V curves were observed (and the zones with the largest resistivities, like for the reef limestone of *La Haute Ville* in Anse-à-Veau, and with the highest SPT-N values, for the volcano-sedimentary facies of *Morne du Cap* in Cap-Haitien). Likewise, the zones with lowest seismic velocities are characterized by H/V curves with pronounced peaks, indicating elevated seismic amplification. This is the case for the alluvial deposits within and near *La Basse Ville* in Anse-à-Veau, and for the coastal alluvial plain in Cap-Haitien.

The geostatistical analysis defines the spatial correlation between the different geophysical parameters, considering the geological and geomorphological context in both study areas. These correlations allow the construction of site characterisation maps, delineating the zones with similar site amplification potential across the study areas. Combining the geophysical parameters in the geostatistical framework improve the quality of final site characterisation maps. For instance, *La Haute Ville* of Anse-à-Veau shows some sectors with low frequency (indicating high site amplification), both the correspondence with low amplitude and high seismic velocity allow to interpret these sectors as zone with low amplification effects.

The geomodels constructed and the resulting numerical models confirm and refine the primary interpretation of the geophysical-seismological results completed by geostatistical analysis. The 2D dynamic modelling (compared to results of standard spectral ratio, for a seismic station installed in *La Basse Ville* of Anse-à-Veau) shows that sediment thickness and impedance contrast

are the dominant factors influencing local ground motion. These conditions produce frequency ranges that are critical for the vulnerability of local building stocks.

The results provide good inputs for seismic hazard mitigation in our two study areas. The identification of zones with high amplification helps guide urban expansion, infrastructure design and risk reduction strategies. The combination of geophysical surveys, geomodelling and dynamic modelling supports the development of reliable microzonation plans.

9 General conclusions

The investigations carried out in Anse-à-Veau and Cap-Haitien present two complementary examples of how modern seismic microzonation can be achieved in environments where geological complexity, data availability and geomorphological constraints vary significantly. The work demonstrates the importance of combining geophysical-seismological investigations, geostatistical modelling, and numerical simulations to characterize the near-surface structure and its influence on seismic site response.

The context of Anse-à-Veau required a methodology grounded in non-invasive geophysical methods (also related to missing funds for borehole logging). Ambient noise recordings, surface wave analysis, electrical resistivity imaging, seismic refraction, and spectral ratio analysis provided the necessary inputs to construct the 3D geomodel and to infer the distribution of soft sediments, transitional marly units, and competent limestone. The HVSR method turned out to be particularly important for identifying fundamental resonance frequencies and for delineating the sedimentary basin geometry. The MASW profiles further constrained S-wave velocities and confirmed the presence of low velocity zones in the alluvial deposits. These geophysical results revealed a clear contrast between soft sediments in *La Basse Ville* and the reef limestone formations in *La Haute Ville*. The spatial transitions in f_0, A_0 and V_{S30} matched geological expectations and allowed the construction of reliable kriging-based maps that captured the behaviour of the basin. They allowed the definition of the soft sediments thickness and provide the inputs parameters to conditionally simulate (via the Sequential Gaussian Simulation) the contact surfaces of the 3D geomodels.

The geophysical data of Cap-Haitien were supplemented with empirical V_S relations from SPT and previous microzonation work. Their integration provides a detailed representation of soil stiffness and allowed the identification of the lithological units used in the geomodels and numerical models: the alluvial deposits of the coastal plain, the colluvial belt along the mountain front, the anthropogenic embankments near the river mouth and the volcanic and limestone formations of *Morne du Cap*. The HVSR curves displayed clear low-frequency peaks in the soft sediments and intermediate to high frequency responses in the colluvial and basement units. The geostatistical analysis confirmed strong spatial anisotropy in both HVSR parameters and V_{S30}, reflecting the geological control exerted by the mountain direction. The cokriging approach (validated by regression kriging), which combined V_{S30} with HVSR information, produced coherent velocity fields that aligned with the geomorphology.

The 3D geomodels in the two study areas provided a robust structural framework for interpreting dynamic behaviour. In Anse-à-Veau, the model clarified the geometry of alluvial deposit, the extent of marly limestone and the continuity of the limestone basement. In Cap-Haitien, the model reproduced the thickness and distribution of alluvial deposits in the coastal plain, the position of colluvial wedges, and the basement unit that combine the underlying bedrock, the volcanic formations, the volcano-sedimentary facies and stiff limestone formation towards the mountain

(*Morne du Cap*). However, the geomodel and numerical model produced for Cap-Haitien are a very simplified compared to the thin multilayered layers revealed by the borehole logs.

The 2D dynamic results show the dominant role of lithological contrasts and sediment thickness in shaping local ground motion. In Anse-à-Veau, the synthetic receivers placed in the alluvial plain consistently showed amplification at low frequencies between 1 and 2 Hz, along with secondary peaks at higher frequencies (~6 Hz). The marly limestone units produce intermediate amplification, and limestone bedrock showed minimal response. The dynamic signatures agree closely with the recorded SSR data at UR01, indicating that the geomodel and velocity structure successfully captured the basin geometry. In Cap-Haitien, the receivers located in the central and southeastern portions of the profile exhibited strong amplification around 0.6 Hz, with additional peaks near 2 Hz. These features match the seismic behaviour expected for very soft and thick alluvium and correspond to previous microzonation results describing long-period site effects and broad constant-acceleration domains in the plain. The colluvial and basement units produced weaker responses with only minor peaks, reflecting their greater stiffness and reduced impedance contrast.

The conclusions drawn from these investigations have direct implications for seismic risk reduction. The identification of soft sediment pockets, transition zones, and mechanically competent formations provides good inputs for urban planning, structural design and emergency preparedness. The strong site amplification observed in the two study areas highlights the need for improved building practices, especially in densely populated or rapidly developing neighbourhoods located on soft ground. The models developed here can support future scenario-based ground motion simulations, infrastructure assessments and the refinement of local seismic hazard maps.

The combined work establishes a framework that can be applied to other Haitian cities with similar geological and geotechnical challenges. As national seismic monitoring and geotechnical database expand, the approaches demonstrated here can evolve toward higher resolution and more accurate prediction of local ground motion. The integration of geophysical surveys, geostatistical analysis and numerical simulations forms a consistent methodology capable of supporting long-term seismic resilience and informed decision-making across the country.

Bibliography

Aki, K., & Richards, P. G. (2002). *Quantitative seismology.* Sausalito, Calif.: University Science Books.

Albarello, D., & Lunedei, E. (2013). Combining horizontal ambient vibration components for H/V spectral ratio estimates. *Geophysical Journal International, 194*, 936–951. doi:10.1093/gji/ggt130

Alcaraz, S., Lane, R., Spragg, K., Milicich, S., Sepulveda, F., & Bignall, G. (2011). 3D geological modelling using new Leapfrog Geothermal software. *Proceedings, Thirty-Sixth Workshop on Geothermal Reservoir Engineering.* Stanford University, Stanford, California.

Ali, S. T., Freed, A. M., Calais, E., Manaker, D. M., & McCann, W. R. (2008). Coulomb stress evolution in Northeastern Caribbean over the past 250 years due to coseismic, postseismic and interseismic deformation. *Geophysical Journal International, 174*, 904–918. doi:10.1111/j.1365-246x.2008.03634.x

Anderson, J. G., Bodin, P., Brune, J. N., Prince, J., Singh, S. K., Quaas, R., & Onate, M. (1986). Strong ground motion from the michoacan, Mexico, earthquake. *Science, 233*, 1043-9. doi:10.1126/science.233.4768.1043

Andrus, R. D., & Stokoe, K. H. (2000). Liquefaction Resistance of Soils from Shear-Wave Velocity. *Journal of Geotechnical and Geoenvironmental Engineering, 126*, 947-1031. doi:10.1061/(asce)1090-0241(2000)126:11(1015)

Apel, M. (2006). From 3d geomodelling systems towards 3d geoscience information systems: Data model, query functionality, and data management. *Computers & Geosciences, 32*, 222-229. doi:10.1016/j.cageo.2005.06.016

Armstrong, M., & Carignan, J. (1997). *Géostatistique linéaire: application au domaine minier.* Presses de l'Ecole des Mines de Paris.

Assimaki, D., Gazetas, G., & Kausel, E. (2005). Effects of Local Soil Conditions on the Topographic Aggravation of Seismic Motion: Parametric Investigation and Recorded Field Evidence from the 1999 Athens Earthquake. *Bulletin of the Seismological Society of America, 95*, 1059-1089. doi:10.1785/0120040055

Atkinson, G. M., & Boore, D. M. (2003). Empirical Ground-Motion Relations for Subduction-Zone Earthquakes and Their Application to Cascadia and Other Regions. *Bulletin of the Seismological Society of America, 93*, 1703-1729. doi:10.1785/0120020156

Avalos, S., & Ortiz, J. M. (2020). Multiple-point statistics: tools and methods. *Computers & geosciences, 141*, 104522. doi:10.1016/j.cageo.2020.104522

Bai, T., & Tahmasebi, P. (2022). Sequential Gaussian simulation for geosystems modeling: A machine learning approach. *Geoscience Frontiers, 13*. doi:10.1016/j.gsf.2021.101258

Bakun, W. H., Flores, C. H., & ten Brink, U. S. (2012). Significant Earthquakes on the Enriquillo Fault System, Hispaniola,1500–2010: Implications for Seismic Hazard. *Bulletin of the Seismological Society of America, 102*, 18–30. doi:10.1785/0120110077

Bard, P. Y., Campillo, M., Chávez-Garcia, F. J., & Sánchez-Sesma, F. (1988). The Mexico Earthquake of September 19, 1985—A Theoretical Investigation of Large- and Small-scale Amplification Effects in the Mexico City Valley. *Earthquake Spectra, 4*, 609-633. doi:10.1193/1.1585493

Bard, P.-Y. (1999). Microtremor measurements: a tool for site effect estimation? In O. &. Irikura (Ed.), *Second International Symposium on the Effects of Surface Geology on seismic motion. 3*, pp. 1251-1279. Balkema.

Bard, P.-Y., & Bouchon, M. (1980). The seismic response of sediment-filled valleys. Part 1. The case of incident SH waves. *Bulletin of the seismological society of America, 70*, 1263-1286.

Bard, P.-Y., & Bouchon, M. (1985). The two-dimensional resonance of sediment-filled valleys. *Bulletin of the Seismological Society of America, 75*, 519–541. doi:10.1785/bssa0750020519

Bardet, J.-P., & Scott, R. F. (1985). Seismic Stability of Fractured Rock Masses with the Distinct Element Method. *Research and Engineering Applications in Rock Masses (Proceedings of the 26th U.S. Symposium on Rock Mechanics). 2*, pp. 139-150. Boston: A. A. Balkema.

Barker, R. D. (2007). Signal contribution sections and their use in resistivity studies. *Geophysical Journal International, 59*, 123-129. doi:10.1111/j.1365-246X.1979.tb02555.x

Bertil, D., Prépetit, C., Belvaux, M., Noury, G., & l'équipe microzonage. (2013). *Microzonage sismique de Port-au-Prince (Haïti) : rapport de synthèse.* Rapport final, BRGM/RC-63100-FR.

Bertil, D., Prépetit, C., Roullé, A., Noury, G., Auclair, S., Bastone, V., . . . Terrier, M. (2014). *Microzonage sismique de Cap-Haïtien (Haïti) : rapport de synthèse.* Rapport final, BRGM/RC-63513-FR.

Bertil, D., Roullé, A., Gildas, N., Prepetit, C., Gilles, R., Sylvain, R., & Jean-Philippe, J. (2014). An IBC approach for seismic microzoning at Cap-Haitien (Haiti). *Second European Conference on Earthquake Engineering and Seismology (2ECEES).* Istanbul.

Bilham, R. (2010). Lessons from the Haiti earthquake. *Nature, 463*, 878-9. doi:10.1038/463878a

BME. (2005). *Notice explicative de la carte géologique d'Haïti au 1/250 000ème.* Tech. rep., Port-au-Prince: Direction de la Géologie et des Mines.

Bonnefoy-Claudet, S., Cornou, C., Bard, P.-Y., Cotton, F., Moczo, P., Kristek, J., & Fah, D. (2006). H/V ratio: a tool for site effects evaluation. Results from 1-D noise simulations. *Geophysical Journal International, 167*, 827-837. doi:10.1111/j.1365-246x.2006.03154.x

Boore, D. M., & Atkinson, G. M. (2008). Ground-motion prediction equations for the averagehorizontal component of PGA, PGV, and 5%-damped PSA at spectral periods between 0.01s and 10.0 s. *Earthquake Spectra, 24*, 99-138. doi:10.1193/1.2830434

Boore, D. M., Stewart, J. P., Seyhan, E., & Atkinson, G. M. (2014). NGA-West2 Equations for Predicting PGA, PGV, and 5% Damped PSA for Shallow Crustal Earthquakes. *Earthquake Spectra, 30*, 1057–1085. doi:10.1193/070113eqs184m

Borcherdt, R. D. (1970). Effects of local geology on ground motion near San Francisco Bay. *Bulletin of the Seismological Society of America, 60*, 29–61. doi:10.1785/BSSA0600010029

Borcherdt, R. D. (1994). Estimates of Site-Dependent Response Spectra for Design (Methodology and Justification). *Earthquake Spectra, 10*. doi:10.1193/1.1585791

Borcherdt, R. D., & Gibbs, J. F. (1976). Effects of local geological conditions in the San Francisco Bay region on ground motions and the intensities of the 1906 earthquake. *Bulletin of the Seismological Society of America, 66*, 467-500. doi:10.1785/bssa0660020467

Borcherdt, R. D., & Glassmoyer, G. (1992). On the characteristics of local geology and their influence on ground motions generated by the Loma Prieta earthquake in the San Francisco Bay region, California. *Bulletin of the Seismological Society of America, 82*, 603–641. doi:10.1785/bssa0820020603

Bormann, P., Engdahl, B., & Kind, R. (2012). Seismic Wave Propagation and Earth models. In P. Bormann (Ed.), *New Manual of Seismological Observatory Practice 2 (NMSOP2)* (pp. 1-105). Potsdam : Deutsches GeoForschungsZentrum GFZ. doi:10.2312/GFZ.NMSOP-2_ch2

Bouchon, M., Hatzfeld, D., Jackson, D. D., & Haghshenas, E. (2006). Some insight on why Bam (Iran) was destroyed by an earthquake of relatively moderate size. *Geophysical Research Letters, 33*, L09309. doi:10.1029/2006gl025906

Bourennane, H. (1997). *Etude des lois de distribution spatiale des sols de Petite Beauce. Application à la cartographie d'un horizon par couplage de méthodes morphométriques et géostatistiques.* Ph.D. dissertation, Université d'Orléans.

Bourges, M., Mari, J.-L., & Jeannée, N. (2012). A practical review of geostatistical processing applied to geophysical data: methods and applications. *Geophysical Prospecting, 60*, 400-412. doi:10.1111/j.1365-2478.2011.00992.x

Bowden, D. C., & Tsai, V. C. (2017). Earthquake ground motion amplification for surface waves. *Geophysical Research Letters, 44*, 121-127. doi:10.1002/2016gl071885

Butkovich, T. R., Walton, O. R., & Heuze, F. E. (1988). Insights in Cratering Phenomenology Provided by Discrete Element Modeling. *Key Questions in Rock Mechanics: Proceedings of the 29th U.S. Symposium (University of Minnesota, June 1988)* (pp. 359-368). Rotterdam: A. A. Balkema.

Butterlin, J. (1960). *Géologie générale et régionale de la République d'Haïti.* (É. de l'IHEAL, Ed.)

Calais, E., & de Lépinay, B. M. (1995). Strike-slip tectonic processes in the northern Caribbean between Cuba and Hispaniola (Windward Passage). *Marine Geophysical Researches, 17*, 63–95. doi:10.1007/bf01268051

Calais, E., Boisson, D., Symithe, S., Prépetit, C., Pierre, B., Ulyse, S., . . . Clouard, V. (2020). A Socio-Seismology Experiment in Haiti. *Front. Earth Sci., 8*, 542654. doi:10.3389/feart.2020.542654

Calais, E., Freed, A., Mattioli, G., Amelung, F., Jónsson, S., Jansma, P., . . . Momplaisir, R. (2010). Transpressional rupture of an unmapped fault during the 2010 Haiti earthquake. *Nature Gesocience, 3*, 794-799. doi:10.1038/ngeo992

Calais, E., Mazabraud, Y., de Lépinay, B. M., Mann, P., Mattioli, G., & Jansma, P. (2002). Strain partitioning and fault slip rates in the northeastern Caribbean from GPS measurements. *Geophysical Research Letters, 29*, 3-1-3-4. doi:10.1029/2002gl015397

Calais, E., Symithe, S. J., & de Lépinay, B. M. (2022). Strain Partitioning within the Caribbean–North America Transform Plate Boundary in Southern Haiti, Tectonic and Hazard Implications. *Bulletin of the Seismological Society of America, 113*, 131–142. doi:10.1785/0120220121

Calais, E., Symithe, S., Monfret, T., Delouis, B., Lomax, A., Courboulex, F., . . . Meng, L. (2022). Citizen seismology helps decipher the 2021 Haiti earthquake. *Science, 376*, 283-287. doi:10.1126/science.abn1045

Calcagno, P., Chilès, J. P., Courrioux, G., & Guillen, A. (2008). Geological modelling from field data and geological knowledge: Part I. Modelling method coupling 3D potential-field interpolation and geological rules. *Physics of the Earth and Planetary Interiors, 171*, 147-157. doi:10.1016/j.pepi.2008.06.013

Campbell, K. W., & Bozorgnia, Y. (2088). NGA Ground Motion Model for the Geometric Mean Horizontal Component of PGA, PGV, PGD and 5% Damped Linear Elastic Response Spectra for Periods Ranging from 0.01 to 10 s. *Earthquake Spectra, 24*, 139–171. doi:10.1193/1.2857546

Carr, J., & Glass, C. (2007). Use of Geostatistics For Accurate Mapping of Earthquake Ground Motion. *Geophysical Journal International, 97*, 31-40. doi:10.1111/j.1365-246X.1989.tb00482.x

Caumon, G., Collon, P., de Veslud, C. L., Viseur, S., & Sausse, J. (2009). Surface-Based 3D Modeling of Geological Structures. *Mathematical Geosciences, 41*, 927-945. doi:10.1007/s11004-009-9244-2

Caumon, G., Collon-Drouaillet, P., de Veslud, C. L., Viseur, S., & Sausse, J. (2009). Surface-Based 3D Modeling of Geological Structures. *Mathematical Geosciences, 41*, 927–945. doi:10.1007/s11004-009-9244-2

Chaljub, E., Maufroy, E., Moczo, P., Kristek, J., Hollender, F., Bard, P.-Y., . . . Chen, X. (2015). 3-D numerical simulations of earthquake ground motion in sedimentary basins: testing accuracy through stringent models. *Geophysical Journal International, 201*, 90–111. doi:10.1093/gji/ggu472

Chatelain, J.-L., Guillier, B., Cara, F., Duval, A.-M., Atakan, K., Bard, P.-Y., & SESAME, T. T. (2008). Evaluation of the influence of experimental conditions on H/V results from ambient noise recordings. *Bulletin of Earthquake Engineering, 6*, 33-74. doi:10.1007/s10518-007-9040-7

Chauvet, P. (1999). *Aide-mémoire de géostatistique linéaire.* Paris: Presses de l'Ecole des mines.

Chilès, J.-P., & Delfiner, P. (2012). *Geostatistics: Modeling Spatial Uncertainty.* Wiley. doi:10.1002/9781118136188

Chiou, B. S.-J., & Youngs, R. R. (2008). An NGA Model for the Average HorizontalComponent of Peak Ground Motionand Response Spectra. *Earthquake Spectra, 24*, 173-215. doi:10.1193/1.2894832

Cornou, C., & Bard, P.-Y. (2003). Site-to-bedrock over 1D transfer function ratio: An indicator of the proportion of edge-generated surface waves? *Geophysical Research Letters, 30*, 1453. doi:10.1029/2002gl016593

Cox, B. R., Bachhuber, J., Rathje, E., Wood, C. M., Dulberg, R., Kottke, A., . . . Olson, S. M. (2011). Shear Wave Velocity- and Geology-Based Seismic Microzonation of Port-au-Prince,Haiti. *Earthquake Spectra, 27*, S67–S92. doi:10.1193/1.3630226

Cressie, N. A. (2015). *Statistics for spatial data* (Revised edition ed.). Hoboken, NJ: John Wiley & Sons, Inc.

Cuba, M. A., Leuangthong, O., & Ortiz, J. M. (2012). Detecting and quantifying sources of non-stationarity via experimental semivariogram modeling. *Stoch Environ Res Risk Assess, 26*, 247–260. doi:10.1007/s00477-011-0501-9

Cundall, P. (1976). Explicit finite difference method in geomechanics. *Second Int. Conf. Numerical Methods in Geomechanics, Blacksburg, 1*, 132–150.

Cundall, P. A. (1974). *Rational Design of Tunnel Supports: A Computer Model for Rock Mass Behaviour Using Interactive Graphics for the Input and Output of Geometrical Data.* Technical Report MRD-2-74, U. S. Army Corps of Engineers, Missouri River Division.

Cundall, P., Hansteen, H., Lacasse, S., & Selnes, P. (1980). *NESSI, Soil Structure Interaction Program for Dynamic and Static Problems.* Report 51508-9, Norwegian Geotechnical Institute.

Daag, A. S., Halasan, O. P., Magnaye, A. A., Grutas, R. N., & Solidum, R. U. (2022). Empirical Correlation between Standard Penetration Resistance (SPT-N) and Shear Wave Velocity (Vs) for Soils in Metro Manila, Philippines. *Applied Sciences, 12*, 8067. doi:10.3390/app12168067

Dahlin, T., & Zhou, B. (2004). A numerical comparison of 2D resistivity imaging with 10 electrode arrays. *Geophysical Prospecting, 52*, 379-398. doi:10.1111/j.1365-2478.2004.00423.x

Danneels, G., Bourdeau, C., Torgoev, I., & Havenith, H.-B. (2008). Geophysical investigation and dynamic modelling of unstable slopes: case-study of Kainama (Kyrgyzstan). *Geophysical Journal International, 175*, 17–34. doi:10.1111/j.1365-246x.2008.03873.x

de Lépinay, B. M., Deschamps, A., Klingelhoefer, F., Mazabraud, Y., Delouis, B., Clouard, V., . . . St-Louis, M. (2011). The 2010 Haiti earthquake: A complex fault pattern constrained by seismologic and tectonic observations. *Geophysical Research Letters., 38*. doi:10.1029/2011gl049799

de Risi, R., Penna, A., & Simonelli, A. L. (2019). Seismic risk at urban scale: the role of site response analysis. *Soil Dynamics and Earthquake Engineering, 123*, 320-336. doi:10.1016/j.soildyn.2019.04.011

DeMets, C., Jansma, P. E., Mattioli, G. S., Dixon, T. H., Farina, F., Bilham, R., . . . Mann, P. (2000). GPS geodetic constraints on Caribbean-North America plate motion. *Geophysical Research Letters, 27*, 437-440. doi:10.1029/1999gl005436

Dorival, V., Havenith, H.-B., Guerrier, K., Ulysse, S., & Boisson, D. (2025). Local amplification assessment supported by geostatistical analysis and geomodelling of geophysical data for the Anse-à-Veau region, Haiti. *Journal of Seismology*. doi:10.1007/s10950-025-10320-0

Douilly, R., Haase, J. S., Ellsworth, W. L., Bouin, M.-P., Calais, E., Symithe, S. J., . . . Hough, S. E. (2013). Crustal Structure and Fault Geometry of the 2010 Haiti Earthquake from Temporary Seismometer Deployments. *Bulletin of the Seismological Society of America, 103*, 2305–2325. doi:10.1785/0120120303

Douilly, R., Mavroeidis, G. P., & Calais, E. (2017). Simulation of broad-band strong ground motion for a hypothetical Mw 7.1 earthquake on the Enriquillo Fault in Haiti. *Geophysical Journal International, 211*, 400–417. doi:10.1093/gji/ggx312

Douilly, R., Paul, S., Monfret, T., Deschamps, A., Ambrois, D., Symithe, S. J., . . . Chèze, J. (2023). Rupture Segmentation of the 14 August 2021 Mw 7.2 Nippes, Haiti, Earthquake Using Aftershock Relocation from a Local Seismic Deployment. *Bulletin of the Seismological Society of America, 113*, 58–72. doi:10.1785/0120220128

Duval, A.-M. (1994). *Détermination de la réponse d'un site aux séismes à l'aide du bruit de fond : évaluation expérimentale.* phdthesis, Université Pierre et Marie Curie, Paris VI.

Emery, X. (2012). Cokriging random fields with means related by known linear combinations. *Computers & Geosciences, 38*, 136-144. doi:10.1016/j.cageo.2011.06.001

Field, E. H., & Jacob, K. H. (1995). A comparison and test of various site-response estimation techniques, including three that are not reference-site dependent. *Bulletin of the Seismological Society of America, 85*, 1127–1143. doi:10.1785/BSSA0850041127

Flores, C. H., ten Brink, U. S., & Bakun, W. H. (2012). *Accounts of Damage from Historical Earthquakes in the Northeastern Caribbean, to Aid in the Determination of their Location and Intensity Magnitudes.* Tech. rep., U.S. Geological Survey. doi:10.3133/ofr20111133

Frankel, A. D. (1995). Mapping Seismic Hazard in The Central and Eastern United States. *Seismological Research Letters, 66*, 8-21. doi:10.1785/gssrl.66.4.8

Frankel, A. D., Mueller, C. S., Barnhard, T. P., Leyendecker, E. V., Wesson, R. L., Harmsen, S. C., . . . Hopper, M. G. (2000). USGS National Seismic Hazard Maps. *Earthquake Spectra, 16*, 1-19. doi:10.1193/1.1586079

Frankel, A. D., Mueller, C. S., Barnhard, T. P., Perkins, D. M., Leyendecker, E. V., Dickman, N., . . . Hopper, M. G. (1996). *National Seismic-Hazard Maps: Documentation June 1996.* Open-File Report 96-532, U.S. Geological Survey. doi:10.3133/ofr96532

Frankel, A., Harmsen, S., Mueller, C., Calais, E., & Haase, J. (2011). Seismic Hazard Maps for Haiti. *Earthquake Spectra, 27*, S23–S41. doi:10.1193/1.3631016

Gaudiosi, I., Francesco, D. M., Giuliano, M., & Marco, T. (2014). Site effects in the Aterno River Valley (L'Aquila, Italy): comparison between empirical and 2D numerical modelling starting from April 6th 2009 Mw 6.3 earthquake. *Bull Earthquake Eng, 12*, 697–716. doi:10.1007/s10518-013-9540-6

Geli, L., Bard, P.-Y., & Jullien, B. (1988). The effect of topography on earthquake ground motion: A review and new results. *Bulletin of the Seismological Society of America, 78*, 42-63. doi:10.1785/bssa0780010042

Gholamy, A., & Kreinovich, V. (2014). Why Ricker wavelets are successful in processing seismic data: Towards a theoretical explanation. *2014 IEEE Symposium on Computational Intelligence for Engineering Solutions (CIES).* doi:10.1109/cies.2014.7011824

Gorum, T., Fan, X., van Westen, C. J., Huang, R. Q., Xu, Q., Tang, C., & Wang, G. (2011). Distribution pattern of earthquake-induced landslides triggered by the 12 May 2008 Wenchuan earthquake. *Geomorphology, 133*, 152-167. doi:10.1016/j.geomorph.2010.12.030

Gräler, B., Pebesma, E., & Heuvelink, G. (2016). Spatio-Temporal Interpolation using gstat. *The R Journal, 8*, 204-218. doi:10.32614/rj-2016-014

Gringarten, E., & Deutsch, C. V. (2001). Teacher's Aide Variogram Interpretation and Modeling. *Mathematical Geology, 33*, 507–534. doi:10.1023/A:1011093014141

Guillen, A., Calcagno, P., Courrioux, G., Joly, A., & Ledru, P. (2008). Geological modelling from field data and geological knowledge: Part II. Modelling validation using gravity and magnetic data inversion. *Physics of the Earth and Planetary Interiors, 171*, 158-169. doi:10.1016/j.pepi.2008.06.014

Guillier, B., Atakan, K., Chatelain, J.-L., Havskov, J., Ohrnberger, M., Cara, F., . . . SESAME, T. T. (2008). Influence of instruments on the H/V spectral ratios of ambient vibrations. *Bull Earthquake Eng, 6*, 3–31. doi:10.1007/s10518-007-9039-0

Hadi, A., Brotopuspito, K. S., Pramumijoyo, S., & Christady, H. (2021). Determination of Weathered Layer Thickness Around the Landslide Zone using the Seismic Refraction Method. *IOP Conference Series Earth and Environmental Science*, *830.* doi:10.1088/1755-1315/830/1/012022

Haghshenas, E., Bard, P.-Y., Theodulidis, N., & SESAME, T. (2008). Empirical evaluation of microtremor H/V spectral ratio. *Bulletin of Earthquake Engineering, 6*, 75-108. doi:10.1007/s10518-007-9058-x

Hakimov, F., Domej, G., Ischuk, A., Reicherter, K., Cauchie, L., & Havenith, H.-B. (2021). Site Amplification Analysis of Dushanbe City Area, Tajikistanto Support Seismic Microzonation. *Geosciences, 11*, 154. doi:10.3390/geosciences11040154

Hakimov, F., Havenith, H.-B., Ischuk, A., & Reicherter, K. (2024). Assessment of Site Effects and Numerical Modeling of Seismic Ground Motion to Support Seismic Microzonation of Dushanbe City, Tajikistan. *Geosciences, 14*, 117. doi:10.3390/geosciences14050117

Hartzell, S. H., Carver, D. L., & King, K. W. (1994). Initial investigation of site and topographic effects at Robinwood Ridge, California. *Bulletin of the Seismological Society of America, 84*, 1336–1349. doi:10.1785/bssa0840051336

Hartzell, S., Mendoza, C., Ramírez-Guzmán, L., Zeng, Y., & Mooney, W. (2013). Rupture history of the 2008 Mw 7.9 Wenchuan, China, earthquake: Evaluation of separate and joint inversions of geodetic, teleseismic, and strong-motion data. *Bulletin of the Seismological Society of America*. doi:10.1785/0120120108

Havenith, H.-B., Guerrier, K., Schlögel, R., Braun, A., Ulysse, S., Mreyen, A.-S., . . . Prépetit, C. (2022). Earthquake-induced landslides in Haiti: analysis of seismotectonic and possible climatic influences. *Natural Hazards and Earth System Sciences, 22*, 3361–3384. doi:10.5194/nhess-22-3361-2022

Havenith, H.-B., Strom, A., Calvetti, F., & Jongmans, D. (2003). Seismic triggering of landslides. Part B: Simulation of dynamic failure processes. *NHESS, 3*, 663–682. doi:10.5194/nhess-3-663-2003

Havenith, H.-B., Torgoev, I., & Ischuk, A. (2018). Integrated Geophysical-Geological 3D Model ofthe Right-Bank Slope Downstream from the Rogun DamConstruction Site, Tajikistan. *International Journal of Geophysics, 2018*. doi:10.1155/2018/1641789

Hegazy, Y. A., & Mayne, P. W. (1995). Statistical correlations between Vs and cone penetration data for different soil types. *Inter. Symp. on Cone Penetration Testing. 2*, pp. 173–178. Sweden: CPT ’95, Linkoping.

Homan, J., & Eastwood, W. J. (2001). The 17 August 1999 Kocaeli (İzmit) Earthquake: Historical Records and Seismic Culture. *Earthquake Spectra, 17*, 617–634. doi:10.1193/1.1423654

Hough, S. E., Altidor, J. R., Anglade, D., Given, D., Janvier, M. G., Maharrey, J. Z., . . . Yong, A. (2010). Localized damage caused by topographic amplification during the 2010 M 7.0 Haiti earthquake. *Nature Geoscience, 3*, 778–782. doi:10.1038/ngeo988

Hough, S. E., Yong, A. K., Altidor, J. R., Anglade, D., Given, D. D., & Mildor, S.-L. (2011). Site characterization and site response in Port-au-Prince, Haiti. *Earthquake Spectra, 27*, 137-155. doi:10.1193/1.3637947

Idriss, I. M., & Boulanger, R. W. (2006). Semi-empirical procedures for evaluating liquefaction potential during earthquakes. *Soil Dynamics and Earthquake Engineering, 26*, 115-130. doi:10.1016/j.soildyn.2004.11.023

Isaaks, E. H., & Srivastava, R. M. (1989). *Applied geostatistics.* (R. M. Srivastava, Ed.) New York, NY [u.a.]: Oxford Univ. Press.

Itasca Consulting Group. (2014). *UDEC—Universal Distinct Element Code, Version 6.0 User’s Manual.* Tech. rep., Itasca: Minneapolis, MN, USA.

Journel, A. G., & Huijbregts, C. J. (1978). *Mining Geostatistics.* Academic Press. doi:10.2307/2287429

Joyner, W. B., & Boore, D. M. (1993). Methods for regression analysis of strong-motion data. *Bulletin of the Seismological Society of America, 83*, 469-487,. doi:10.1785/bssa0830020469

Kim, H.-S., Sun, C.-G., & Cho, H.-I. (2017). Geospatial Big Data-Based Geostatistical Zonation of Seismic Site Effects in Seoul Metropolitan Area. *ISPRS Int. J. Geo-Inf., 6*, 174. doi:10.3390/ijgi6060174

Kirar, B., Maheshwari, B. K., & Muley, P. (2016). Correlation Between Shear Wave Velocity (Vs) and SPT Resistance (N) for Roorkee Region. *Int. J. of Geosynth. and Ground Eng., 2*. doi:10.1007/s40891-016-0047-5

Klin, P., Priolo, E., & Seriani, G. (2010). Numerical simulation of seismic wave propagation in realistic 3-D geo-models with a Fourier pseudo-spectral method. *Geophysical Journal International, 183*, 905–922. doi:10.1111/j.1365-246x.2010.04763.x

Kudo, K., Kanno, T., Okada, H., Özel, O., Erdik, M., Sasatani, T., . . . Yoshida, K. (2002). Site-Specific Issues for Strong Ground Motions during the Kocaeli, Turkey, Earthquake of 17 August 1999, as Inferred from Array Observations of Microtremors and Aftershocks. *Bulletin of the Seismological Society of America, 92*, 448–465. doi:10.1785/0120000812

Kuhlemeyer, R. L., & Lysmer, J. (1973). Finite Element Method Accuracy for Wave Propagation Problems. *Journal of the Soil Mechanics and Foundations Division, 99*, 421-427. doi:10.1061/jsfeaq.0001885

Lachet, C. D., & Bard, P.-Y. (1994). Numerical and Theoretical Investigations on the Possibilities and Limitations of Nakamura's Technique. *Journal of Physics of the Earth, 42*, 377-397. doi:10.4294/jpe1952.42.377

Lankston, R. W. (1989). The seismic refraction method: A viable tool for mapping shallow targets into the 1990s. *Geophysics, 54*, 1535–1542. doi:10.1190/1.1442621

Lerch, C., & Hoppe, A. (2007). Development of a geological 3D-model for improved calculations of groundwater vulnerability. *Grundwasser, 12*, 144–153. doi:10.1007/s00767-007-0022-0

Loke, M. H. (2018). *Tutorial: 2-D and 3-D Electrical Imaging Surveys.* Tutorial, Malaysia: Geotomo Software.

Loke, M. H., & Barker, R. D. (1996). Rapid Least-Squares Inversion of Apparent Resistivity Pseudosections Using a Quasi-Newton Method. *Geophysical Prospecting, 44*, 131-152. doi:10.1111/j.1365-2478.1996.tb00142.x

Lombardo, L., & Tanyas, H. (2022). From scenario-based seismic hazard to scenario-based landslide hazard: fast-forwarding to the future via statistical simulations. *Stoch Environ Res Risk Assess, 36*, 2229–2242. doi:10.1007/s00477-021-02020-1

Luo, Y., Fana, X., Huanga, R., Wanga, Y., Yunusa, A. P., & Havenith, H. B. (2020). Topographic and near-surface stratigraphic amplification of the seismic response of a mountain slope revealed by field monitoring and numerical simulations. *Engineering Geology, 271*, 105607. doi:10.1016/j.enggeo.2020.105607

Lysmer, J., & Kuhlemeyer, R. L. (1969). Finite Dynamic Model For Infinite Media. *J. Eng. Mech., Div. ASCE, 95*, 859-877. doi:10.1061/jmcea3.0001144

Manaker, D. M., Calais, E., Freed, A. M., Ali, S. T., Przybylski, P., Mattioli, G., . . . de Chabalier, J. B. (2008). Interseismic Plate coupling and strain partitioning in the Northeastern Caribbean. *Geophysical Journal Int., 174*, 889-903. doi:10.1111/j.1365-246x.2008.03819.x

Mann, P., Burke, K., & Matumoto, T. (1984). Neotectonics of Hispaniola: plate motion, sedimentation, and seismicity at a restraining bend. *Earth and Planetary Science Letters, 70*, 311-324. doi:10.1016/0012-821x(84)90016-5

Mann, P., Calais, E., Ruegg, J.-C., DeMets, C., Jansma, P. E., & Mattioli, G. S. (2002). Oblique collision in the northeastern Caribbean from GPS measurements and geological observations. *Tectonics, 21*, 7-1-7-26. doi:10.1029/2001tc001304

Mann, P., Prentice, C. S., Burr, G., Peña, L. R., & Taylor, F. W. (1998). Tectonic geomorphology and paleoseismology of the Septentrional fault system, Dominican Republic. In P. Mann, & J. F. Dolan (Eds.), *Active Strike-Slip and Collisional Tectonics of the Northern Caribbean Plate Boundary Zone* (pp. 63-123). Geological Society of America. doi:10.1130/0-8137-2326-4.63

Mann, P., Taylor, F., Edwards, R., & Ku, T. (1995). Actively evolving microplate formation by oblique collision and sideways motion along strike-slip faults: An example from the northeastern Caribbean plate margin. *Tectonophysics, 246*, 1-69. doi:10.1016/0040-1951(94) 00268-E

Marshall, J. D., Lang, A. F., Baldridge, S. M., & Popp, D. R. (2011). Recipe for Disaster: Construction Methods, Materials, and Building Performance in the January 2010 Haiti Earthquake. *Earthquake Spectra, 27*, 323-343. doi:10.1193/1.3637031

Matheron, G. (1970). *La théorie des variables regionalisées, et ses applications.* Ecole des Mines de Paris.

Mauffret, A., & Leroy, S. (1999). Neogene intraplate deformation of the Caribbean plate at the Beata Ridge. *Caribbean Basins, Vol. 4: Sedimentary Basins of the World, pp. 667–669, ed. Mann, P., Elsevier Science,Amsterdam, The Netherlands.*

Maurer, J., Dutta, R., Vernon, A., & Vajedian, S. (2022). Complex Rupture and Triggered Aseismic Creep During the 14 August 2021 Haiti Earthquake From Satellite Geodesy. *Geophysical Research Letters, 49*, e2022GL098573. doi:10.1029/2022gl098573

Mayne, P. W. (2006). In-situ test calibrations for evaluating soil parameters. *Characterization and Engineering Properties of Natural Soils II.* Singapore.

McCann, W. R. (2006). Estimating the threat of tsunamagenic earthquakes and earthquake induced landslide tsunamis in the Caribbean. In M. Aurelio, & L. Philip (Eds.), *Caribbean Tsunami Hazard* (pp. 43–65). World Scientific Publishing, Singapore.

Mirowski, P. W., Tetzlaff, D. M., Davies, R. C., McCormick, D. S., Williams, N., & Signer, C. (2008). Stationarity Scores on Training Images for Multipoint Geostatistics. *Mathematical Geosciences, 41*. doi:10.1007/s11004-008-9194-0

Momplaisir, R. (1986). *Contribution à l'Etude Géologique de la Partie Orientale du Massif de la Hotte (Presqu'Ile du Sud d'Haiti). Synthèse Structurale des Marges de la Presqu'Ile du Sud à Partir de Données Sismiques.* Ph.D. dissertation, University of Paris VI.

Monthel, J., Bialkowski, A., Jean, P., & Jean-Baptiste, M. (2013). *Cartographie géologique des villes de Cap-Haïtien, Fort-Liberté et Ouanaminthe (République d'Haïti).* Rapport final, BRGM/RP-61951-FR.

Mukul, M. (1998). A spatial statistics approach to the quantification of finite strain variation in penetratively deformed thrust sheets: an example from the Sheeprock Thrust Sheet, Sevier Fold-and-Thrust belt, Utah. *Journal of Structural Geology, 20*, 371-384. doi:10.1016/s0191-8141(97)00088-6

Myers, D. E. (1989). To Be or Not to Be... Stationary? That Is the Question. *Mathematical Geology, 21*, 347–362. doi:10.1007/bf00893695

Nakamura, Y. (1989). A method for dynamic characteristics estimation of subsurface using microtremor on the ground surface. *Q. Rep.Railway Tech. Res. Inst., 30*, 25-33.

Nakamura, Y. (2000). Clear identification of fundamental idea of Nakamura's technique and its applications. *The 12th World Conf. on Earthquake Engineering, Auckland, New Zealand*, 8.

Nakamura, Y. (2009). Basic Structure of QTS (HVSR) and Examples of Applications. In M. Mucciarelli, M. Herak, & J. Cassidy (Eds.), *Increasing Seismic Safety by Combining Engineering Technologies and Seismological Data* (pp. 33–51). Springer Netherlands. doi:10.1007/978-1-4020-9196-4_4

Nakamura, Y., & Saito, A. (1983). Estimations of seismic response characteristics and maximum acceleration of surface ground using strong motion records. *Proc. of the 17th JSCE Earthquake Engineering Symposium*, 25-28.

Natali, M., Lidal, E. M., Parulek, J., Viola, I., & Patel, D. (2013). Modeling Terrains and Subsurface Geology. *INPROCEEDINGS, EuroGraphics 2013 State of the Art Reports (STARs)* (pp. 155 – 173). Eurographics 2013 - State of the Art Reports.

Nogoshi, M., & Igarashi, T. (1971). On the Amplitude Characteristics of Microtremor (Part 2). *Journal of the Seismological Society of Japan. 2nd ser., 24*, 26-40. doi:10.4294/zisin1948.24.1_26

Ohmachi, T., Kawamura, M., Yasuda, S., Mimura, C., & Nakamura, Y. (1988). Damage Due to the 1985 Mexico Earthquake and the Ground Conditions. *Soils and Foundations, 28*, 149-159. doi:10.3208/sandf1972.28.3_149

Okuwaki, R., & Fan, W. (2022). Oblique convergence causes both thrust and strike-slip ruptures during the 2021 M 7.2 Haiti earthquake. *Geophysical Research Letters, 49*, e2021GL096373. doi:10.1029/2021GL096373

Oldenburg, D. W., & Li, Y. (1994). Inversion of induced polarization data. *Geophysics, 59*, 1327–1341. doi:10.1190/1.1443692

O'Sullivan, M. J., Pruess, K., & Lippmann, M. J. (2001). State of the art of geothermal reservoir simulation. *Geothermics, 30*, 395-429. doi:10.1016/s0375-6505(01)00005-0

Oubaiche, E. H., Chatelain, J.-L., Bouguern, A., Bensalem, R., Machane, D., Hellel, M., . . . Guillier, B. (2012). Experimental Relationship Between Ambient Vibration H/V Peak Amplitude and Shear-wave Velocity Contrast. *Seismological Research Letters, 83*, 1038–1046. doi:10.1785/0220120004

Panzera, F., Alber, J., Imperatori, W., Bergamo, P., & Fäh, D. (2022). Reconstructing a 3D model from geophysical data for local amplification modelling: The study case of the upper Rhone valley, Switzerland. *Soil Dynamics and Earthquake Engineering, 155*, 107163. doi:10.1016/j.soildyn.2022.107163

Park, C. B., Miller, R. D., & Xia, J. (1999). Multichannel analysis of surface waves. *Geophysics, 64*, 800–808. doi:10.1190/1.1444590

Paultre, P., Calais, É., Proulx, J., Prépetit, C., & Ambroise, S. (2013). Damage to engineered structures during the 12 January 2010, Haiti (Léogâne) earthquake. *Canadian Journal of Civil Engineering, 40*, 1-14. doi:10.1139/cjce-2012-0247

Petersen, M. D., Frankel, A. D., Harmsen, S. C., andKathleen M. Haller, C. S., Wheeler, R. L., Wesson, R. L., . . . Rukstales, K. S. (2008). *Documentation for the 2008 Update of the United States National Seismic Hazard Maps.* Open-File Report 2008-1128, 61 p., U.S. Geological Survey. doi:10.3133/ofr20081128

Pischiutta, M., Fondriest, M., Demurtas, M., Magnoni, F., di Toro, G., & Rovelli, A. (2017). Structural control on the directional amplification of seismic noise (Campo Imperatore, central Italy). *Earth and Planetary Science Letters, 471*, 10-18. doi:10.1016/j.epsl.2017.04.017

Prentice, C. S., Mann, P., Crone, A. J., Gold, R. D., Hudnut, K. W., Briggs, R. W., . . . Jean, P. (2010). Seismic hazard of the Enriquillo–Plantain Garden fault in Haiti inferred from palaeoseismology. *Nature Geoscience, 3*, 789-793. doi:10.1038/ngeo991

Prentice, C. S., Mann, P., Pena, L. R., & Burr, G. (2003). Slip rate and earthquake recurrence along the central Septentrional fault, North American-Caribbean plate boundary, Dominican Republic. *Journal of Geophysical Research, 108*, 2149–2166. doi:10.1029/2001jb000442

Pubellier, M., Mauffret, A., Leroy, S., Vila, J. M., & Amilcar, H. (2000). Plate boundary readjustment in oblique convergence: Example of the Neogene of Hispaniola, Greater Antilles. *Tectonics, 19*, 630-648. doi:10.1029/2000TC900007

R Core Team. (2024). *A Language and Environment for Statistical Computing.* Tech. rep., R Foundation for Statistical Computing, Vienna, Austria.

Raimbault, B., Jolivet, R., Calais, E., Symithe, S., Fukushima, Y., & Dubernet, P. (2023). Rupture Geometry and Slip Distribution of the Mw 7.2 Nippes Earthquake, Haiti, From Space Geodetic Data. *Geochemistry, Geophysics, Geosystems, 24*, e2022GC010752. doi:10.1029/2022gc010752

Rathje, E. M., Bachhuber, J., Dulberg, R., Cox, B. R., Kottke, A., Wood, C., . . . Rix, G. (2011). Damage Patterns in Port-au-Prince during the 2010 Haiti Earthquake. *Earthquake Spectra, 27*, S117–S136. doi:10.1193/1.3637056

Regnier, J., Bonilla, L. F., Bertrand, E., & Semblat, J. F. (2014). Influence of the Vs profiles beyond 30 m depth on linear site effects: assessment from the KiK-net data. *Bulletin of the Seismological Society of America, 104*, 2337-2348. doi:10.1785/0120140018

Reynolds, J. M. (1997). *An introduction to applied and environmental geophysics* (Repr. ed.). Chichester: John Wiley & Sons Ltd.

Ricker, N. (1953). The form and laws of propagation of seismic wavelets. *Geophysics, 18*, 10–40. doi:10.1190/1.1437843

Rong, M., Li, H., & Yu, Y. (2019). The difference between horizontal-to-vertical spectra ratio and empirical transfer function as revealed by vertical arrays. *PLoS One, 14*, e0210852. doi:10.1371/journal.pone.0210852

Roullé, A., Noury, G., Auclair, S., Vanoudheusden, E., Bertil, D., Bastone, V., . . . Terrier, M. (2014). *Microzonage sismique de Cap-Haïtien (Haïti) : Effets de site et Liquéfaction.* Rapport final, BRGM/RC-63514-FR.

Saint-Fleur, N., Feuillet, N., Grandin, R., Jacques, E., Weil-Accardo, J., & Klinger, Y. (2015). Seismotectonics of southern Haiti: A new faulting model for the 12 January 2010 M7.0 earthquake. *Geophysical Research Letters, 42*, 10,273–10,281. doi:10.1002/2015GL065505

Sausse, J., Dezayes, C., Dorbath, L., Genter, A., & Place, J. (2010). 3D model of fracture zones at Soultz-sous-Forêts based on geological data, image logs, induced microseismicity and vertical seismic profiles. *Comptes Rendus Geoscience, 342*, 531-545. doi:10.1016/j.crte.2010.01.011

Scherer, J. (1912). Great Earthquakes in the Island of Haiti. *Bulletin of the Seismological Society*. doi:10.1785/bssa0020030161

Seed, R. B., Dickenson, S. E., & Idriss, I. M. (1991). Principal Geotechnical Aspects of the 1989 Loma Prieta Earthquake. *Soils and Foundations, 31*, 1-26. doi:10.3208/sandf1972.31.1

SESAME. (2004). *Guidelines for the implementation of the H/V spectral ratio technique on ambient vibrations. Measurements, Processing and Interpretation.* resreport, Sesame project - Deliverable D23.12 - WP12. European Commission – Research General Directorate Project No. EVG1-CT-2000-00026. Retrieved from https://www.earth-prints.org/handle/2122/47182

Sgobba, S., Felicetta, C., Bortolotti, T., Menafoglio, A., Lanzano, G., & Pacor, F. (2024). A geostatistical modelling of empirical amplification functions and related site proxies for shaking scenarios in central Italy. *Soil Dynamics and Earthquake Engineering, 179*, 108496. doi:10.1016/j.soildyn.2024.108496

Smerzini, C., Pitilakis, K., & Hashemi, K. (2017). Evaluation of earthquake ground motion and site effects in the Thessaloniki urban area by 3D finite-fault numerical simulations. *Bulletin of Earthquake Engineering, 15*, 787–812. doi:10.1007/s10518-016-9977-5

Spudich, P., Hellweg, M., & Lee, W. H. (1996). Directional topographic site response at Tarzana observed in aftershocks of the 1994 Northridge, California, earthquake: Implications for mainshock motions. *Bulletin of the Seismological Society of America, 86*, S193–S208. doi:10.1785/bssa08601bs193

St-Fleur, S., Bertrand, E., Courboulex, F., de Lépinay, B. M., Deschamps, A., Hough, S. E., . . . Prepetit, C. (2016). Site effects in Port-au-Prince (Haiti) from the analysis of spectral ratio and numerical simulations. *Bulletin of the Seismological Society of America, 106*, 1298-1315. doi:10.1785/0120150238

Symithe, S. J., Calais, E., Haase, J. S., Freed, A. M., & Douilly, R. (2013). Coseismic Slip Distribution of the 2010 M 7.0 Haiti Earthquake and Resulting Stress Changes on Regional Faults. *Bulletin of the Seismological Society of America, 103*, 2326–2343. doi:10.1785/0120120306

Symithe, S., Calais, E., de Chabalier, J. B., Robertson, R., & Higgins, M. (2015). Current block motions and strain accumulation on active faults in the Caribbean. *J. Geophys. Res. Solid Earth*. doi:10.1002/2014JB011779

Terrier, M., Bialkowski, A., Nachbaur, A., Prépetit, C., & Joseph, Y. F. (2014). Revision of the geological context of the Port-au-Prince metropolitan area, Haiti: implications for slope failures and seismic hazard assessment. *Nat. Hazards Earth Syst. Sci., 14*, 2577-2587. doi:10.5194/nhess-14-2577-2014

Thokchom, S., Rastogi, B. K., Dogra, N. N., Pancholi, V., Sairam, B., Bhattacharya, F., & Patel, V. (2017). Empirical correlation of SPT blow counts versus shear wave velocity for different types of soils in Dholera, Western India. *Natural Hazards, 86*, 1291–1306. doi:10.1007/s11069-017-2744-3

Thompson, E. M., Baise, L. G., Kayen, R. E., Tanaka, Y., & Tanaka, H. (2010). A geostatistical approach to mapping site response spectral amplifications. *Engineering Geology, 114*, 330-342. doi:10.1016/j.enggeo.2010.05.010

Torcal, F., Posadas, A. M., Chica, M., & Serrano, I. (1999). Application of conditional geostatistical simulation to calculate the probability of occurrence of earthquakes belonging to a seismic series. *Geophysical Journal International, 139*, 703–725. doi:10.1046/j.1365-246x.1999.00972.x

Ulysse, S., Boisson, D., Dorival, V., Guerrier, K., Préptit, C., Cauchie, L., . . . Havenith, H.-B. (2021). Site Effect Potential in Fond Parisien, in the East of Port-au-Prince, Haiti. *Geosciences, 11*, 175. doi:10.3390/geosciences11040175

Ulysse, S., Boisson, D., Prépetit, C., & Havenith, H.-B. (2018). Site Effect Assessment of the Gros-Morne Hill Area in Port-au-Prince, Haiti, Part A: Geophysical-Seismological Survey Results. *Geosciences, 8*, 142. doi:10.3390/geosciences8040142

Ulysse, S., Boisson, D., Prépetit, C., & Havenith, H.-B. (2018). Site Effect Assessment of the Gros-Morne Hill Area in Port-au-Prince, Haiti, Part B: Mapping and Modelling Results. *Geosciences, 8*, 233. doi:10.3390/geosciences8070233

Verly, G. (1993). Sequential Gaussian simulation: a Monte Carlo method for generating models of porosity and permeability. *Generation, Accumulation and Production of Europe's Hydrocarbons III. 3.* Springer, Berlin, Heidelberg. doi:10.1007/978-3-642-77859-9_28

Victor, K. H., & Dorival, V. (2022). *Évaluation de l'aléa mouvement de terrain sur la RN7 (Cayes-Jérémie, PK 18+000 à 41+000) suite au séisme du 14 août 2021.* Tech. rep., URGéo-FDS-UEH.

Wald, D. J. (1996). Slip history of the 1995 Kobe, Japan, earthquake determined from strong motion, teleseismic, and geodetic data. *Journal of Physics of the Earth, 44*, 489-503. doi:10.4294/jpe1952.44.489

Wathelet, M., Chatelain, J.-L., Cornou, C., di Giulio, G., Guillier, B., Ohrnberger, M., & Savvaidis, A. (2020). Geopsy: A User-Friendly OpenSource Tool Set for Ambient Vibration Processing. *Seismological Research Letters, 91*, 1878–1889. doi:10.1785/0220190360

Wolter, A., Gischig, V., Stead, D., & Clague, J. J. (2016). Investigation of Geomorphic and Seismic Effects on the 1959 Madison Canyon, Montana, Landslide Using an Integrated Field, Engineering Geomorphology Mapping, and Numerical Modelling Approach. *Rock Mechanics and Rock Engineering, 49*, 2479–2501. doi:10.1007/s00603-015-0889-5

Woodring, W. P., Brown, J. S., & Burbank, W. S. (1924). *Geology of the Republic of Haiti* (first ed.). Dept. Of Public Works, Rep. Of Haiti, Port-au-Prince.

Wu, C., Wu, J., Luo, Y., Zhang, L., & Degloria, S. D. (2009). Spatial Estimation of Soil Total Nitrogen Using Cokriging with Predicted Soil Organic Matter Content. *Soil Science Society of America Journal, 73*, 1676-1681. doi:10.2136/sssaj2008.0205

Xia, J., Miller, R. D., & Park, C. B. (1999). Estimation of near-surface shearwave velocity by inversion of Rayleigh waves. *Geophysics, 64*, 691-700. doi:10.1190/1.1444578

Yongbin, W., & Yitang, Z. (2007). 3D vizualization geological modeling based on Petrel. *Computer Applications of Petroleum, 8*.

Youd, T. L. (2003). Liquefaction Mechanisms and Induced Ground Failure. *International Geophysics, 81*, 1159-1173. doi:10.1016/s0074-6142(03)80184-5

Youd, T. L., & Idriss, I. M. (2001). Liquefaction Resistance of Soils: Summary Report from the 1996 NCEER and 1998 NCEER/NSF Workshops on Evaluation of Liquefaction Resistance of Soils. *Journal of Geotechnical and Geoenvironmental Engineering, 127*, 297-384. doi:10.1061/(asce)1090-0241(2001)127:4(297)

Zhang, J., & Toksöz, M. N. (1998). Non-linear refraction travel time tomography. *Geophysics, 63*, 1726–1737. doi:10.1190/1.1444468

Zhou, H. (2018). Review on the study of topographic effect on seismic ground motion. *Earthq Sci, 31*, 110-116. doi:10.29382/eqs-2018-0110-8

Appendix A. Surveys result in Anse-à-Veau

Appendix A1: Results of H/V measurements for the study area of Anse-à-Veau

The results of ambient noise H/V spectral ratio are mainly average curves called H/V curves. The shape of the curve is influenced by the depth of the superficial layer (of the measurement site) and its impedance contrast with the underlying hard rock. For a site on soft sediments with a clear impedance contrast with the hard rock, the H/V curve shows a peak indicating the fundamental resonance frequency f_0 of the site and the amplitude A_0. When the surface layer is very compact, the H/V curve is flat, the amplitude A_0 is then very low and the fundamental frequency is not considered. A multilayered superficial deposit with clear impedance contrast between the layers and with the bedrock can produce H/V curve with additional peaks (f_1, A_1,…) characterizing the different layers.

The following tables and figures present the results of the ambient noise H/V measurements in the study area of Anse-à-Veau, processed using the software Geopsy (Wathelet et al. 2020).

Table A.1 Summary of the H/V measurements in Anse-à-Veau (HV 001 – HV 002).

No	code	latitude	longitude	f_0 (Hz)	A_0	f_1 (Hz)	A_1
HV 001	HVSR 01 P1	18.505139	-73.34575	2.04	1.89		
HV 002	HVSR 02 P1	18.505139	-73.345583	2.25	2.17		
HV 003	HVSR 01 P2	18.504222	-73.3455	1.48	1.72		
HV 004	HVSR 02 P2	18.504333	-73.345722	1.74	1.96		
HV 005	HVSR 01 P3	18.501556	-73.345944	6.1	3.25		
HV 006	HVSR 02 P3	18.501472	-73.345972	6.42	3.1		

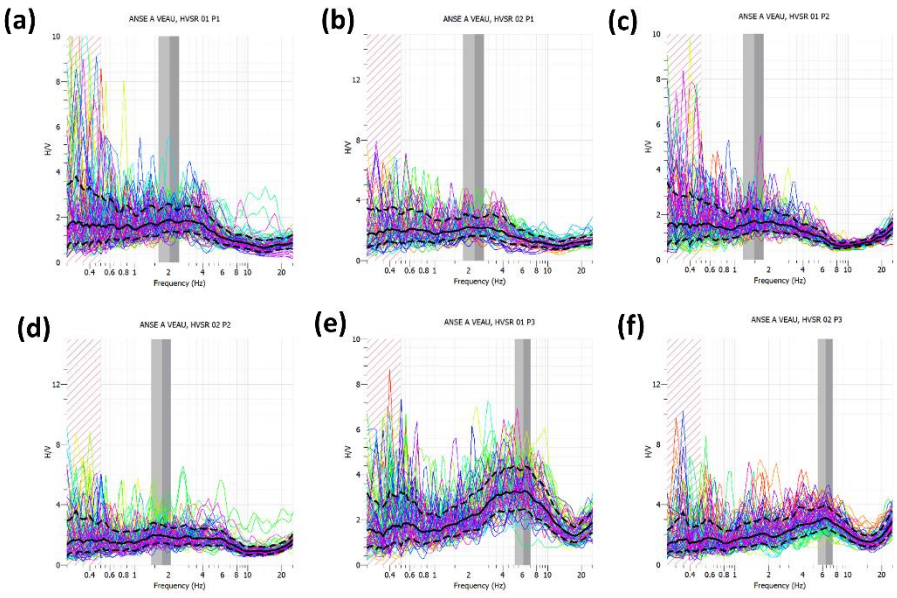

Fig. A.1 H/V curves for the measurements in Table A.1. **(a)** HV 001 – HVSR 01 P1. **(b)** HV 002 – HVSR 02 P1. **(c)** HV 003 – HVSR 01 P2. **(d)** HV 004 – HVSR 02 P2. **(e)** HV 005 – HVSR 01 P3. **(f)** HV 006 – HVSR 02 P3.

Table A.2 Summary of the H/V measurements in Anse-à-Veau (HV 007 – HV 015).

No	code	latitude	longitude	f_0 (Hz)	A_0	f_1 (Hz)	A_1
HV 007	HVSR 01 P4	18.499028	-73.346472	0.92	6.33		
HV 008	HVSR 02 P4	18.498722	-73.346444	0.93	5.47		
HV 009	HVSR 01 P5	18.497139	-73.346972	1.18	5.58		
HV 010	HVSR 02 P5	18.497083	-73.346917	1.2	6.31		
HV 011	HVSR 01 P6	18.504917	-73.343861	1.82	1.75		
HV 012	HVSR 02 P6	18.504806	-73.344	2.56	2.2		
HV 013	HVSR 01 P7	18.503139	-73.344056	2.43	1.67		
HV 014	HVSR 03 P7	18.503028	-73.344111	1.75	1.49		
HV 015	HVSR 01 P8	18.5015	-73.344611	3.59	2.21		

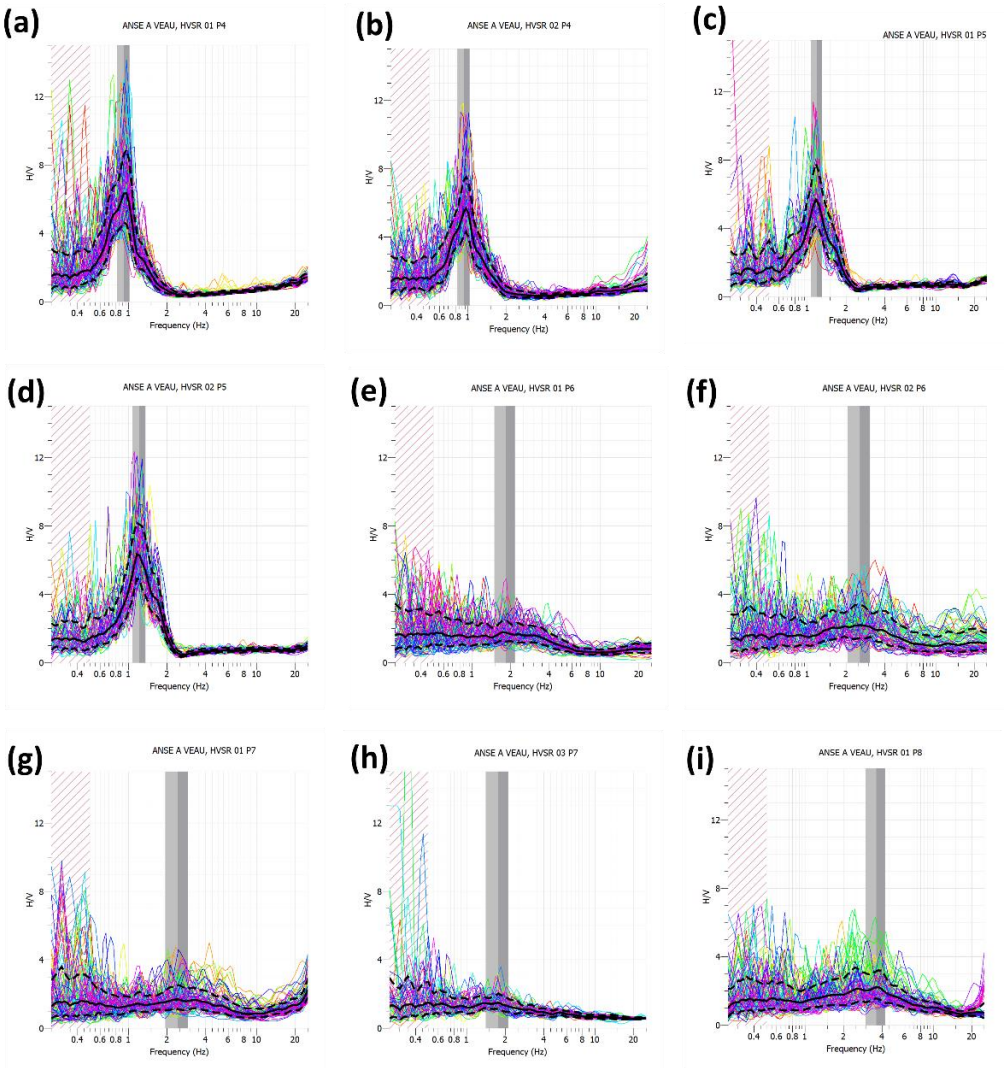

Fig. A.2 H/V curves for the measurements in Table A.2. **(a)** HV 007 – HVSR 01 P4. **(b)** HV 008 – HVSR 02 P4. **(c)** HV 009 – HVSR 01 P5. **(d)** HV 010 – HVSR 02 P5. **(e)** HV 011 – HVSR 01 P6. **(f)** HV 012 – HVSR 02 P6. **(g)** HV 013 – HVSR 01 P7. **(h)** HV 014 – HVSR 03 P7. **(i)** HV 015 – HVSR 01 P8.

Table A.3 Summary of the H/V measurements in Anse-à-Veau (HV 016 – HV 024).

No	code	latitude	longitude	f_0 (Hz)	A_0	f_1 (Hz)	A_1
HV 016	HVSR 02 P8	18.5015	-73.344444	1.76	1.97		
HV 017	HVSR 01 P9	18.5	-73.343778	2.13	2.75		
HV 018	HVSR 02 P9	18.500111	-73.343778	2.17	2.02		
HV 019	HVSR 01 P10	18.497028	-73.343889	1.37	4.02		
HV 020	HVSR 02 P10	18.496944	-73.343889	1.3	4.1		
HV 021	HVSR 01 P11	18.504389	-73.341944	0.63	1.76		
HV 022	HVSR 02 P11	18.504417	-73.341917	0.56	1.52		
HV 023	HVSR 01 P12	18.502528	-73.3405	2.51	1.38		
HV 024	HVSR 02 P12	18.502556	-73.340639	2.73	1.42		

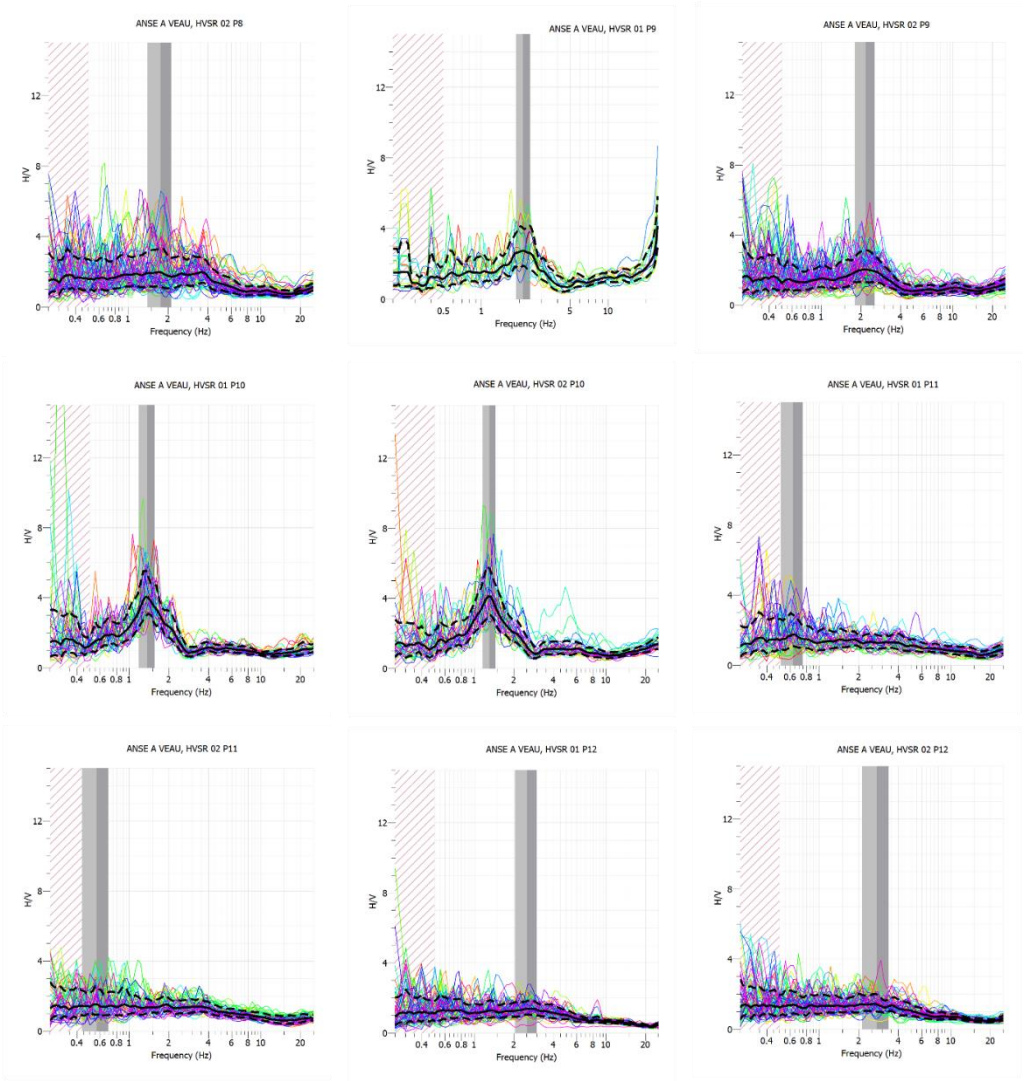

Fig. A.3 H/V curves for the measurements in Table A.3. **(a)** HV 016 – HVSR 02 P8. **(b)** HV 017 – HVSR 01 P9. **(c)** HV 018 – HVSR 02 P9. **(d)** HV 019 – HVSR 01 P10. **(e)** HV 020 – HVSR 02 P10. **(f)** HV 021 – HVSR 01 P11. **(g)** HV 022 – HVSR 02 P11. **(h)** HV 023 – HVSR 01 P12. **(i)** HV 024 – HVSR 02 P12.

Table A.4 Summary of the H/V measurements in Anse-à-Veau (HV 025 – HV 033).

No	code	latitude	longitude	f_0 (Hz)	A_0	f_1 (Hz)	A_1
HV 025	HVSR 01 P13	18.501083	-73.342361	2.62	1.53		
HV 026	HVSR 02 P13	18.500972	-73.341833	2.44	2.1		
HV 027	HVSR 01 P14	18.498639	-73.341444	1.63	2.54		
HV 028	HVSR 02 P14	18.498556	-73.341444	1.63	2.63		
HV 029	HVSR 01 P15	18.49625	-73.340333	1.22	3.17	21.38	6
HV 030	HVSR 02 P15	18.49625	-73.340667	1.2	3.62	12.72	5.54
HV 031	HVSR 01 P16	18.503972	-73.337028	3.06	2.6		
HV 032	HVSR 02 P16	18.503917	-73.337028	1.95	2.05		
HV 033	HVSR 01 P17	18.502972	-73.338472	18.97	3.9		

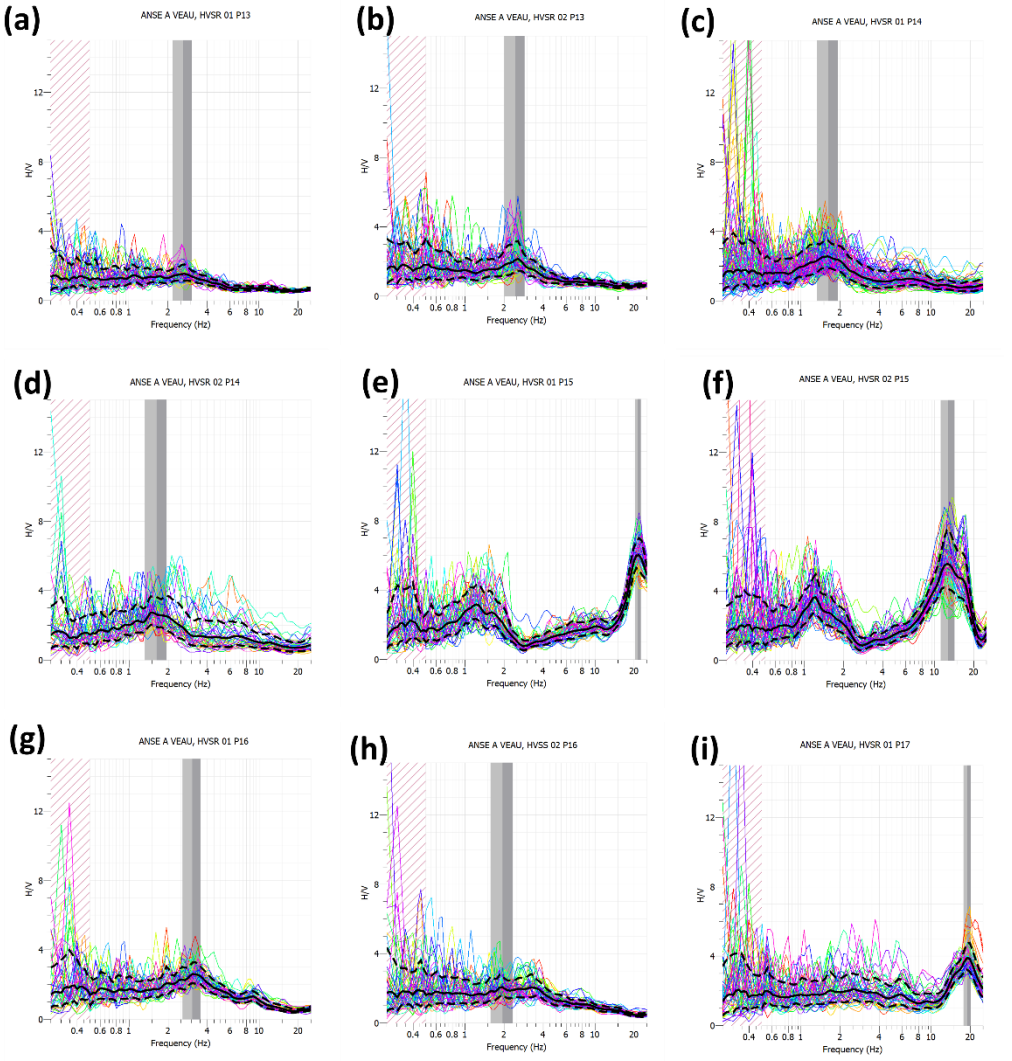

Fig. A.4 H/V curves for the measurements in Table A.4. **(a)** HV 025 – HVSR 01 P13. **(b)** HV 026 – HVSR 02 P13. **(c)** HV 027 – HVSR 01 P14. **(d)** HV 028 – HVSR 02 P14. **(e)** HV 029 – HVSR 01 P15. **(f)** HV 030 – HVSR 02 P15. **(g)** HV 031 – HVSR 01 P16. **(h)** HV 032 – HVSR 02 P16. **(i)** HV 033 – HVSR 01 P17.

Table A.5 Summary of the H/V measurements in Anse-à-Veau (HV 034 – HV 042).

No	code	latitude	longitude	f_0 (Hz)	A_0	f_1 (Hz)	A_1
HV 034	HVSR 02 P17	18.502833	-73.338667	18.93	3.71		
HV 035	HVSR 01 P18	18.499611	-73.339028	2.45	1.97		
HV 036	HVSR 03 P18	18.499972	-73.338861	2.88	1.58		
HV 037	HVSR 01 P19	18.497833	-73.338944	1.89	3.64		
HV 038	HVSR 02 P19	18.498194	-73.338917	1.79	2.87		
HV 039	HVSR 01 P20	18.494583	-73.338417	1.33	2.8		
HV 040	HVSR 02 P20	18.494667	-73.338361	1.58	2.85		
HV 041	HVSR 01 P21	18.494278	-73.343417	1.54	3.76	17.14	3.1
HV 042	HVSR 02 P21	18.494222	-73.343694	1.65	5.21	18.56	4.82

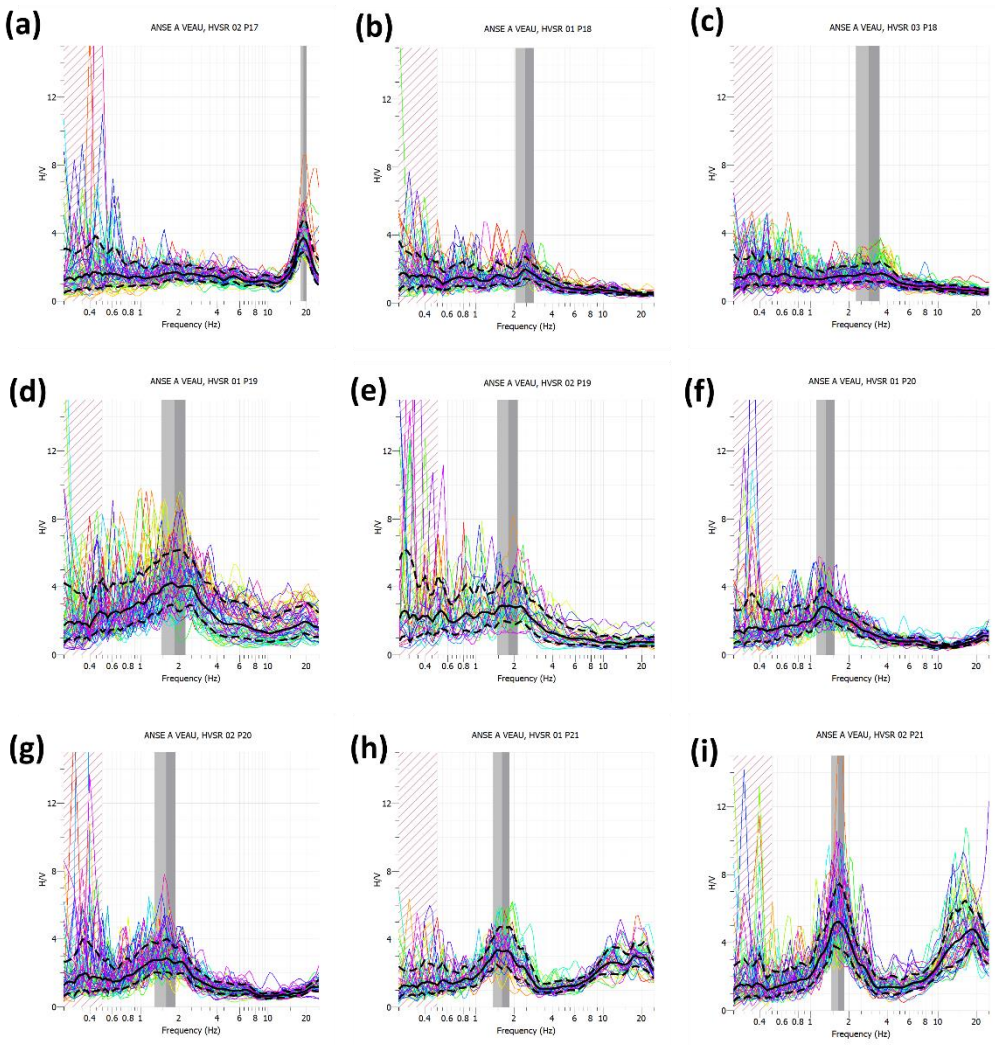

Fig. A.5 H/V curves for the measurements in Table A.5. **(a)** HV 034 – HVSR 02 P17. **(b)** HV 035 – HVSR 01 P18. **(c)** HV 036 – HVSR 03 P18. **(d)** HV 037 – HVSR 01 P19. **(e)** HV 038 – HVSR 02 P19. **(f)** HV 039 – HVSR 01 P20. **(g)** HV 040 – HVSR 02 P20. **(h)** HV 041 – HVSR 01 P21. **(i)** HV 042 – HVSR 02 P21.

Table A.6 Summary of the H/V measurements in Anse-à-Veau (HV 043 – HV 051).

No	code	latitude	longitude	f_0 (Hz)	A_0	f_1 (Hz)	A_1
HV 043	HVSR 01 P22	18.496556	-73.347944	1.28	5.71		
HV 044	HVSR 02 P22	18.496611	-73.348056	1.36	4.91		
HV 045	HVSR 01 P23	18.496806	-73.348639	1.33	5.02		
HV 046	HVSR 02 P23	18.496833	-73.348556	1.34	5.3		
HV 047	HVSR 01 P24	18.497417	-73.347778	1.26	4.7		
HV 048	HVSR 02 P24	18.497306	-73.34775	1.23	4.82		
HV 049	HVSR 01 P25	18.497389	-73.348306	1.33	4.17		
HV 050	HVSR 02 P25	18.497389	-73.34825	1.31	5.15		
HV 051	HVSR 01 P26	18.497528	-73.350294	1.16	3.96		

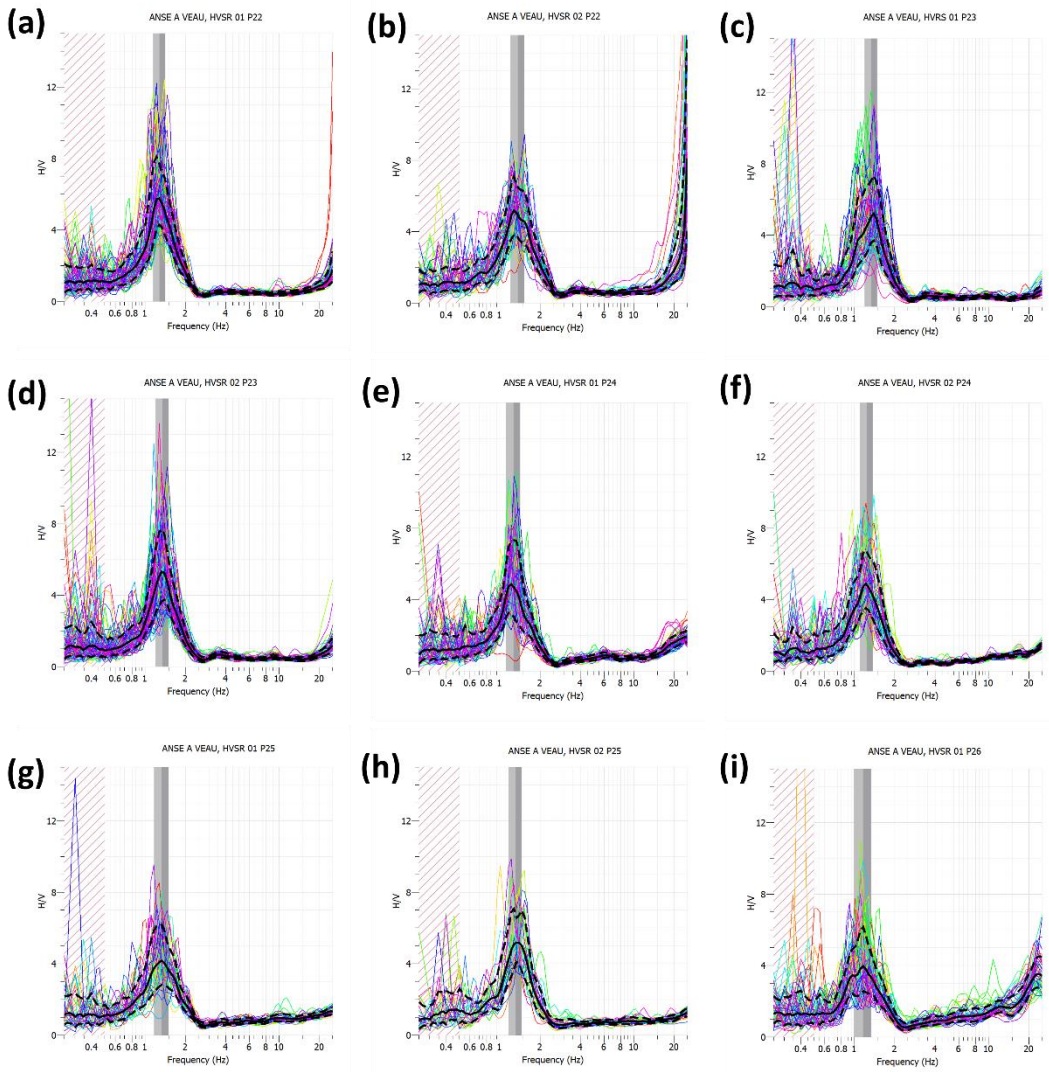

Fig. A.6 H/V curves for the measurements in Table A.6. **(a)** HV 043 – HVSR 01 P22. **(b)** HV 044 – HVSR 02 P22. **(c)** HV 045 – HVSR 01 P23. **(d)** HV 046 – HVSR 02 P23. **(e)** HV 047 – HVSR 01 P24. **(f)** HV 048 – HVSR 02 P24. **(g)** HV 049 – HVSR 01 P25. **(h)** HV 050 – HVSR 02 P25. **(i)** HV 051 – HVSR 01 P26.

Table A.7 Summary of the H/V measurements in Anse-à-Veau (HV 052 – HV 060).

No	code	latitude	longitude	f_0 (Hz)	A_0	f_1 (Hz)	A_1
HV 052	HVSR 02 P26	18.4975	-73.350528	1.14	3.76	16.97	3.04
HV 053	HVSR 01 P27	18.498667	-73.351694	0.98	5.6		
HV 054	HVSR 02 P27	18.498667	-73.351528	0.97	6.2		
HV 055	HVSR 01 P28	18.498889	-73.353528	2.43	2.61		
HV 056	HVSR 02 P28	18.499333	-73.353472	4.57	3.87		
HV 057	HVSR 01 P29	18.500111	-73.355444	1.36	2.29		
HV 058	HVSR 02 P29	18.500056	-73.35525	2.93	3.05		
HV 059	HVSR 01 P30	18.499639	-73.3565	1.36	2.01		
HV 060	HVSR 02 P30	18.499667	-73.356583	1.73	2.82		

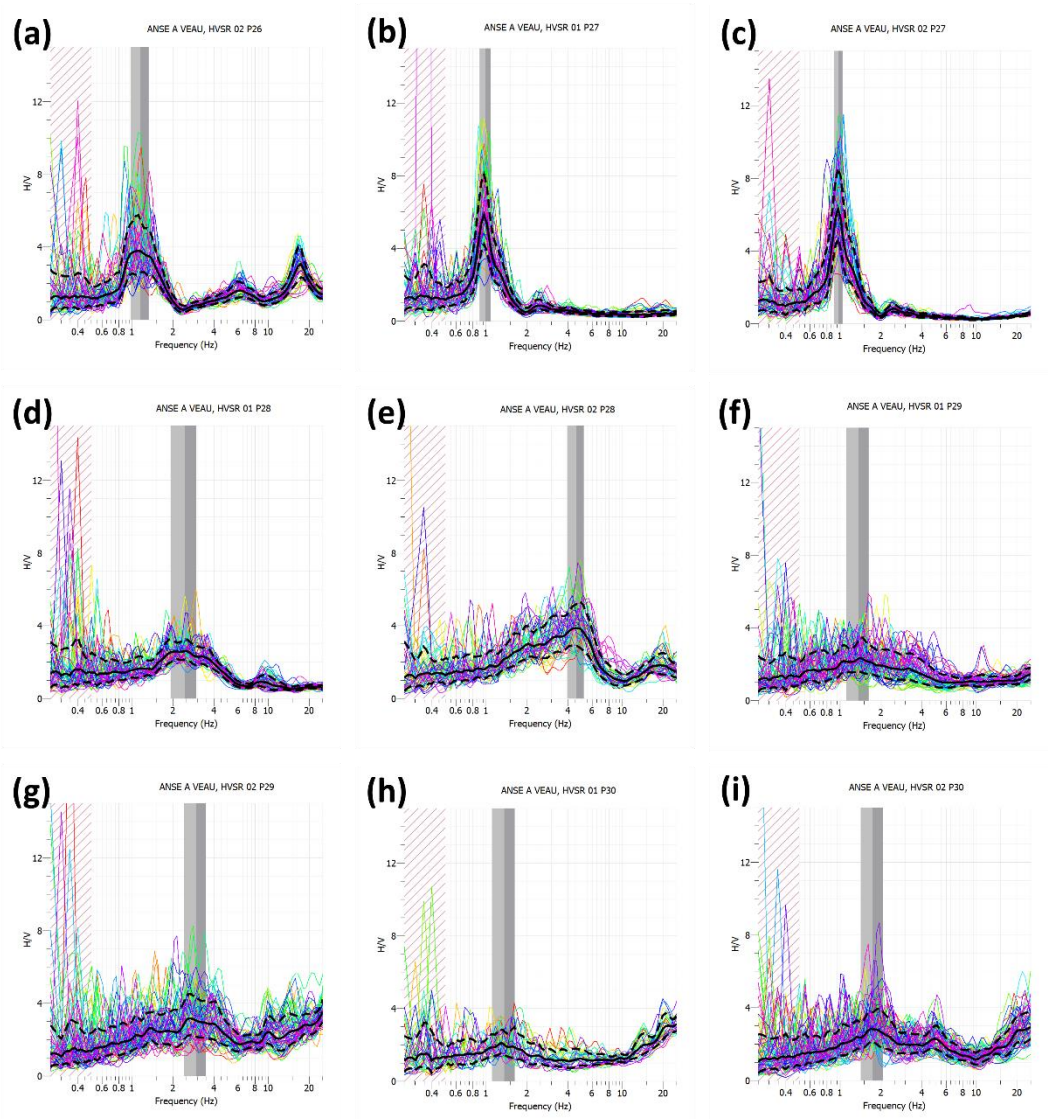

Fig. A.7 H/V curves for the measurements in Table A.7. **(a)** HV 052 – HVSR 02 P26. **(b)** HV 053 – HVSR 01 P27. **(c)** HV 054 – HVSR 02 P27. **(d)** HV 055 – HVSR 01 P28. **(e)** HV 056 – HVSR 02 P28. **(f)** HV 057 – HVSR 01 P29. **(g)** HV 058 – HVSR 02 P29. **(h)** HV 059 – HVSR 01 P30. **(i)** HV 060 – HVSR 02 P30.

Table A.8 Summary of the H/V measurements in Anse-à-Veau (HV 061 – HV 070).

No	code	latitude	longitude	f_0 (Hz)	A_0	f_1 (Hz)	A_1
HV 061	HVSR 01 P31	18.500833	-73.359056	1.31	2.55		
HV 062	HVSR 02 P31	18.500889	-73.359111	1.29	2.59		
HV 063	HVSR 01 P32	18.498417	-73.358528	2.4	3.46		
HV 064	HVSR 02 P32	18.498556	-73.358528	3.88	3.46		
HV 065	HVSR 01 P33	18.498944	-73.357306	1.44	2.58	10.54	2.1
HV 066	HVSR 02 P33	18.499167	-73.357111	1.44	2.58	10.54	2.1
HV 067	HVSR 01 P34	18.499028	-73.355389	1.59	2.32		
HV 068	HVSR 02 P34	18.498917	-73.355528	1.52	3.07		
HV 069	HVSR 01 P35	18.49775	-73.354528	2.38	4.55		
HV 070	HVSR 02 P35	18.497694	-73.355	2.15	4.47		

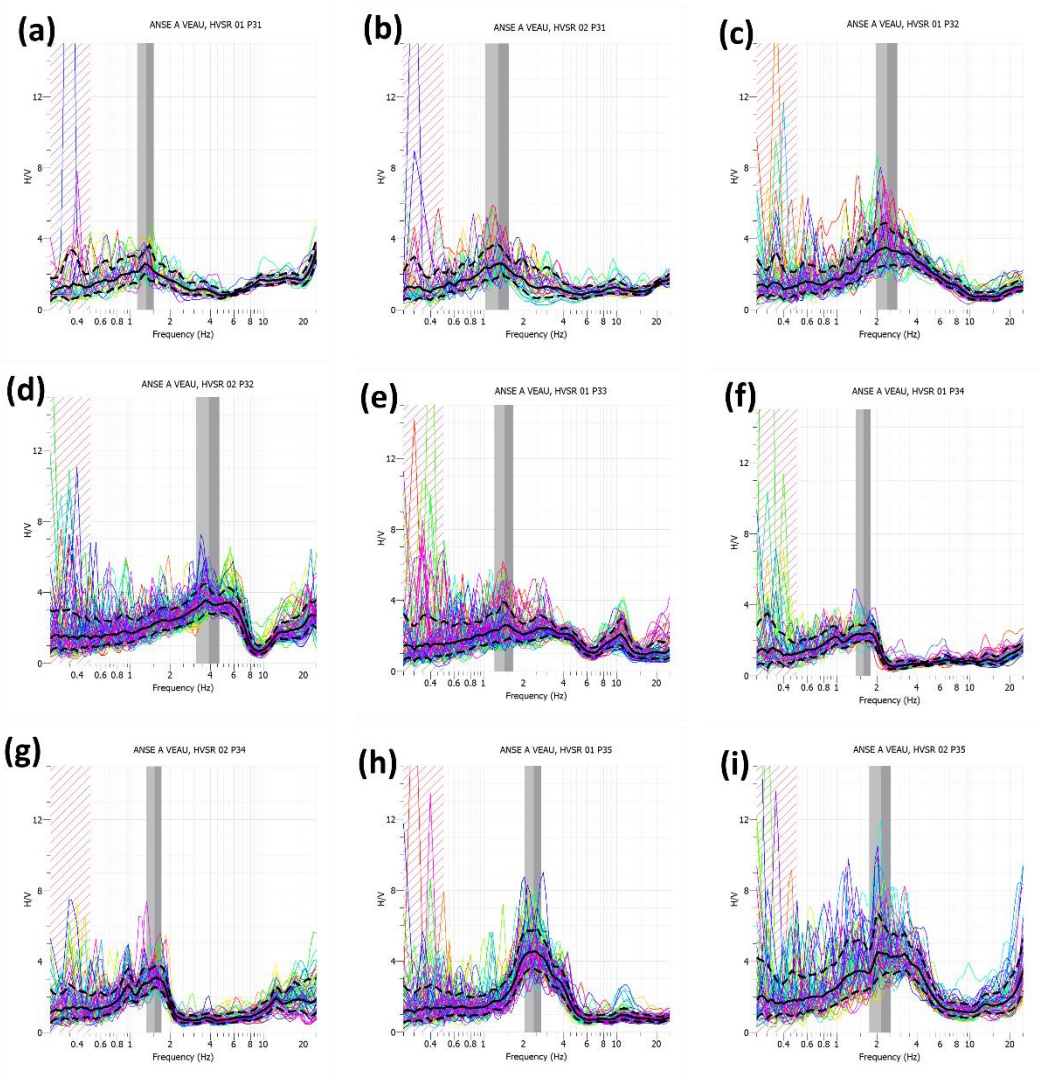

Fig. A.8 H/V curves for the measurements in Table A.8. **(a)** HV 061 – HVSR 01 P31. **(b)** HV 062 – HVSR 02 P31. **(c)** HV 063 – HVSR 01 P32. **(d)** HV 064 – HVSR 02 P32. **(e)** HV 065 – HVSR 01 P33. **(f)** HV 067 – HVSR 01 P34. **(g)** HV 068 – HVSR 02 P34. **(h)** HV 069 – HVSR 01 P35. **(i)** HV 070 – HVSR 02 P35.

Table A.9 Summary of the H/V measurements in Anse-à-Veau (HV 071 – HV 079).

No	code	latitude	longitude	f_0 (Hz)	A_0	f_1 (Hz)	A_1
HV 071	HVSR 01 P36	18.496778	-73.355111	3.12	7.57	18.55	3.17
HV 072	HVSR 02 P36	18.496944	-73.355111	2.55	5.67		
HV 073	HVSR 01 P37	18.497167	-73.356167	1.71	2.98		
HV 074	HVSR 02 P37	18.496833	-73.35625	1.44	1.7		
HV 075	HVSR 01 P38	18.497222	-73.358694	1.8	3.3		
HV 076	HVSR 02 P38	18.497028	-73.358778	9.74	6.74		
HV 077	HVSR 01 P39	18.496	-73.351889	1.71	3.33		
HV 078	HVSR 02 P39	18.495917	-73.351667	1.73	3.28		
HV 079	HVSR 01 P40	18.494972	-73.350056	1.17	5.59		

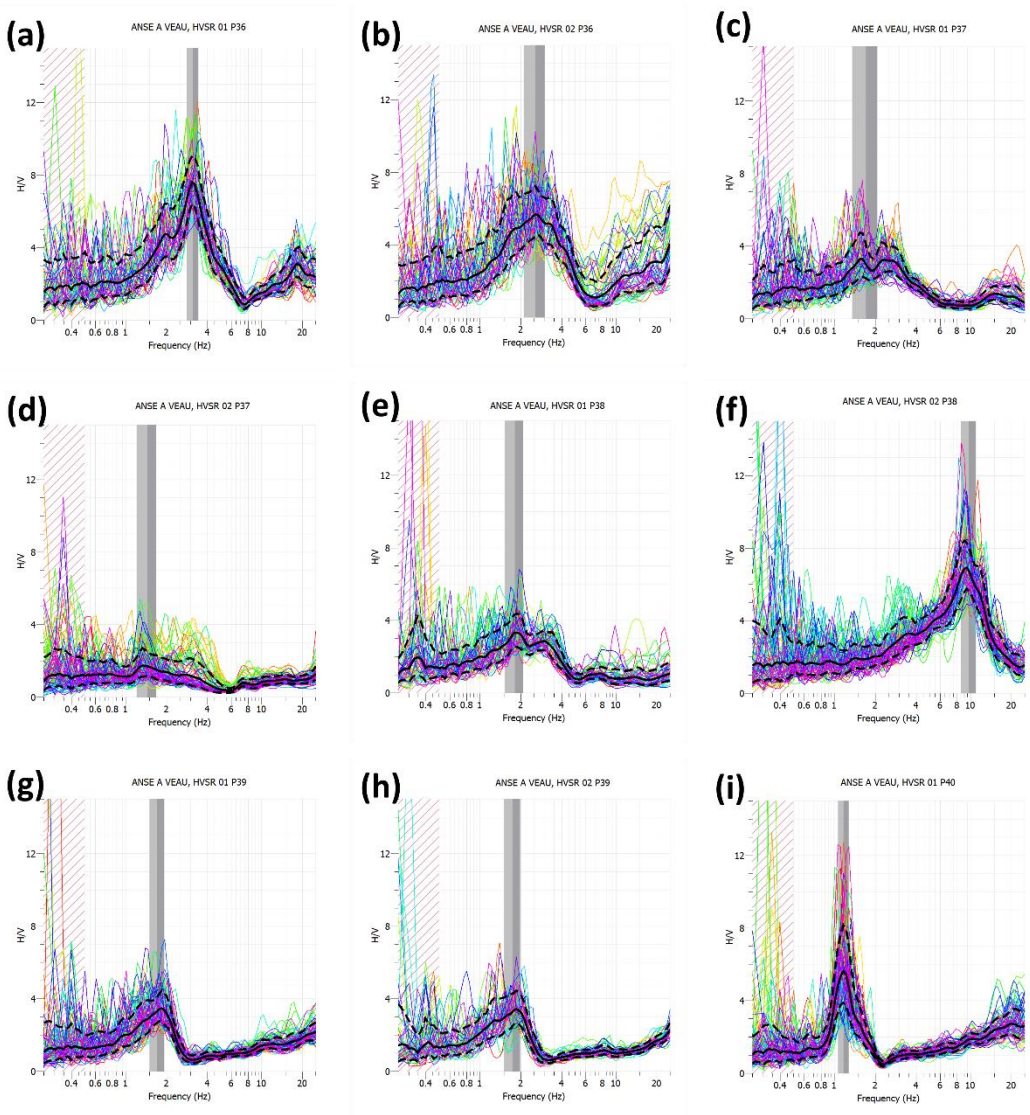

Fig. A.9 H/V curves for the measurements in Table A.9. **(a)** HV 071 – HVSR 01 P36. **(b)** HV 072 – HVSR 02 P36. **(c)** HV 073 – HVSR 01 P37. **(d)** HV 074 – HVSR 02 P37. **(e)** HV 075 – HVSR 01 P38. **(f)** HV 076 – HVSR 02 P38. **(g)** HV 077 – HVSR 01 P39. **(h)** HV 078 – HVSR 02 P39. **(i)** HV 079 – HVSR 01 P40.

Table A.10 Summary of the H/V measurements in Anse-à-Veau (HV 080 – HV 088).

No	code	latitude	longitude	f_0 (Hz)	A_0	f_1 (Hz)	A_1
HV 080	HVSR 02 P40	18.495083	-73.350028	1.14	5.61		
HV 081	HVSR 01 P41	18.493361	-73.351389	2.11	4.55		
HV 082	HVSR 02 P41	18.493611	-73.351806	2.02	5.09		
HV 083	HVSR 01 P42	18.490833	-73.355528	3.11	5.93	21.95	4.85
HV 084	HVSR 02 P42	18.490639	-73.355417	3.47	2.47		
HV 085	HVSR 01 P43	18.488917	-73.356083	5.86	3.01		
HV 086	HVSR 02 P43	18.488778	-73.355833	5.38	2.92		
HV 087	HVSR 01 P44	18.486861	-73.357694	13.19	2.95		
HV 088	HVSR 02 P44	18.486944	-73.357639	20.89	2.96		

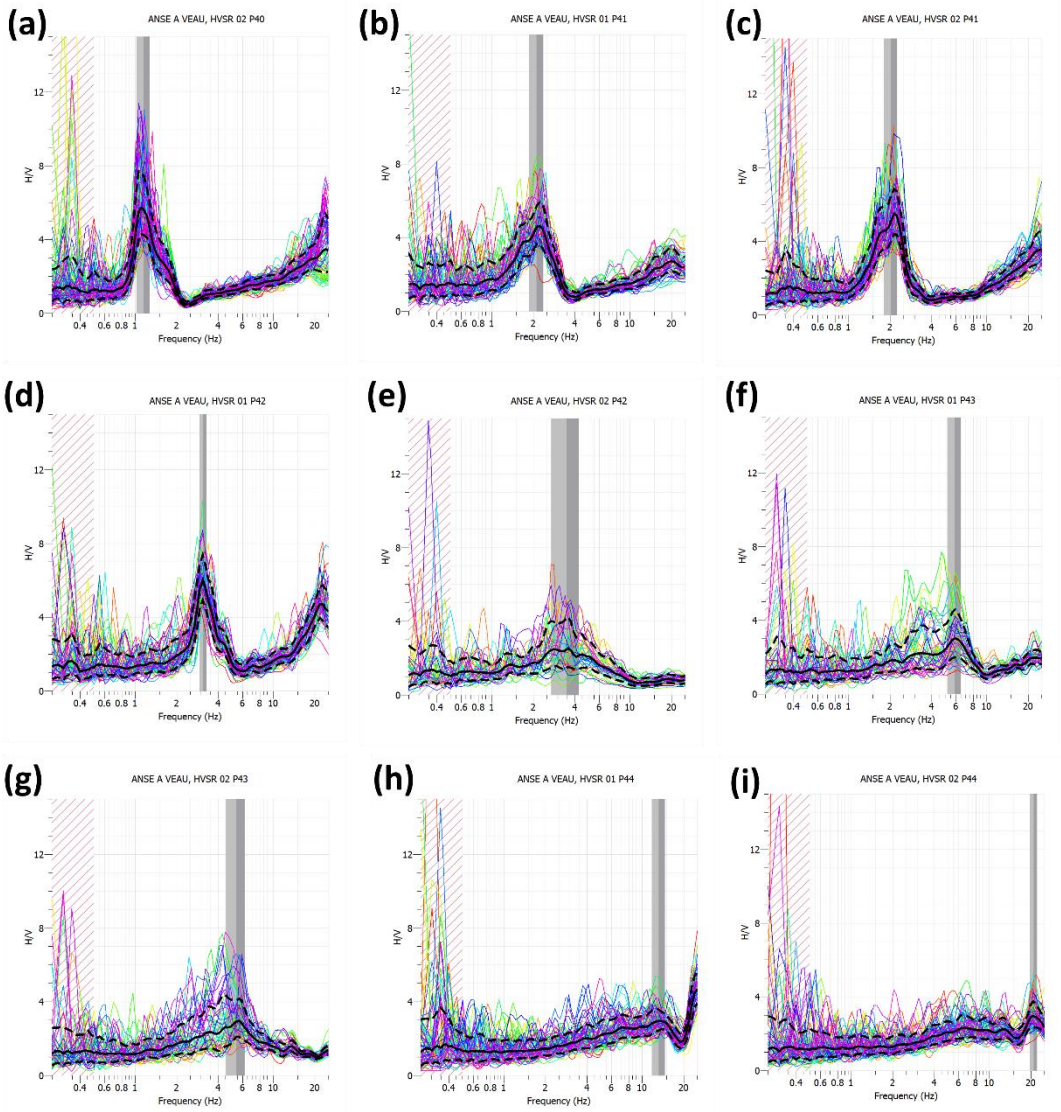

Fig. A.10 H/V curves for the measurements in Table A.10. **(a)** HV 080 – HVSR 02 P40. **(b)** HV 081 – HVSR 01 P41. **(c)** HV 082 – HVSR 02 P41. **(d)** HV 083 – HVSR 01 P42. **(e)** HV 084 – HVSR 02 P42. **(f)** HV 085 – HVSR 01 P43. **(g)** HV 086 – HVSR 02 P43. **(h)** HV 087 – HVSR 01 P44. **(i)** HV 088 – HVSR 02 P44.

Table A.11 Summary of the H/V measurements in Anse-à-Veau (HV 089 – HV 097).

No	code	latitude	longitude	f_0 (Hz)	A_0	f_1 (Hz)	A_1
HV 089	HVSR 01 P45	18.485917	-73.356333	7.52	1.29		
HV 090	HVSR 02 P45	18.486056	-73.356194	6.4	1.95		
HV 091	HVSR 01 P46	18.483889	-73.356389	4.42	4.46		
HV 092	HVSR 02 P46	18.484028	-73.356361	5.09	3.21		
HV 093	HVSR 01 P47	18.481444	-73.357139	4.95	4.3		
HV 094	HVSR 02 P47	18.481556	-73.356917	4.55	2.22		
HV 095	HVSR 01 P48	18.480528	-73.357472	4.84	1.75		
HV 096	HVSR 02 P48	18.480389	-73.357806	19.57	5.84		
HV 097	HVSR 01 P49	18.477944	-73.354806	20.45	10.1		

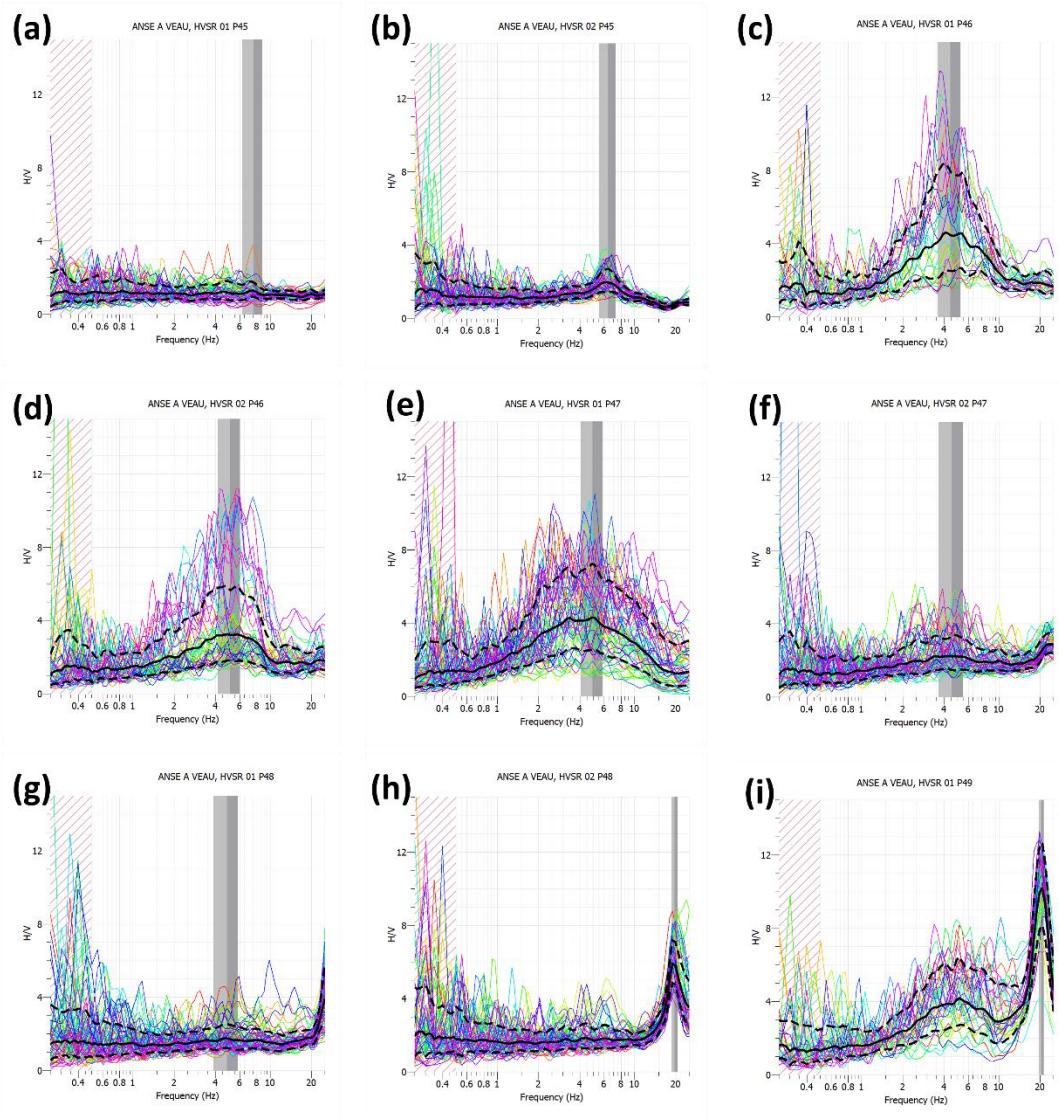

Fig. A.11 H/V curves for the measurements in Table A.11. **(a)** HV 089 – HVSR 01 P45. **(b)** HV 090 – HVSR 02 P45. **(c)** HV 091 – HVSR 01 P46. **(d)** HV 092 – HVSR 02 P46. **(e)** HV 093 – HVSR 01 P47. **(f)** HV 094 – HVSR 02 P47. **(g)** HV 095 – HVSR 01 P48. **(h)** HV 096 – HVSR 02 P48. **(i)** HV 097 – HVSR 01 P49.

Table A.12 Summary of the H/V measurements in Anse-à-Veau (HV 098 – HV 106).

No	code	latitude	longitude	f_0 (Hz)	A_0	f_1 (Hz)	A_1
HV 098	HVSR 02 P49	18.477944	-73.354722	16.99	6.18		
HV 099	HVSR 01 P50	18.476833	-73.357083	6.03	4.3		
HV 100	HVSR 02 P50	18.477028	-73.356972	5.33	5.75		
HV 101	HVSR 01 P51	18.474806	-73.357889	4.52	4.02		
HV 102	HVSR 02 P51	18.474833	-73.358028	4.35	3.85		
HV 103	HVSR 03 P1	18.50486111	-73.34533333	2.33	2.21		
HV 104	HVSR 03 P8	18.50175	-73.34505556	1.55	1.58		
HV 105	HVSR 03 P15	18.49711111	-73.34027778	1.18	2.1	19.42	2.97
HV 106	HVSR 03 P17	18.50275	-73.33883333	22.12	10.49		

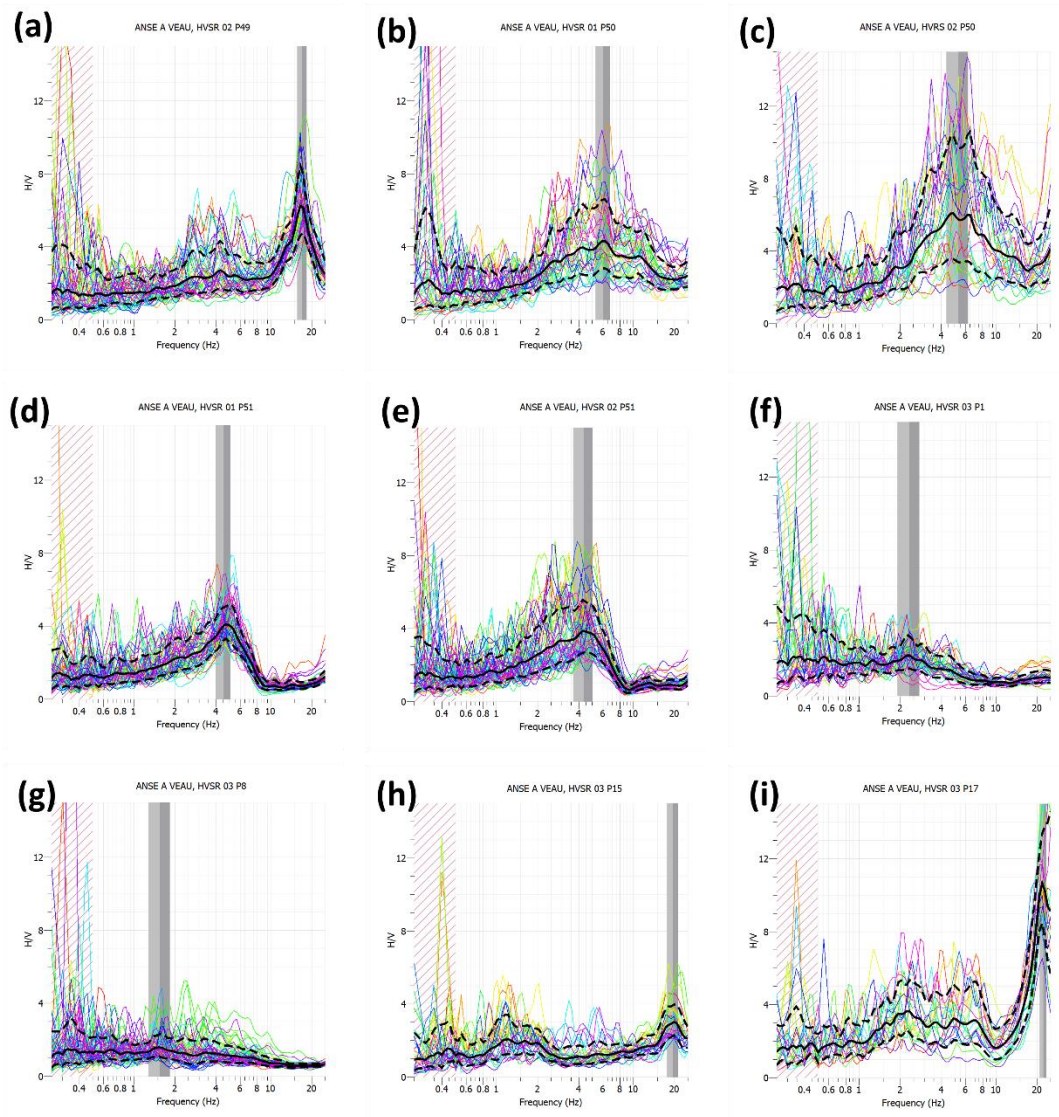

Fig. A.12 H/V curves for the measurements in Table A.12. **(a)** HV 098 – HVSR 02 P49. **(b)** HV 099 – HVSR 01 P50. **(c)** HV 100 – HVSR 02 P50. **(d)** HV 101 – HVSR 01 P51. **(e)** HV 102 – HVSR 02 P51. **(f)** HV 103 – HVSR 03 P1. **(g)** HV 104 – HVSR 03 P8. **(h)** HV 105 – HVSR 03 P15. **(i)** HV 106 – HVSR 03 P17.

Table A.13 Summary of the H/V measurements in Anse-à-Veau (HV 107 – HV 115).

No	code	latitude	longitude	f_0 (Hz)	A_0	f_1 (Hz)	A_1
HV 107	HVSR 01 P68	18.50213889	-73.34808333	2.72	2.55		
HV 108	HVSR 02 P68	18.50241667	-73.34797222	7.25	3.49		
HV 109	HVSR 01 P69	18.50216667	-73.332	15.47	3.14		
HV 110	HVSR 02 P69	18.50230556	-73.33155556	2.78	2.81	20.7	5.68
HV 111	HVSR 03 P69	18.50136111	-73.33230556	4.64	1.77		
HV 112	HVSR 01 P70	18.49716667	-73.33519444	2.56	2.96		
HV 113	HVSR 02 P70	18.49644444	-73.33416667	1.7	3.97		
HV 114	HVSR 01 P71	18.49663889	-73.33755556	1.58	3.59		
HV 115	HVSR 02 P71	18.4965	-73.33744444	1.5	3.25		

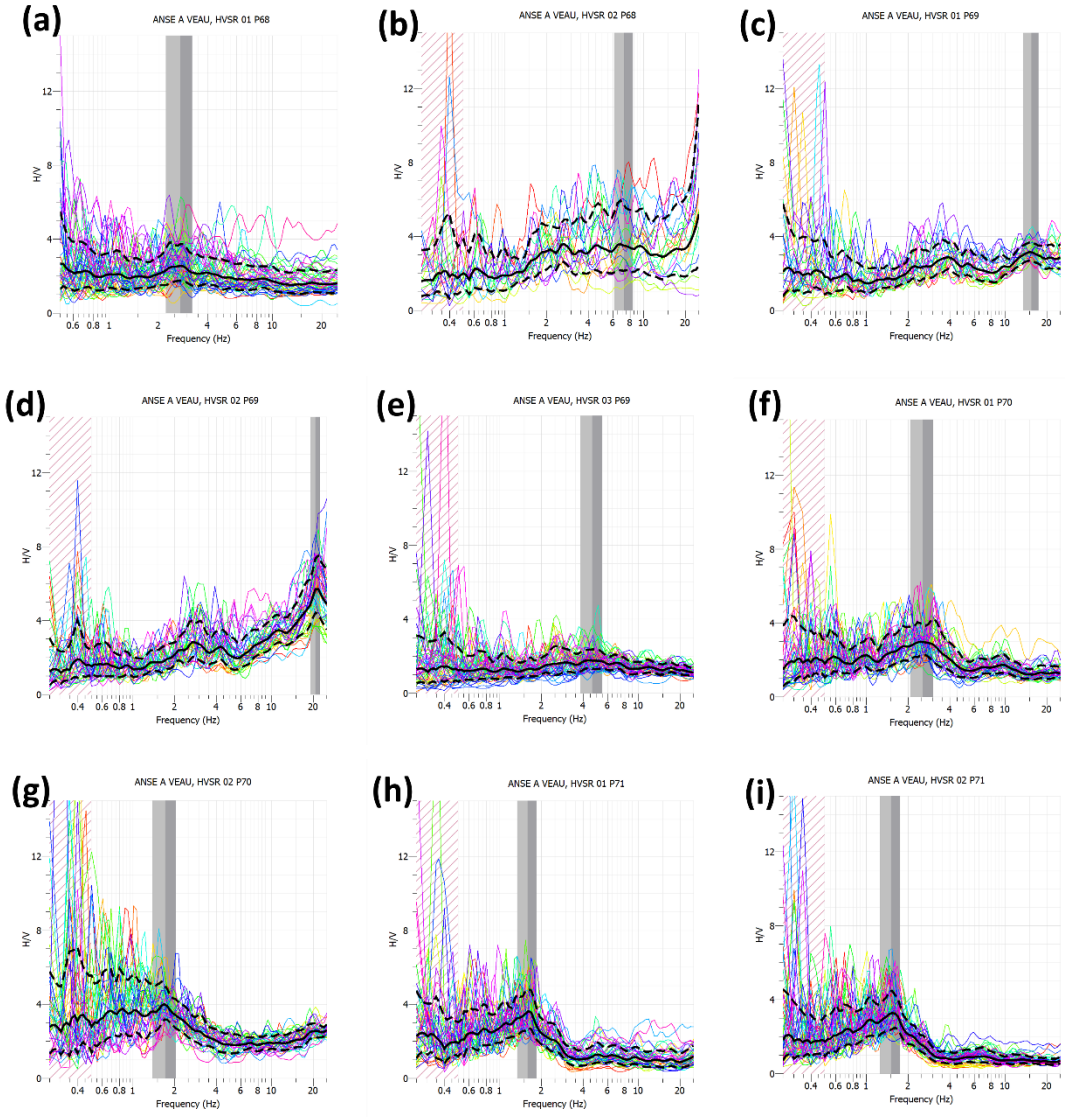

Fig. A.13 H/V curves for the measurements in Table A.13. **(a)** HV 107 – HVSR 01 P68. **(b)** HV 108 – HVSR 02 P68. **(c)** HV 109 – HVSR 01 P69. **(d)** HV 110 – HVSR 02 P69. **(e)** HV 111 – HVSR 03 P69. **(f)** HV 112 – HVSR 01 P70. **(g)** HV 113 – HVSR 02 P70. **(h)** HV 114 – HVSR 01 P71. **(i)** HV 115 – HVSR 02 P71.

Table A.14 Summary of the H/V measurements in Anse-à-Veau (HV 116 – HV 125).

No	code	latitude	longitude	f_0 (Hz)	A_0	f_1 (Hz)	A_1
HV 116	HVSR 01 P72	18.495	-73.33980556	1.18	2.96		
HV 117	HVSR 02 P72	18.49522222	-73.33969444	1.23	4.79		
HV 118	HVSR 01 P73	18.49188889	-73.34536111	5.92	5.49		
HV 119	HVSR 02 P73	18.49163889	-73.34497222	4.61	3.41		
HV 120	HVSR 01 P74	18.49025	-73.34944444	4.9	2.68		
HV 121	HVSR 02 P74	18.49013889	-73.34958333	5.16	2.64		
HV 122	HVSR 01 P75	18.48697222	-73.33780556	5.16	2.64		
HV 123	HVSR 02 P75	18.48763889	-73.33763889	4.71	1.58		
HV 124	HVSR 01 P76	18.49247222	-73.33461111	1.71	4.85		
HV 125	HVSR 02 P76	18.49227778	-73.33430556	2.02	4.01	13.24	3.27

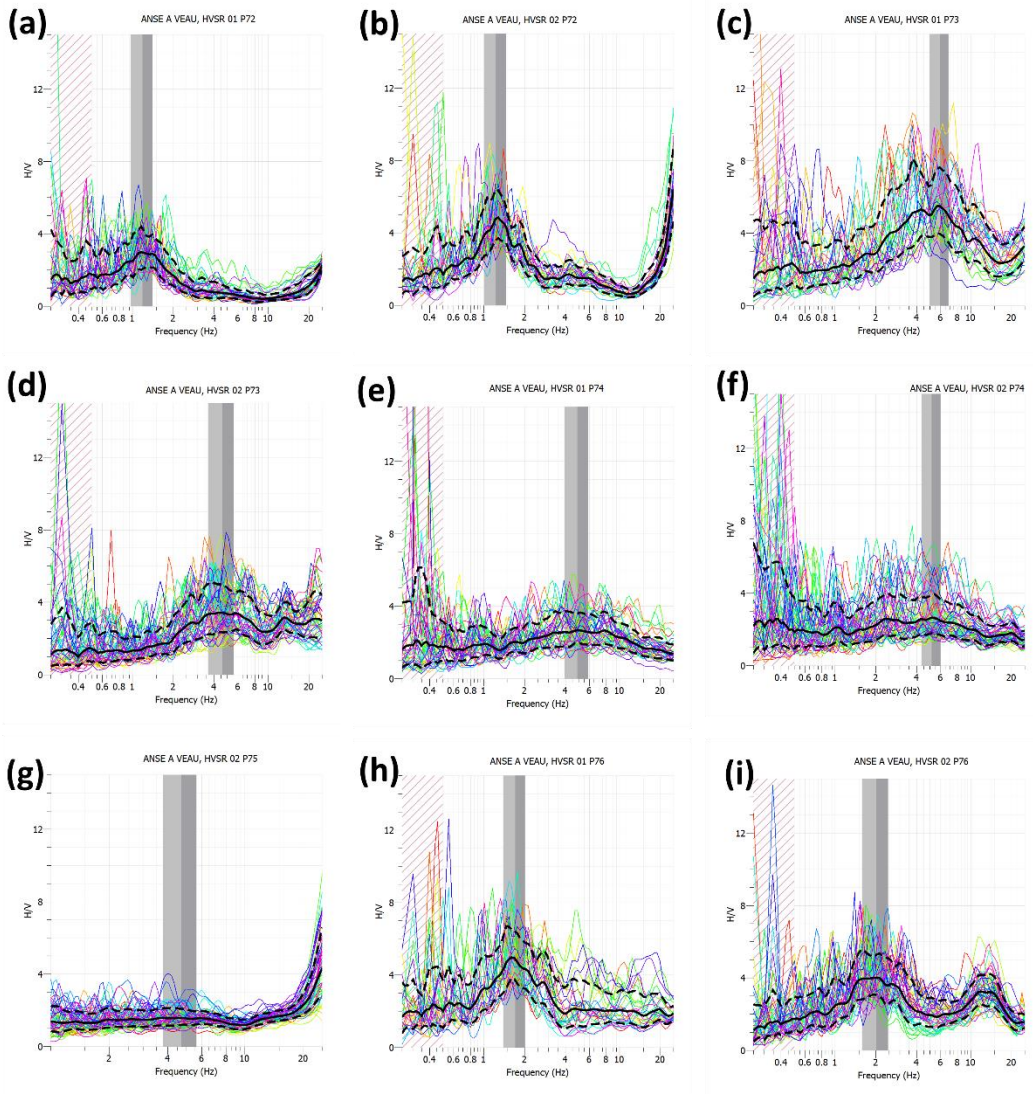

Fig. A.14 H/V curves for the measurements in Table A.14. **(a)** HV 116 – HVSR 01 P72. **(b)** HV 117 – HVSR 02 P72. **(c)** HV 118 – HVSR 01 P73. **(d)** HV 119 – HVSR 02 P73. **(e)** HV 120 – HVSR 01 P74. **(f)** HV 121 – HVSR 02 P74. **(g)** HV 123 – HVSR 02 P75. **(h)** HV 124 – HVSR 01 P76. **(i)** HV 125 – HVSR 02 P76.

Table A.15 Summary of the H/V measurements in Anse-à-Veau (HV 126 – HV 134).

No	code	latitude	longitude	f_0 (Hz)	A_0	f_1 (Hz)	A_1
HV 126	HVSR 01 P52	18.473056	-73.365	4.13	2.88	13.49	3.64
HV 127	HVSR 02 P52	18.473098	-73.366439	4.45	3.06		
HV 128	HVSR 01 P54	18.482222	-73.368889	3.59	5		
HV 129	HVSR 01 P55	18.479167	-73.364444	5.65	2.52		
HV 130	HVSR 01 P56	18.483889	-73.361667	0.82	1.37		
HV 131	HVSR 01 P57	18.489444	-73.36	3.73	3.07		
HV 132	HVSR 01 P58	18.489722	-73.366389	9.12	2.44		
HV 133	HVSR 01 P59	18.492906	-73.354069	7.01	8.22		
HV 134	HVSR 02 P59	18.492688	-73.355312	14.23	4.76		

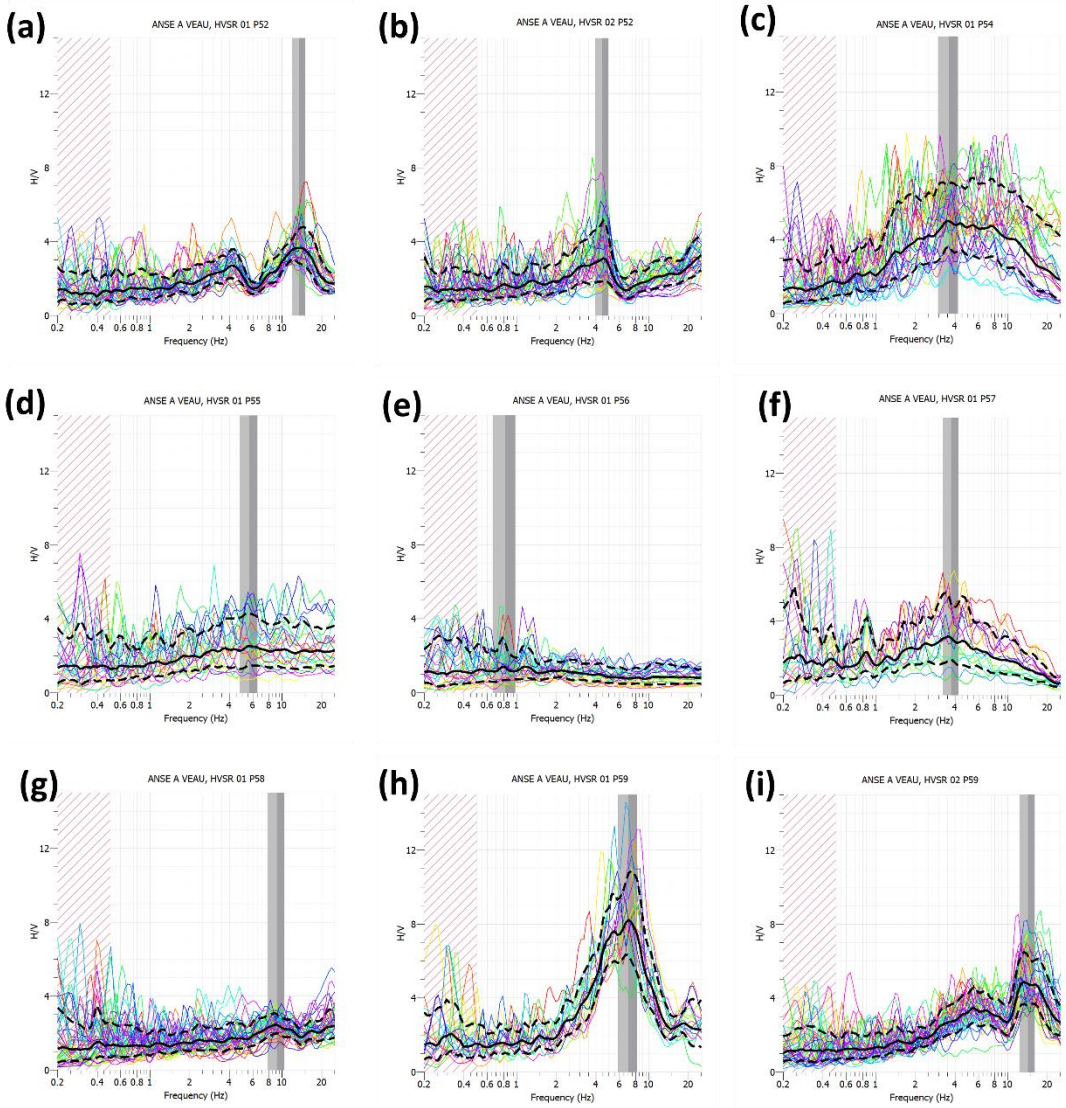

Fig. A.15 H/V curves for the measurements in Table A.15. **(a)** HV 126 – HVSR 01 P52. **(b)** HV 127 – HVSR 02 P52. **(c)** HV 128 – HVSR 01 P54. **(d)** HV 129 – HVSR 01 P55. **(e)** HV 130 – HVSR 01 P56. **(f)** HV 131 – HVSR 01 P57. **(g)** HV 132 – HVSR 01 P58. **(h)** HV 133 – HVSR 01 P59. **(i)** HV 134 – HVSR 02 P59.

Table A.16 Summary of the H/V measurements in Anse-à-Veau (HV 135 – HV 143).

No	code	latitude	longitude	f_0 (Hz)	A_0	f_1 (Hz)	A_1
HV 135	HVSR 01 P61	18.49495	-73.364921	1.89	3.63		
HV 136	HVSR 01 P62	18.499167	-73.370556	2.18	4.9		
HV 137	HVSR 01 P63	18.498618	-73.363021	1.55	2.45	21.1	5.01
HV 138	HVSR 01 P64	18.501899	-73.37076	1.88	4.85		
HV 139	HVSR 02 P64	18.502623	-73.370629	1.44	4.19		
HV 140	HVSR 01 P65	18.509722	-73.370278	1.74	1.72		
HV 141	HVSR 01 P67	18.501801	-73.358698	1.1	1.64		
HV 142	HVSR 02 P67	18.503198	-73.358511	1.58	2.62		
HV 143	HVSR 01 P77	18.498056	-73.329167	2.75	3.73		

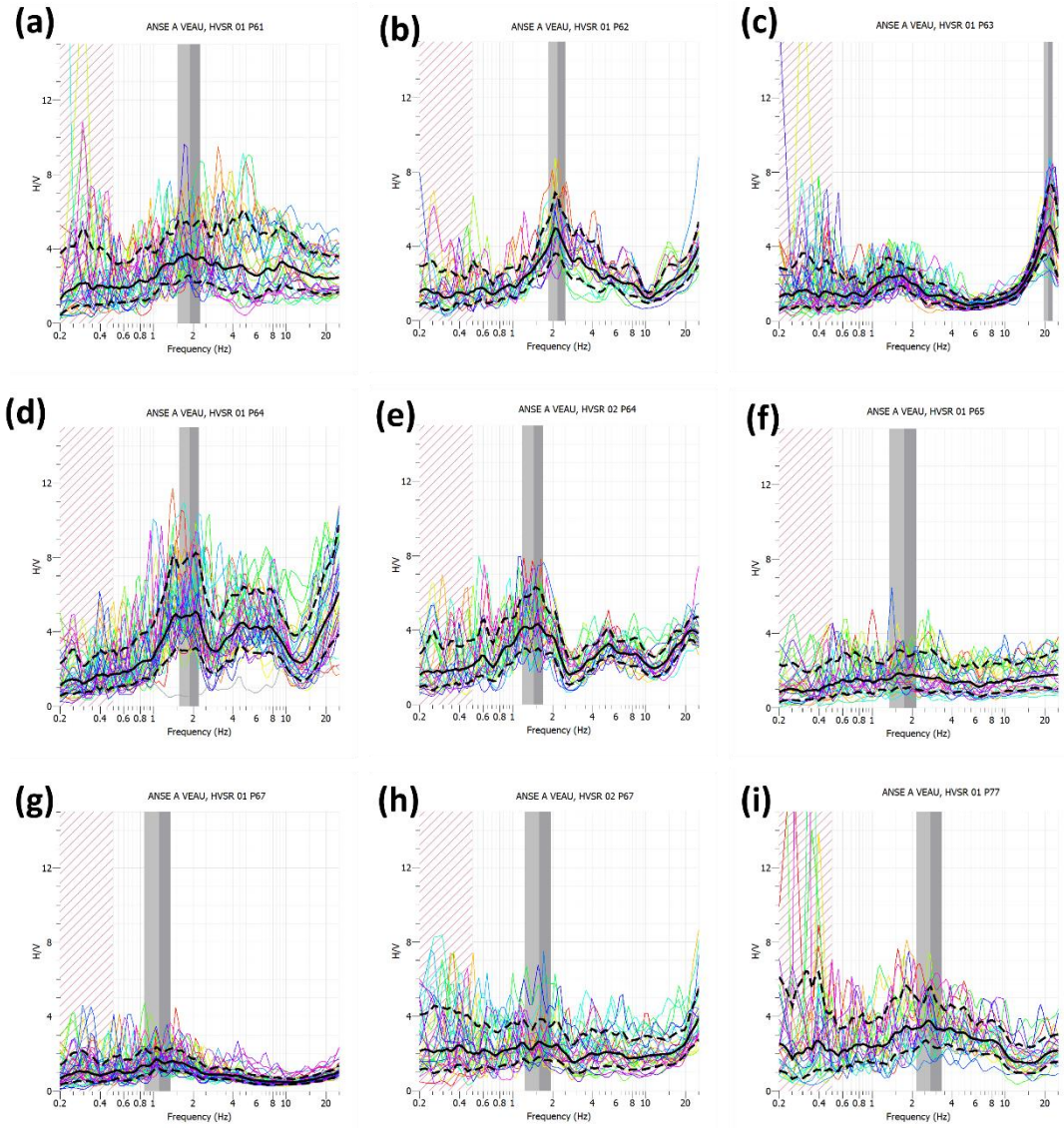

Fig. A.16 H/V curves for the measurements in Table A.16. **(a)** HV 135 – HVSR 01 P61. **(b)** HV 136 – HVSR 01 P62. **(c)** HV 137 – HVSR 01 P63. **(d)** HV 138 – HVSR 01 P64. **(e)** HV 139 – HVSR 03 P64. **(f)** HV 140 – HVSR 01 P65. **(g)** HV 141 – HVSR 01 P67. **(h)** HV 142 – HVSR 02 P67. **(i)** HV 143 – HVSR 01 P77.

Table A.17 Summary of the H/V measurements in Anse-à-Veau (HV 144 – HV 152).

No	code	latitude	longitude	f_0 (Hz)	A_0	f_1 (Hz)	A_1
HV 144	HVSR 01 P78	18.4925	-73.327778	1.71	4.72		
HV 145	HVSR 01 P79	18.487778	-73.322778	8.14	1.74		
HV 146	HVSR 01 P80	18.488611	-73.319444	3.5	7.82		
HV 147	HVSR 01 P81	18.486538	-73.315034	2.38	3.81	15.05	4.79
HV 148	HVSR 02 P81	18.485833	-73.315556	2.24	5.59		
HV 149	HVSR 01 P82	18.480556	-73.321944	21.27	5.08		
HV 150	HVSR 01 P83	18.480556	-73.315833	16.28	5.55		
HV 151	HVSR 01 P84	18.479444	-73.324722	4.71	1.76		
HV 152	HVSR 01 P86	18.472855	-73.348524	4.74	1.76		

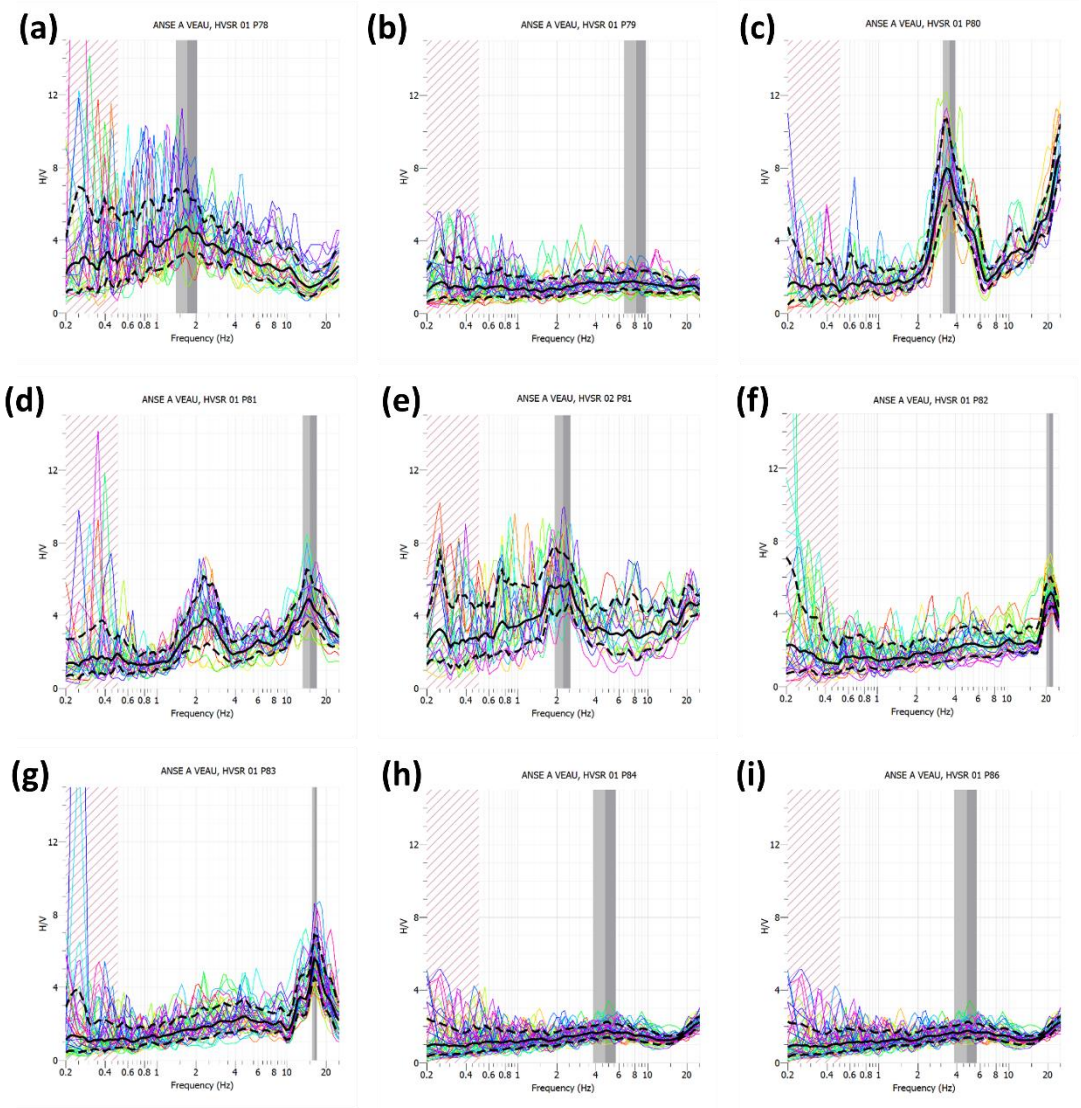

Fig. A.17 H/V curves for the measurements in Table A.17. **(a)** HV 144 – HVSR 01 P78. **(b)** HV 145 – HVSR 01 P79. **(c)** HV 146 – HVSR 01 P80. **(d)** HV 147 – HVSR 01 P81. **(e)** HV 148 – HVSR 02 P81. **(f)** HV 149 – HVSR 01 P82. **(g)** HV 150 – HVSR 01 P83. **(h)** HV 151 – HVSR 01 P84. **(i)** HV 152 – HVSR 01 P86.

Table A.18 Summary of the H/V measurements in Anse-à-Veau (HV 153 – HV 159).

No	code	latitude	longitude	f_0 (Hz)	A_0	f_1 (Hz)	A_1
HV 153	HVSR 01 P87	18.472523	-73.342691	2.45	3.79		
HV 154	HVSR 02 P87	18.471779	-73.341953	3.76	4.26		
HV 155	HVSR 01 P88	18.471389	-73.332222	3.1	3.61		
HV 156	HVSR 01 P89	18.471944	-73.317222	2.04	4.75		
HV 157	HVSR 02 P89	18.470833	-73.323333	1.78	6.45		
HV 158	HVSR 01 P90	18.476553	-73.316357	4.72	2.59		
HV 159	HVSR 02 P90	18.475556	-73.315833	5.51	5.75		

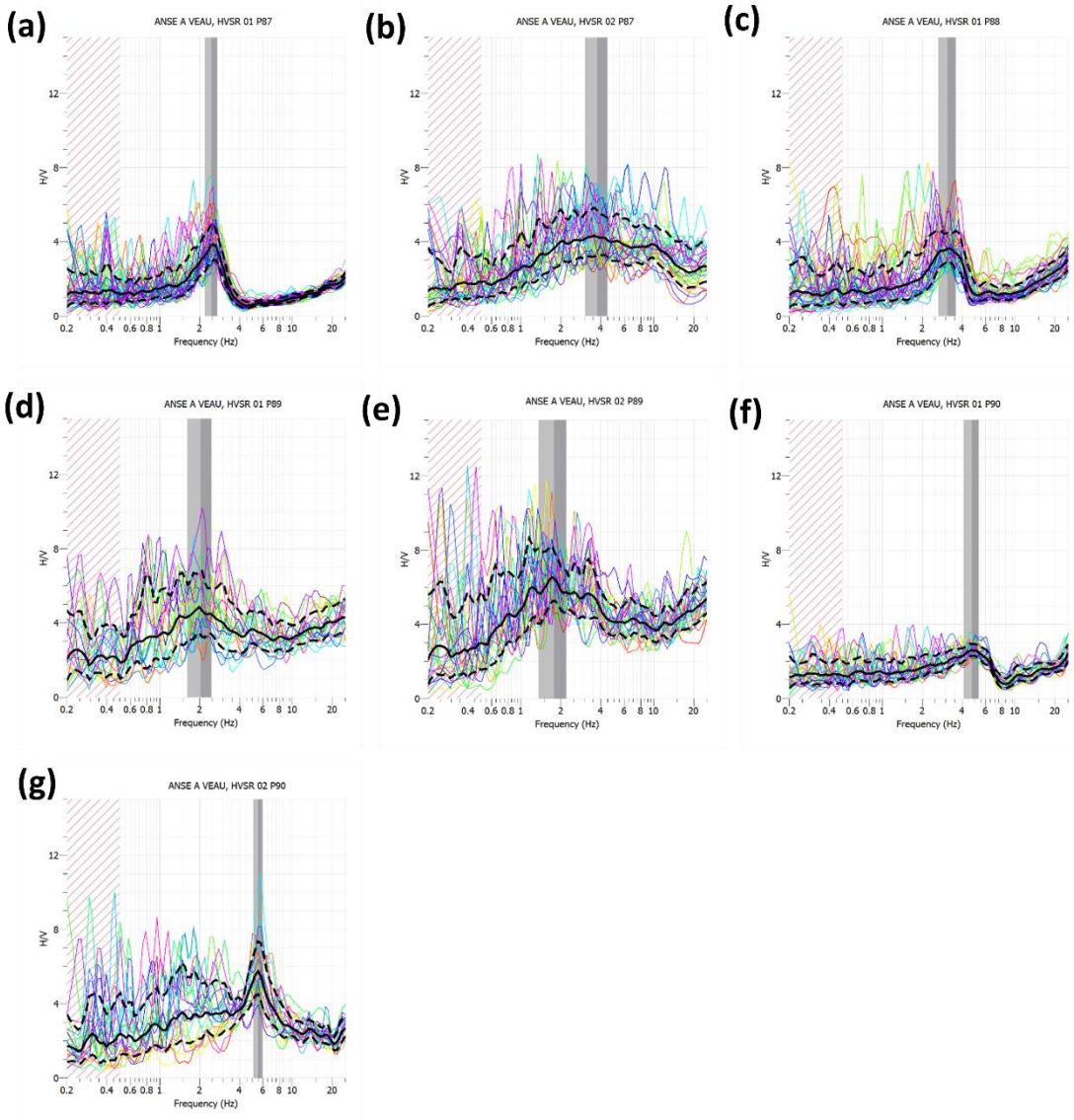

Fig. A.18 H/V curves for the measurements in Table A.18. **(a)** HV 153 – HVSR 01 P87. **(b)** HV 154 – HVSR 02 P87. **(c)** HV 155 – HVSR 01 P88. **(d)** HV 156 – HVSR 01 P89. **(e)** HV 157 – HVSR 02 P80. **(f)** HV 158 – HVSR 01 P90. **(g)** HV 159 – HVSR 02 P90.

Appendix A2: Results of MASW profiles for the study area of Anse-à-Veau

The multichannel analysis of surface waves (MASW) provides a 1-D profile of S-waves velocities (V_S) as a function of the depth. From the 1D S-Wave profile, it is possible to deduce a standardized geomechanical parameter, V_{S30}, which is involved in soil classification according to the International Building Code or the Eurocode 8 (IBC or EC8). The V_{S30} is an average of the S-waves velocity over the first 30 m below the seismic profile on the site.

The MASW surveys were carried out using a number of 24 receivers (geophones, generally with 5 m spacing) connected to a seismograph. The seismic source was generated by the impact of a 9.1 kg (20 lb) mass on a rigid plastic striking plate, at the beginning and at the end the profiles (respectively, direct and inverse shots, noted G1 and G24 in the following tables). The data were processed with the software SeisImager, Geometrics.

Table A.19 Summary of the MASW profiles in Anse-à-Veau (MASW 01 – MASW 02).

No	code	latitude	longitude	V_{S30} (m/s)	IBC class
MASW 01	G1 P1	18.50408333	-73.34561111	688.8	C
	G24 P1	18.50513889	-73.3455	705.8	C
MASW 02	G1 P3	18.50086111	-73.34569444	114.5	E
	G24 P3	18.50027778	-73.34580556	100.9	E

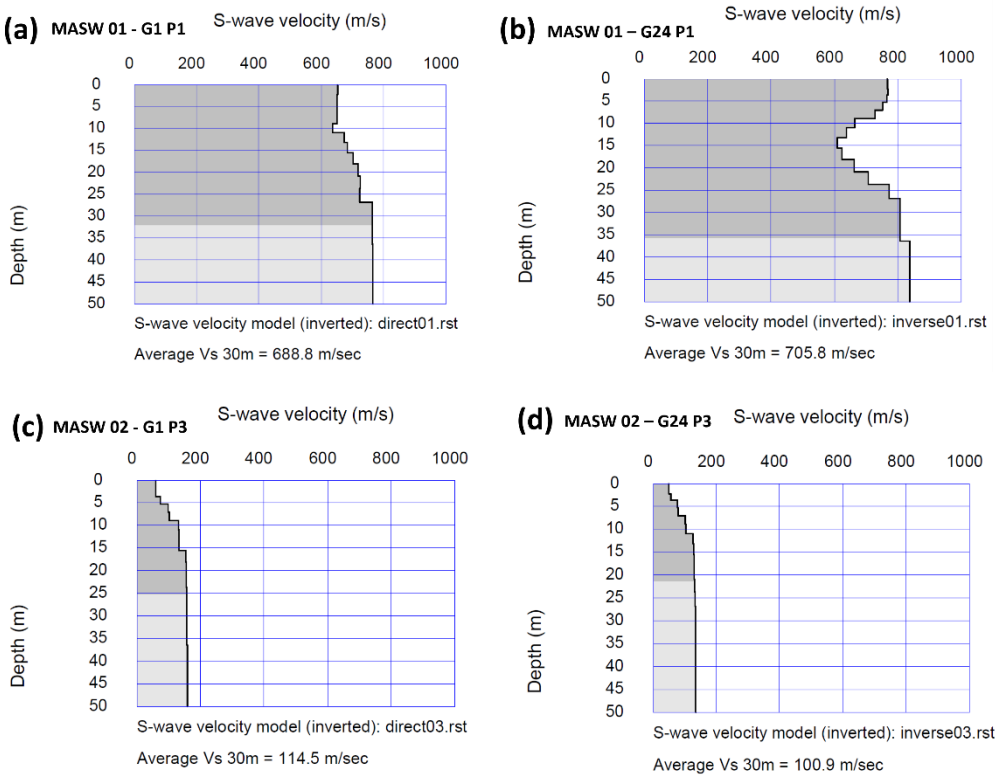

Fig. A.19 V_S profiles for the MASW in Table A.19. **(a)** MASW 01 – G1 P1. **(b)** MASW 01 – G24 P1. **(c)** MASW 02 – G1 P3. **(d)** MASW 02 – G24 P3.

Table A.20 Summary of the MASW profiles in Anse-à-Veau (MASW 03 – MASW 05).

No	code	latitude	longitude	V_{S30} (m/s)	IBC class
MASW 03	G1 P4	18.49919444	-73.34561111	101.9	E
	G24 P4	18.49852778	-73.34647222	108.3	E
MASW 04	G1 P5	18.49702778	-73.34647222	203.7	D
	G24 P5	18.49741667	-73.34552778	202.7	D
MASW 05	G1 P6	18.50425	-73.34263889	751.8	C
	G24 P6	18.50444444	-73.34366667	752.4	C

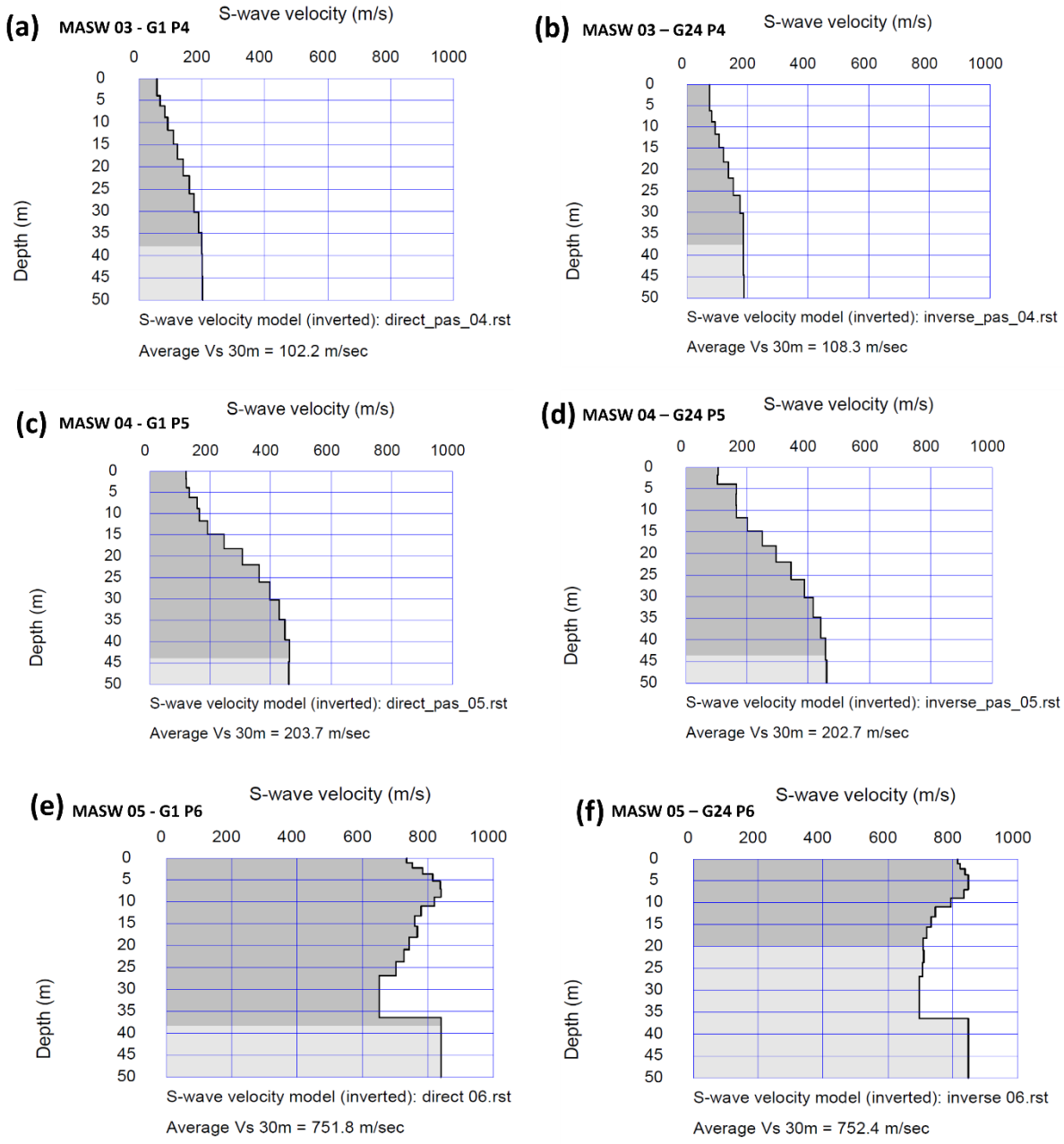

Fig. A.20 V_S profiles for the MASW in Table A.20. **(a)** MASW 03 – G1 P4. **(b)** MASW 03 – G24 P4. **(c)** MASW 04 – G1 P5. **(d)** MASW 04 – G24 P5. **(e)** MASW 05 – G1 P6. **(f)** MASW 05 – G24 P6.

Table A.21 Summary of the MASW profiles in Anse-à-Veau (MASW 06 – MASW 08).

No	code	latitude	longitude	V_{S30} (m/s)	IBC class
MASW 06	G1 P8	18.50147222	-73.34433333	660.1	C
	G24 P8	18.50158333	-73.34538889	643.6	C
MASW 07	G1 P10	18.49636111	-73.34297222	470.4	C
	G24 P10	18.49738889	-73.34319444	471.3	C
MASW 08	G1 P13	18.50213889	-73.34272222	709.5	C
	G24 P13	18.50113889	-73.34297222	691	C

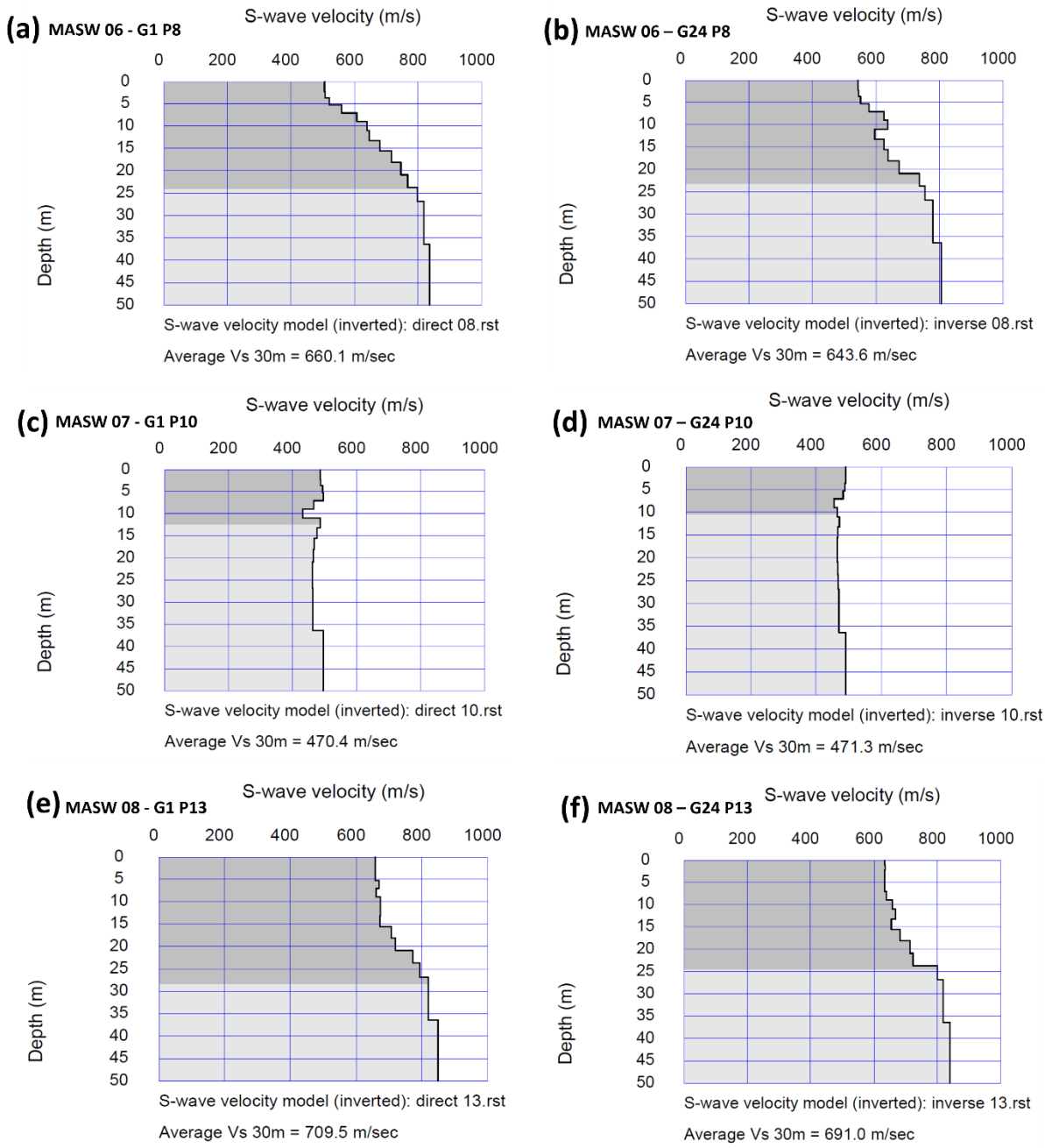

Fig. A.21 V_S profiles for the MASW in Table A.21. **(a)** MASW 06 – G1 P8. **(b)** MASW 06 – G24 P8. **(c)** MASW 07 – G1 P10. **(d)** MASW 07 – G24 P10. **(e)** MASW 08 – G1 P13. **(f)** MASW 08 – G24 P13.

Table A.22 Summary of the MASW profiles in Anse-à-Veau (MASW 09 – MASW 11).

No	code	latitude	longitude	V_{S30} (m/s)	IBC class
MASW 09	G1 P17	18.50266667	-73.33827778	809.7	B
	G24 P17	18.50266667	-73.33936111	772.4	B
MASW 10	G1 P19	18.498	-73.33713889	424.8	C
	G24 P19	18.49777778	-73.33816667	431.9	C
MASW 11	G1 P20	18.49591667	-73.33880556	563.1	C
	G24 P20	18.49694444	-73.33866667	547.4	C

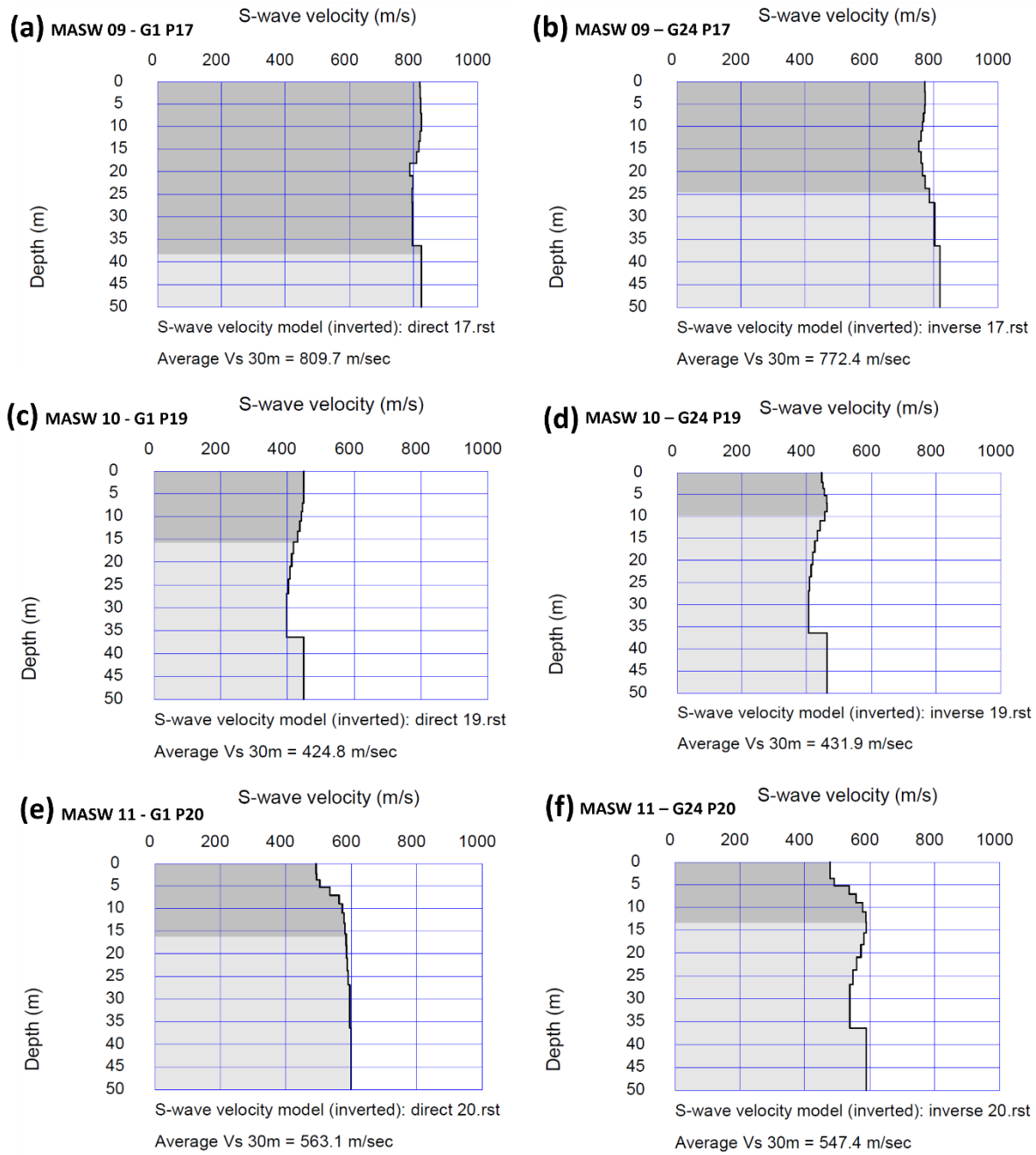

Fig. A.22 V_S profiles for the MASW in Table A.22. **(a)** MASW 09 – G1 P17. **(b)** MASW 09 – G24 P17. **(c)** MASW 10 – G1 P19. **(d)** MASW 10 – G24 P19. **(e)** MASW 11 – G1 P20. **(f)** MASW 11 – G24 P20.

Table A.23 Summary of the MASW profiles in Anse-à-Veau (MASW 12 – MASW 15).

No	code	latitude	longitude	V_{S30} (m/s)	IBC class
MASW 12	G1 P69	18.50225	-73.33161111	508.6	C
	G24 P69	18.50161111	-73.33244444	497.2	C
MASW 13	G1 P76	18.49175	-73.33366667	296.6	D
	G24 P76	18.49219444	-73.33463889	282.8	D
MASW 15	G1 P52	18.473276	-73.3661	491	C
	G24 P52	18.47341	-73.364986	488	C

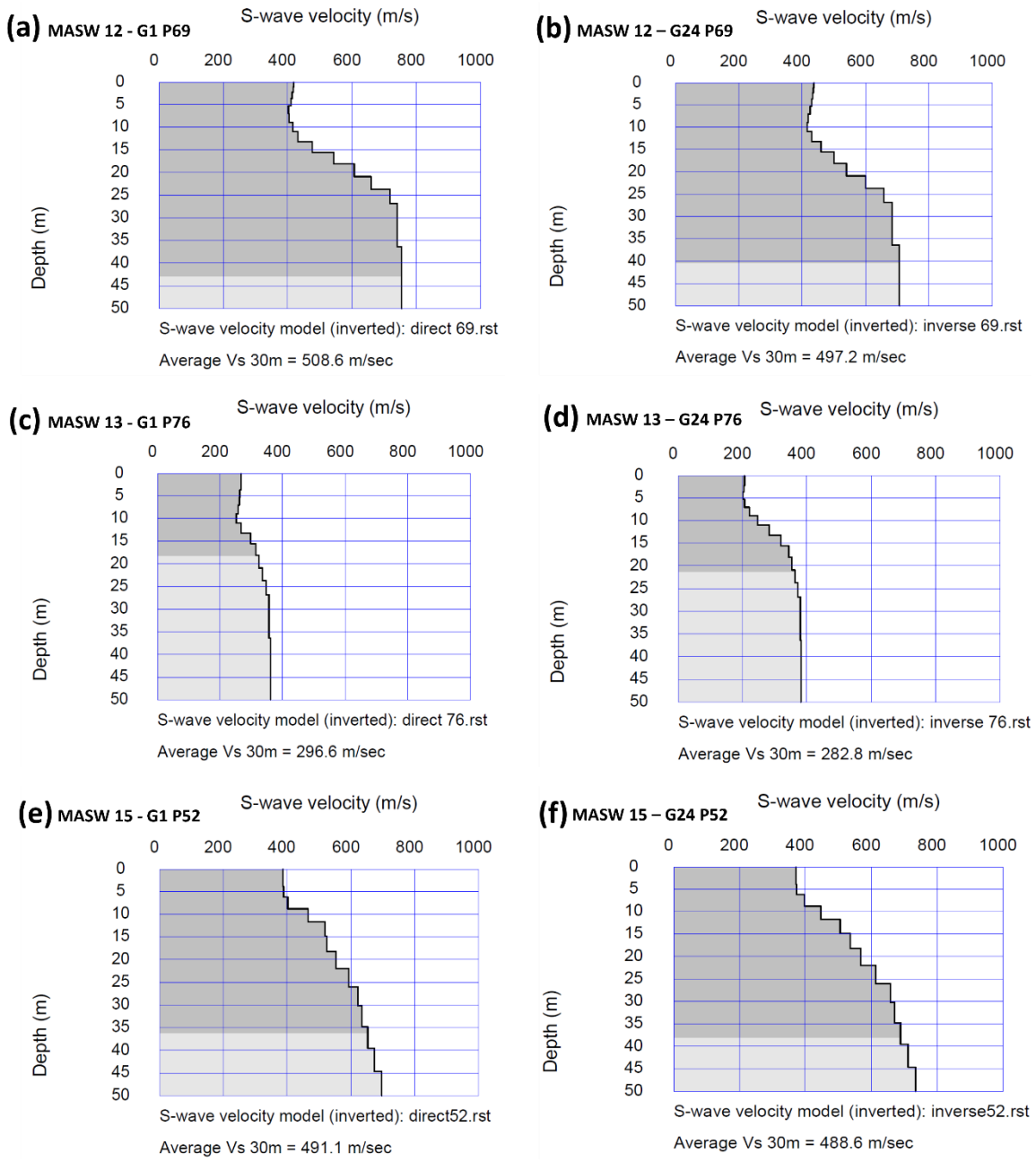

Fig. A.23 V_S profiles for the MASW in Table A.23. **(a)** MASW 12 – G1 P69. **(b)** MASW 12 – G24 P69. **(c)** MASW 13 – G1 P76. **(d)** MASW 13 – G24 P76. **(e)** MASW 15 – G1 P52. **(f)** MASW 15 – G24 P52.

Table A.24 Summary of the MASW profiles in Anse-à-Veau (MASW 16 – MASW 18).

No	code	latitude	longitude	V_{S30} (m/s)	IBC class
MASW 16	G1 P59	18.492647	-73.353998	413	C
	G24 P59	18.492892	-73.354773	404	C
MASW 17	G1 P64	18.502548	-73.37027	346	D
	G24 P64	18.501493	-73.370371	448	C
MASW 18	G1 P67	18.502528	-73.358466	434	C
	G24 P67	18.501677	-73.358565	439	C

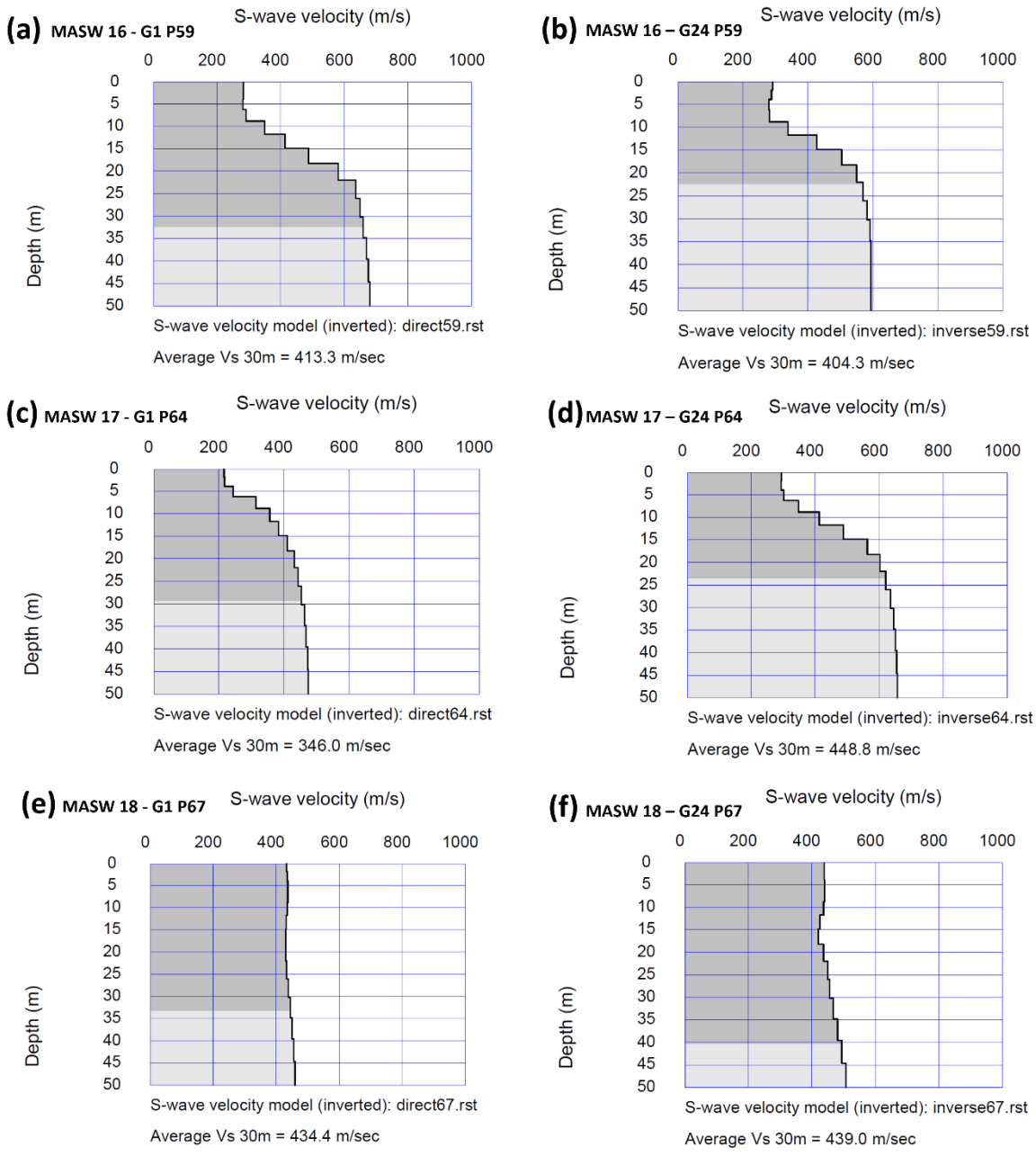

Fig. A.24 *Vs* profiles for the MASW in Table A.24. **(a)** MASW 16 – G1 P59. **(b)** MASW 16 – G24 P59. **(c)** MASW 17 – G1 P64. **(d)** MASW 17 – G24 P64. **(e)** MASW 18 – G1 P67. **(f)** MASW 18 – G24 P67.

Table A.25 Summary of the MASW profiles in Anse-à-Veau (MASW 19 – MASW 22).

No	code	latitude	longitude	V_{S30} (m/s)	IBC class
MASW 19	G1 P81	18.485875	-73.315832	279	D
	G24 P81	18.486697	-73.315133	279	D
MASW 20	G1 P87	18.471892	-73.341801	302	D
	G24 P87	18.472509	-73.342692	237	D
MASW 22	G1 P34	18.497639	-73.355222	110.5	E
	G24 P34	18.498639	-73.355417	105.8	E

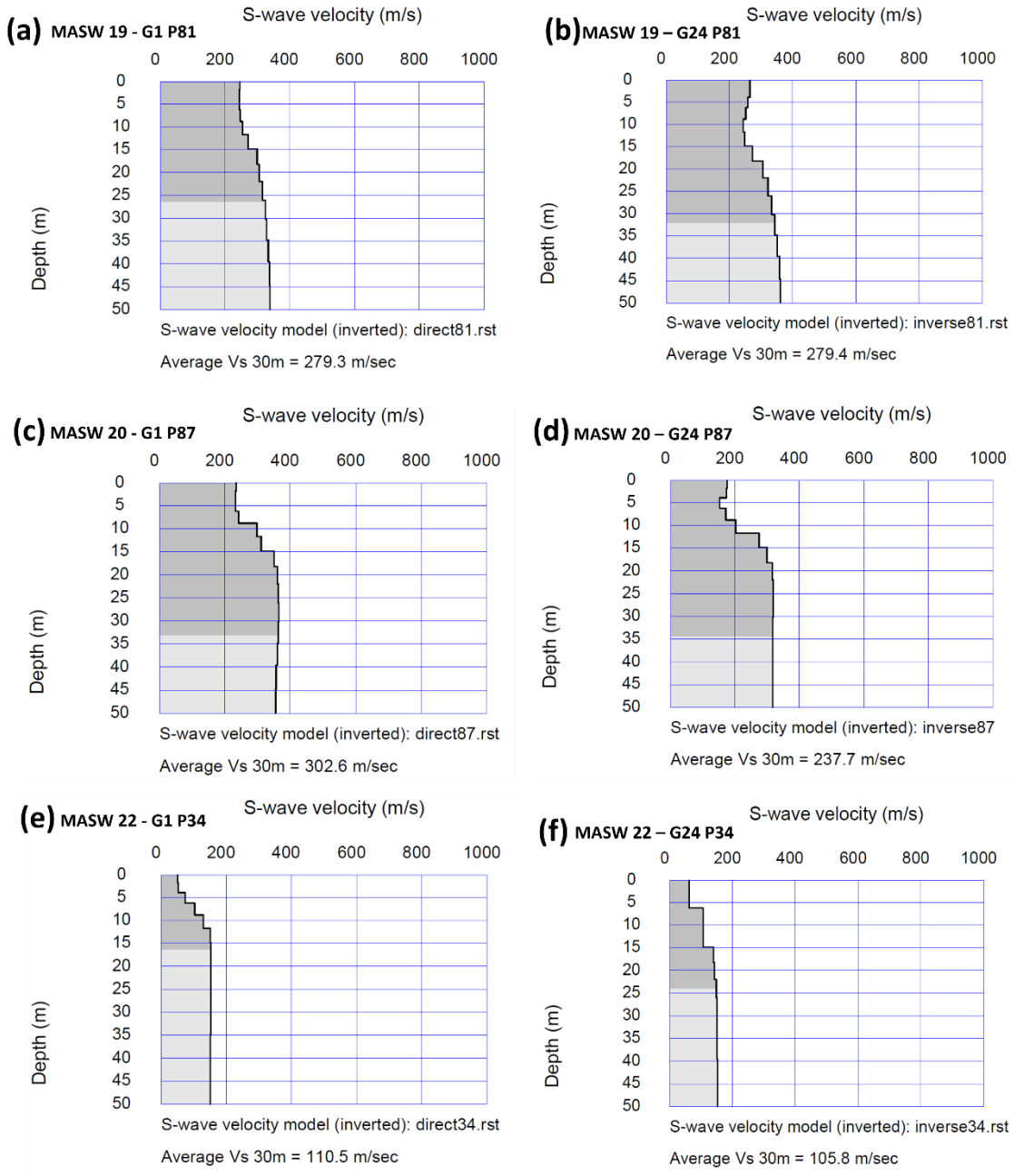

Fig. A.25 V_S profiles for the MASW in Table A.25. **(a)** MASW 19 – G1 P81. **(b)** MASW 19 – G24 P81. **(c)** MASW 20 – G1 P87. **(d)** MASW 20 – G24 P87. **(e)** MASW 22 – G1 P34. **(f)** MASW 22 – G24 P34.

Appendix A3: Results of SRT profiles for the study area of Anse-à-Veau

The seismic refraction tomography (SRT) provides a cross-section representing the different P-wave velocities (V_P) of the soil layers below the line of the profile. The propagation velocities of the P-waves are determined using the refraction properties of the wave at interfaces between layers with different physical properties.

As for the MASW profiles in the study area of Anse-à-Veau, the SRT surveys were carried out using a number of 24 receivers (geophones, generally with 5 m spacing) connected to a seismograph. The seismic source was generated by the impact of a 9.1 kg (20 lb) mass on a rigid plastic striking plate, at the beginning and at the end the profiles (offset shots, noted G1 and G24 in the following tables) as well as along the profiles, every two or three geophones. The data were also processed with the software SeisImager, Geometrics.

Table A.26 Summary of the SRT profiles in Anse-à-Veau (SRT 01 – SRT 04).

No	code	latitude	longitude	elevation (m)
SRT 01	G1 P1	18.50408333	-73.34561111	14.357
	G24 P1	18.50513889	-73.3455	13.909
SRT 02	G1 P3	18.50086111	-73.34569444	0.961
	G24 P3	18.50027778	-73.34580556	0.701
SRT 03	G1 P4	18.49919444	-73.34561111	0.718
	G24 P4	18.49852778	-73.34647222	0.82
SRT 04	G1 P5	18.49702778	-73.34647222	1.811
	G24 P5	18.49741667	-73.34552778	2.097

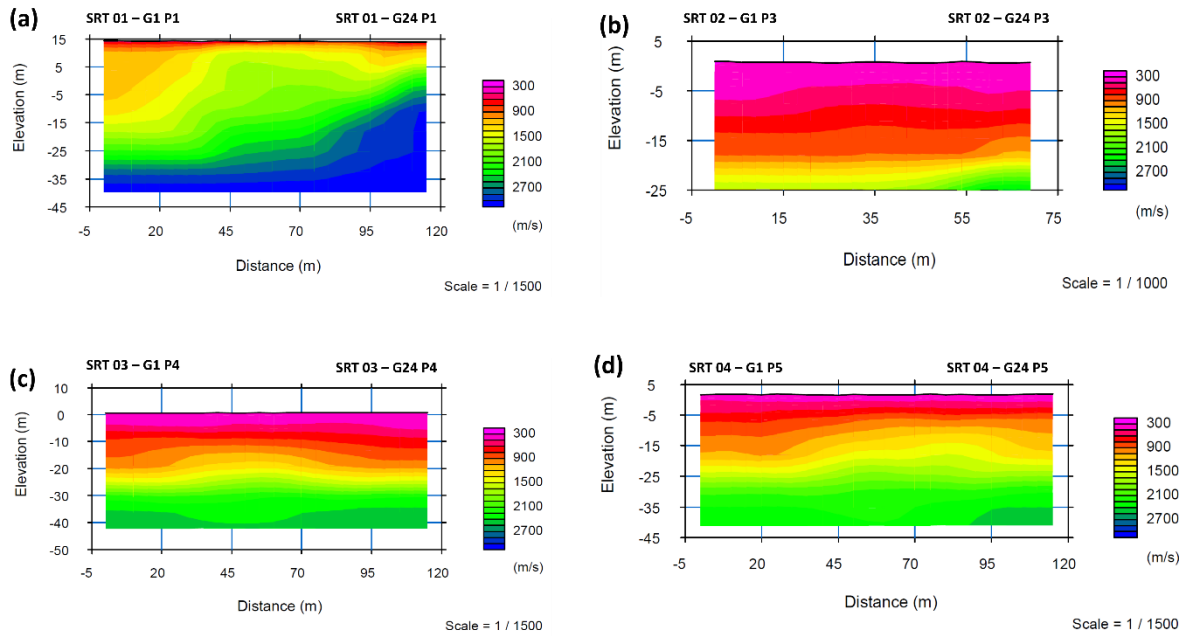

Fig. A.26 V_P distribution for the SRT in Table A.26. **(a)** SRT 01 (G1 P1 – G24 P1). **(b)** SRT 02 (G1 P3 – G24 P3). **(c)** SRT 03 (G1 P4 – G24 P4). **(d)** SRT 04 (G1 P5 – G24 P5).

Table A.27 Summary of the SRT profiles in Anse-à-Veau (SRT 05 – SRT 10).

No	code	latitude	longitude	elevation (m)
SRT 05	G1 P6	18.50425	-73.34263889	15.056
	G24 P6	18.50444444	-73.34366667	13.336
SRT 06	G1 P8	18.50147222	-73.34433333	26.748
	G24 P8	18.50158333	-73.34538889	21.637
SRT 07	G1 P10	18.49636111	-73.34297222	22.171
	G24 P10	18.49738889	-73.34319444	21.145
SRT 08	G1 P13	18.50213889	-73.34272222	25.9
	G24 P13	18.50113889	-73.34297222	32.45
SRT 09	G1 P17	18.50266667	-73.33827778	15.654
	G24 P17	18.50266667	-73.33936111	17.549
SRT 10	G1 P19	18.498	-73.33713889	34.329
	G24 P19	18.49777778	-73.33816667	36.787

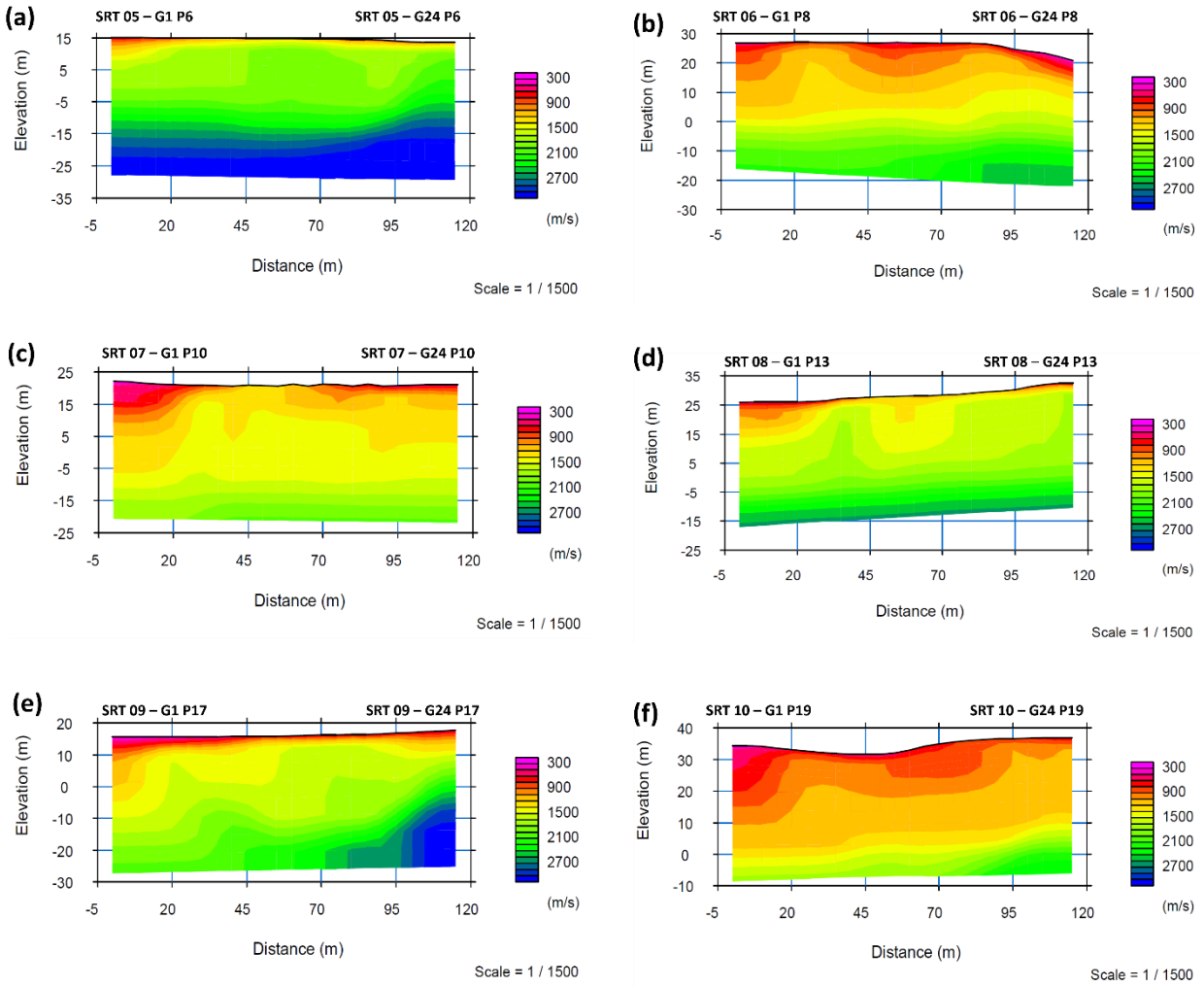

Fig. A.27 V_P distribution for the SRT in Table A.27. **(a)** SRT 05 (G1 P6 – G24 P6). **(b)** SRT 06 (G1 P8 – G24 P8). **(c)** SRT 07 (G1 P10 – G24 P10). **(d)** SRT 08 (G1 P13 – G24 P13). **(e)** SRT 09 (G1 P17 – G24 P17). **(f)** SRT 10 (G1 P19 – G24 P19).

Table A.28 Summary of the SRT profiles in Anse-à-Veau (SRT 11 – SRT 17).

No	code	latitude	longitude	elevation (m)
SRT 11	G1 P20	18.49591667	-73.33880556	35.903
	G24 P20	18.49694444	-73.33866667	37.286
SRT 12	G1 P69	18.50225	-73.33161111	11.911
	G24 P69	18.50161111	-73.33244444	4.553
SRT 13	G1 P76	18.49175	-73.33366667	32.015
	G24 P76	18.49219444	-73.33463889	31.869
SRT 15	G1 P52	18.473276	-73.3661	49.834
	G24 P52	18.47341	-73.364986	49.507
SRT 16	G1 P59	18.492647	-73.353998	6.254
	G24 P59	18.492892	-73.354773	5.966
SRT 17	G1 P64	18.502548	-73.37027	28.42
	G24 P64	18.501493	-73.370371	31.126

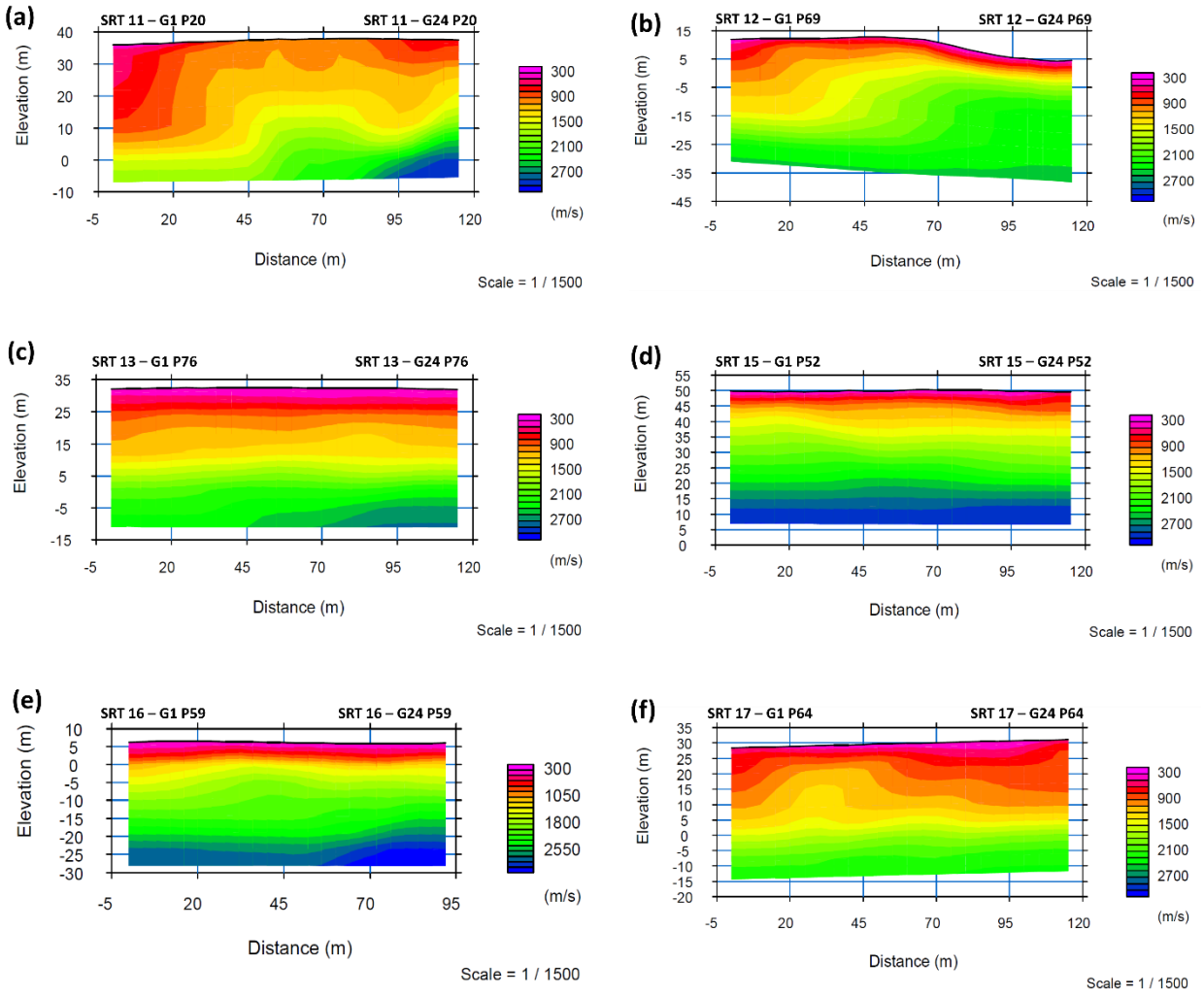

Fig. A.28 V_P distribution for the SRT in Table A.28. **(a)** SRT 11 (G1 P20 – G24 P20). **(b)** SRT 12 (G1 P69 – G24 P69). **(c)** SRT 13 (G1 P76 – G24 P76). **(d)** SRT 15 (G1 P52 – G24 P52). **(e)** SRT 16 (G1 P59 – G24 P59). **(f)** SRT 17 (G1 P64 – G24 P64).

Table A.29 Summary of the SRT profiles in Anse-à-Veau (SRT 18 – SRT 21).

No	code	latitude	longitude	elevation (m)
SRT 18	G1 P67	18.502528	-73.358466	35.173
	G24 P67	18.501677	-73.358565	35.652
SRT 19	G1 P81	18.485875	-73.315832	30.973
	G24 P81	18.486697	-73.315133	33.711
SRT 20	G1 P87	18.471892	-73.341801	76.057
	G24 P87	18.472509	-73.342692	77.872
SRT 21	G1 P90	18.475599	-73.315626	8.933
	G24 P90	18.476492	-73.316239	15.099

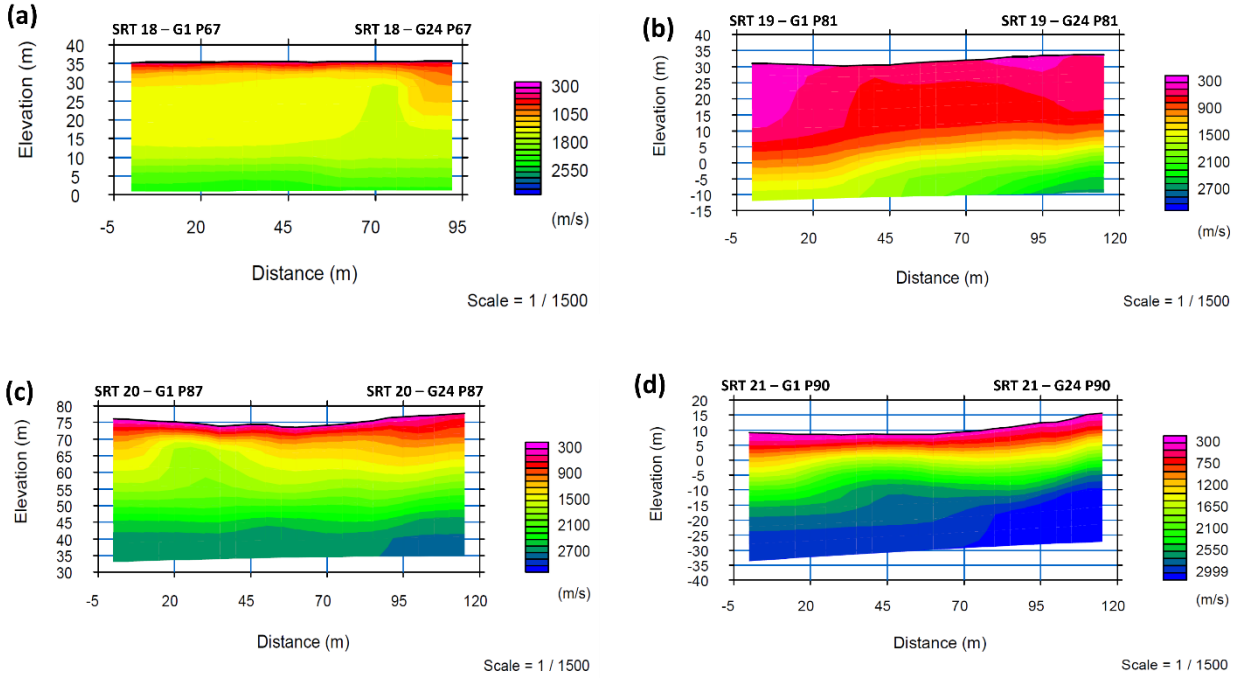

Fig. A.29 V_P distribution for the SRT in Table A.29. **(a)** SRT 18 (G1 P67 – G24 P67). **(b)** SRT 19 (G1 P81 – G24 P81). **(c)** SRT 20 (G1 P87 – G24 P87). **(d)** SRT 21 (G1 P90 – G24 P90).

Appendix A4: Results of ERT profiles for the study area of Anse-à-Veau

The electrical resistivity tomography (ERT) provides an electrical image of the subsoil (a section of the resistivity as a function of depth) by measuring the resistance profile for different combinations of electrodes and potential. The measurements are performed by injecting a direct current into the ground using 2 current electrodes and 2 potential electrodes according to a predefined sequence. Among the configurations (Wenner, Schlumberger, Dipole-dipole, etc.) conventionally used (for injecting the current and measuring the resulting potential), the Wenner configuration, which is more sensitive to a vertical variation of the resistivity, was used for the ERT profiles of Anse-à-Veau. The collected data were processed with the software Res2Dinv (Loke and Barker 1996).

Table A.30 Summary of the SRT profiles in Anse-à-Veau (ERT 01 – ERT 03).

No	code	latitude	longitude	elevation (m)	profile length (m)
ERT 01	E1 P3	18.50155556	-73.34605556	2.365	124
	E32 P3	18.50261111	-73.34588889	13.957	
ERT 02	E1 P5	18.49661111	-73.34747222	2.394	217
	E32 P5	18.49741667	-73.34561111	1.718	
ERT 03	E1 P6	18.50422222	-73.34241667	15.156	155
	E32 P6	18.50441667	-73.34388889	13.685	

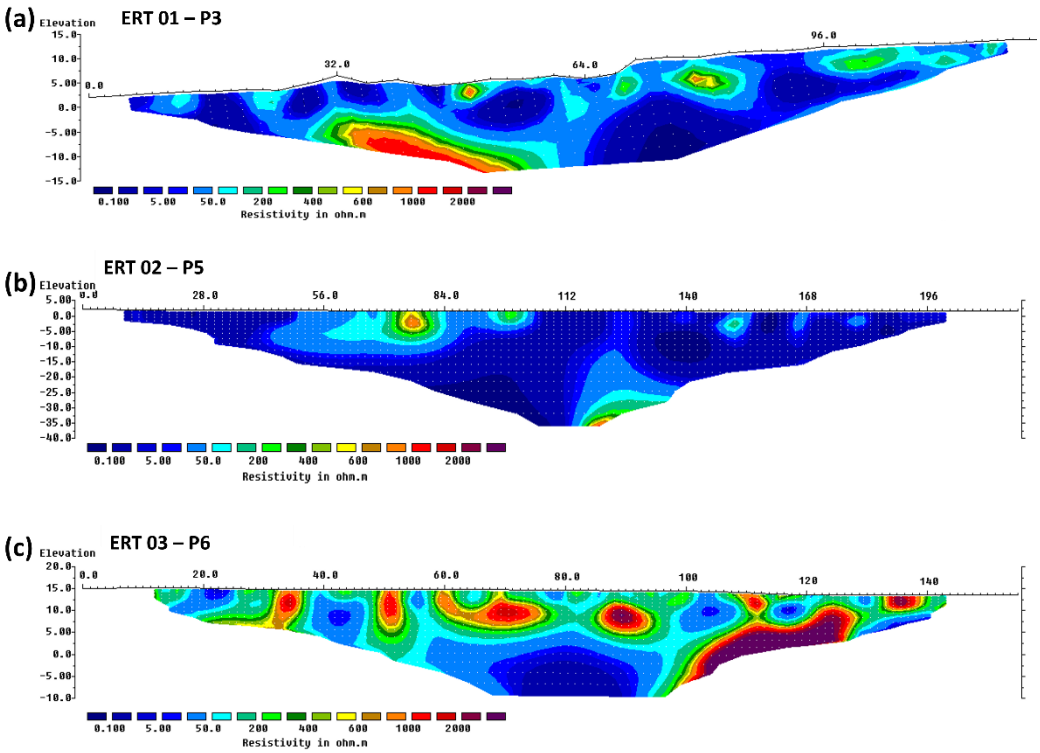

Fig. A.30 Electrical resistivity distribution for the ERT in Table A.30. **(a)** ERT 01 (E1 P3 – E32 P3). **(b)** ERT 02 (E1 P5 – E32 P5). **(c)** ERT 03 (E1 P6 – E32 P6).

Table A.31 Summary of the SRT profiles in Anse-à-Veau (ERT 04 – ERT 08).

No	code	latitude	longitude	elevation (m)	profile length (m)
ERT 04	E1 P10	18.49588889	-73.34286111	25.313	217
	E32 P10	18.49780556	-73.34325	23.717	
ERT 05	E1 P15	18.49727778	-73.33883333	36.741	310
	E32 P15	18.49758333	-73.34172222	34.576	
ERT 06	E1 P23	18.49683333	-73.34863889	3.174	217
	E32 P23	18.49772222	-73.35047222	2.761	
ERT 07	E1 P69	18.50225	-73.33155556	11.683	124
	E32 P69	18.50158333	-73.33252778	7.04	
ERT 08	E1 P70	18.49419444	-73.33438889	32.913	248
	E32 P70	18.49641667	-73.33419444	32.789	

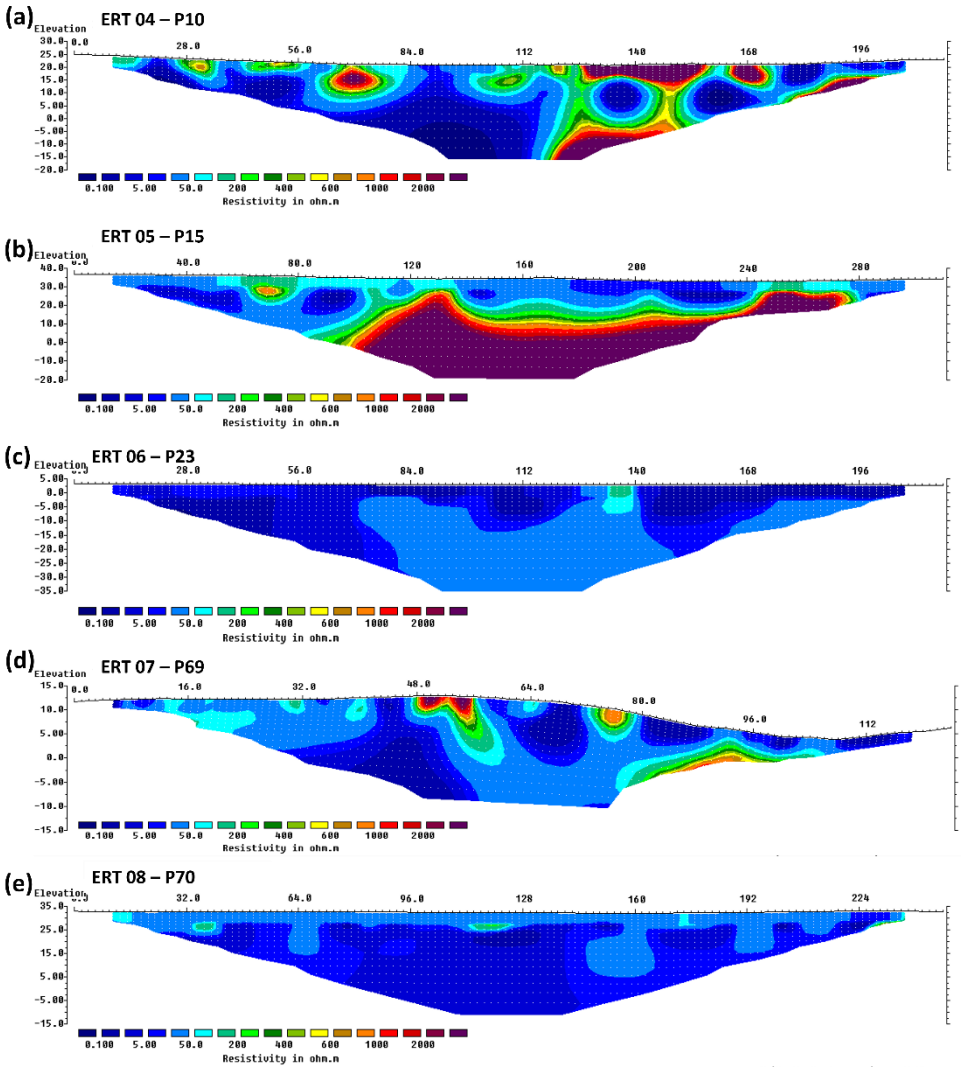

Fig. A.31 Electrical resistivity distribution for the ERT in Table A.31. **(a)** ERT 04 (E1 P10 – E32 P10). **(b)** ERT 05 (E1 P15 – E32 P15). **(c)** ERT 06 (E1 P23 – E32 P23). **(d)** ERT 07 (E1 P69 – E32 P69). **(e)** ERT 08 (E1 P70 – E32 P70).

Appendix A5: EDA and variogram models for the study area of Anse-à-Veau

The exploratory data analysis (EDA) is a series of descriptive and graphical analysis performed, as first step, in geostatistical modelling to better understand the structure, trends, and spatial variability of data. The second step is the calculation of an experimental variogram to quantify the spatial correlation of the data and the modelling (of the experimental variogram) to existing theoretical variogram models. The variogram is the basic tool used in geostatistical interpolation and simulation such as kriging and conditional simulation employed in the present study.

The EDA and variogram modelling were performed using R Statistical Software (R Core Team 2024), which is an interpreted programming language that is widely used in data analysis and statistics. The analysed data include the fundamental frequency (f_0) and amplitude (A_0) from the HVSR results, and the S-wave velocities (V_{S30}) derived from the MASW profiles. The following graphs illustrate the results of the EDA and variogram modelling for the study area of Anse-à-Veau.

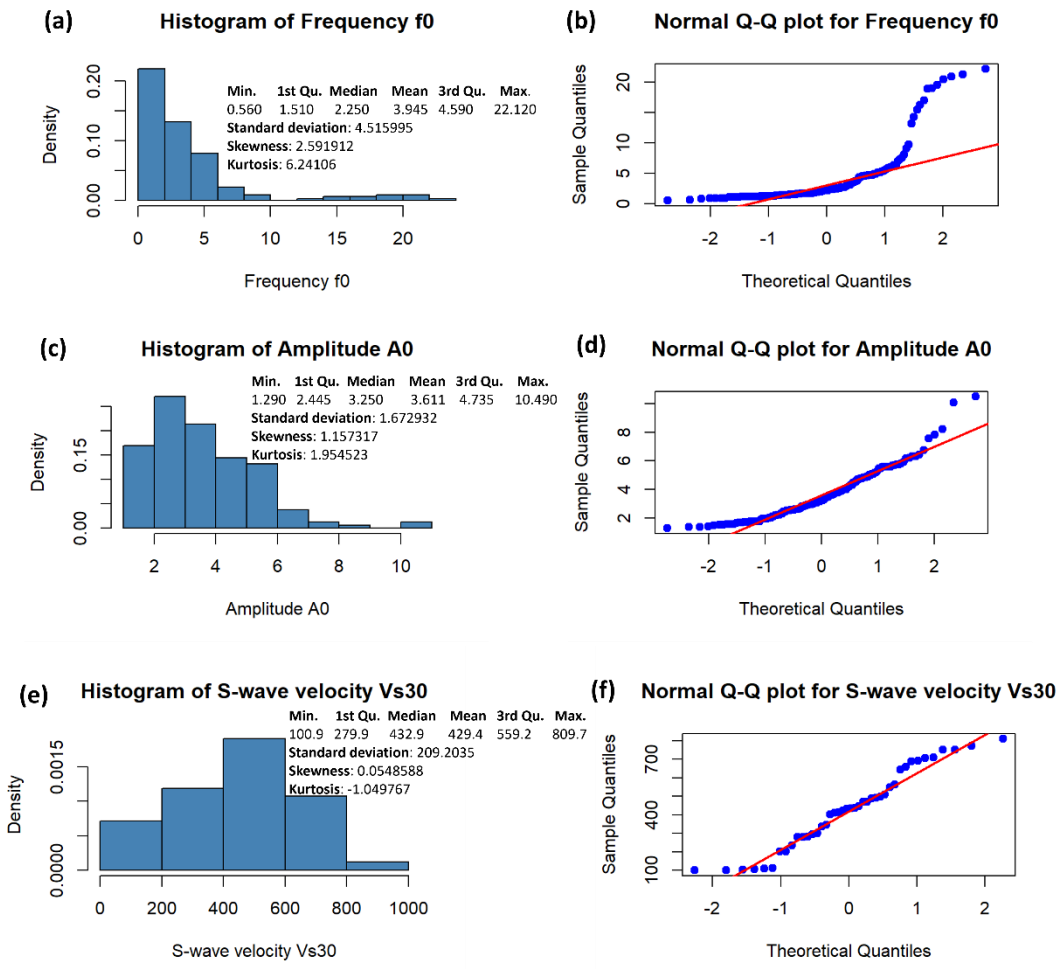

Fig. A.32 Exploratory data analysis for the study area of Anse-à-Veau. **(a)** Histogram and descriptive statistics of the fundamental resonance frequency (f_0). **(b)** Normal Q-Qplot of f_0. **(c)** Histogram and descriptive statistics of the amplitude (A_0). **(d)** Normal QQplot of A_0. **(e)** Histogram and descriptive statistics of the S-wave velocities (V_{S30}). **(f)** Normal Q-Qplot of V_{S30}.

Because geostatistical methods such as kriging and sequential Gaussian simulation (SGS) rely on an underlying normal (Gaussian) distribution, the raw data cannot be used directly. A normalizing transformation was therefore applied. After transformation, the three variables exhibit almost perfectly symmetric distributions.

The histograms and Q-Q plots of the transformed data illustrate this improvement clearly. Most points lie close to the one-to-one line (the red line in the figures), with only slight deviations at the extremes. This transformation step allows the variables to be treated as Gaussian fields and provides a sound basis for the construction of stationary variogram models.

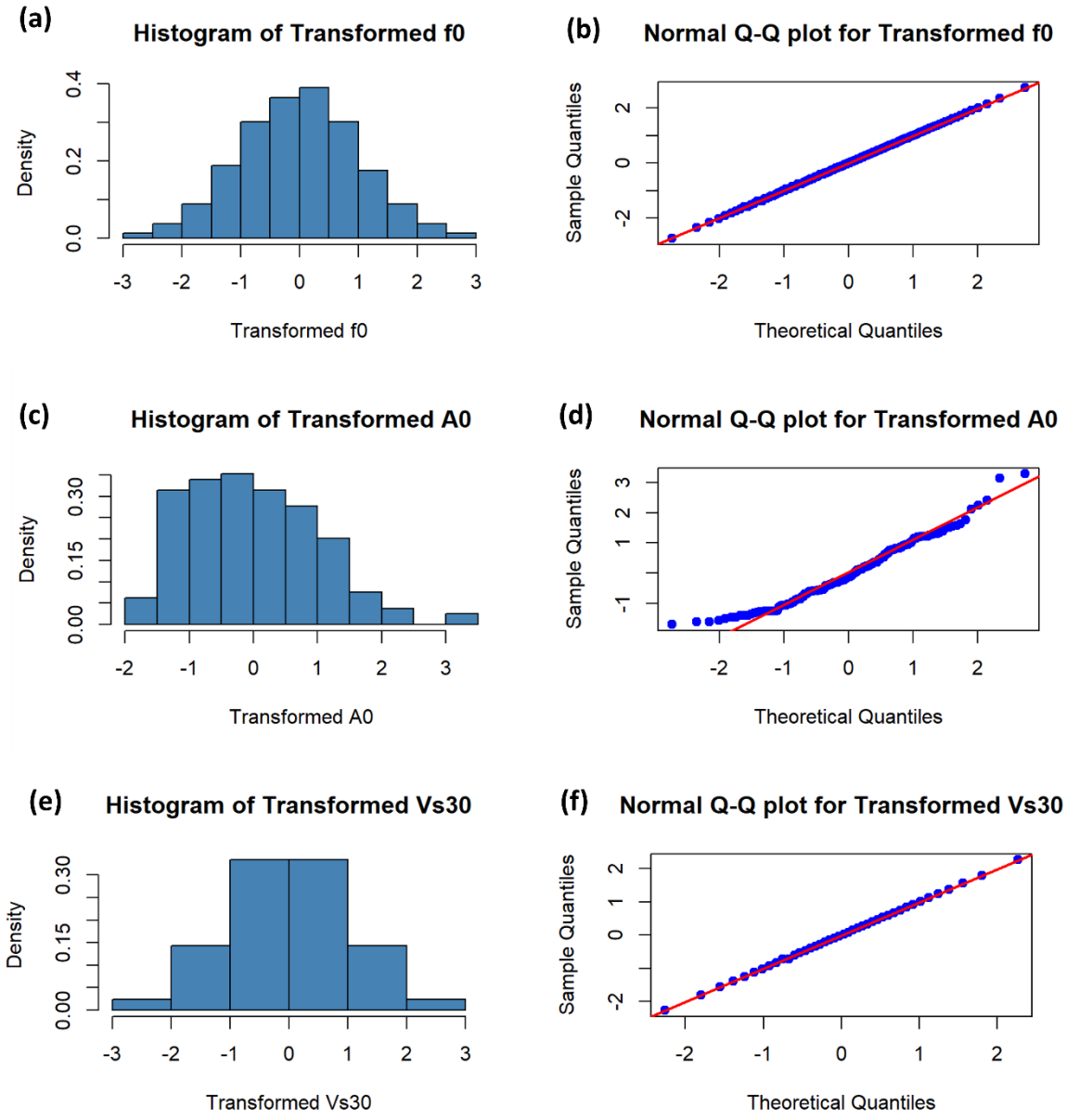

Fig. A.33 Exploratory data analysis for the study area of Anse-à-Veau. **(a)** Histogram and descriptive statistics of the normal transform of f_0. **(b)** Normal Q-Qplot of the normal transform of f_0. **(c)** Histogram and descriptive statistics of the normal transform A_0. **(d)** Normal QQplot of the normal transform of A_0. **(e)** Histogram and descriptive statistics of the normal transform of V_{S30}. **(f)** Normal Q-Qplot of the normal transform of V_{S30}.

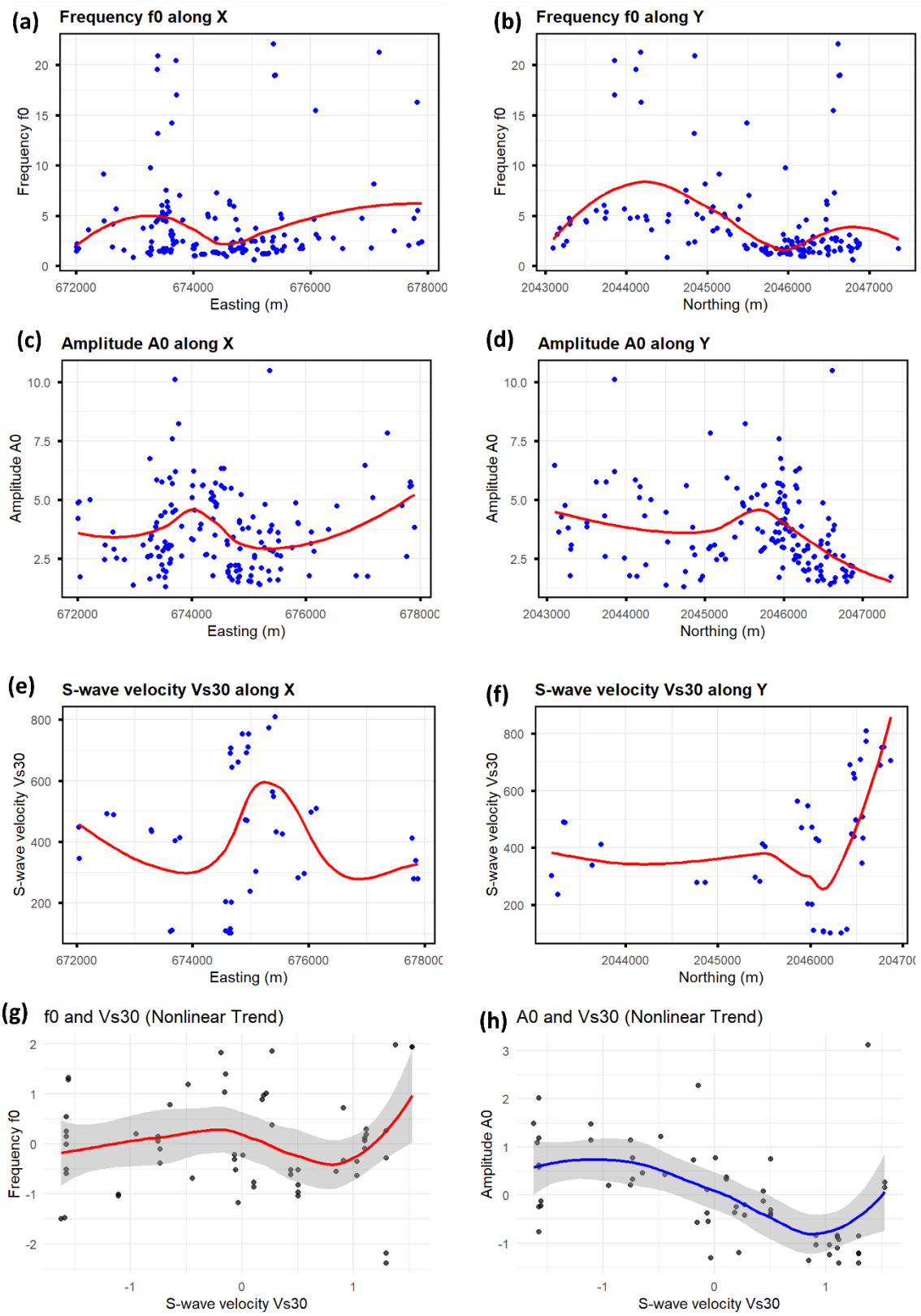

Fig. A.34 Exploratory data analysis for the study area of Anse-à-Veau. **(a)** Spatial distribution of f_0 in the E-W direction. **(b)** Spatial distribution of A_0 in the N-S direction. **(c)** Spatial distribution of A_0 in the E-W direction. **(d)** Spatial distribution of f_0 in the N-S direction. **(e)** Spatial distribution of V_{S30} in the E-W direction. **(f)** Spatial distribution of V_{S30} in the N-S direction. **(g)** Nonlinear trend of V_{S30} with f_0. **(h)** Nonlinear trend of V_{S30} with A_0.

The variogram models (at the left) captures the degree of similarity between observations as a function of distance, reflecting both geological structure and measurement uncertainty. The variogram maps (at the right) represent the spatial variability in two dimensions and offer an invaluable tool for identifying anisotropy related to geological structures or topographic trends.

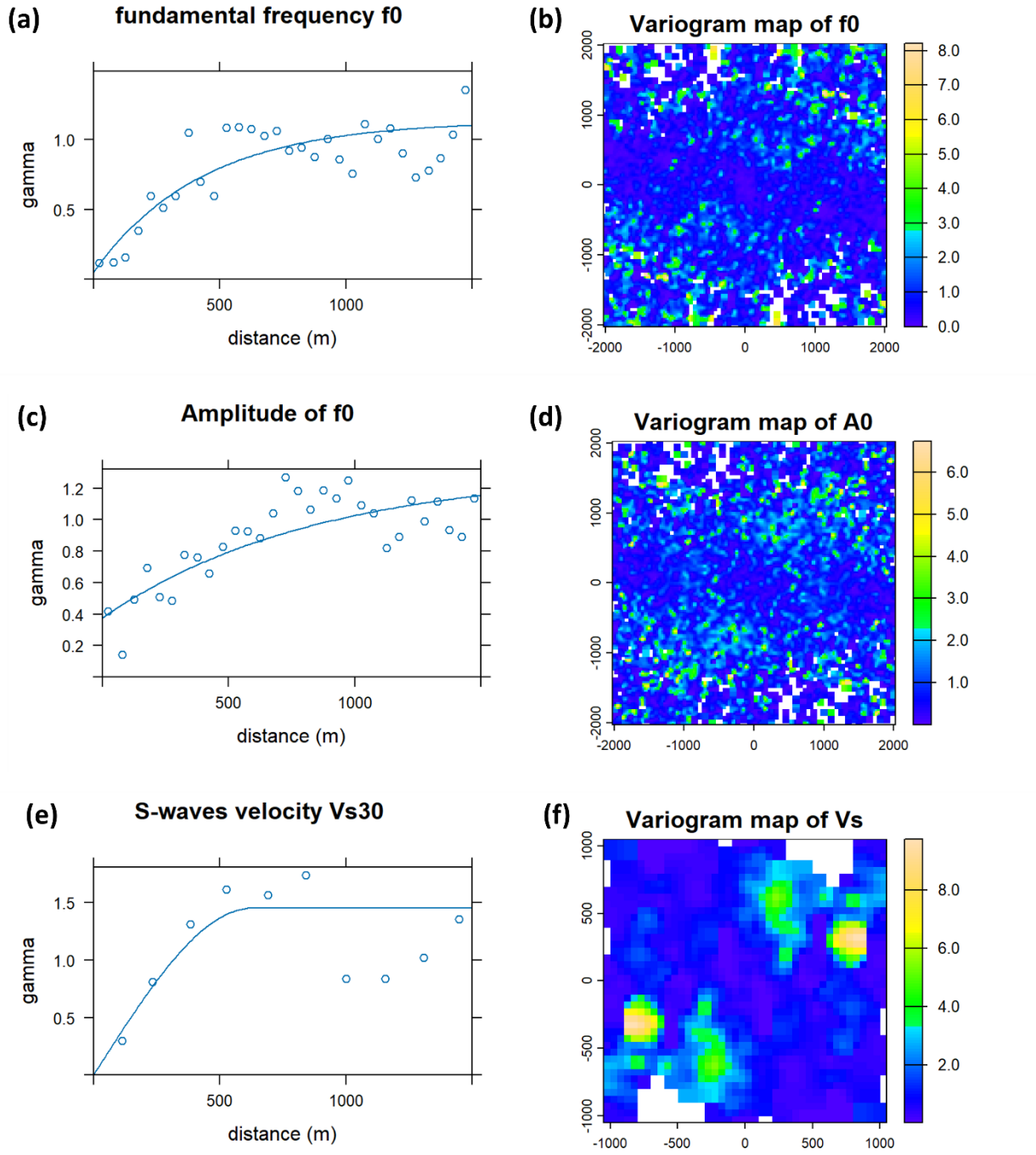

Fig. A.35 Variogram modelling of geophysical data in the study area of Anse-à-Veau. **(a)** Variogram model of f_0. **(b)** Variogram map of f_0. **(c)** Variogram model of A_0. **(d)** Variogram map of A_0. **(e)** Variogram model of A_0. **(f)** Variogram map of A_0.

Appendix A6: Static results from numerical modelling in the study area of Anse-à-Veau

Dynamic analysis was performed for the study area of Anse-à-Veau to characterize the seismic site response. The process was carried out in UDEC (Universal Distinct Element Code), a numerical modelling software developed by Itasca Consulting Group ©. Before the dynamic analysis, the model is submitted to a static process that ensures that the system is in a stable equilibrium state, free from artificial velocities or unbalanced forces.

In the static process, UDEC is cycled in a quasi-static manner to allow the system to approach the static equilibrium. The cycling proceeds until the system reaches static equilibrium, which is confirmed when the ratio of unbalanced forces to applied forces falls below a specified threshold (10^{-9}, in the present case). The following graphs illustrate the maximum variation of these unbalanced forces, during the quasi-static process, for three profiles extracted from the geomodel of the study area.

For every profile (noted section A-A', B-B' and C-C' in the following graphs), two models have been established: one model characterized by only one uniform layer (very compact) across the whole model for pure topographic effect analysis, and another one characterized by different surface layers for combined lithological and topographic effect analysis.

Section A-A'

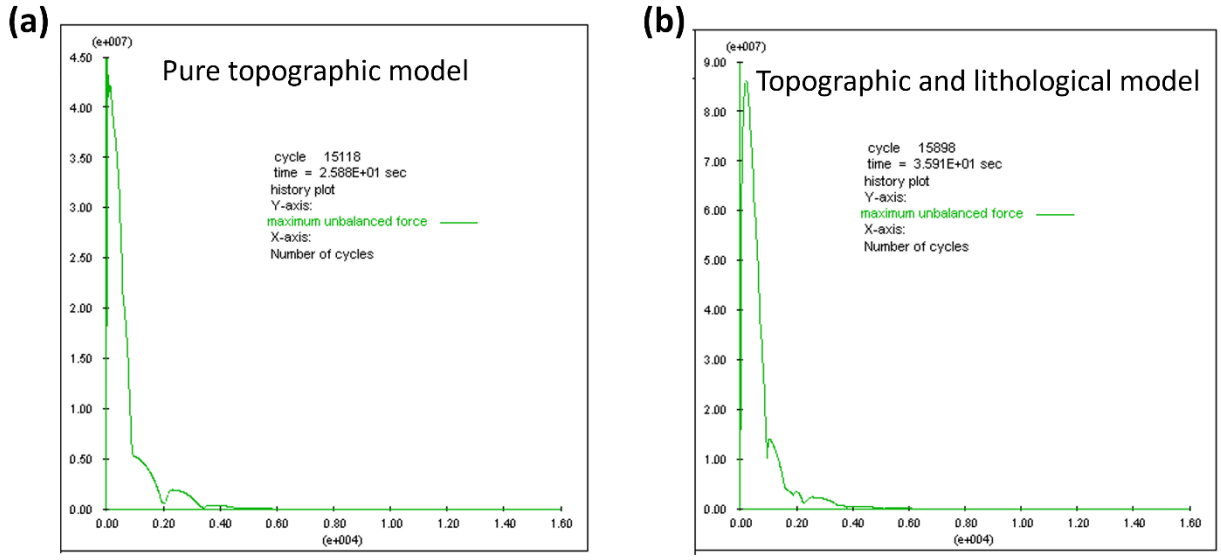

Fig. A.36 Variation of the maximum unbalance force from the static analysis of the 2D model A-A' in Anse-à-Veau. **(a)** Topographic model. **(b)** Combined topographic and lithological model.

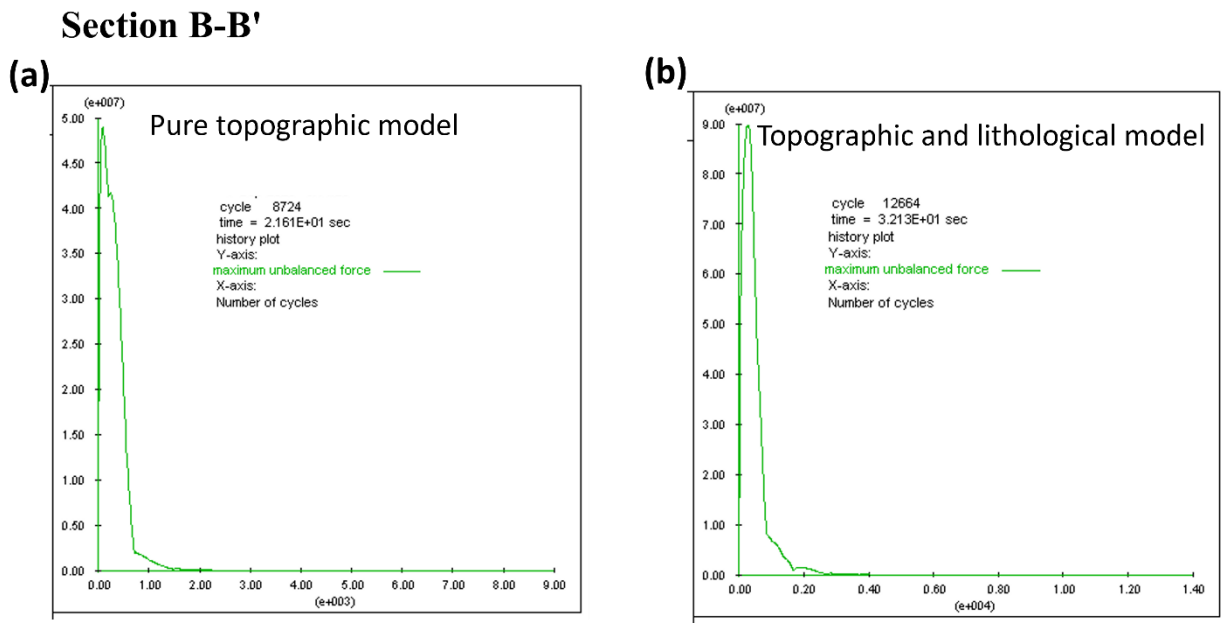

Fig. A.37 Variation of the maximum unbalance force from the static analysis of the 2D model B-B' in Anse-à-Veau. **(a)** Topographic model. **(b)** Combined topographic and lithological model.

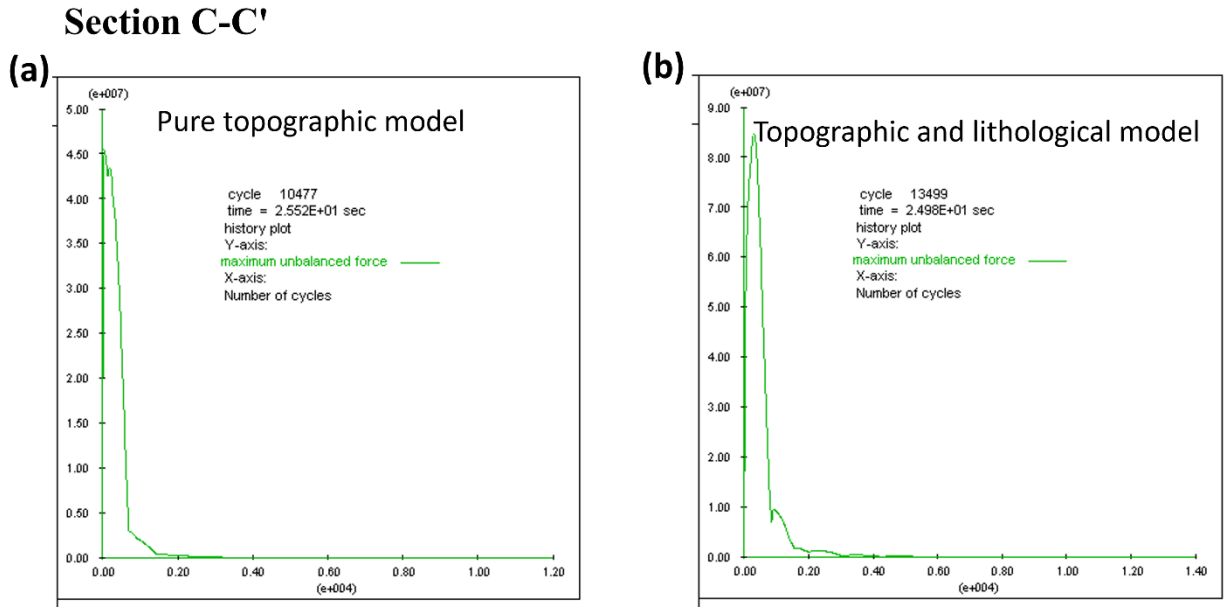

Fig. A.38 Variation of the maximum unbalance force from the static analysis of the 2D model C-C' in Anse-à-Veau. **(a)** Topographic model. **(b)** Combined topographic and lithological model.

Appendix B. Surveys result in Cap-Haitien

Appendix B1: Results of H/V measurements for the study area of Cap-Haitien

The ambient noise H/V surveys and processing for the study area of Cap-Haitien have been carried out in the framework of the seismic microzonation of the Cap-Haitien region. The microzonation study was realized on behalf of the Haitian government by a cooperation of the BRGM (*Bureau de Recherches Géologiques et Minières*, France), the BME (*Bureau des Mines et de l'Energie*, Haiti), and the LNBTP (*Laboratoire National du Bâtiment et des Travaux Publics*, Haiti).

The H/V results presented in the following table are the fundamental resonance frequency f_0 and the amplitude A_0, directly compiled from the microzonation reports (Bertil et al. 2014; Roullé et al. 2014).

Table B.1 Summary of the H/V data compiled for the study area of Cap-Haitien.

No	code	latitude	longitude	f_0 (Hz)	A_0
HV 001	CAP009_01	19.760108	-72.197525	2.3	2.8
HV 002	CAP024_01	19.76197	-72.19596	1.8	7.2
HV 003	CAP024_02	19.76248	-72.19567	2.2	8
HV 004	CAP024_03	19.76227	-72.19576	1.9	7.5
HV 005	CAP025_01	19.74786	-72.20274	2.1	4.8
HV 006	CAP025_02	19.74766	-72.20246	2	6.3
HV 007	CAP005_01	19.763712	-72.1977783	5.1	5.9
HV 008	CAP016_01	19.766072	-72.195405	4.1	7.4
HV 009	CAP016_02	19.766333	-72.1954444	4.3	10.4
HV 010	CAP016_03	19.76625	-72.19575	4.1	10
HV 011	CAP018_01	19.76286	-72.19635	2.6	5.9
HV 012	CAP018_02	19.76378	-72.19638	2.2	5.3
HV 013	CAP018_04	19.76382	-72.19684	3.7	5.5
HV 014	CAP026_01	19.75425	-72.2071	5.2	5.9
HV 015	CAP027_01	19.76838	-72.19421	4.9	9.2
HV 016	CAP028_01	19.753229	-72.20694	4.5	6.8
HV 017	CAP003_01	19.76155	-72.20065	5.3	3.5
HV 018	CAP003_02	19.76153	-72.2007	5.3	2.4
HV 019	CAP004_01	19.76108	-72.20015	4.8	2.9
HV 020	CAP007_01	19.764492	-72.197665	10.3	3.4
HV 021	CAP008_01	19.762972	-72.20566	4.2	1.9
HV 022	CAP010_01	19.75897	-72.20559	11.8	1.9
HV 023	CAP010_02	19.759203	-72.205245	9.4	4.3
HV 024	CAP010_03	19.759222	-72.2053611	11.4	2.2
HV 025	CAP010_04	19.759417	-72.2058333	14.4	1.9
HV 026	CAP030_01	19.764	-72.2055	5.2	2.4
HV 027	CAP030_02	19.763472	-72.2054167	5.7	4.2
HV 028	CAP022_01	19.73534	-72.18266	0.6	3.9
HV 029	CAP022_02	19.734667	-72.1829444	0.7	4.4

No	code	latitude	longitude	f_0 (Hz)	A_0
HV 030	CAP022_03	19.734778	-72.1828611	0.6	3.8
HV 031	CAP031_01	19.720583	-72.1927778	0.7	5.4
HV 032	CAP031_02	19.721194	-72.1931667	0.7	4.5
HV 033	CAP002_01	19.735022	-72.1964117	1.1	4.7
HV 034	CAP002_02	19.735298	-72.1965733	1	6
HV 035	CAP002_03	19.735825	-72.19592	1.1	5.9
HV 036	CAP002_04	19.736107	-72.195415	1.2	5.9
HV 037	CAP013_01	19.72036	-72.214415	1.2	4.6
HV 038	CAP013_02	19.7206	-72.21472	0.9	4.2
HV 039	CAP014_01	19.710418	-72.207125	1	3.6
HV 040	CAP015_01	19.718092	-72.191845	1.3	3.7
HV 041	CAP029_02	19.74415	-72.20053	0.9	7.6
HV 042	CAP038_01	19.72685	-72.21132	1.2	4.2
HV 043	CAP038_02	19.72684	-72.21132	1.1	4.6
HV 044	CAP049_01	19.72504	-72.21897	1.3	11
HV 045	CAP049_02	19.722519	-72.21907	1.3	8.6
HV 046	CAP051_01	19.7374	-72.21177	1.7	3.9
HV 047	CAP051_02	19.73747	-72.21213	1.5	4.3
HV 048	CAP001_01	19.727215	-72.226985	3.1	4.6
HV 049	CAP001_02	19.727232	-72.227668	4.1	3.6
HV 050	CAP006_01	19.728298	-72.2240767	3.7	1.7
HV 051	CAP011_01	19.743245	-72.2169033	5.3	7.1
HV 052	CAP011_02	19.742444	-72.2164444	3.4	9.3
HV 053	CAP011_03	19.742444	-72.2163056	3.4	8.1
HV 054	CAP017_01	19.731117	-72.219965	1.6	3.6
HV 055	CAP017_02	19.731302	-72.2198217	1.48	2.6
HV 056	CAP017_03	19.731582	-72.2208233	3.38	2
HV 057	CAP023_01	19.73881	-72.19373	4.7	3.9
HV 058	CAP034_01	19.74056	-72.22299	16	2.2
HV 059	CAP034_02	19.74083	-72.22293	11	3.8
HV 060	CAP037_01	19.73677	-72.22235	13.2	5
HV 061	CAP037_02	19.73657	-72.22195	7.2	2.3

Appendix B2: Results of MASW profiles for the study area of Cap-Haitien

The MASW profiles were carried out in the framework of the seismic microzonation of the region of Cap-Haitien. The results listed in the following table are the parameter V_{S30}, directly compiled from the microzonation reports (Bertil et al. 2014; Roullé et al. 2014).

Table B.2 Summary of the MASW profiles compiled for the study area of in Cap-Haitien.

No	code	latitude	longitude	V_{S30} (m/s)
MASW 01	CSW003	19.734667	-72.1829444	196
MASW 02	CSW002	19.735022	-72.1964117	152
MASW 03	CSW011	19.742444	-72.2164444	304
MASW 04	CSW014	19.720583	-72.1927778	165
MASW 05	CSW015	19.76382	-72.19684	257
MASW 05	CSW031	19.73751	-72.21213	233
MASW 06	CSW001	19.7272	-72.2269	270
MASW 08	CSW021	19.74766	-72.20246	250
MASW 09	CSW022	19.74415	-72.20053	134
MASW 10	CSW026	19.72685	-72.21132	132
MASW 11	CSW029	19.72502	-72.21897	165
MASW 12	CSW017	19.76248	-72.19567	222
MASW 13	CSW018	19.7206	-72.21472	129
MASW 14	CSW006	19.766333	-72.1954444	261
MASW 15	CSW013	19.764	-72.2055	377
MASW 16	CSW016	19.7538	-72.2075	392
MASW 17	CSW020	19.74083	-72.22293	441
MASW 18	CSW007	19.751417	-72.2130556	845
MASW 19	CSW012	19.759222	-72.2053611	577
MASW 20	CSW025	19.73677	-72.22235	695
MASW 21	CSW032	19.7644	-72.1977	716

Appendix B3: EDA and variogram models for the study area of Cap-Haitien

The EDA and variogram modelling for the study area of Cap-Haitien were also performed using R Statistical Software (R Core Team 2024). The analysed data include the fundamental frequency (f_0) and amplitude (A_0) from the HVSR results, and the S-wave velocities (V_{S30}) derived from the MASW profiles and empirical relationships with the borehole data. The following graphs illustrate the results of the EDA and variogram modelling for the study area of Cap-Haitien.

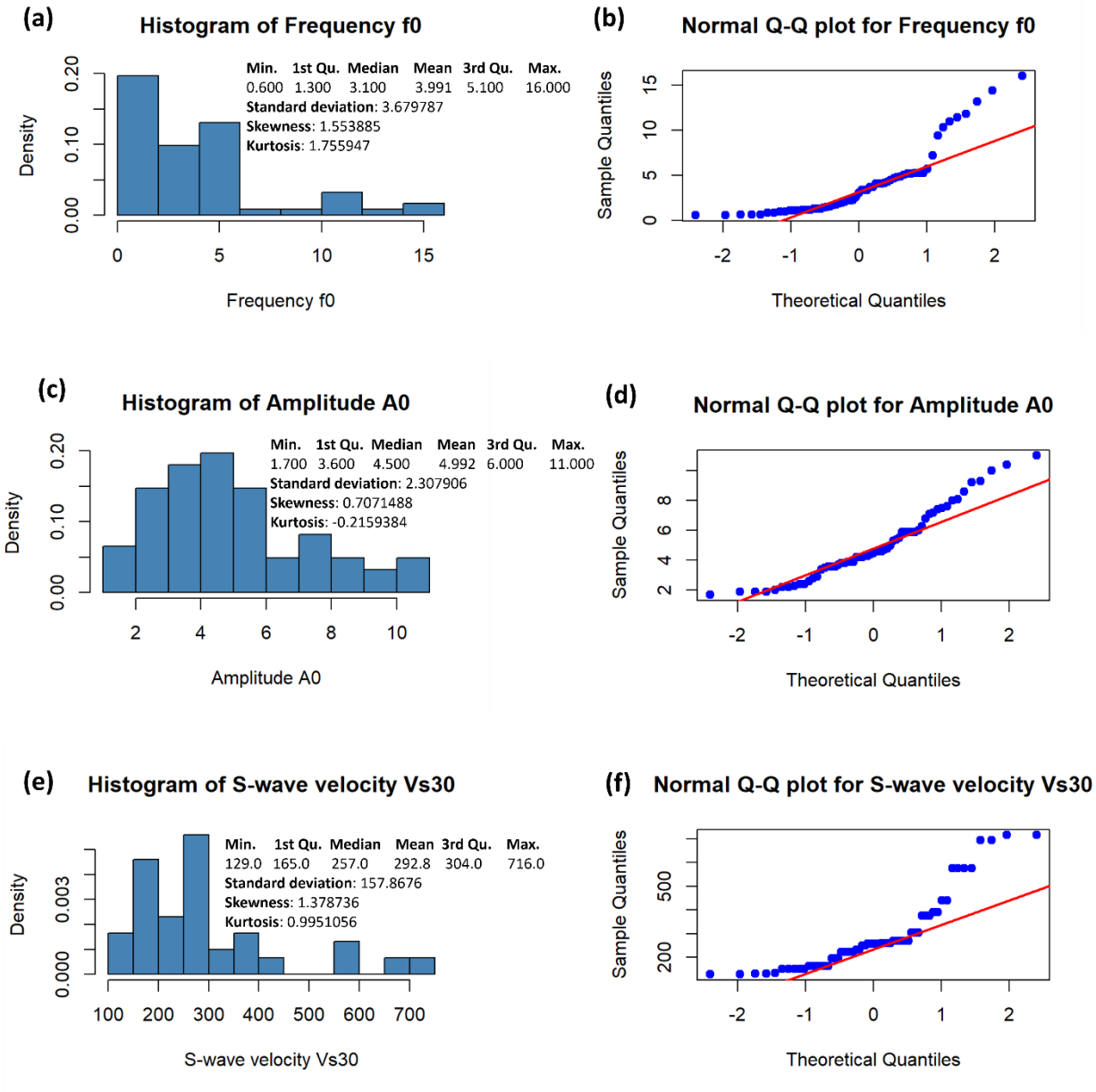

Fig. B.1 Exploratory data analysis for the study area of Cap-Haitien. **(a)** Histogram and descriptive statistics of the fundamental resonance frequency (f_0). **(b)** Normal Q-Qplot of f_0. **(c)** Histogram and descriptive statistics of the amplitude (A_0). **(d)** Normal QQplot of A_0. **(e)** Histogram and descriptive statistics of the S-wave velocities (V_{S30}). **(f)** Normal Q-Qplot of V_{S30}.

All three parameters (f_0, A_0 and V_{S30}) were transformed using a monotonic normalizing transformation (like for the study area of Anse-à-Veau). The transformed histograms demonstrate a substantial improvement in symmetry and variance homogeneity for all variables.

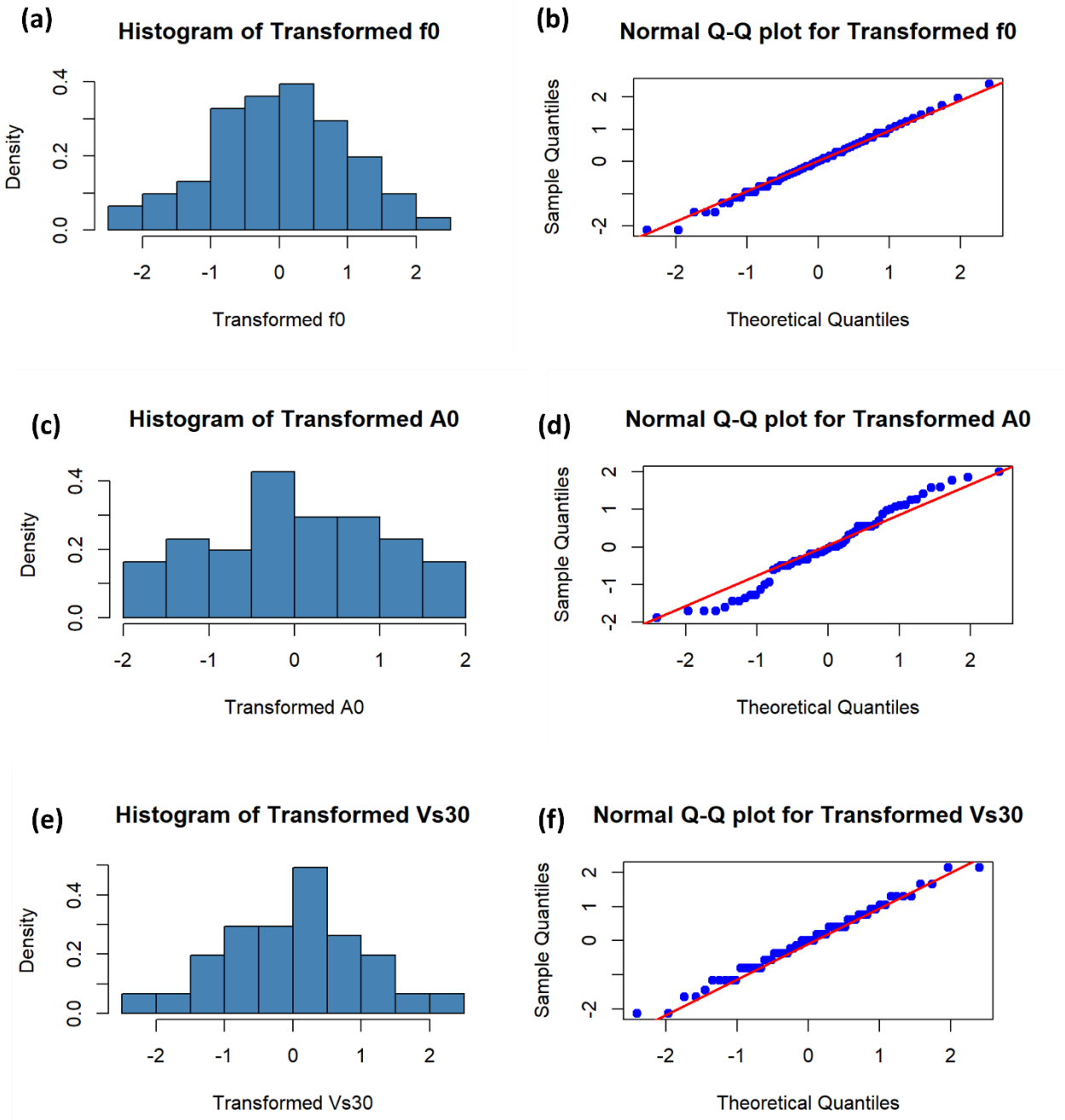

Fig. B.2 Exploratory data analysis for the study area of Cap-Haitien. **(a)** Histogram and descriptive statistics of the normal transform of f_0. **(b)** Normal Q-Qplot of the normal transform of f_0. **(c)** Histogram and descriptive statistics of the normal transform A_0. **(d)** Normal QQplot of the normal transform of A_0. **(e)** Histogram and descriptive statistics of the normal transform of V_{S30}. **(f)** Normal Q-Qplot of the normal transform of V_{S30}.

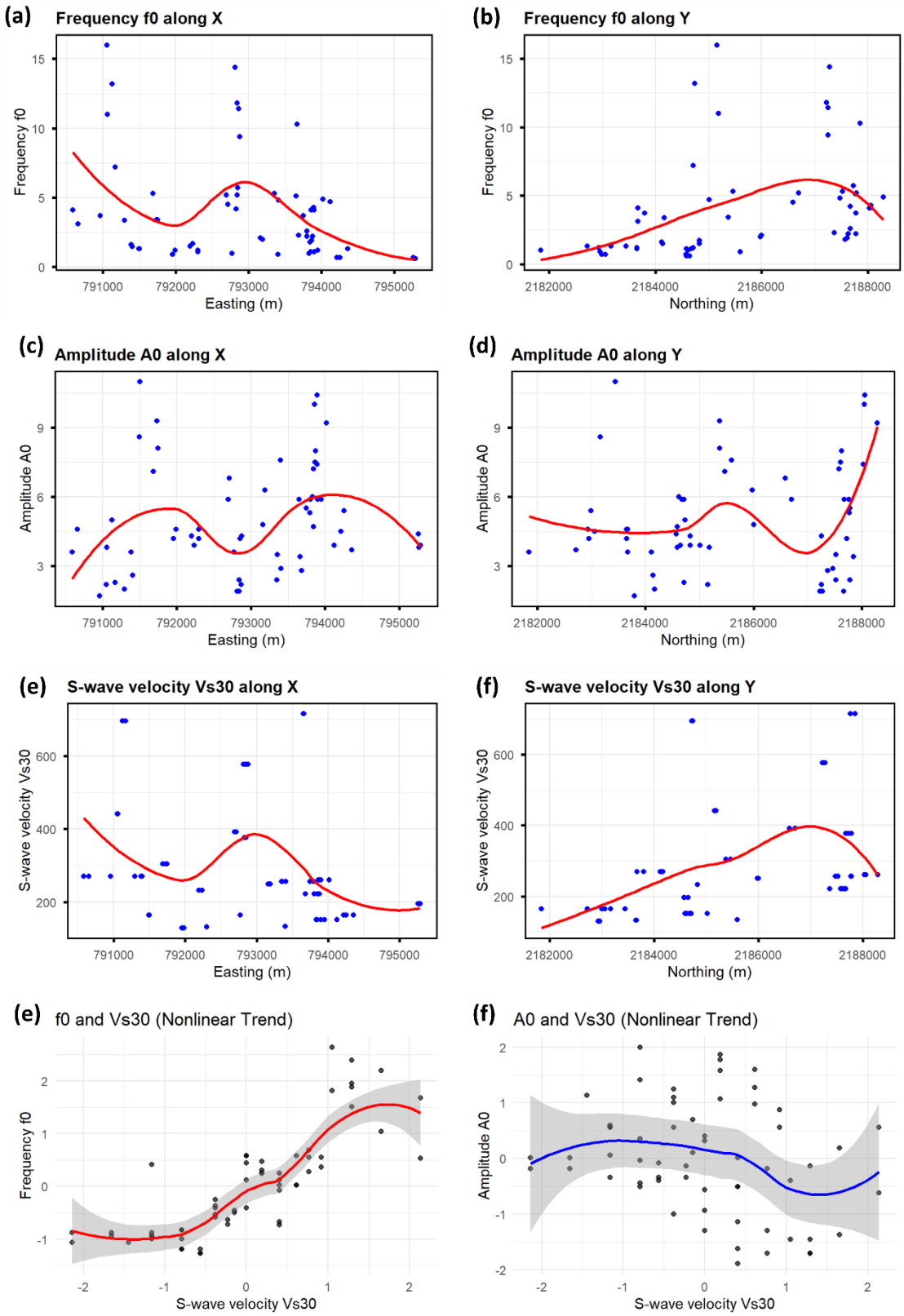

Fig. B.3 Exploratory data analysis for the study area of Cap-Haitien. **(a)** Spatial distribution of f_0 in the E-W direction. **(b)** Spatial distribution of A_0 in the N-S direction. **(c)** Spatial distribution of A_0 in the E-W direction. **(d)** Spatial distribution of f_0 in the N-S direction. **(e)** Spatial distribution of V_{S30} in the E-W direction. **(f)** Spatial distribution of V_{S30} in the N-S direction. **(g)** Nonlinear trend of V_{S30} with f_0. **(h)** Nonlinear trend of V_{S30} with A_0.

Like in the case of Anse-à-Veau, the variogram models (at the left) and maps (at the right) are presented for the three principal variables: the fundamental resonance frequency f_0, the amplitude A_0, and the S-wave velocities V_{S30}.

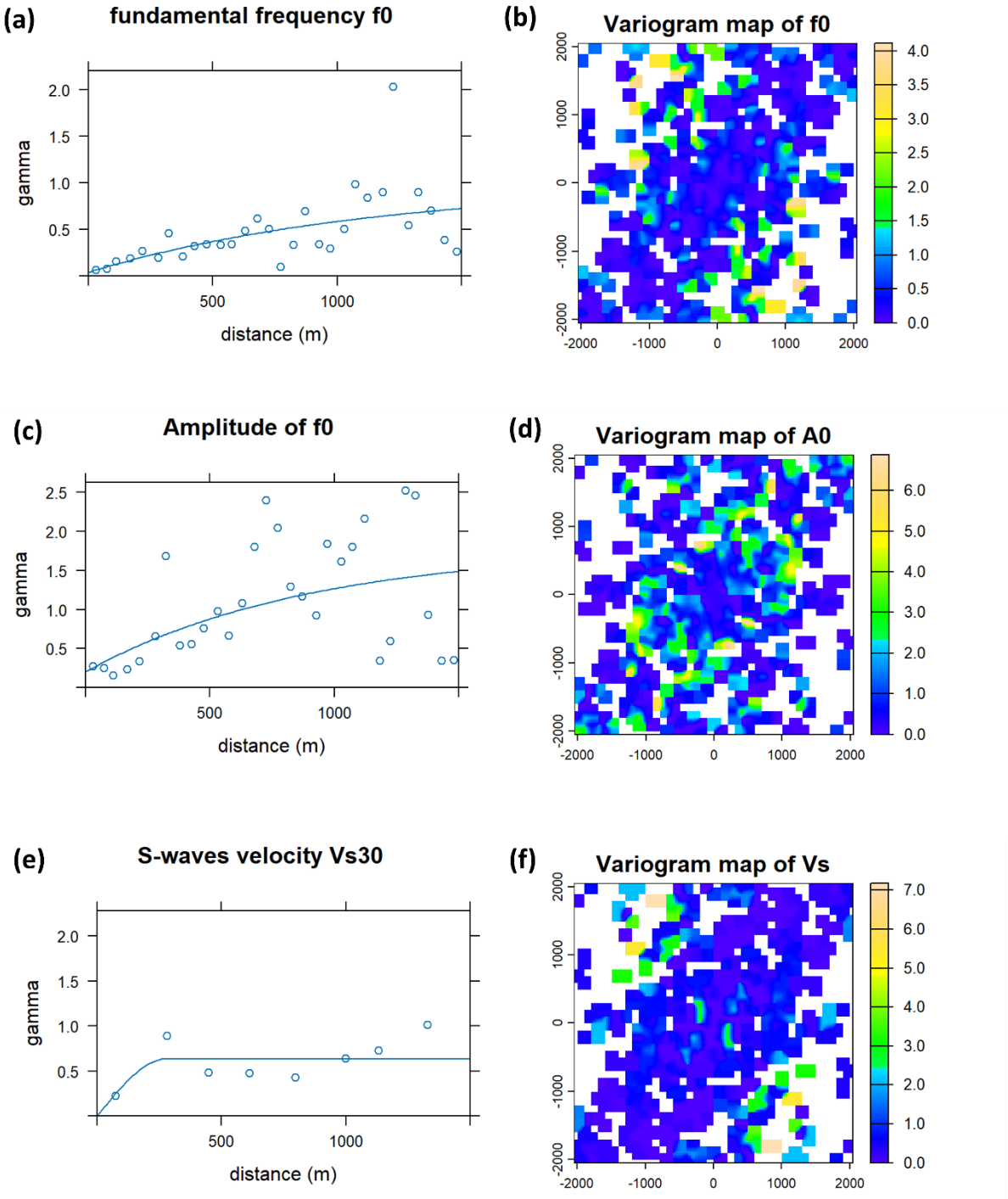

Fig. B.4 Variogram modelling of geophysical data in the study area of Cap-Haitien. **(a)** Variogram model of f_0. **(b)** Variogram map of f_0. **(c)** Variogram model of A_0. **(d)** Variogram map of A_0. **(e)** Variogram model of A_0. **(f)** Variogram map of A_0.

Appendix B4: Static results from numerical modelling for the study area of Cap-Haitien

The dynamic analysis was also carried out for the study area of Cap-Haitien using UDEC (Universal Distinct Element Code) developed by Itasca Consulting Group ©. The maximum variation of the unbalanced forces, during the quasi-static process, is presented here for one single profile extracted from the geomodel of the study area. Like in the case of Anse-à-Veau, two models have been established: one model characterized by only one uniform layer (very compact) across the whole model for pure topographic effect analysis, and another one characterized by different surface layers for combined lithological and topographic effect analysis.

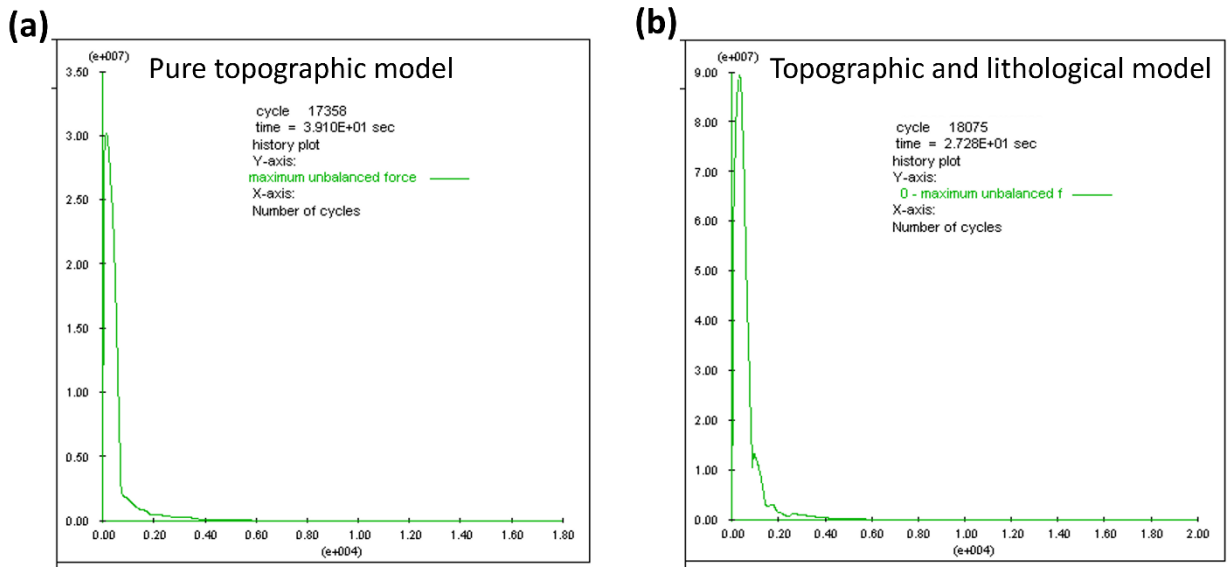

Fig. B.5 Variation of the maximum unbalanced force from the static analysis of the single 2D model of Cap-Haitien. **(a)** Topographic model. **(b)** Combined topographic and lithological model.